THE UNIVERSITY OF CHICAGO

SCIENCE FORECASTING AND DETECTOR DEVELOPMENT FOR A HIGH-FREQUENCY SOUTH POLE TELESCOPE CAMERA

A DISSERTATION SUBMITTED TO
THE FACULTY OF THE DIVISION OF THE PHYSICAL SCIENCES
IN CANDIDACY FOR THE DEGREE OF
DOCTOR OF PHILOSOPHY

DEPARTMENT OF ASTRONOMY AND ASTROPHYSICS

BY
KARIA RADHA DIBERT

CHICAGO, ILLINOIS
DECEMBER 2024

Abstract

I present a collection of forecasting, analysis, and instrumentation work related to the science cases and detector development for an upcoming camera for the 10-meter South Pole Telescope (SPT), called SPT-3G+. SPT-3G+ is a high-frequency, high-sensitivity camera designed to observe the cosmic microwave background (CMB) at 220, 285, and 345 GHz, targeting a variety of astrophysical and cosmological science cases. I first present forecasts of the expected sensitivity of SPT-3G+ to the recombination-era Rayleigh scattering of the CMB, a signal which probes the expansion and ionization history of the universe just after recombination, and whose first detection is sought by SPT-3G+. I find that, in combination with SPT-3G and Planck data, the expected detection significance is about 1.6-sigma, and that the cosmic infrared background, or CIB, is the major foreground inhibiting a higher detection significance. I next present an attempt to characterize the CIB using data from the 2019-2020 SPT-3G observing seasons, employing an existing physically-motivated model that relates CIB emission to an underlying star-formation rate. Instead of the CIB autospectrum, I fit the CIB x CMB lensing spectrum, which is less susceptible to systematic bias from contaminants such as galactic dust. Finally I present my work on the design, fabrication, and laboratory characterization of feedhorn-coupled direct absorbing 220 GHz microwave kinetic inductance detectors (MKIDs) for SPT-3G+. The detectors perform well from both a microwave and an optical perspective. Resonances are of the intended shape and quality, and are located within the intended microwave readout bandwidth. The detectors show background-dominated performance under a representative optical load, indicating that they possess the required sensitivity for use on the SPT-3G+ focal plane. They show an optical efficiency of approximately $\eta_{\mathrm{opt}} \approx 70\%$. I have begun scaling up to triangular submodule fabrication, and will discuss future plans for the optical testing of deployment-scale submodules.

Contents

List of Figures

List of Tables

Acknowledgements

I would first like to thank my advisor Brad Benson, and my thesis committee of Tom Crawford, John Carlstrom, and Wayne Hu for their attention to the progress of my research and their feedback on my thesis. Throughout my PhD, I worked with a wide range of people on a wide range of projects. Brad, thank you for supporting my work, for respecting my ideas, and for allowing me to function independently while remaining invested in my academic and personal well-being. Your jovial and reliable advising style really creates a positive atmosphere in which to do research. Thank you also for fostering creative expression in the group through fashion-forward t-shirt design and the curation of playlists. Pete, thank you for your continued mentorship in both detector physics and career navigation, and thanks for staying up late while in quarantine to provide me with remote tech support for cleanroom tools. Tom, thank you for demonstrating how to think precisely and logically about research problems, and for making the collaboration a better place through your activism. Erik, thank you for teaching me how to operate the fridge, and for your dedication to the lab. You are missed. Tyler, thank you for stepping up to help with the SLIM spectral response measurements and converting my inefficient code into a functional process. Yuuki, thank you for your guidance through the twists and turns of the CIB project and for your constant availability for discussions. Adam, thank you for being a thoughtful, consistent, and knowledgable resource on all scientific and laboratory topics. Thank you also to Amy, Tom Cecil, Marharyta, Clarence, and Zhaodi at Argonne, to Matt at Fermilab, and to Maclean at McGill who spent so much time transporting, fabricating, and testing detectors. And thank you to Shawn Manner for your administrative support and positive energy!

I would like to thank the grad students and postdocs who I worked with in and around SPT: Ryan and Elly, thanks for technical and moral support in the detector lab. Cyndia and John Hood, thank you for the spontaneous chats and general lab-based commiseration. Kyra and Emily, thank you for listening to my semi-coherent explanations of processes and equipment. I'm excited to see what you accomplish over the next few years! Paul and Alec, thanks for being a solid SPT cohort. Paul, thank you for your contributions to the party planning committee, and for the audacity. Alec, thanks for injecting surrealism into daily life. Kyle, thanks for being an overall cool person. Wei, thank you for being an exceptional office mate, and for your helpful introduction to SPT when I joined the group. Though I couldn't name every single person in the extended Chicagoland SPT group here, I would like to thank everyone for maintaining such a positive and collaborative community throughout my time in Chicago.

I would also like to thank my friends both in and outside of Chicago: Miranda, Jingxuan, Abby, Shreya, Grace, Tanvi, Carly, Jazmine, Natalia, Andrew, and Anastasia. Your friendship made life better, especially during lockdown. Finally I would like to thank my sister Kassi, my parents, and my extended family for their love and support.

This thesis is dedicated to the memories of Rekha Puranik and Eleanor Dibert.

Chapter 1

Introduction

1.1 The microwave sky

This thesis concerns the development of an instrument to observe the microwave sky. It is important to understand the components of the microwave sky to give context to the work presented here, which focuses on the detection and analysis of microwave signals. This introductory section briefly covers some of the cosmological, astrophysical, and atmospheric signals involved in this thesis.

1.1.1 The cosmic microwave background

Within three minutes of the Big Bang, the universe had cooled sufficiently to form protons and neutrons, which had begun to combine into the first light atomic nuclei. The universe at this time was still far too hot for the stable existence of neutral atoms, and any electron captured by a nucleus would shortly be freed again by an ionizing photon. The dense plasma of energized protons, neutrons, photons and free electrons was in constant electrothermal interaction. Photons could travel only a tiny fraction of the total size of the universe before Thomson scattering off of a nearby free electron. Thus the universe at this time was opaque to radiation. It would take another 380,000 years of expansion for the universe to become cool enough to allow the stable existence of hydrogen atoms. As the universe expanded and the photon population redshifted, it became less and less likely for a captured electron to encounter a photon with enough energy to release it. This period, known as recombination, marked the transition between an opaque universe and the transparent one we know today, in which photons travel freely across distances comparable to the size of the universe [1]. The last scattering surface, at redshift $z \sim 1100$ and a temperature of roughly $3000\,^{\circ}$K, is defined by the final interactions of primordial photons before their release to free-streaming. These oldest observable photons carry with them the imprint of the universe at the time of last scattering, and are observed today as the cosmic microwave background, or CMB. The primordial density fluctuations present on the last scattering surface source the primary temperature and polarization anisotropies of the CMB [2]. CMB experiments probe these fluctuations by measuring the CMB temperature, which is a scalar field, and the CMB polarization, which is a pseudo-vector field that is usually decomposed into the gradient-like "electric" field, called E-modes, and the curl-like "magnetic" field, called B-modes [3].

Penzias and Wilson's first detection of the CMB in 1965 manifested as an excess antenna temperature of $\sim 3.5^{\circ}$K that was shockingly isotropic [4]. This had major cosmological implications as it was the most compelling evidence yet for a hot dense primordial state of thermal equilibrium [1]. Thus began an era of increasingly ambitious experiments designed to characterize the CMB. The CMB temperature anisotropy was detected in 1992 by the COBE DMR instrument [5]. After accounting for the 3 mK dipole resulting from the Earth's peculiar velocity, the CMB temperature was confirmed to be uniform to less than one part in 10^5. The $2.726\,^{\circ}$K blackbody spectrum of the CMB was characterized using data taken at the same time by the COBE FIRAS instrument [6]. In 2002, the DASI experiment detected the polarization of the CMB, measuring the polarization E-mode spectrum with high significance and setting an upper bound on the B-mode amplitude [7]. Polarization B-modes were later detected by the SPTpol experiment [8]. The WMAP satellite made full-sky maps of the CMB temperature and polarization [9], followed by the Planck satellite, which made its own full-sky maps with increased frequency coverage and sensitivity [10]. The analysis of CMB data over the years has placed constraints on the standard ΛCDM cosmological model, pinning down the parameters that describe the evolution and geometry of the universe. Today there are numerous proposed and existing experiments designed to measure the CMB at high sensitvity across many frequency bands, in a shared effort to constrain the cosmological paramters with ever-increasing precision.

The CMB angular power spectrum

CMB experiments produce maps of the CMB temperature and polarization over some patch of the sky. This section will focus on the CMB temperature. The CMB temperature as a function of position can be written $T(\hat{\mathbf{n}})$, where $\hat{\mathbf{n}}$ points toward some spatial position in the sky. Functions on the sky can be expressed in terms of angular scale using spherical harmonics, which are a set of unique functions defined on the surface of a sphere for each pair of angular multipoles ℓ and $-\ell \leq m \leq \ell$ [2]. The spherical harmonic functions $Y_{\ell m}$ are orthonormal under the inner product:

$$\int d\hat{\mathbf{n}} Y_{\ell m}(\hat{\mathbf{n}}) Y^*_{\ell' m'}(\hat{\mathbf{n}}) = \delta_{\ell \ell'} \delta_{m m'}, \tag{1.1}$$

and the set of spherical harmonic functions are an orthonomal basis for the surface of a sphere. In other words, any function defined on a spherical surface can be written as a linear combination of spherical harmonic functions. The CMB temperature, which is a function defined on the celestial sphere, can be thus represented as a linear combination of spherical harmonics with multipole coefficients $a_{\ell m}$:

$$T(\hat{\mathbf{n}}) = \sum_{\ell=0}^{\infty} \sum_{m=-\ell}^{\ell} a_{\ell m} Y^*_{\ell m}(\hat{\mathbf{n}}) \tag{1.2}$$

$$a_{\ell m} = \int d\hat{\mathbf{n}} T(\hat{\mathbf{n}}) Y^*_{\ell m}(\hat{\mathbf{n}}) \tag{1.3}$$

In general, the power spectrum of a function over some orthonormal basis describes the distribution of the function's square amplitude over its basis modes. In this case, the CMB temperature angular power spectrum describes the amplitude of the CMB temperature fluctuations at each angular scale ℓ. For the CMB temperature, the power spectrum is defined as the variance of the spherical harmonic coefficients $a_{\ell m}$:

$$\delta_{\ell\ell'}\delta_{mm'}C_\ell = \langle a_{\ell m} a^*_{\ell' m'} \rangle \tag{1.4}$$

The primordial density distribution is thought to be sourced by quantum fluctuations that constitute a Gaussian random field, and the CMB we observe today arises from only one realization of that field [11]. Every amplitude $a_{\ell m}$ can be thought of as a random draw from its underlying Gaussian distribution. The expression for C_ℓ above is the theoretical CMB angular power spectrum, which is what we would measure if we could observe infinitely many realizations of the CMB and average all of them to obtain the true mean value of C_ℓ for each ℓ. Unfortunately, the scientific community does not currently have access to an infinite multiverse [12]. To estimate C_ℓ, we only have access to the $(2\ell + 1)$ modes corresponding to each value of m, which we can average over to estimate the angular power spectrum:

$$\hat{C}_\ell = \frac{1}{2\ell+1} \sum_{m=-\ell}^{\ell} |a_{\ell m}|^2 \,. \tag{1.5}$$

Measurements of the temperature power spectrum, and of the CMB polarization power spectra, are fit with cosmological models to extract information about the shape and content of the universe. As CMB measurements become more and more precise, constraints on these parameters tighten. However, the restriction to a limited number of m modes per multipole ℓ imposes an implicit cosmic variance on CMB angular power spectrum measurements:

$$\sigma^2_{\text{cosmic}} = \frac{2}{2\ell+1}\hat{C}^2_\ell. \tag{1.6}$$

No matter how sensitive of an instrument is used to measure the CMB, its measurement will always be limited by the cosmic variance. This motivates the exploration of secondary CMB anisotropies as a source of additional cosmological information.

1.1.2 Secondary CMB anisotropies

To reach our telescopes, CMB photons must to travel through the entire observable universe, from the last-scattering surface to the present day. Along the way, they interact with the contents of the universe. Such interactions can alter the paths and the energy of the CMB photons, distorting the CMB anisotropies from their primordial pattern and spectrum. These distortions are called secondary CMB anisotropies. There are many sources of secondary anisotropies, but I will only describe below those that are relevant to this thesis.

CMB Lensing

The gravitational lensing of the CMB arises from the interactions of CMB photons with the gravitational potentials of the large-scale structure of the universe. The local change in the curvature of spacetime caused by a dark matter halo's gravitational potential causes CMB photons to deflect around the halo, creating distortions in the CMB temperature and polarization anisotropies. The lensing potential ϕ sources the photon deflection angle $\alpha = \nabla\phi$. Analysis of the combined T, E, and B maps of the CMB allows the lensing potential to be reconstructed, producing a CMB lensing map [13]. This measurement is a probe of the mass distribution of the universe over cosmic time, and provides additional cosmological information to that offered by the primary CMB alone. Lensing maps and power spectra are often presented in terms of the unitless surface density:

$$\kappa = \frac{1}{2}\nabla^2\phi, \tag{1.7}$$

which can be thought of as the gravitational equivialent of the charge density in an electromagnetic field. The CMB lensing signal peaks around redshift $z = 2$, which is halfway between the last-scattering surface and the present day.

Kinematic and thermal Sunyaev Zel-dovich effects

The Sunyaev-Zel'dovich (SZ) effect refers to the inverse Compton scattering of CMB photons off of free high-energy electrons in the intracluster medium, which is the superheated plasma within galaxy clusters. The kinematic SZ effect (kSZ) occurs when the electrons that inverse Compton scatter CMB photons have bulk peculiar velocities relative to the Hubble flow. The anisotropy from the kSZ effect due to scattered CMB photons is proportional to the peculiar bulk velocity of the electrons that caused the scattering. The two largest contributions to the kSZ effect come from the reionization-era variation in ionization fraction ("patchy kSZ") and from the more recent bulk motion of massive galaxy clusters ("late-time kSZ") [14]. The patchy kSZ effect originates from the reionization period, when emission from dense star-forming regions ionized the universe in expanding bubbles. The scattering of CMB photons off of these dynamic bubbles sources the patchy kSZ effect. Measurements of the patchy kSZ effect can constrain the duration $\Delta z_{\rm re}$ and optical depth τ of reionization [15]. The late-time kSZ is sourced by the bulk motion of large galaxy clusters. Late-time kSZ measurements can be used to study the growth and evolution of cosmic large-scale structure [16]. The thermal SZ effect (tSZ), which occurs when intracluster electron temperatures are extremely high, and is significantly brighter than the kSZ effect at the frequencies considered in this work. The energy imparted to the scattered CMB photons via the tSZ effect depends primarily on the temperature of the intracluster medium [17]. The tSZ effect causes hot or cold spots (depending on observation frequency) to appear in CMB maps at the locations of galaxy clusters, and is used to identify these clusters and to characterize their properties [18]. It also causes a characteristic distortion to the primary CMB power spectrum.

Recombination-era Rayleigh scattering

Just after recombination, the universe is not fully transparent to CMB photons as is often assumed; rather the photons are able to scatter off of newly formed neutral hydrogen atoms. Because the size of the hydrogen atom is much smaller than the wavelength of the CMB at this time, this is a Rayleigh scattering process, with a frequency-dependent cross-section which scales as ν^4. The recombination-era Rayleigh scattering of the CMB effectively forms a second scattering surface after recombination whose redshift is frequency-dependent [19]. This second scattering of the CMB results in small frequency-dependent distortions to the CMB temperature and polarization anisotropies, inducing a blurring effect at small angular scales. The amplitude of the Rayleigh scattering signal is only a few percent of that of the primary CMB anisotropy and has not yet been detected at high significance. A measurement of the Rayleigh scattering signal would be valuable, as it probes the CMB at a slightly lower reshift than at recombination, adding additional information that can help break degeneracies in the parameter constraints produced by current recombination-only measurements of the CMB. In particular, a measurement of the Rayleigh scattering signal would independently constrain the primordial helium fraction Y_{He}, which is degenerate with the effective number of relativistic neutrino species N_{eff} in current models [20].

1.1.3 Astrophysical signals

There are many signals of astrophysical interest which are viewed as foregrounds to the CMB. I will describe a small selection of those which are relevant to this thesis.

Extragalactic

The primary component of extragalactic microwave emission at the wavelengths considered in this work is the cosmic infrared background, or CIB. The CIB is sourced by ultraviolet emission from young stars inside the dense molecular clouds of gas and dust that comprise active star-forming regions. The stellar emission is absorbed by the surrounding dust and re-emitted at infrared wavelengths. The aggregate redshifted infrared emission from all the star-forming galaxies in the universe makes up the CIB [21]. CIB emission is often divided into a clustered component that traces cosmic large-scale structure, and a shot-noise component from bright sources in the low-number-density regime. The CIB is often viewed as a nuisance foreground to the CMB, as it dominates CMB temperature power spectra at high frequencies and at small angular scales. An accurate understanding of the CIB and the ability to remove it from sky maps would increase the sensitivity of CMB experiments to some of the secondary anisotropies described above. The development of a physically motivated CIB model that fits existing observational data is a topic of ongoing study [22]. Such modeling also has the potential to extract astrophysical information from the CIB as a tracer of cosmic star-formation history. An understanding of the relationship between star-formation and CIB emission would allow CIB measurements to be used to probe the formation and evolution of star-forming galaxies throughout cosmic time. Another source of extragalactic emission comes from radio-bright galaxies. Radio galaxy emission is usually assumed to be Poisson-distributed, and contributes a shot-noise term to the total sky power spectrum [23]. Radio contamination is most significant at low observation frequencies.

Galactic

Like their extragalactic counterparts, dust grains in the Milky Way also absorb stellar radiation and re-emit it thermally. This emission is known to be partially polarized, resulting from the rotation and alignment of dust grains to magnetic fields in the Milky Way. Galactic dust emission is a known source of contamination to both CMB temperature and polarization measurements. However, work has been done to mitigate this by characterizing and subtracting dust emission from CMB power spectra [23, 24]. Another mitigation technique for deep-field surveys is to choose an observation patch that contains as little galactic dust as possible. For wide-field surveys, the presence of galactic dust is somewhat unavoidable, but data cuts can be imposed to remove regions of high dust contamination [25]. The galaxy also produces synchotron emission, which is a significant contaminant to the CMB at frequencies well below the peak of the CMB blackbody spectrum [26].

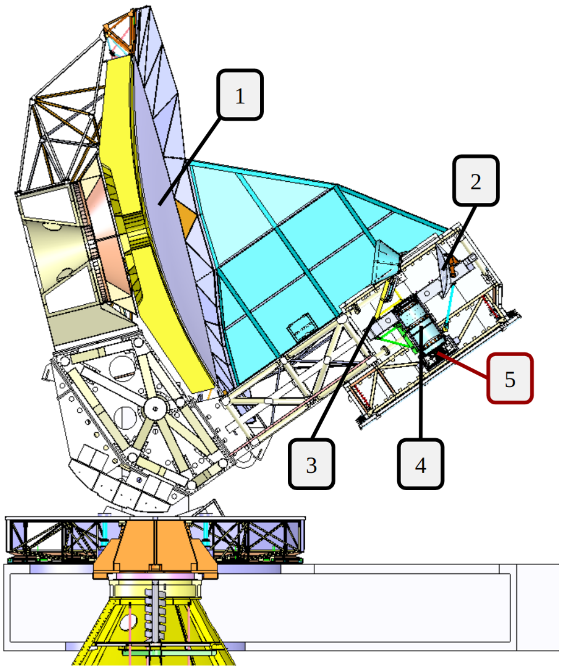

Figure 1.1: Diagram of the SPT, adapted from [28], showing the telescope's three mirrors and the current SPT-3G receiver. The primary, secondary, and tertiarly mirros are located at positions 1, 2, and 3 respectively. The cold optics is located at position 4, and the receiver's focal plane is located at position 5.

1.1.4 The atmosphere

Atmospheric emission at microwave wavelengths is primarily sourced by the rotational and vibrational transitions of ozone and water-vapor molecules suspended in the atmosphere. Ground-based CMB experiments choose their observation bandwidths to avoid these lines, at which the atmosphere is opaque to the CMB. However, precipitable water vapor in the atmosphere still contributes significantly to the loading and low-angular-scale noise of CMB experiments [27]. Because of this, ground-based experiments seek the driest possible environments at the highest possible altitudes in order to minimize the amount of water vapor between the telescope and the signals of interest. Atmospheric water vapor is distributed anisotropically (in clouds) and its distribution varies on short timescales, so water vapor emission can be averaged down over long observation periods.

1.2 The South Pole Telescope

The South Pole Telescope (SPT) is a 10-meter diameter sub-millimeter quality telescope located at the Amundsen-Scott South Pole station in Antractica [29, 30]. The SPT is designed to make high-sensitivy, high-angular resolution measurements of the mm/sub-mm sky, targeting science cases in cosmology and astrophysics. The South Pole is the best developed site on Earth for mm/sub-mm wave observations, with its high-altitude and low precipitable water vapor. Though the weather in Antarctica can change on a dime, the South Pole site experiences relatively stable weather conditions [30, 31]. Additionally the South Pole enjoys six months of continuous darkness during the winter, minimizing atmospheric changes related to the diurnal cycle. This, coupled with the fact that the same sky is always above the horizon at the South Pole, allows the SPT to observe continuously throughout the winter season, with breaks only for maintence and calibration.

The SPT is an off-axis Gregorian telescope, whose optics are designed for high throughput and minimal loss from optical abberations, reflections, and scattering [32, 30, 28]. A diagram of the telescope, adapted from [28], is shown in Figure 1.1. Light from the sky enters the telescope at the 10-meter primary mirror, located at position 1 in Figure 1.1. It then passes through a Zotefoam window into the telescope cabin, where it hits the 1.7-meter secondary mirror, located at position 2 in Figure 1.1. Though previous receivers coupled directly to the previous secondary mirror, the current SPT-3G receiver makes use of a 0.8-meter flat tertiary mirror, located at position 3 in Figure 1.1. Light reflects off of the tertiary mirror and into the cryostat through a vacuum window and a series of infrared filters. The receiver is housed in a cryostat containing the cold optics and detector-filled focal plane. This cryostat is the cyan-colored cylindrical object located at position 4 in Figure 1.1, within which the cold optics can be seen. Light passes through the cold optics and terminates on the focal plane, which is located at position 5 in Figure 1.1.

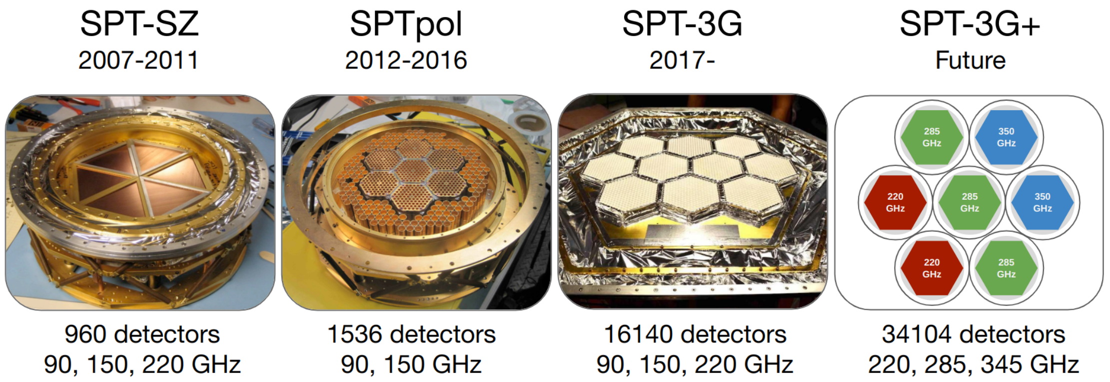

Figure 1.2: Evolution of South Pole Telescope receivers. Receiver photos were taken by Brad Benson.

1.2.1 SPT evolution

Though Figure 1.1 shows the SPT-3G receiver, which is currently operating on the telescope, the SPT has completed two previous surveys with earlier-generation receivers. These are the SPT-SZ [30] and the SPTpol [33] receivers. The SPT-SZ survey was the inaugural survey on the South Pole Telescope. From February 2007 until November 2011, the SPT-SZ receiver observed fields totaling 2500 square degrees at 95, 150 and 220 GHz [30]. This survey produced fine angular-scale measurements of the CMB primary temperature anisotropy and of secondary anisotropies, particularly the SZ effect [34, 35, 36, 37], which were used to constrain cosmological parameters and to identify new galaxy clusters at high redshfit [38, 39, 18] and massive dusty star-forming galaxies [40, 41]. The SPT-SZ focal plane consisted of 960 feedhorn-coupled transition edge sensor (TES) bolometers [30, 42]. A photo of the SPT-SZ focal plane is shown in the left panel of Figure 1.2, and its detector counts are given in Table 1.1.

In January 2012, a new receiver was installed on the SPT, and the second-generation SPTpol survey began [33]. Until late 2016, SPTpol observed fields totaling 500 square degrees of the sky at 90 and 150 GHz. As its name implies, SPTpol was optimized for measurements of the CMB polarization, in particular the measurement of inflationary and lensing polarization B-modes. The SPTpol survey made the first detection of B-modes [8] and measured the B-mode angular power spectrum [43, 44, 45]. It also improved upon cosmological constraints using measurements of the CMB temperature and E-mode angular power spectra [46, 47] as well as the CMB lensing potential [48, 49, 50], and expanded the depth and breadth of the SPT cluster-finding effort [51, 52, 53]. The SPTpol receiver contained 768 feedhorn coupled pixels, with each pixel consisting of two detectors coupled to orthogonal polarization modes. This equates to a total of 1536 TES bolometers across the SPTpol focal plane [33]. A photo of the SPTpol focal plane is shown in the second panel of Figure 1.2, and its detector counts are given in Table 1.1.

1.2.2 SPT-3G

The SPT-3G receiver is currently in operation on the SPT, and was installed in late 2016. Observations began in January 2017, however the first year of SPT-3G observation did not achieve the expected sensitivity targets. In late 2017, the entire focal plane was replaced with a new set of wafers as part of a series of improvements intended to increase the receiver's total sensitivity [54]. The improvements were successful; the survey resumed in 2018 and is ongoing. The main SPT-3G survey observes a 1500 square degree patch on the sky that overlaps with both the SPT-SZ and SPTpol main patches [54], and is designed to observe the CMB polarization with unprecedented sensitivity and angular resolution [55]. In addition to the main winter survey, there is also a 2650 square degree summer survey and a year-long 6000 square degree wide survey [56]. Though still operating, SPT-3G has already produced a myriad of scientific results. The first year of survey data has again produced measurements of the CMB temperature and polarization power spectra and the associated constraints on cosmological parameters [57, 58, 59], as well as a measurement of the CMB lensing potential [60]. Due to its high resolution and multi-frequency coverage, SPT-3G has proved to be well-suited to the detection of millimeter transients, including stellar flares, asteroids, and extragalactic sources [61, 62, 63]. Analysis of data from later years of the SPT-3G survey is underway.

	Frequency	Pixel count	Detector count
SPT-SZ	90	161	161
	150	483	483
	220	322	322
SPTpol	90	180	360
	150	588	1176
SPT-3G	90	2690	5380
	150	2690	5380
	220	2690	5380
SPT-3G+	220	4872	9744
	285	7308	14616
	345	4872	9744

Table 1.1: Evolution of the detector counts of SPT receivers.

In fact, the data used for the analysis done in Chapter 3 of this thesis comes from the 2019-2020 observation seasons of SPT-3G.

The SPT-3G receiver consists of 2690 tri-chroic pixels distributed across ten hexagonal wafers [28]. Each pixel contains a lenslet-coupled broadband sinuous antenna. Light received by the antenna passes through on-chip filters that define the observing bands and is deposited onto one of six TES bolometers that cover two orthogonal polarization angles for each of the three SPT-3G frequency bands [28]. This equates to a total of 16140 TES bolometers across the full SPT-3G focal plane, which is an order-of-magnitude increase on the detector count of SPTpol. The detectors are read out using a frequency-domain multiplexing system optimized to handle large numbers of detectors over a large frequency bandwidth [64, 54]. The SPT-3G design attempted to both maximize the available field of view of the SPT telescope, while also maxing out the detector count that could be readout for a trichroic TES detector architecture [54]. A photo of the SPT-3G focal plane is shown in the third panel of Figure 1.2, and its detector counts are given in Table 1.1.

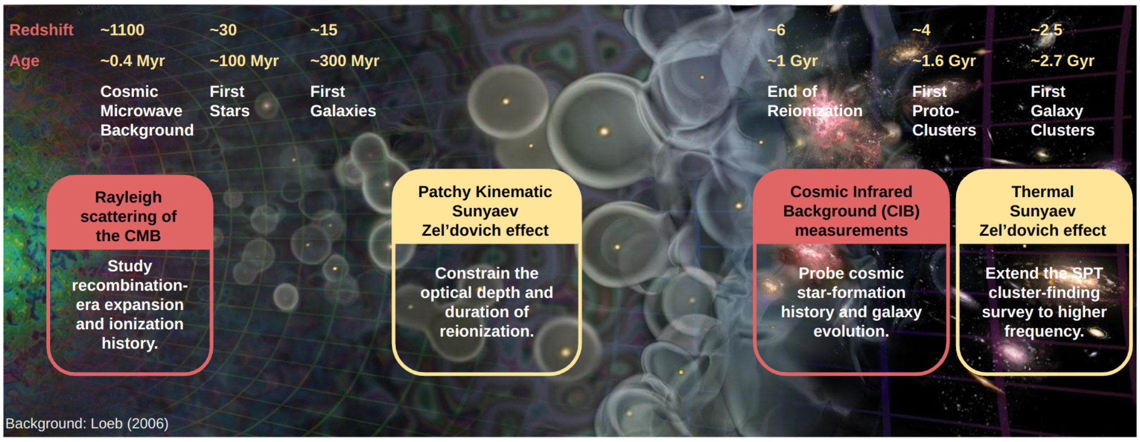

Figure 1.3: Schematic of some SPT-3G+ science cases superimposed on a depiction of the evolution of cosmic structure. The red Rayleigh scattering and CIB science cases make up portions of this thesis. Background taken from Loeb (2006) [65].

1.3 SPT-3G+: A high-frequency camera for the South Pole Telescope

At the conclusion of the SPT-3G survey, the current SPT-3G receiver will be replaced by SPT-3G+, the fourth-generation receiver and focal plane, shown as a sketch in the right panel of Figure 1.2. Though my PhD work consists of three seemingly disparate topics, they all relate to the science targets and instrumention development for the SPT-3G+ camera. This section will discuss the SPT-3G+ science goals and the SPT-3G+ instrument to provide context for the work presented in the following chapters.

1.3.1 Scientific motivations

Observing the same 1500 square degree field as its predecessor, SPT-3G+ will enable high-sensitivity measurements of the temperature and polarization of the mm/sub-mm sky at observing frequencies of 225, 285, and 345 GHz. In combination with existing SPT-3G 90 and 150 GHz maps, SPT-3G+ will pursue a variety of astrophysical and cosmological observables [66]. Some of these are shown schematically in Figure 1.3. The background of Figure 1.3 depicts the evolution of cosmic structure from the time of recombination until the present day, and is taken from Loeb

(2006) [65]. On the left side of Figure 1.3, the CMB is released at recombination at $z = 1100$. One of the earliest signals of interest for SPT-3G+ is the recombination-era Rayleigh scattering of the CMB, which originates just after this. The universe is mostly neutral until roughly $z = 30$, at which time the clouds of gas and dust throughout the universe have collapsed into sufficiently dense structures to form stars. Emission from these stars begins to ionize the surrounding gas in expanding bubbles around the star-forming regions. As more structure forms, producing more ionizing emission, the bubbles grow until the universe is fully reionized. The second signal of interest for SPT-3G+ is the patchy kinematic Sunyaev Zel'dovich effect, which originates from this period of reionization, and is shown in the second box in Figure 1.3. As the universe evolves past the epoch of reionization, star-formation continues. Stellar emission from star-forming regions is absorbed by the surrounding dust and re-emitted as the CIB. Another science goal of SPT-3G+, shown in the third box in Figure 1.3, is the measurement and characterization of the CIB for both foreground removal and to extract astrophysical information. Finally, SPT-3G+ will use the thermal Sunyaev Zel'dovich effect to detect clusters and galaxies at high redshift, probing the early evolution of these objects [66], as indicated by the final box on Figure 1.3. Below, I will expand on each of the science cases shown in Figure 1.3 along with a few other SPT-3G+ science goals. The Rayleigh scattering and CIB measurement science cases in Figure 1.3 are highlighted in red, as these topics each constitue a chapter of my thesis work. These will be introduced briefly below in the context of SPT-3G+, and then described again in much greater detail in Chapters 2 and 3.

Detection of the Rayleigh scattering of the CMB

As mentioned above, SPT-3G+ seeks to make a first detection of the recombination-era Rayleigh scattering of the CMB. Such a detection would require successfully separating the Rayleigh scattering signal from the CMB, SZ effect, CIB, and other foregrounds including the atmosphere and galactic dust. To do this requires high-sensitivity measurements at multiple frequency bands across the CMB blackbody spectrum. The combination of the SPT-3G and SPT-3G+ frequency bands is well-placed to make such a detection. Since the Rayleigh scattering signal scales with frequency as ν^4, the signal is higher in the SPT-3G+ bands, just past the peak of the CMB blackbody spectrum, than it is in SPT-3G. Combining SPT-3G+ with SPT-3G (and eventually with high-frequency Planck data) enables foreground separation and the extraction of the Rayleigh scattering signal [67].

One portion of my PhD work is the development of a forecasting pipeline for detection of the Rayleigh scattering signal by ground-based CMB experiments. The noise model for this pipeline includes instrumental noise as well as foreground contributions from atmospheric, galactic, and extragalactic sources. The result of this work, which will be discussed extensively in Chapter 2, shows that in combination with both SPT-3G and Planck data, SPT-3G+ has the potential to make the first detection of the Rayleigh scattering signal. It also shows that the significance of the Rayleigh scattering detection could be majorly enhanced by effective subtraction of the CIB.

Probing reionization with the kSZ effect

The second SPT-3G+ science goal mentioned above is the measurement of the combined patchy and late-time kSZ effects to probe the reionization era. The kSZ is a small-amplitude signal with respect to the primary CMB, and its measurement requires the precise separation of the kSZ signal from the CMB, tSZ, and all atmospheric, galactic, and extragalactic foregrounds. As it traces large-scale structure, the kSZ is correlated with the tSZ and CIB and residual contamination from these foregrounds can bias kSZ measurements [14]. As with Rayleigh scattering above, the deep high-frequency SPT-3G+ maps in combination with existing lower-frequency SPT-3G maps are well-suited to perform the component separation necessary to extract a low-noise detection of the kSZ signal. Collaboration members have developed a forecasting pipeline for constraints on Δz_{re} and τ from SPT-3G+, using a method that combines the kSZ 2-point and 4-point functions to distinguish the patchy and late-time kSZ dependence on these parameters [14]. Similar work applied to SPT-3G+ found that when combined with Planck data, SPT-3G+ could constrain τ at a 20% tighter level than the currently existing primary CMB constraint [66].

Measurement and characterization of the CIB

Both of the above science cases involve the detection of a signal whose amplitude is very small compared to the primary CMB, and which requires foreground removal to detect. At the SPT-3G+ frequencies, the dominant foreground is the CIB, especially at small angular scales. While the CIB can be mitigated using internal linear combination methods, such as those employed in Chapter 2 and in the kSZ forecasting mentioned above [14], a physically-motivated well-fitting model for the CIB remains elusive. The dominance of the CIB in the SPT-3G+ bands makes SPT-3G+ an excellent platform for CIB measurements. The CIB angular power spectra from the SPT-3G+ survey can be compared to proposed CIB models. Chapter 3 of this thesis contains an attempt to constrain cosmic star-formation rate density using the model from [22]. Rather than fit the CIB autospectrum, I fit the cross-spectrum between the CIB and the CMB lensing signal using data from the SPT-3G 2019-2020 observing seasons. This work and its implications for SPT-3G+ is discussed extensively in Chapter 3.

Detection of clusters and galaxies at high redshift

SPT-3G+ will continue the tradition of cluster-finding with the SPT, and will extend the SPT cluster catalog to higher frequency and higher redshift [66]. With its high angular resolution and sensitivity to dust emission, SPT-3G+ is expected to identify clusters at $z > 2$ using measurements of the tSZ effect. The dust sensitivity of SPT-3G+ will also allow it to detect dusty star-forming galaxies at much higher redshifts than previous surveys. These discoveries of high redshift clusters and galaxies will probe the relationship between the state of the cluster environment and the evolution

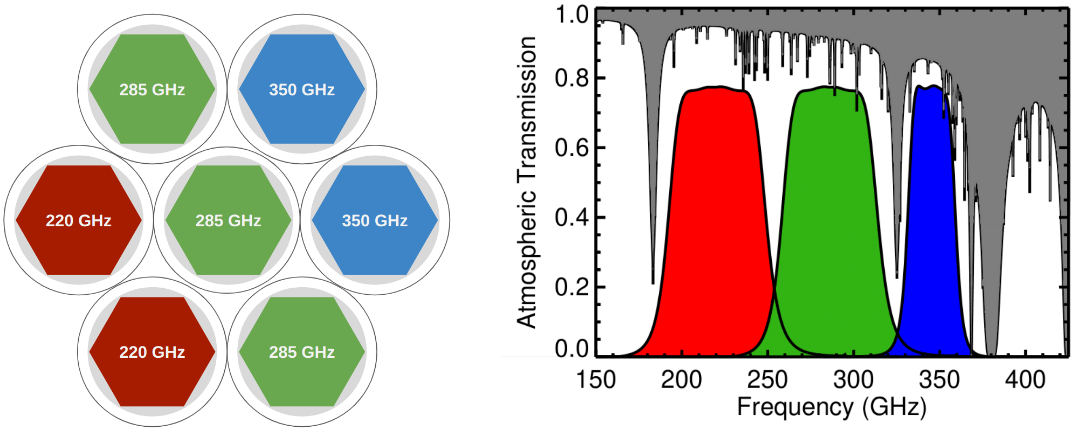

Figure 1.4: *Left:* A cartoon depiction of the SPT-3G+ focal plane, which consists of seven indpendent optics tubes. Each optics tube is populated with a hexagonal wafer of 5000 monochroic MKIDs at 220, 285, and 345 GHz *Right:* Simulated SPT-3G+ bands (red, green, and blue) compared to South Pole average atmospheric transmission (gray), created by Brad Benson.

of galaxies at early times[66].

Additional SPT-3G+ science

In addition to the science cases mentioned above, SPT-3G+ will detect transient sources in the mm/sub-mm sky. The SPT has already detected hundreds of transient sources, including stellar flares, asteroids, and extragalactic blazars [63, 62, 68], and SPT-3G+ will extend SPT transient observations to higher frequency and angular resolution. Another SPT-3G+ science case is the characterization of polarized Galactic dust. SPT-3G+ has the potential to make the best measurement yet of galactic dust polarization in the main 1500 square degree SPT field. These high-resolution dust measurements will be useful to avoid foreground contamination when using SPT-3G data for delensing purposes [66]. Finally, a Galactic/wide 8500 square degree survey will map dusty emission within the Milky way, and observe Galactic transients. High-resolution measurements of the Milky Way dust emission could help unlock new information about the turbulence and magnetic fields of the interstellar medium [66].

1.3.2 The SPT-3G+ Receiver

The SPT-3G+ science goals require an experiment with sensitivity beyond that which is presently available. As demonstrated by previous SPT cameras, the sensitivity of superconducting TESs for CMB observation is no longer limited by individual detector noise, but by temporal fluctuations in the incident photon signal. Detectors that achieve this performance are said to be photon-noise dominated or background-dominated. Since the detector noise is so much lower than that of the photon noise, the only way to increase the sensitivity of the focal plane is to increase the density of detectors. The detector density of the SPT-3G focal plane is now approaching a practical limit due to the number of wires (and hence bondpads around the edge of each wafer) that are needed to bias and readout each of SPT-3G's 16k TES detectors [69, 28]. The drive for even greater detector density motivates the use of a more multiplexable CMB detector technology on the SPT-3G+ focal plane. For this reason, the SPT-3G+ detectors will be microwave kinetic inductance detectors (MKIDs).

MKID focal plane

Microwave kinetic inductance detectors (MKIDs) exploit the change in inductance produced by the breaking of Cooper pairs in a strip of superconducting metal. When this superconducting strip is coupled to a capacitor, the resulting circuit resonates at a specific frequency. If exposed to a sufficiently energetic photon source, the resonant frequency shifts as incident photons break Cooper pairs inside the strip, and this frequency shift can be used to monitor the intensity of incident light [70]. A more detailed and quantitative explanation of how MKIDs operate is given at the beginning of Chapter 4. MKIDs are advantageous for use in densely-packed arrays, as their resonator-based design makes them naturally multiplexible in the frequency domain. With sufficient control of the resonance shape through design and material quality, hundreds or even thousands of MKIDs can be read out from a single feedline. Increased multiplexing reduces the number of coaxial cables and cold amplification required to operate the detectors, which in turn reduces the amount of cooling power needed to keep the detectors at their operating temperature. Another advangate of MKIDs is their relatively simple fabrication process compared to that of the traditional TES bolometer. This allows for rapid prototyping and testing of devices, which accelerates the array development cycle. These advantages have made MKIDs desirable as a detector for high-density telescope arrays. Several astrophysics and cosmology experients utilizing MKID arrays have been deployed in recent years [71, 72, 73] or are planned for upcoming years [74].

SPT-3G+ will use seven arrays of densely-packed MKIDs to achieve its sensitivity goals. Each of the hexagonal wafers in Figure 1.4 will be populated with 4872 MKIDs, for a total SPT-3G+ detector count of 34104 MKIDs on the focal plane. This is more than a factor of two increase in detector density from the current SPT-3G camera. These will be some of the most dense CMB arrays deployed to-date, with a pixel-to-pixel spacing of 2.2 millimeters [75]. Each of the seven arrays will observe a single frequency, as shown schematically in Figure 1.4. The design of each array will be modular, and will consist of six triangular wedges containing 812 MKIDs each. The ambitious spatial density and multiplexing goals of the SPT-3G+ focal plane present many design, fabrication, and testing challenges. The instrumentation portion of my PhD work attempted to address some of these challenges through the design of densely-packable feedhorn-coupled MKID pixels at each of the SPT-3G+ observation frequencies. The design, fabrication, and testing of MKIDs for the SPT-3G+ focal plane is detailed in Chapters 4 and 5.

Optics and Cryostat

While all previous SPT cameras consisted of a single optics tube, the SPT-3G+ camera will consist of seven seperate optics tubes, each terminating on a wafer of single-frequency MKIDs. A rendering of the SPT-3G+ cryostat design showing the optics tubes is shown in the left panel of Figure 1.5. The lenses, shown in the optical ray-trace diagram in the right panel of Figure 1.5, will be 20cm diameter silicon

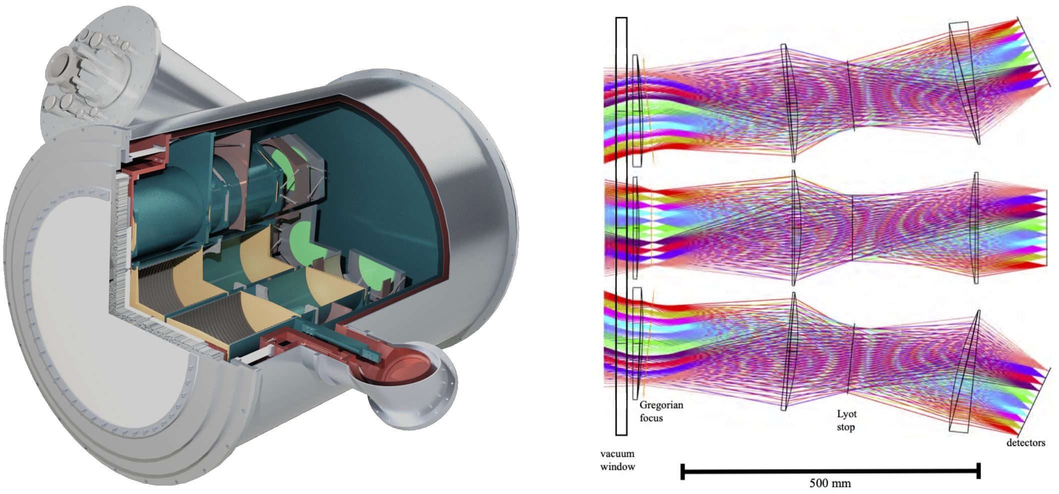

Figure 1.5: *Left:* A cutaway rendering of the SPT-3G+ cryostat with the optics tubes shown. The postions of the detector wafers are indicated in green. This rendering was created by Alec Hrycuik. *Right:* Ray-trace diagram of the SPT-3G+ optics configuration, created by Tony Stark.

lenses with meta-material anti-reflection coatings. Each tube contains three silicon lenses. Between the second and third lenses, is a Lyot stop designed to control time-reversed illumination of the primary mirror by terminating off-axis rays on a cold surface [66]. All tubes will share the same vacuum space and initial Zotefoam and alumina IR filters at 300K and 50K. Each tube will also have an individual metal-mesh low-pass filter at the 4K Lyot stop, whose cutoff depends on the observation frequency of that tube. The metal-mesh filter cutoffs determine the high end of the bandpass for each observation frequency.

The SPT-3G+ cryostat builds upon the design of the existing SPT-3G cryostat, and will replace the SPT-3G cryostat when deployed. It will be located at the same position in the telescope cabin as the SPT-3G cryostat (location 4 in Figure 1.1). A crucial addition to the SPT-3G+ cryostat is the change in final-stage cooling method from a three-stage 3He-3He-4He sorption refrigerator on SPT-3G to a dilution refrigerator (DR) on SPT-3G+. The increased cooling power offered by the DR is necessary to cool the detectors to their 100 mK operating temperature. Another advantage of the DR is that it does not need to be cycled once cold; while the helium-10 fridge requires gaseous helium to be recondensed into liquid periodically, the DR remains cold continuosly. This will allow observing to continue uninterrupted over the course of the South Pole winter. The seven optics tubes described above will share the same cryostat. Light from the tertiary SPT mirror will be coupled into the cryostat through a vacuum window made of ultra-high-molecular-weight polyethylene. The lenses and cold stages of the cryostat will be cooled to 4K by a pulse-tube cooler. The detector wafers, shown in green in the rendering in Figure 1.5 are further cooled to 100mK by the DR. For more information about cooling via helium dilution, see Section 5.1.1.

Readout

The readout setup for SPT-3G+ consists of a cold and warm phase. The cold readout electronics include coaxial cables running into and out of the cryostat. These are largely NbTi between temperature stages, and regular cryogenic copper-nickel cables for isothermal transitions. Each readout line will pass through a low noise amplifier (LNA) at the 4K stage [66]. This is the entirety of the cold readout for SPT-3G+, with a total of one input line, one LNA, and one output line per triangular subsection of each wafer. This comes out to an auspicious total of 42 readout lines in the SPT-3G+ cryostat. The simplicity of the cold readout phase underlines the natural frequency multiplexability of MKIDs. For the warm readout, SPT-3G+ is baselining the ICE readout system from McGill University, which is currently used to read out the SPT-3G TES bolometers. The ICE boards for SPT-3G+ have been modified with a specialized mezzanine board for MKID readout [76]. The boards are controlled using the hidfmux software package, which was also designed for MKID readout.

1.4 Structure of this thesis

My PhD work consists of three separate projects, which are all related to the SPT-3G+ camera. This chapter has provided general background information along with the scientific motivation and receiver design for SPT-3G+. Chapter 2 presents an analysis of the sensitvity of SPT-3G+, along with other upcoming ground-based CMB telescopes, to the reionization-era Rayleigh scattering of the CMB, one of the SPT-3G+ science targets. This work was published in [75], and the content of this paper is reproduced in this thesis with minor updates to the text. Chapter 3 describes a currently ongoing analysis project on the characterization of the CIB using the CIB × CMB lensing signal from SPT-3G data. This project also includes a forecast for the expected constraints on this model that will be achievable using SPT-3G+ data. The majority of this chapter is reproduced from a draft that is in preparation for future publication. Chapter 4 describes the design, simulation, and fabrication of MKIDs for the SPT-3G+ focal plane. This includes an overview of the physics of MKIDs, a discussion of design considerations for SPT-3G+, the resulting pixel and array designs, and the fabrication process for these detectors. Some subsections of this Chapter are reproduced from the conference proceedings [77] and [78]. Chapter 5 describes the testing of SPT-3G+ MKIDs. This includes documentation of the cryogenic testbed, readout electronics, and laboratory methods for each type of test used to characterize these detectors. It also includes the test results for SPT-3G+ 220 GHz detectors. Again, some subsections of this chapter are reproduced from [77] and [78]. Finally, I conclude in Chapter 6.

Chapter 2

Forecasting sensitivity to the Rayleigh scattering of the CMB

The following work is reproduced from [67].

2.1 Introduction

Cosmic microwave background (CMB) measurements continue to produce ever-tightening constraints on ΛCDM cosmological parameters. With several next-generation CMB experiments such as SPT-3G+[77], Simons Observatory [79], and CCAT-prime [74, 80] deploying soon, and with CMB-S4 [81] on the horizon, we expect measurements of the primary CMB temperature and polarization power spectra to approach the cosmic variance limit in the coming decades. Further reduction in the uncertainties of cosmological parameters will thus require new and improved measurements of secondary CMB anisotropies. Secondary anisotropies are distortions to the primary CMB generated through interactions between the CMB and its environment over the course of its journey from last-scattering to detection. Gravitational lensing of the CMB is one example of a secondary anisotropy. Secondary CMB anisotropy can also be generated through the interaction of the CMB with neutral hydrogen atoms just after recombination. The usual picture after recombination is of a completely transparent post-recombination universe, but this is not strictly accurate. CMB photons are able to interact with neutral hydrogen atoms through a process known as Rayleigh scattering, in which CMB photons scatter off the induced dipoles of the hydrogen atoms. This interaction has a frequency-dependent cross section which is proportional to ν^4 [82, 19, 20]. Rayleigh scattering can be thought of as a screen just in front of the primary last-scattering surface, providing a frequency-dependent contribution to the primary CMB temperature and polarization signals.

The Rayleigh scattering of the CMB has a number of measurable effects on the CMB temperature and polarization power spectra. On small scales, the increased photon diffusion resulting from Rayleigh scattering leads to the suppression of both temperature and polarization anisotropies. The frequency dependence of the Rayleigh scattering cross section causes the size of the sound horizon to also be frequency dependent, leading to a shift in the locations of acoustic peaks in both the temperature and polarization power spectra. Additionally, Rayleigh scattering boosts E-mode polarization anisotropies on large scales. This results from the shift in the visibility function induced by the scattering of photons after recombination. Effectively, last scattering appears to happen later, at a time when the local temperature quadrupole is larger. This leads to increased E-mode anisotropies on the largest scales [20, 19]. High-sensitivity measurements of Rayleigh scattering have the potential to improve cosmological parameter constraints. It has previously been shown that the cosmological information available from Rayleigh scattering could significantly improve upon the constraint on the primordial helium abundance [20] and on primordial non-Gaussianity constraints [83]. It has also been shown that constraints could be placed on the expansion history and sound speed of the universe at recombination, which could provide information about the parameters upon which these observables depend [84, 20].

A detection of the Rayleigh scattering contribution to the CMB anisotropy is a primary science goal for the next camera on the South Pole Telescope (SPT), called SPT-3G+ [75]. This new higher-frequency camera will observe beyond the peak of the CMB blackbody spectrum, complementing the lower-frequency SPT-3G data [**?**

] (see Table A1). To estimate the signal-to-noise achievable on the Rayleigh scattering signal by the combined survey, we require a forecasting pipeline that includes the effects of all potential contaminants. Previous work has forecasted the achievable Rayleigh scattering signal-to-noise of ground-based CMB experiments in the presence of atmospheric emission [19, 20, 84]. However, the effect of astrophysical foregrounds on Rayleigh scattering sensitivity has only recently begun to be investigated [74]. In this paper, we describe our Rayleigh scattering forecasting pipeline, which includes astrophysical foregrounds in addition to more standard instrumental and atmospheric effects, and estimate the detection significance for upcoming ground-based CMB experiments.

2.2 The Rayleigh Scattering Signal

As described in [19], [85] the Rayleigh scattering cross section of photons off ground-state neutral hydrogen is given by a frequency-dependent modification to the Thomson scattering cross section:

$$\sigma_R \approx \sigma_T \left[\left(\frac{\nu}{\nu_{\text{eff}}} \right)^4 + \frac{648}{243} \left(\frac{\nu}{\nu_{\text{eff}}} \right)^6 + \frac{1299667}{236196} \left(\frac{\nu}{\nu_{\text{eff}}} \right)^8 + ... \right], \tag{2.1}$$

where σ_T is the Thomson cross section and ν_{eff} is roughly the frequency of an H ionizing photon. The initial ν^4 term largely dominates, and will be the only Rayleigh scattering cross section considered in this analysis. This is because $\nu \ll \nu_{\text{eff}}$ for any millimeter or submillimeter frequency.

We model the total CMB temperature signal as a sum of a primary CMB component and a frequency-dependent distortion induced by Rayleigh scattering: $\widetilde{T} = T + \Delta T$. Here, $\widetilde{T}$ represents the total Rayleigh-distorted temperature signal, T represents the primary CMB temperature signal without Rayleigh distortion, and ΔT represents the frequency-dependent Rayleigh scattering contribution to the temperature signal. This means that the total CMB temperature power spectrum of a Rayleigh scattered CMB has the form:

$$C_\ell^{\widetilde{T}\widetilde{T}} = \langle \widetilde{T}\ \widetilde{T} \rangle = \langle T\ T \rangle + 2\langle T\ \Delta T \rangle + \langle \Delta T\ \Delta T \rangle. \tag{2.2}$$

A similar form can also be written for the Rayleigh scattering distortion of the E-mode polarization power spectrum. Using the modified version of CAMB described in [19] to model Rayleigh scattering power spectra, we calculate the Rayleigh cross- and auto-spectra expected for the SPT-3G and SPT-3G+ observing bands, shown in Figure 2.1. The solid black lines indicate the absolute values of the primary CMB temperature and E-mode polarization power spectra C_ℓ^{TT} and C_ℓ^{EE} respectively. The solid colored lines indicate the absolute values of the primary-Rayleigh temperature and polarization cross-spectra $C_\ell^{T\Delta T}$ and $C_\ell^{E\Delta E}$ respectively. Note the ν^4 dependence of the amplitudes of these cross-spectra. Dotted colored lines indicate the absolute values of the Rayleigh temperature and polarization auto-spectra $C_\ell^{\Delta T\Delta T}$ and $C_\ell^{\Delta E\Delta E}$ respectively. The auto-spectra have a ν^8 dependence, and an amplitude so much lower than their cross-spectrum counterparts as to be essentially negligible in comparison. Indeed, in the following section we neglect Rayleigh auto-spectrum terms throughout our derivation of the total Rayleigh scattering signal-to-noise. This assumption will turn out to be well-motivated, as the Rayleigh auto-spectrum amplitude is several orders of magnitude less than the already difficult-to-detect Rayleigh cross-spectrum.

2.3 Methods

Our method of computing the total Rayleigh signal-to-noise at each multipole consists of two steps. The first is to separate the Rayleigh scattering signal from the primary CMB signal in the presence of noise and foregrounds. This component separation results in expected signal and noise power spectra for each primary CMB auto-spectrum, primary-Rayleigh cross-spectrum, and Rayleigh auto-spectrum. The second step uses these values to compute the total Rayleigh scattering signal-to-noise via the Fisher formalism.

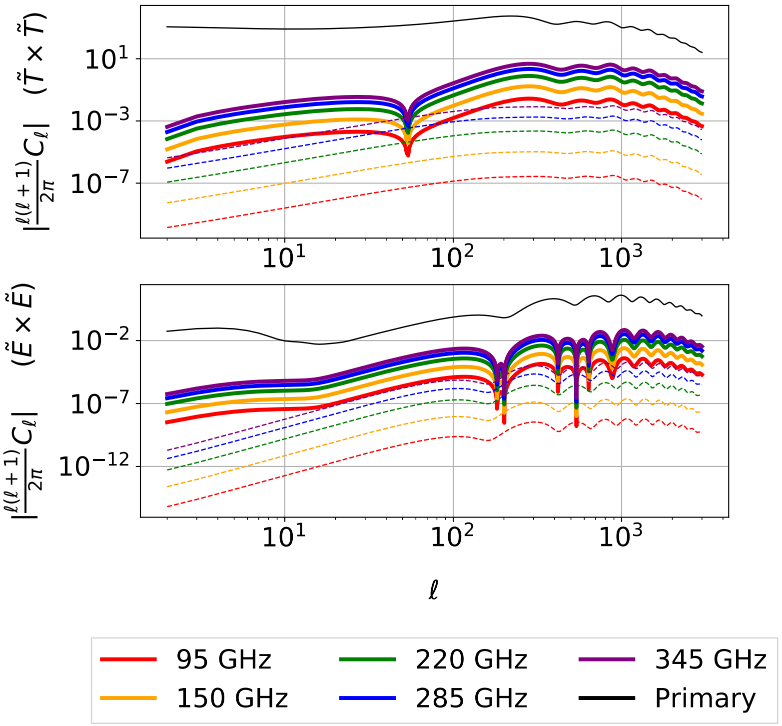

Figure 2.1: CAMB predictions of Rayleigh scattering power spectral contributions for SPT-3G and proposed SPT-3G+ bands. *Top*: Rayleigh scattering contributions to the CMB temperature power spectrum. The absolute value of the primary-primary temperature power spectrum is shown in black, while solid-colored lines represent the absolute value of the primary-Rayleigh cross-spectrum for each frequency band. Dotted lines represent the absolute value of the Rayleigh auto-spectrum for each frequency band. *Bottom:* Rayleigh scattering contributions to the CMB E-mode polarization power spectrum. Black, solid-colored, and dotted lines have meanings analogous to those of the corresponding lines in the top panel.

2.3.1 Component separation

We employ a constrained linear combination algorithm similar to the one described in [86] to separate the Rayleigh scattering signal from the primary CMB signal. Note that though our method follows the algebraic component separation methodology outlined in [86], we are not performing an ILC in the sense that we are not using simulated maps to produce these forecasts. Instead, we use models of individual foreground power spectra to directly compute covariance matrices for each component. We recognize that the assumption of these foreground models when attempting to extract a Rayleigh detection from an actual set of maps could result in excess variance from foreground residuals, but we neglect this potential source of variance in our Fisher-level forecast.

For a set of maps at various frequencies, this method identifies linear combinations of maps with the minimum possible variance, one of which 1) is an unbiased representation of the Rayleigh scattering signal, and 2) contains formally zero primary CMB signal, and the other of which is an unbiased representation of primary CMB with no response to Rayleigh signal. For a set of temperature and E-mode maps at frequencies ν, $\boldsymbol{X} \equiv [T_\nu, E_\nu]$, the best estimate for orthogonal primary CMB and Rayleigh maps $\hat{\boldsymbol{Y}} \equiv [\hat{T}, \hat{E}, \Delta\hat{T}, \Delta\hat{E}]$ are given by:

$$\boldsymbol{Y} = \boldsymbol{w}^t \boldsymbol{X}, \tag{2.3}$$

where

$$\boldsymbol{w}^t = (\boldsymbol{a}^t(\boldsymbol{C}+\boldsymbol{N})^{-1}\boldsymbol{a})^{-1}\ \boldsymbol{a}^t(\boldsymbol{C}+\boldsymbol{N})^{-1}, \tag{2.4}$$

$\boldsymbol{a}$ is a 2-by-# of bands matrix representing the frequency dependence of the primary CMB and Rayleigh signals, and $\boldsymbol{C}$ and $\boldsymbol{N}$ are the band-band signal and noise covariance matrices. If we choose to work in multipole space, and we assume all sources of signal and noise are statistically isotropic and Gaussian-distributed, then we can assume $\boldsymbol{C}$ and $\boldsymbol{N}$ are only functions of ℓ (not m) and are diagonal in ℓ space. In this case, we can perform the calculation independently at each value of ℓ and write $\boldsymbol{C}$ as $\boldsymbol{C}_\ell(\nu_i, \nu_j)$, and similarly with $\boldsymbol{N}$.

The signal covariance matrix $\boldsymbol{C}_\ell(\nu_i, \nu_j)$ is constructed from the CAMB-modeled Rayleigh and primary CMB power spectra in the previous section. This means, for example:

$$\boldsymbol{C}_\ell^{\widetilde{T}\widetilde{E}}(\nu_i, \nu_j) = C_\ell^{TE}(\nu_i, \nu_j) + C_\ell^{T\Delta E}(\nu_i, \nu_j) + C_\ell^{\Delta TE}(\nu_i, \nu_j) + C_\ell^{\Delta T\Delta E}(\nu_i, \nu_j). \quad (2.5)$$

For the purposes of this analysis, we assume the final auto-spectrum term to be negligible, meaning that each matrix entry is a sum of a frequency-independent primary CMB term and two ν^4-dependent Rayleigh-primary cross-spectrum terms. The noise part of the covariance matrix, $\boldsymbol{N}_\ell(\nu_i, \nu_j)$, is constructed using models for detector noise, atmospheric emission, and galactic/extragalactic foregrounds. These models are discussed extensively in Section 2.4.

2.3.2 Fisher calculation

We compute the total Rayleigh signal-to-noise using the Fisher formalism. This method produces a combined signal-to-noise value that takes into account correlations between the various primary-Rayleigh cross-spectra. Using the outputs of the component-separation procedure in the previous section, $\hat{\boldsymbol{Y}} \equiv [\hat{T}, \hat{E}, \Delta\hat{T}, \Delta\hat{E}]$, we construct our best estimates of the Rayleigh-primary cross-spectra, for example:

$$\begin{aligned} \hat{C}_\ell^{T\Delta T} &= \frac{1}{2\ell+1}\sum_{m=-\ell}^{\ell} \hat{T}_{\ell m}\Delta\hat{T}_{\ell m} & (2.6)\\ &= \frac{1}{2\ell+1}\sum_{m=-\ell}^{\ell} \boldsymbol{w}_{T,\ell}^t \boldsymbol{X}_\ell \boldsymbol{X}_\ell \boldsymbol{w}_{\Delta T,\ell}, \end{aligned}$$

where $\boldsymbol{w}_{T,\ell}^t$ and $\boldsymbol{w}_{\Delta T,\ell}^t$ are the T and ΔT components of the weights defined in Equation 2.4. We note that the expectation value of this estimate is equal to

$$\langle \hat{C}_\ell^{T\Delta T} \rangle = C_\ell^{T\Delta T} + N_\ell^{T\Delta T}, \quad (2.7)$$

where $N_\ell^{T\Delta T} = \boldsymbol{w}^t_{T,\ell}\boldsymbol{N}_\ell^{\widetilde{T}\widetilde{T}}\boldsymbol{w}_{\Delta T,\ell}$. We also note that the $T\Delta E$ and ΔTE versions of this have no noise bias term. We thus adopt as our data vector:

$$\boldsymbol{d}_\ell = \left[\hat{C}_\ell^{T\Delta T} - N_\ell^{T\Delta T}, \hat{C}_\ell^{T\Delta E}, \hat{C}_\ell^{\Delta TE}, \hat{C}_\ell^{E\Delta E} - N_\ell^{E\Delta E}\right]. \tag{2.8}$$

Our model of this data vector $\boldsymbol{d}_\ell$ is that it is equal to some constant amplitude A times the model cross-spectra $\boldsymbol{s_\ell}$ calculated by CAMB plus the noise $\boldsymbol{n}_\ell$:

$$\begin{aligned} \boldsymbol{d}_\ell &= A\boldsymbol{s}_\ell + \boldsymbol{n}_\ell, \\ \boldsymbol{s}_\ell &= \left[C_\ell^{T\Delta T}, C_\ell^{T\Delta E}, C_\ell^{\Delta TE}, C_\ell^{E\Delta E}\right]. \end{aligned} \tag{2.9}$$

The total Rayleigh scattering cross-spectrum signal-to-noise is then given by the signal-to-noise on the parameter A. The Fisher matrix, which in this one-parameter case is a single value F_ℓ, is defined:

$$F_\ell = -\frac{\partial^2 \ln \mathcal{L}}{\partial A^2}, \tag{2.10}$$

where $\mathcal{L}$ is the likelihood function:

$$\mathcal{L}_\ell \propto \exp\left[-\frac{1}{2}[\boldsymbol{d}_\ell - A\boldsymbol{s}_\ell]^\intercal \boldsymbol{\Xi}_\ell^{-1}[\boldsymbol{d}_\ell - A\boldsymbol{s}_\ell]\right]. \tag{2.11}$$

Here $\boldsymbol{\Xi}_\ell$ is the covariance matrix of the primary-Rayleigh cross-spectra, whose elements are:

$$\begin{aligned} \Xi_{\ell,(AB,CD)} =& \frac{1}{(2\ell+1)f_{\text{sky}}}\left[\left(C_\ell^{AC} + N_\ell^{AC}\right)\left(C_\ell^{BD} + N_\ell^{BD}\right)\right. \\ &+ \left.\left(C_\ell^{AD} + N_\ell^{AD}\right)\left(C_\ell^{BC} + N_\ell^{BC}\right)\right], \end{aligned} \tag{2.12}$$

with $A, B, C, D \in \{T, \Delta T, E, \Delta E\}$. For example, the Rayleigh temperature cross-spectrum on-diagonal term $\Xi_{\ell,(T\Delta T,T\Delta T)}$ is:

$$\frac{(C_\ell^{TT} + N_\ell^{TT})(C_\ell^{\Delta T \Delta T} + N_\ell^{\Delta T \Delta T}) + (C_\ell^{T \Delta T} + N_\ell^{T \Delta T})^2}{(2\ell + 1) f_{\rm sky}}. \tag{2.13}$$

Note that this is equivalent in form to the expression for the temperature cross-spectrum Fisher noise given in Equation 18 of [86]. Inserting Equations 2.11 and 2.12 into Equation 2.10, the single Fisher matrix element reduces to:

$$F_\ell = \boldsymbol{s}^\intercal \Xi^{-1} \boldsymbol{s} \tag{2.14}$$

The signal-to-noise on A at a given ℓ is then:

$$S/N(\ell) = \sqrt{F_\ell} = \sqrt{\boldsymbol{s}_\ell^\intercal \Xi_\ell^{-1} \boldsymbol{s}_\ell}. \tag{2.15}$$

We assume noise and foregrounds to be Gaussian and hence uncorrelated between multipoles, however we note that some foregrounds are likely to be mildly non-Gaussian. Therefore the signal-to-noise forecasts presented below should be taken as upper bounds. The cumulative Rayleigh signal-to-noise over all multipoles is the quadrature sum of the signal-to-noise at each multipole:

$$S/N = \left[\sum_{\ell > 50} \boldsymbol{s}_\ell^\intercal \Xi_\ell^{-1} \boldsymbol{s}_\ell \right]^{1/2}. \tag{2.16}$$

In Equation 2.16, we impose a minimum multipole on the sum. Beyond the limitations from atmospheric noise and large-angular-scale galactic foregrounds (which are accounted for in the Fisher forecast), the minimum multipole accessible by a ground-based experiment is also limited by the partial sky coverage and potentially by contamination from terrestrial features picked up by the far sidelobes of the beam. We choose $\ell_{\rm min} = 50$, which is well above the fundamental limit set by the size of the $f_{\rm sky} = 0.03$ patch that is the main survey field for SPT-3G and the planned main survey field for SPT-3G+. The difference in total S/N between $\ell_{\rm min} = 50$ and no minimum is negligible ($< 1\%$). Equation 2.16 with $\ell_{\rm min} = 50$ is what we report as the "total Rayleigh signal" for a given experiment and set of foregrounds.

2.4 Noise Model

Our noise model includes contributions from instrumental detector noise, atmospheric emission, and galactic and extragalactic foregrounds. Our models for detector noise and atmospheric emission are similar to those presented in [19], [20], and [84]. Each foreground is modeled as an independent noise component with its own covariance matrix. The noise input to the component separation algorithm described above is the sum of these foreground covariance matrices, the atmospheric covariance matrix, and the diagonal matrix representing the detector noise. Foregrounds are broadly grouped into galactic and extraglactic sources. The following subsections will describe the functional forms of all noise components considered in our analysis, while the foreground model parameters are included in the appendix to this thesis.

2.4.1 Instrument detector noise

For an instrument observing at a set of frequencies ν_i, with the contribution to map noise from detectors in each band equal to N_{det_i}, the detector noise covariance matrix is just the diagonal matrix:

$$\boldsymbol{N}^{\mathrm{det}}(\nu_i, \nu_j) = N_i^{\mathrm{det}} \delta_{ij} \tag{2.17}$$

Table A1 gives the estimated full-survey detector noise values (N_{det}) for SPT-3G/SPT-3G+ along with other upcoming CMB experiments.

2.4.2 Atmospheric emission

All ground-based CMB experiments must consider emission from atmospheric water vapor as a major source of signal contamination. Similarly to [84], we define for each frequency band and observing site a characteristic ℓ_{knee} below which white detector noise is overtaken by noise from atmospheric water vapor, which we model as a power law in ℓ with index α. Atmospheric noise in a given frequency band is modeled as:

$$\boldsymbol{N}_\ell^{\rm atmos}(\nu_i) = N_i^{\rm det}\left(\frac{\ell_{\rm knee}(\nu_i)}{\ell}\right)^\alpha. \tag{2.18}$$

With this in mind, the covariance matrix for atmospheric noise is:

$$\boldsymbol{N}_\ell^{\rm atmos}(\nu_i, \nu_j) = N_i^{\rm det}\left(\frac{\ell_{\rm knee}(\nu_i)}{\ell}\right)^\alpha \delta_{ij}. \tag{2.19}$$

Atmospheric noise parameters for SPT along with several upcoming ground-based CMB experiments are given in Table A1. Note that by this definition, we assume that the atmospheric noise is totally uncorrelated between bands; we explore the effect of the opposite assumption (100% correlation between bands) in Section 2.5.2.

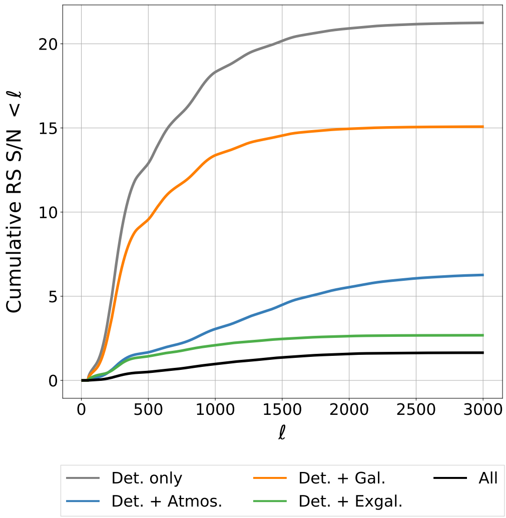

Figure 2.2: Effect of each noise component on cumulative Rayleigh scattering signal-to-noise for SPT-3G and SPT-3G+ data combined with Planck. Atmosphere and extragalactic foregrounds strongly limit the achievable signal-to-noise at low ℓ, while extragalactic foregrounds alone become the dominant limiting factor as ℓ increases.

2.4.3 Galactic sources

Emission from dust grains in our Galaxy is a known contaminant to measurements of the CMB. The contribution of galactic dust emission to the TT or EE spectra is modeled by a power law in $D_\ell \equiv \frac{\ell(\ell+1)}{2\pi}C_\ell$:

$$D_\ell(\nu) = A_{\rm dust}(\nu)\left(\frac{\ell}{80}\right)^\alpha. \tag{2.20}$$

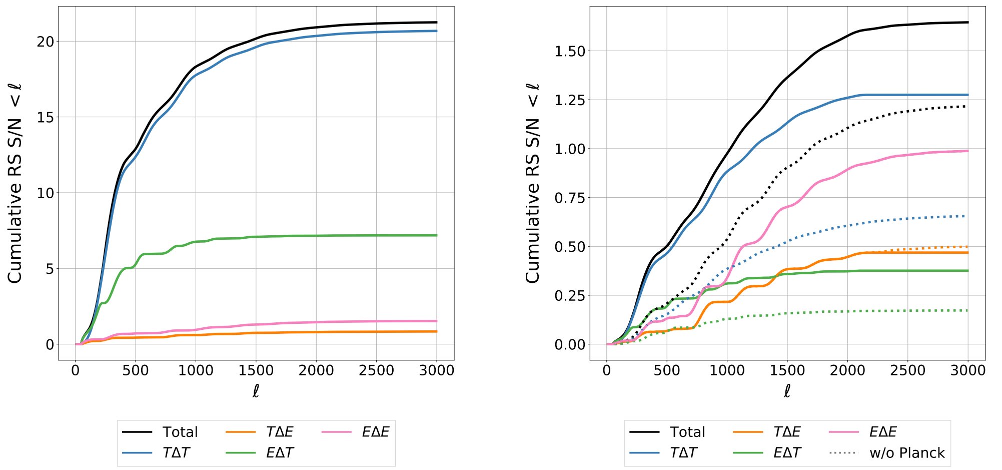

(a) Detector noise only

(b) Detector noise, atmosphere, and all foregrounds

Figure 2.3: Rayleigh signal-to-noise for the combination of SPT-3G, SPT-3G+, and Planck broken down by spectrum, *Left* in the absence of foregrounds and *Right* including all foregrounds and atmosphere. These spectra are correlated, which causes the total combined Rayleigh signal-to-noise for SPT to be less than the quadrature sum of the signal-to-noise of the individual spectra. As expected, the total cumulative Rayleigh signal-to-noise is dominated by that of the $T\Delta T$ cross-spectrum. The $T\Delta T$ and $E\Delta T$ signal-to-noise are severely diminished by the addition of foregrounds, most notably extragalactic foregrounds. The $T\Delta E$ and $E\Delta E$ signal-to-noise are less affected, and this slight degradation is mostly due to galactic dust. The dotted lines in the right panel show the signal-to-noise for each spectrum when Planck data is excluded. These lines are not included in the left panel because they are visually indistinguishable from the corresponding solid lines.

Following [87], we use the publicly available Python Sky Model (pySM) simulations [88, 89] to estimate $A_{\rm dust}$ and α at 145 GHz for TT and EE. Galactic dust temperature and polarization amplitudes for all experiments considered here are given in Table A2 in the Appendix to this paper. We assume the TE spectrum for galactic dust to be the geometric mean of the TT and EE factors times a correlation coefficient of 0.35. We scale this amplitude to other frequency bands using a modified blackbody approximation, the details of which are discussed in Appendix A.2. Assuming full correlation of the galactic dust signal between frequency bands, the noise covariance matrix for galactic dust is:

$$\boldsymbol{N}_\ell^{\rm dust}(\nu_i, \nu_j) = \frac{2\pi}{\ell(\ell+1)}\sqrt{D_\ell(\nu_i)D_\ell(\nu_j)}, \tag{2.21}$$

where the prefactor converts from D_ℓ to C_ℓ space.

Galactic synchrotron emission is also generally considered to be an important contaminant for CMB experiments, particularly at frequencies below the peak of the CMB blackbody spectrum. We model synchrotron using a power law as in Equation 2.20, with temperature and polarization amplitudes for each experiment again given in Table A2. See Appendix A.2 for further discussion of these values and their scaling to other frequency bands.

2.4.4 Extragalactic sources

Our extragalactic foreground model consists of thermal Sunyaev-Zel'dovich (tSZ) and cosmic infrared background (CIB) components, as well as extragalactic radio sources. The tSZ component is modeled as a power law in ℓ:

$$D_\ell(\nu) = A_{\rm tSZ}(\nu)\left(\frac{\ell}{3000}\right)^\alpha, \tag{2.22}$$

where $A_{\rm tSZ} = 4\,\mu{\rm K}^2$ and $\alpha = 0$ at 150 GHz, as seen in Table A2. The method for scaling the tSZ amplitude to other frequency bands is described in Appendix A.3. We neglect any polarized tSZ component.

Modeling the CIB is a challenging task that has been the subject of many detailed studies (e.g., [90, 91]). For this work, we are primarily interested in: 1) correctly reproducing the total power and frequency scaling of the CIB reported in the literature, including frequency decorrelation; and 2) being able to separate the clustered and shot-noise components of the CIB. To this end, we have modeled the CIB as originating from two separate infinitely thin screens at redshifts $z = 0.5$ and $z = 3.5$. At each redshift, there is a clustered component and a shot-noise ("Poisson") component, for a total of four independent components. The Poisson component is flat in C_ℓ, while the ℓ-space shape of the clustered CIB components is assumed to follow a power law like that in Equation 2.22, but with an index $\alpha = -1.2$, following, e.g., [23]. The amplitudes of the four CIB components are given in Table A2. Scaling of these amplitudes to other frequency bands is described in Appendix A.3. While this model is clearly *ad hoc* and unphysical, it does reproduce key results in the literature for clustered and Poisson CIB power at 150 and 220 GHz [23] and the degree of correlation in CIB power between bands from 95 to 1200 GHz [92]. The clustered and Poisson CIB are considered to be unpolarized. While the clustered component is unpolarized by construction, the Poisson component has been suggested to be 4% polarized as an upper bound [93]. We have repeated these forecasts for a case in which the Poisson CIB component is 4% polarized and found negligible change in the results of the forecasts.

Extragalactic radio sources are primarily a contaminant at low frequencies. While their effect on the high-frequency SPT-3G+ bands is negligible, their inclusion is necessary when forecasting the Rayleigh scattering sensitivity of other planned experiments. We assume the clustering power of radio sources to be negligible and only forecast the Poisson signal, adopting a value of $A_{\mathrm{radio}} = 0.17\,\mu\mathrm{K}^2$ at 150 GHz, as seen in Table A2. This is lower than the measured value in, e.g., [23], because we assume a flux cut of 1 mJy (roughly the 5σ detection threshold in the SPT-3G 150 GHz band), compared to roughly 6 mJy in that work. When we forecast for other experiments, we keep this power constant despite the fact that those experiments will have slightly different source detection thresholds. We have checked that using the Simons Observatory 145 GHz detection threshold of roughly 2.7 mJy (which results in a radio Poisson amplitude of $A_{\rm radio} = 0.51\,\mu{\rm K}^2$) has no measurable effect on our results.[1] We assume extragalactic radio sources to be 3% polarized following [95], [93]. The scaling of this model to other frequency bands is again detailed in Appendix A.3.

Using the above expressions for each D_ℓ, the covariance matrix for each extragalactic foreground component (assuming 100% correlation between bands) can be expressed:

$$\boldsymbol{N}_\ell^{\rm fg}(\nu_i, \nu_j) = \frac{2\pi}{\ell(\ell+1)} \sqrt{D_\ell(\nu_i) D_\ell(\nu_j)}, \tag{2.23}$$

where the prefactor again converts from D_ℓ to C_ℓ space.

2.5 Results and Discussion

Using the component separation and Fisher calculation methods described in Section 2.3, with the noise part of the covariance matrix constructed from the components described in Section 2.4, the total Rayleigh signal-to-noise at each multipole can be calculated. We first present these forecasts for SPT, including the current SPT-3G camera and the planned SPT-3G+ camera. Throughout this section, we assume that all experiments will perform a joint analysis with Planck data, however we will quantify the impact of this assumption on our forecasts. For SPT, which observes approximately 3% of the sky, we include Planck data from the same sky patch. Quantitatively, this means we add rows and columns to our correlation matrix corresponding to Planck's frequency bands, but maintain $f_{\rm sky} = 0.03$ throughout the Fisher calculation. The frequency bands used in this forecast include SPT-3G's 95, 150, and 220 GHz bands, SPT-3G+'s, 225, 285, and 345 GHz bands and Planck's

---

[1] We note that the dusty source Poisson amplitude is insensitive to source cut threshold down to below 1 mJy at 150 GHz [e.g., 94], at which point the number of sources masked approaches the number of independent resolution elements in the map—i.e., the dusty source Poisson power is dominated by sources at or below the confusion limit for a ∼1-arcmin beam.

30, 44, 70, 100, 143, 217, 353, 545, and 857 GHz bands. Detector noise values for the SPT bands are given in Appendix A, while Planck detector noise values come from Table 4 of [96]. Being a space-based experiment, Planck has no atmospheric noise component.

Figure 2.2 shows the resulting SPT Rayleigh signal-to-noise for four scenarios: (1) detector noise only in gray, (2) detector noise plus atmospheric emission in blue, (3) detector noise plus galactic dust in green, and (4) detector noise plus extragalactic sources in orange. The black line represents the total Rayleigh signal-to-noise when all noise components are considered together. The curves on this plot represent the cumulative Rayleigh signal-to-noise up to each multipole ℓ. This is the result of Equation 6 for a given ℓ, and is equal to the quadrature sum of all individual multipole signal-to-noise values up to and including ℓ. It is immediately apparent that extragalactic foregrounds have the most dramatic effect on the Rayleigh scattering signal-to-noise for SPT. This effect is comparable to the effect of the atmosphere at low multipoles, but persists through higher multipoles at which atmospheric contamination is of less concern. Figure 2.2 demonstrates that for SPT, the Rayleigh scattering detection is limited by extragalactic foregrounds more than it is limited by atmospheric noise or detector noise.

The Rayleigh scattering signal-to-noise is dominated by contribution from the primary CMB temperature–Rayleigh temperature cross-spectrum $T\Delta T$. This is illustrated by Figure 2.3, which shows the relative signal-to-noise of each of the four available primary-Rayleigh cross-spectra: $T\Delta T, T\Delta E, E\Delta T$, and $E\Delta E$ in relation to the total combined signal-to-noise. The left panel includes no foregrounds, and the right panel includes all foregrounds. As one would expect, multiple pairs of spectra are strongly correlated, meaning that the Rayleigh scattering information contained within each of these signals is not independent. We see this manifest in the total combined Rayleigh signal-to-noise (black line in Figure 2.3) being lower than the quadrature sum of the signal-to-noise values of the individual cross-spectra in Figure 2.3. These four cross-spectra respond differently to the presence of foregrounds.

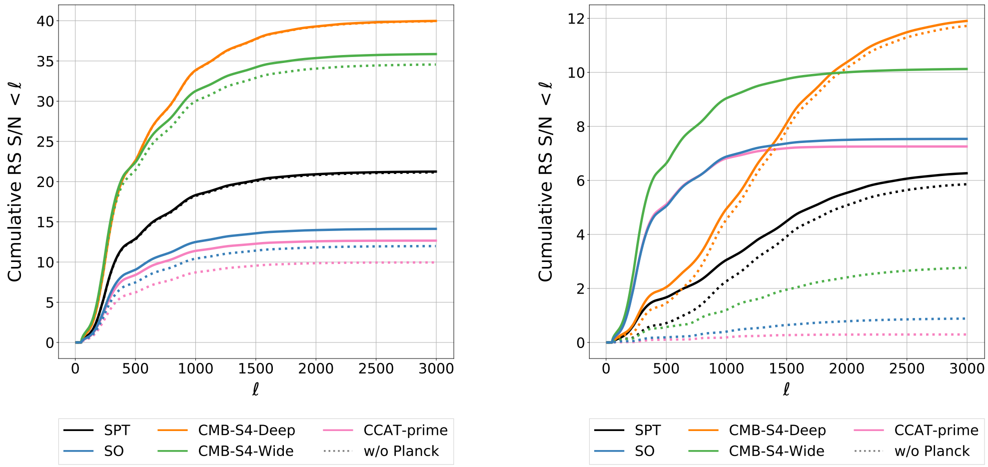

(a) Detector noise only

(b) Detector noise and atmosphere

Figure 2.4:]

Comparison of the forecasted Rayleigh signal-to-noise for upcoming CMB experiments. *Left:* Achievable signal-to-noise with detector noise as the only component in the noise model. *Right:* Signal-to-noise achievable with both detector noise and atmospheric components included in the noise model. All experiments are assumed to be combined with Planck data. Dotted lines represent the Rayleigh signal-to-noise achievable for each experiment without Planck data. The addition of the atmosphere severely impacts wide experiments, and the majority of their Rayleigh detections come from Planck. The addition of atmosphere also removes low-ℓ signal-to-noise from deep experiments, but Planck data only constitutes a small portion of their Rayleigh detections.

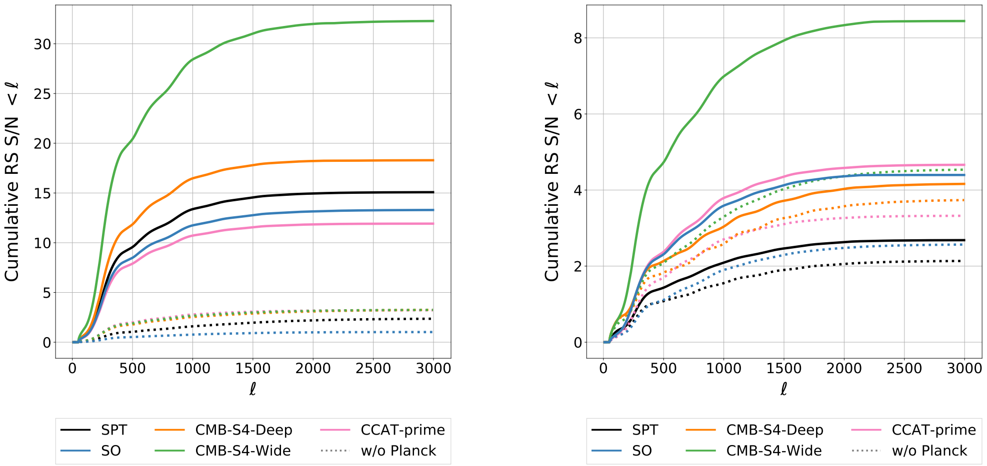

(a) Detector noise and galactic foregrounds (b) Detector noise and extragalactic foregrounds

Figure 2.5: Comparison of the total forecasted Rayleigh signal-to-noise for upcoming CMB experiments with galactic (*Left*) and extragalactic (*Right*) foregrounds included in addition to detector noise. Again all experiments are assumed to be combined with Planck data, and dotted lines represent the achievable Rayleigh signal-to-noise for each experiment without Planck data. The left panel illustrates the ability of Planck data to remove the galactic dust component from CMB maps. CMB-S4-Wide, with its large field, benefits the most from this effect. The right panel reveals that extragalactic foregrounds severely decrease the Rayleigh detection significance of all ground-based experiments, even when Planck data is included. For deep experiments, this loss is more significant than that caused by the atmosphere.

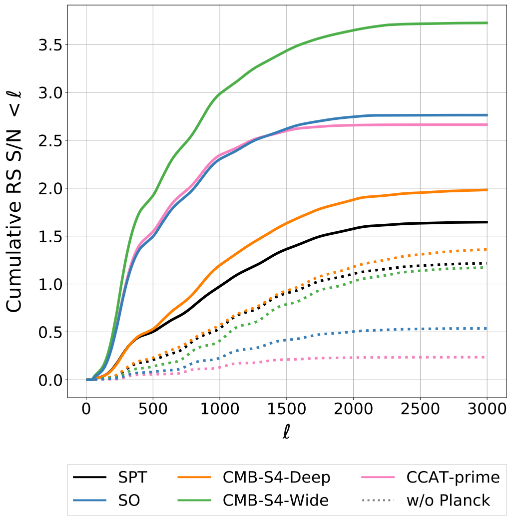

Figure 2.6: Total forecasted Rayleigh scattering signal-to-noise for upcoming ground-based experiments. As above, dotted lines represent the signal-to-noise for each experiment if Planck data is not included. The inclusion of Planck data majorly benefits wide experiments, which are able to utilize a larger portion of Planck's sky coverage. Without Planck, deep experiments expect slightly more significant Rayleigh scattering detections.

Largely unpolarized extragalactic foregounds are the limiting noise component for $\langle T\Delta T\rangle$ and $\langle E\Delta T\rangle$, which degrade severely between the left and right panels of Figure 2.3. The remaining spectra, $\langle T\Delta E\rangle$ and $\langle E\Delta E\rangle$, are only midly affected, mostly by the 10% polarized galactic dust component.

2.5.1 Forecasts for other upcoming experiments

Figure 2.4 shows the Rayleigh signal-to-noise forecasted for SPT-3G+ (black) along with Simons Observatory [79] (blue), CCAT-prime [74, 80] (pink), and the CMB-S4 [81] wide field survey (green) and deep field survey (orange) in the presence of only detector and atmospheric noise. Detector noise and atmospheric parameters used for each of these experiments are given in Table A1, while galactic foreground estimates are shown in Table A2. All cumulative signal-to-noise values reported in this section for each experiment with and without including Planck data are recorded in Table 2.1.

Solid colored lines in Figure 2.4 indicate the total Rayleigh signal-to-noise achievable for each experiment when combined with Planck data. In this analysis, each

Experiment (f_{sky})	Detectors		Det. + Atmos.		Det. + Gal.		Det. + Exgal.		All	
	w/ Planck	Alone	w/ Planck	Alone	w/ Planck	Alone	w/ Planck	Alone	w/ Planck	Alone
SPT (3%)	21.2	21.1	6.3	5.9	15.1	2.4	2.7	2.1	1.6	1.2
Simons Obs. (40%)	14.1	12.0	7.5	0.9	13.3	1.0	4.4	2.6	2.8	0.5
CCAT-prime (44%)	12.7	10.0	7.3	0.3	11.9	3.2	4.7	3.3	2.7	0.2
CMB-S4 Deep (3%)	40.0	39.9	11.9	11.7	18.3	3.2	4.2	3.7	2.0	1.4
CMB-S4 Wide (65%)	35.9	34.6	10.1	2.8	32.3	3.2	8.4	4.5	3.7	1.2
Planck (65%)	-	8.7	-	8.7	-	8.1	-	3.7	-	3.2

Table 2.1: Total forecasted Rayleigh scattering signal-to-noise for upcoming ground-based CMB experiments combined with Planck data. This table summarizes the results displayed in Figures 2.4, 2.5, and 2.6. Column labels indicate which noise components are included in the model to produce the forecasts in a given column. For each set of noise components, subcolumns indicate the forecasted Rayleigh scattering signal-to-noise with and without the addition of Planck data. The bottom row shows forecasts for Planck data only, assuming 65% sky coverage.

ground-based experiment is combined with the Planck data that overlaps each experiment's observing area on the sky. Thus, wide experiments are able to utilize a larger portion of the available Planck information than are deep experiments. The dotted lines in Figure 2.4 indicate the Rayleigh signal-to-noise achievable by each experiment without including Planck data. The left panel of Figure 2.4 shows Rayleigh forecasts in the absence of any foregrounds or atmosphere. In this limit, all experiments show significant improvements over Planck in Rayleigh sensitivity. The right panel of Figure 2.4 shows the effect of adding the atmospheric noise component described in the previous section. The atmospheric noise decreases the detection significance of the wide survey experiments more significantly, such that the resulting Rayleigh detection of a wide experiment comes mostly from the Planck data with which it is combined. Deep experiments lose significant low-ell signal-to-noise, but the majority of the Rayleigh scattering detection for each deep experiment still comes from the experiment itself (not Planck).

The left panel of Figure 2.5 shows the Rayleigh forecasts for upcoming ground-based experiments in the presence of detector noise and galactic foregrounds only. Galactic foregrounds do not affect the achievable Rayleigh signal-to-noise of ground-based experiments as much as the atmospheric contamination. With galactic dust and synchrotron emission as the only foregrounds, all upcoming ground-based CMB experiments perform relatively similarly when combined with Planck, with the exception of CMB-S4-Wide, which performs significantly better. Without Planck, the Rayleigh detection significance of all ground-based experiments falls to a similar 3-4-σ level, highlighting the ability of Planck data to remove galactic dust contamination during component separation. CMB-S4-Wide, with the largest observing field among the experiments considered here, benefits the most from combination with Planck data. The right panel of Figure 2.5 shows the Rayleigh forecasts in the presence of detector noise and extragalactic foregrounds (tSZ, CIB, and extragalactic radio sources) only. This panel illustrates the significant impact of extragalactic foregrounds on Rayleigh scattering detections, even when Planck data is utilized. For wide experiments combined with Planck, the loss in detection significance due to extragalactic foregrounds alone is approximately equal to the loss due to atmosphere. For deep experiments combined with Planck, this loss is significantly more severe than atmospheric loss. Comparing to the left panel, it is clear that Planck is not nearly as successful at removing extragalactic foregrounds during component separation as it is at removing galactic foregrounds.

Including all of the above noise components in our model, we produced total forecasts for Rayleigh scattering signal-to-noise for upcoming experiments in the presence of atmospheric, galactic, and extragalactic foregrounds. These total forecasts are presented in Figure 2.6. All forecasted signal-to-noise values are shown in Table 2.1. These forecasts indicate that, in combination with Planck data, all upcoming ground-based CMB experiments can expect a Rayleigh scattering detection with a signal-to-noise of roughly 1-4. For wide experiments, the majority of this detection comes from Planck data, as indicated by the dotted lines. Though deep experiments can expect slightly lower signal-to-noise than wide experiments, their Rayleigh scattering detections come mostly from the experiments themselves. Without Planck, the highest-significance Rayleigh scattering detections of 1.5-2 come from deep experiments. It is also relevant to note that this model predicts that a roughly 3-σ Rayleigh scattering detection is potentially present in the Planck dataset

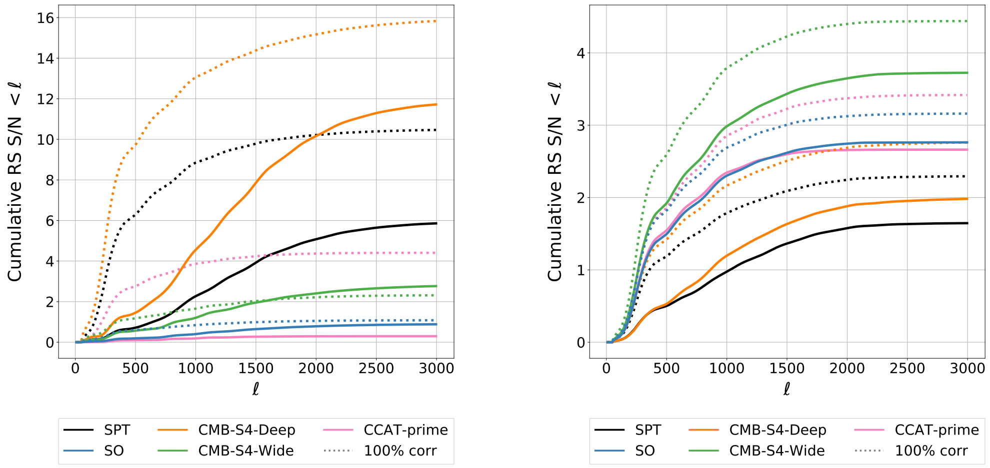

(a) Detector noise and atmosphere only (no Planck)

(b) All foregrounds combined with Planck

Figure 2.7: Rayleigh forecasts when the atmosphere is taken to be totally correlated between bands. *Left:* Forecasts including only detectors and correlated atmosphere. In this plot, experiments are not combined with Planck so that the effect of correlated atmosphere may be clearly seen. Solid lines correspond with the dotted lines in the right panel of Figure 2.4, and dotted lines represent the same forecasts with a fully correlated atmosphere. *Right:* Forecasts including Planck data, all foregrounds and a fully correlated atmosphere. Solid lines here correspond to the solid lines in Figure 2.6, and dotted lines represent the same forecasts with a fully correlated atmosphere.

corresponding to the CMB-S4-Wide observing patch, which encompasses 65% of the sky. This is backed up by the forecasted signal-to-noise values for Planck alone with $f_{\rm sky} = 0.65$, which are shown in the last row of Table 2.1. Of the components present in our extragalactic foregrounds model, we found the CIB to be the largest limiter of total achievable Rayleigh signal-to-noise.

2.5.2 Atmospheric correlation

As noted in Section 2.4.2, in our fiducial forecasting pipeline we assume low-ℓ noise from the atmosphere to be uncorrelated between frequency bands. Depending on the specific experiment configuration, and in the limit that the low-ℓ noise from the atmosphere comes entirely from clouds of water vapor that are optically thin at all observing frequencies, this contribution could in principle be nearly 100% correlated between detectors and frequency bands. One promising path towards mitigating atmospheric contamination recalls early CMB/tSZ experiments such as

SuZIE [97], in which the atmosphere is at least partially mitigated by forming linear combinations of channels that are least sensitive to atmosphere—i.e., treating the atmosphere in the same way we treat correlated foregrounds in this work [98]. We produce an alternate set of forecasts in which the atmospheric contribution is 100% correlated between bands. The most straightforward way to achieve this would be to modify Equation 2.19 to read

$$\boldsymbol{N}_\ell^{\rm atmos}(\nu_i,\nu_j) = \sqrt{N_i^{\rm det} N_j^{\rm det}} \times \left(\frac{\ell_{\rm knee}(\nu_i)}{\ell}\right)^{\alpha_i/2} \left(\frac{\ell_{\rm knee}(\nu_j)}{\ell}\right)^{\alpha_j/2}. \tag{2.24}$$

The problem with this formulation is that the values of $\ell_{\rm knee}$ (in temperature) for the various upcoming experiments were estimated assuming that the atmospheric noise will integrate down at least partially as the number of detectors is increased. If atmospheric noise is instead 100% correlated across all detectors and bands, its power spectrum in a given band will be independent of detector number. To create a self-consistent atmospheric noise covariance matrix for the fully correlated case, we must scale the amplitude back up by the amount it was assumed to scale down in the uncorrelated case.

The values of $\ell_{\rm knee}$ for the future South Pole experiments SPT-3G+ and CMB-S4 Deep are taken directly from measurements in SPT-3G; as such, they implicitly assume that the atmospheric noise will integrate down with the number of detectors. The values of $\ell_{\rm knee}$ for the future Chile experiments SO, CCAT-prime, and CMB-S4 Wide are calculated using the SO Noise Calculator (as described in [79]), which starts with noise power spectra measured with ACTPol and assumes that independent camera sub-modules or optics tubes will see independent atmosphere—i.e., that the atmospheric noise will scale from ACTPol to a future instrument by the inverse number of optics tubes. There is also a factor-of-2 reduction assumed from the larger focal planes of the future instruments. Our self-consistent model for atmospheric noise covariance in the fully correlated case thus looks like

$$\boldsymbol{N}_\ell^{\rm atmos}(\nu_i,\nu_j) = \sqrt{f_i N_i^{\rm det} f_j N_j^{\rm det}} \times \left(\frac{\ell_{\rm knee}(\nu_i)}{\ell}\right)^{\alpha_i/2} \left(\frac{\ell_{\rm knee}(\nu_j)}{\ell}\right)^{\alpha_j/2}, \tag{2.25}$$

where f_i is a scaling factor that is equal to $n_i^{\text{det}}/n_i^{\text{det, SPT-3G}}$ (where n_i^{det} is the number of detectors in band i) for the future experiments at the South Pole and $2 \times n_i^{\text{tube}}$ (where n_i^{tube} is the number of optics tubes in band i) for the future experiments in Chile. Finally, we note that because SPT-3G and SPT-3G+ will not observe simultaneously, we zero the atmospheric noise correlations between the SPT-3G and SPT-3G+ bands in the SPT covariance matrix. The dotted lines in Figure 2.7 show the effects of the fully correlated atmosphere model relative to the fully uncorrelated model used above. These represent two extremes of atmosphere correlation, meaning that with Planck data and all foregrounds included, the true Rayleigh scattering signal-to-noise should lie somewhere between the solid and dotted lines in the right-hand panel of Figure 2.7.

2.6 Conclusions

A ground-based Rayleigh scattering detection is challenging in that it requires an experiment to have high sensitivity at frequencies beyond the peak of the CMB blackbody spectrum as well as the ability to mitigate both atmospheric and astrophysical foreground contamination. With many upcoming CMB ground-based experiments proposing low-noise, high-frequency cameras, a first detection of Rayleigh scattering is moving closer into reach. Our Rayleigh scattering forecasting pipeline, based on the constrained linear combination method described in [86], indicates that, though upcoming experiments will be severely limited by atmospheric emission and extragalactic foregrounds, a first Rayleigh scattering detection may still be possible in the upcoming decade if experiments combine their data with Planck and place high priority on understanding and removing both atmospheric contamination and that from extragalactic foregrounds. Extragalactic foregrounds, particularly the CIB, strongly limit the achievable significance of a Rayleigh scattering detection. This effect is approximately equal to that of the atmosphere for wide experiments, and exceeds the effect of the atmosphere for deep experiments. Thus it is vital for future ground-based Rayleigh scattering detections that attention be paid to understanding and mitigating extragalactic foreground contamination.

When all noise components are included in our model, significant Rayleigh scattering detections are only achievable if ground-based experiments combine their data with the Planck data that overlaps their observation patch. This is particularly true for wide experiments, for whom the majority of the Rayleigh scattering detection comes from the Planck data overlapping their large observation fields. Table 2.1 summarizes the forecasted Rayleigh signal-to-noises for each experiment combined with Planck, where quantities in parentheses indicate how much of each detection comes from Planck data. Without the addition of Planck data, we have found that upcoming experiments can expect a Rayleigh scattering detection signficance of around 1-σ. This is in agreement with the Rayleigh forecasts presented for CCAT-prime alone in [74], and in fact, our Rayleigh signal-to-noise forecast for CCAT-prime without Planck with all foregrounds included ($S/N \approx 0.3$) matches that presented in [74]. Our forecasts for Simons Observatory, CCAT-prime, and CMB-S4-Wide without Planck and with only atmosphere included also roughly match those presented in [84]. For deep experiments, though the forecasted Rayleigh detection significance when including Planck data is lower than that of wide experiments, the majority of the signal-to-noise in these deep experiment detections comes from the deep experiments themselves (Figure 2.6). We find that Planck data alone, with $f_{\mathrm{sky}} = 0.65$, may already contain a roughly 3-σ Rayleigh scattering detection, as shown in the last row of Table 2.1. A higher Rayleigh detection may also be achievable by combining deep ground-based experiments with all available Planck data, rather than just the Planck data that overlaps these experiments' $f_{\mathrm{sky}} = 0.03$ observing patches. Further progress on atmospheric and CIB removal, beyond that considered here, will likely be necessary for current and planned ground-based experiments to significantly increase the Rayleigh scattering detection significance beyond what should be achievable from Planck data alone.

Chapter 3

Probing cosmic star-formation history with CMB temperature and lensing maps

The previous chapter showed that the cosmic infrared background (CIB) is the main foreground inhibiting a significant detection of the Rayleigh scattering signal by SPT-3G+. A better understanding of the CIB would enable its subtraction from SPT-3G data, leading to higher-significance detections of the Rayleigh scattering signal and other small-amplitude secondary anistropies. This chapter makes an attempt to characterize the CIB using data from SPT-3G. This attempt is documented below, and may be partially reproduced in a future publication.

3.1 Introduction

Experiments such as *Planck* [99], the Atacama Cosmology Telescope (ACT) [100] and the South Pole Telescope (SPT) [30, 69] observe the sky at millimeter wavelengths with the primary goal of mapping the anisotropies of the cosmic microwave background (CMB). However, in addition to the CMB, many astrophysical signals appear in maps of the millimeter sky. At frequencies greater than 220 GHz, small scale features in the maps primarily come from infrared emission from star forming galaxies. Emission from the brightest galaxies appear as point sources in maps, and their astrophysical properties as well as clustering statistics have been studied by other targeted sub-mm surveys such as SCUBA-2 and ALMA [101, 102]. Galaxies on the faint end of the spectrum collectively make up the cosmic infrared background (CIB), a diffuse infrared emission that traces out the large-scale structure of the universe. The CIB is sourced by star-formation in dense molecular clouds. Young, recently-formed stars emit ultraviolet radiation, which is absorbed by surrounding dust. The dust re-emits this energy as infrared radiation. The redshifted infrared spectrum is observed at microwave frequencies as the CIB. Hence a galaxy's CIB emission is related to its star-formation rate, and thus the CIB provides a unique window into the history of galaxy formation [21]. Since the CIB is emitted by individual galaxies which follow the distribution of large-scale structure, observation of the CIB also probes structure formation at higher redshifts beyond the reach of optical galaxy surveys. Studies using cross-correlation with galaxies have found that the CIB emission peaks at $z \sim 2$, but extends from the early universe to the present day [103].

Attempts have been made to fit models to the CIB autospectrum, but these models have generally not produced good fits to the data. It is unknown whether this is due to inherent model problems or from some other source of contamination in the CIB autospectra biasing the fits. This motivates us to look at cross-correlations with other tracers of the large-scale structure, which results in measurements that are more robust against systematic effects. CMB lensing is well-suited for this purpose, as it peaks at $z \sim 2$ (approximately midway between the last scattering surface and today) and overlaps well with the redshift distribution of the CIB. The CMB lensing signal is sourced by the gravitational deflection of CMB photons by the large-scale structure of the universe between recombination and today. Information about this large-scale structure is imprinted on the CMB as distortions to its temperature and polarization.

Though often considered a nuisance foreground for CMB analyses, the CIB's correlation with large-scale structure and its direct relation with the cosmic star formation rate makes it an interesting subject from an astrophysical standpoint. Characterization of the CIB also benefits CMB science, as the CIB is a major contaminant in reconstructed Compton-y maps [104, 105, 106] especially at small angular scales. These biases get picked up in both auto-spectrum analysis and in cross-correlation studies with large-scale structure [107, 108]. The CIB is also a potential source of biases in temperature-based lensing reconstruction [109, 110, 111]. A better understanding of the CIB allows for better deprojection of the CIB from maps of interest, and leads to a cleaner analysis and extraction of astrophysical or cosmological information from these maps. The auto-correlation of CIB and the cross-correlation between CIB and CMB lensing have been forecasted and measured in various studies using data from *Planck* [112, 113, 114, 115, 116, 117], *Herschel* [118], ACT [119, 120], and SPT [121]. Other studies have also measurements of higher-order statistics beyond two-point correlations [122]. The measurement presented in this paper uses both CIB and CMB lensing data products derived from two years of SPT-3G data. In particular, we cross-correlate the SPT-3G 220 GHz temperature map with a CMB lensing map reconstructed using the combined 90, 150 and 220 GHz data.

The intent of this work is to extract astrophysical information from the cross-correlation between CIB and CMB lensing at ground-based observation frequencies. Though the CIB is significantly brighter at higher observation frequencies (the Planck 353, 545, and 857 GHz bands for example), than it is in the the SPT 220 GHz band, the 220 GHz measurement probes a different set of higher-redshift galaxies near the peak of cosmic star-formation. Figure 3.1 shows the simulated mean intensity of the CIB as a function of redshift, constructed from the AGORA simulations described in [111]. To understand the evolution of CIB parameters and of star-formation throughout cosmic time, it is desirable to combine bright lower-redshift CIB observations such as the *Planck* high-frequency bands with deep observations at lower frequencies such as the SPT-3G 220 GHz band. Though the 220 GHz band

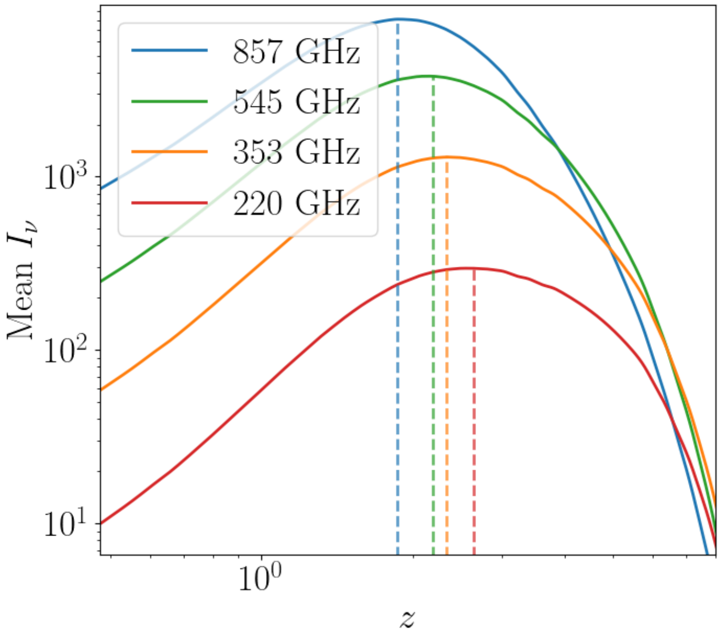

Figure 3.1: Simulated mean contribution to the CIB intensity as a function of redshift constructed from Agora simulations [111]. Vertical dashed lines indicate redshift corresponding to the peak mean intensity for each frequency. The SPT 220 GHz CIB emission peaks at a higher redshift but significantly lower intensity than does the *Planck*-band emission.

will individually lack the constraining power of higher frequency CIB measurements, its combination with higher-frequency observations will help to constrain the aspects of the CIB model that evolve with redshift.

This chapter is structured as follows. In Section 3.2 we describe the CIB model, adapted from [22]. This model allows us to directly relate the CIB to cosmic star-formation rate density, and thus to reconstruct cosmic star-formation rate density curves from CIB power spectral measurements. In Section 3.3 we describe the data used in this analysis, including the SPT-3G 2019-2020 data (both the 220 GHz temperature map and the CMB lensing map) as well as the *Planck* data. In Section 3.4 we show the angular power spectrum of the cross-correlation between SPT-3G 220 GHz and CMB lensing maps, and in 3.5 we present our constraints on the CIB model parameters. In Section 3.6, we present a forecast using a simulated data vector that matches the specifications of the upcoming SPT-3G+ experiment, and forecast the CIB model constraints expected from this future experiment. Finally we conclude in Section 3.7.

3.2 Models

3.2.1 CIB model

One of the most commonly adopted models for the CIB is the Shang (2012) model [123], which assumes a relationship between the host halo mass ($M_{\rm h}$) and the galaxy luminosity function. Due to the large number of parameters of this model, it is relatively flexible, and can be fitted to a wide range of observations. The main drawback of the model is that it is an empirical model that does not assume any underlying astrophysical processes. This makes it difficult to relate the parameters of this model to astrophysical observables. As we seek to extract astrophysical information from the CMB, we use the Maniyar (2021) CIB model [22]. This model describes a halo's star formation efficiency, as the ratio between its star formation rate (SFR) and its baryon accretion rate (BAR). The star formation efficiency is parameterized as a maximum efficiency, $\eta_{\rm max}$, times a log-normal distribution of halo masses centered around the most efficient star-forming halo mass $M_{\rm eff}$ with standard deviation $\sigma_{M_{\rm h}}$:

$$\frac{\rm SFR_c}{\rm BAR}(M_{\rm h}, z) = \eta = \eta_{\rm max} \exp\left[-\frac{(\log_{10} M_{\rm h} - \log_{10} M_{\rm eff})^2}{2\sigma^2_{M_{\rm h}}(z)}\right] \tag{3.1}$$

In the original model of [22], the standard deviation is parametrized as:

$$\sigma_{\rm M_h}(z) = \sigma_{M_{\rm h,0}} - \tau \times \max(0, z_{\rm c} - z). \tag{3.2}$$

However, this has the potential of producing negative variance depending on the value of $\sigma_{M_{h,0}}$ and τ, motivating us to make slight modification and reparametrize it as:

$$\sigma_{M_{\rm h}}(z) = \sigma_{M_{\rm h,0}} \left(1 - e^{-(\frac{z}{z_{\rm p}})^\lambda}\right), \tag{3.3}$$

where $\sigma_{M_{\mathrm{h}},0}$ is the standard deviation of the halo mass distribution at redshift zero. In Equation 3.3, z_{p} is the 'pivot' redshift around which star formation rolls off, and λ controls the slope of this roll-off. We vary both z_{p} and λ in this analysis. The baryon accretion rate BAR is defined as :

$$\begin{aligned}\mathrm{BAR}(M_{\mathrm{h}}, z) &= \langle M(M_{\mathrm{h}}, z)\rangle \times \Omega_{\mathrm{b}}(z)/\Omega_{\mathrm{m}} z \\ &= 46.1\mathrm{M}_{\odot}\mathrm{yr}^{-1}\left(\frac{M_{\mathrm{h}}}{10^{12}M_{\odot}}\right) \times (1+1.11z)\sqrt{\Omega_{\mathrm{m}}(1+z)^3+\Omega_{\Lambda}}, \qquad (3.4)\end{aligned}$$

where Ω_{m}, Ω_{b}, and Ω_{Λ} are the cosmological matter density, baryon density, and dark energy density parameters respectively. For subhalos, star formation density is taken as the minimum of two methods of calculation:

$$\mathrm{SFR}_{\mathrm{s}} = \min\left(\eta(m_{\mathrm{sub}}, z) \times \mathrm{BAR}(m_{\mathrm{sub}}, z),\ \mathrm{SFR}_{\mathrm{c}}(M_{\mathrm{h}}, z) \times \frac{m_{\mathrm{sub}}}{M_{\mathrm{h}}}\right) \qquad (3.5)$$

The reasoning for this is explained in [22]; taking the minimum of the two methods mitigates unphysical values resulting from cases in which either peak-efficiency halos contain very low-mass subhalos, or in which very massive halos contain subhalos near the peak-efficiency mass. The total emission from all halos (including central and satellite galaxies) within a given mass range are combined to compute the angular power spectrum of the CIB. The resulting CIB power spectrum is the sum of a one-halo and two-halo term. We also include a constant term representing the shot-noise component of the CIB.

$$C_{\ell}^{\mathrm{CIB}} = C_{\ell}^{1\mathrm{h}} + C_{\ell}^{2\mathrm{h}} + C_{\ell}^{\mathrm{shot}} \qquad (3.6)$$

The one-halo term accounts for the structure within a halo of mass M_{h}, while the two-halo term accounts for the clustering between two halos of masses M_{h} and M'_{h}:

$$
\begin{aligned}
C^{1\mathrm{h}}_{\ell,\nu,\nu'} = \int \frac{d\chi}{dz}\left(\frac{a}{\chi}\right)^2 \int \Bigg[& \frac{dj_{\nu,\mathrm{c}}}{d\log M_\mathrm{h}}\frac{dj_{\nu',\mathrm{s}}}{d\log M_\mathrm{h}}u(k, M_\mathrm{h}, z) \\
+ & \frac{dj_{\nu',\mathrm{c}}}{d\log M_\mathrm{h}}\frac{dj_{\nu,\mathrm{s}}}{d\log M_\mathrm{h}}u(k, M_\mathrm{h}, z) \\
+ & \frac{dj_{\nu,\mathrm{s}}}{d\log M_\mathrm{h}}\frac{dj_{\nu',\mathrm{s}}}{d\log M_\mathrm{h}}u^2(k, M_\mathrm{h}, z)\left(\frac{dn}{d\log M_\mathrm{h}}\right)^{-1} d\log M_\mathrm{h}\Bigg] dz, \qquad (3.7)
\end{aligned}
$$

$$
\begin{aligned}
C^{2\mathrm{h}}_{\ell,\nu,\nu'} = \int \frac{d\chi}{dz}\left(\frac{a}{\chi}\right)^2 \int\int & \left[\frac{dj_{\nu,\mathrm{c}}}{d\log M_\mathrm{h}} + \frac{dj_{\nu,\mathrm{s}}}{d\log M_\mathrm{h}}u(k, M_\mathrm{h}, z)\right] \\
\times & \left[\frac{dj_{\nu',\mathrm{c}}}{d\log M'_\mathrm{h}} + \frac{dj_{\nu',\mathrm{s}}}{d\log M'_\mathrm{h}}u(k, M'_\mathrm{h}, z)\right] \times b(M_\mathrm{h}, z) b(M'_\mathrm{h}, z) \\
\times & P_\mathrm{lin}(k, z) d\log M_\mathrm{h} d\log M'_\mathrm{h} dz. \qquad (3.8)
\end{aligned}
$$

In the above equations, $u(k, M_\mathrm{h}, z)$ is the Fourier transform of the halo's assumed NFW density profile. The halo mass function, $\frac{dn}{d\log M_\mathrm{h}}$ is taken from [124]. The halo bias $b(M_\mathrm{h}, z)$ is from [125]. $P_\mathrm{lin}(k, z)$ is the linear matter power spectrum, and the $\frac{dj_{\nu,c}}{d\log M_\mathrm{h}}$ and $\frac{dj_{\nu,s}}{d\log M_\mathrm{h}}$ terms are the differential emissivities for central halos and subhalos respectively. These are defined as:

$$
\frac{dj_{\nu,\mathrm{c}}}{d\log M_\mathrm{h}}(M_\mathrm{h}, z) = \frac{dn}{d\log M_\mathrm{h}} \times \chi^2(1+z) \times \frac{\mathrm{SFR_c}}{K} \times S^{\mathrm{eff}}_\nu(z) \qquad (3.9)
$$

$$
\begin{aligned}
\frac{dj_{\nu,\mathrm{s}}}{d\log M_\mathrm{h}}(M_\mathrm{h}, z) = & \frac{dn_\mathrm{s}}{d\log M_\mathrm{h}} \times \chi^2(1+z) \\
& \times \int\left(\frac{dn}{d\log m_\mathrm{sub}}(m_\mathrm{sub}|M_\mathrm{h}) \times \frac{\mathrm{SFR_s}}{K} \times S^{\mathrm{eff}}_\nu(z)\right) d\log m_\mathrm{sub} \qquad (3.10)
\end{aligned}
$$

Here $\frac{dn}{d\log m_\mathrm{sub}}(m_\mathrm{sub}|M_\mathrm{h})$ is the subhalo mass function, taken from [125], $K = 10^{-10} M_\odot L_\odot^{-1}\mathrm{yr}^{-1}$ is the Kennicutt constant, and $S^{\mathrm{eff}}_\nu(z)$ is the redshift-dependent SED of the CIB at frequency ν. One advantage of using this model is that, for a given profile, the cosmic star formation rate density can be easily computed from the model parameters:

$$
\begin{aligned}
\rho_{\mathrm{SFR}}(z) &= \rho_{\mathrm{SFR,c}} + \rho_{\mathrm{SFR,s}} \\
&= \int \left(\frac{dn}{d\log M_{\mathrm{h}}}\right) \times \mathrm{SFR_c}(M_{\mathrm{h}}) \times d\log M_{\mathrm{h}} \\
&+ \int \left(\frac{dn}{d\log M_{\mathrm{h}}}\right) \left(\int \left(\frac{dn}{d\log m_{\mathrm{sub}}}\right) \times \mathrm{SFR_s} \times d\log m_{\mathrm{sub}}\right) d\log M_{\mathrm{h}}. \quad (3.11)
\end{aligned}
$$

3.2.2 SED model

In [22], the spectral energy distribution (SED) of the CIB at each redshift is fixed, assuming those derived in [126]. To allow for flexibility in the SED model and to enable marginalization over the SED parameters, we used a modified blackbody model for the SED, with a dust temperature T_{d} that varies as a function of redshift:

$$T_{\mathrm{d}} = T_0(1+z)^{\alpha}, \quad (3.12)$$

where T_0 is the dust temperature at redshift $z = 0$, and α describes the redshift evolution of the dust temperature [1]. The dust temperature T_{d} is set as the modified blackbody temperature. The full SED at a given frequency ν is:

$$S_\nu \propto \left\{ \begin{array}{ll} \nu^{\beta} B_\nu(T_{\mathrm{d}}), & \text{if } \nu < \nu_0 \\ \nu^{\gamma}, & \text{if } \nu \geq \nu_0 \end{array} \right\}, \quad (3.13)$$

where $B_\nu(T_{\mathrm{d}})$ is the blackbody spectrum at frequency ν and temperature T_d, and β and γ are the spectral indices above and below the pivot frequency ν_0. The functions are connected smoothly at ν_0, at which $d\ln S_\nu/d\ln\nu = -\gamma$ as in [127] and [123]. In this analysis, we fix $\gamma = -2.0$, and vary the SED parameters T_0, α, and β, in addition to the model parameters described above. We confirmed the SED produced by this model for a given frequency and redshift roughly match with the result of

---

[1] We have verified that using our best-fit parameters, the dust temperature does not fall below the CMB temperature at the redshifts involved in this work

the [126] model mentioned above.

3.2.3 Lensing and CIB × lensing models

The CMB lensing model used in this analysis is the same as that used [126] and [22], and is described in detail in [116] and [117]. It is very briefly summarized here. The angular power spectrum of the lensing convergence κ is given by:

$$C_\ell^{\kappa\kappa} = \int \frac{d\chi}{\chi^2} W^\kappa(\chi)^2 P_{\text{lin}}\left(k = \frac{\ell}{\chi}, z\right), \tag{3.14}$$

where χ is the radial comoving distance, $P_{\text{lin}}(k, z)$ is the linear matter power spectrum, and W^κ is the lensing convergence kernel:

$$W^\kappa(\chi) = \frac{3}{2}\left(\frac{H_0}{c}\right)^2 \frac{\Omega_{\text{m}}}{a}\chi\left(1 - \frac{\chi}{\chi_{\text{CMB}}}\right). \tag{3.15}$$

Here, H_0 is the Hubble constant, Ω_{m} is again the matter density parameter, a is the scale factor, c is the speed of light, and χ_{cmb} is the comoving distance to the CMB. The cross-spectrum between the CIB at a given frequency ν and the CMB lensing convergence is given by:

$$C_\ell^{\nu\kappa} = \int \frac{d\chi}{\chi^2} a(\chi)\bar{j}_\nu(k, z) W^\kappa(\chi) P_{\text{lin}}(k, z). \tag{3.16}$$

The $\bar{j}_\nu(k, z)$ term is the bias-weighted CIB emissivity:

$$\bar{j}_\nu(k, z) = \int b(M_{\text{h}}, z)\left(\frac{dj_{\nu,\text{c}}}{d\log M_{\text{h}}} + \frac{dj_{\nu,\text{s}}}{d\log M_{\text{h}}} u(k, M_{\text{h}}, z)\right) d\log M_{\text{h}}. \tag{3.17}$$

We do not vary any parameters in the lensing model or any cosmological parameters in this work. Only the CIB model parameters are varied in this analysis.

Frequency [GHz]	N_{white} [μK-arcmin]
90	5.5
150	4.5
220	16.5

Table 3.1: South Pole Telescope temperature map depths for the 2019-2020 observing season, from [128].

3.3 Data

3.3.1 SPT-3G 220 GHz data

The SPT-3G camera is the third-generation SPT camera, which observes at 90, 150, and 220 GHz. Bandpasses for SPT-3G are shown in Figure 3.3 (solid lines). The main SPT-3G survey covers approximately 1500 square degrees, extending from $-50°$ to $+50°$ in right ascension, and $-42°$ to $-70°$ in declination. This field is divided into four sub-fields which are observed separately over the course of an observing season. Each sub-field map is calibrated separately and co-added to produce the full field map. The procedure in which these maps are created is documented in detail in [128]. This 2019-2020 dataset has three times lower noise than the previous SPT-3G data set from the 2018 season, leading to deeper maps for all three observation frequencies [128]. The 2019-2020 SPT-3G temperature map depths are summarized in Table 3.1.

In this work, the 220 GHz temperature map is used as a CIB map, since the anisotropies in the 220 GHz map are primarily sourced by the CIB with very little contribution from other astrophysical sources. On the other hand, 90 and 150 GHz maps have significant contributions from radio galaxies as well as the thermal Sunyaev Zel'dovich effect and therefore require more components to model. We treat the 220 GHz temperature power spectrum as the sum of CIB and CMB power spectra. When an estimate of the CIB autospectrum is necessary, such as when constructing a covariance matrix, we subtract a simulated CMB temperature power spectrum from the power spectrum of the SPT-3G 220 GHz temperature map. The

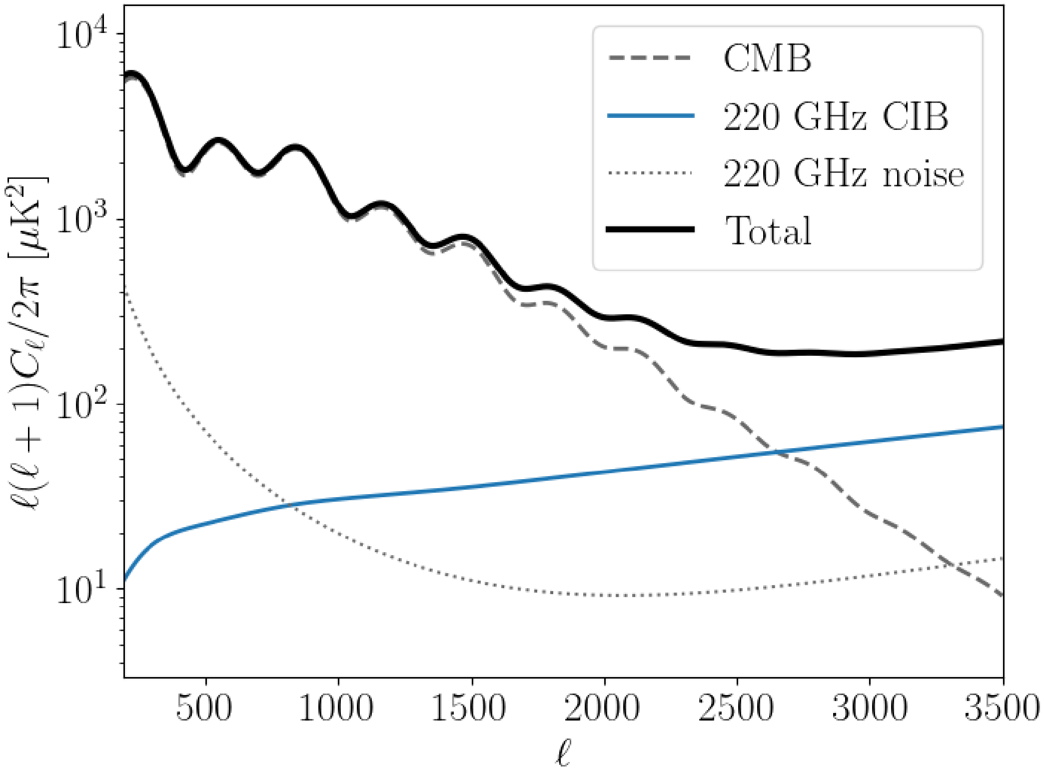

Figure 3.2: Comparison of the 220 GHz simulated CIB power spectrum amplitude to the simulated CMB amplitude and simulated 220 GHz noise of the SPT-3G 2019/2020 dataset. The CIB dominates at small angular scales due to the amplitude of the CIB shot-noise.

simulated CMB power spectrum is computed using the CAMB[2] software using a fixed cosmology based the *Planck* 2018 combined TT, TE, EE, and 2018 low E results [129], and is show as a gray dashed line in Figure 3.4.

3.3.2 SPT-3G CMB lensing data

The lensing map used in this analysis is constructed using 90, 150, and 220 GHz data from the same 2019-2020 observation season [128]. The 90, 150, and 220 GHz data are linearly combined in harmonic space to form minimum variance maps of the CMB temperature T and polarization modes E and B. Inverse-variance filtering is then applied to the maps, and pairs of T, E, and B maps are used to reconstruct the CMB lensing map using the quadratic estimator approach from [13]:

---

[2] `https://camb.info/`

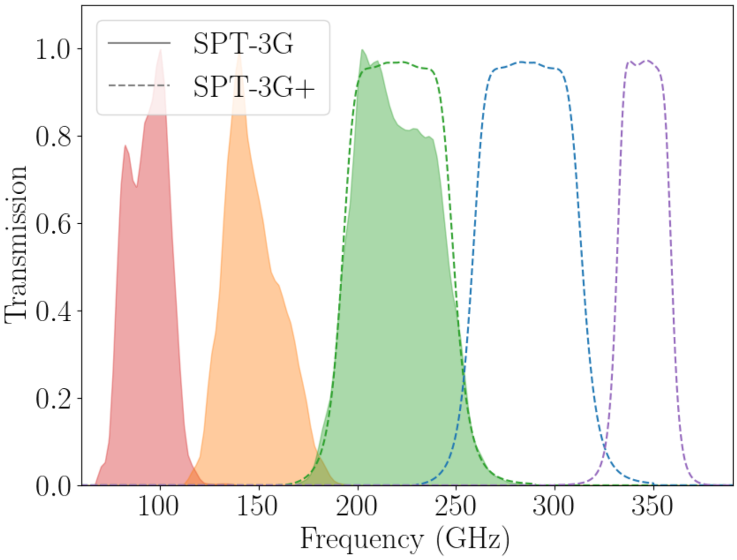

Figure 3.3: South Pole Telescope current and future bandpasses. These are measured array-averages for the current SPT-3G camera (solid, filled) and simulated bandpasses for the future SPT-3G+ camera (dashed). This analysis uses the SPT-3G 220 GHz data (solid green). Forecasts for SPT-3G+ use the dotted lines as fiducial bandpasses when computing filtered CIB SEDs and color corrections.

$$\bar{\phi}_{LM} = \frac{(-1)^M}{2} \sum_{\ell_1 m_1 \ell_2 m_2} \begin{pmatrix} \ell_1 & \ell_2 & L \\ -m_1 & -m_2 & M \end{pmatrix} \times$$

$$W^{\phi}_{\ell_1 \ell_2 L} X^{\mathrm{ivf}}_{\ell_1 m_1} Y^{\mathrm{ivf}}_{\ell_2 m_2}, \quad (3.18)$$

where W^{ϕ} is the lensing weight function and X^{ivf}, Y^{ivf} are inverse variance weighted maps of T, Q, and U. The estimate filtered map is debiased by subtracting off the simulated mean-field term $\bar{\phi}^{\mathrm{MF}}_{LM} \equiv \langle \bar{\phi}^{\mathrm{sim}}_{LM} \rangle$, and normalized by the response function $\mathcal{R}$ to take into account the filtering that is applied prior to the quadratic estimator. Finally the map is converted from lensing potential ϕ into the convergence $\kappa \equiv \frac{1}{2}\vec{\nabla}^2\phi$ by applying factors of multipole number in harmonic space:

$$\kappa = \frac{1}{2}\frac{1}{\mathcal{R}} \ell(\ell+1)(\bar{\phi} - \bar{\phi}^{\mathrm{MF}}) \quad (3.19)$$

The resulting convergence map is referred to as the SPT-3G lensing map in this work. Note that this is a minimum-variance lensing map, and thus contains a temperature portion. Future consistency checks will be performed against SPT polarization-only and profile-hardened lensing maps, to ensure that no bispectrum-type bias from galactic dust contamination is present in the cross-spectrum between the CIB and this lensing map.

3.3.3 Planck data

The *Planck* 353, 545, and 857 GHz CIB maps used in this analysis come from [25]. This dataset includes multiple masking options to avoid strong galactic dust contamination, which mask areas of the sky above varying HI column densities. For this analysis, we used the mask whose column density threshold is $N_{\rm HI} = 2.5 \times 10^{20} {\rm cm}^{-2}$, following the analysis in [25]. We cross-correlated these masked maps with the *Planck* minimum variance lensing map described in [130]. The resulting binned spectra are described below and are shown in Figure 3.4.

3.3.4 Independent $\rho_{\rm SFR}$ observations

In addition to data from SPT and Planck, we use a set of observed cosmic star-formation rate densities ($\rho_{\rm SFR}$). This dataset is fit jointly with the SPT and Planck data, and is assumed to be independent of both Planck and SPT. The $\rho_{\rm SFR}$ observations used for joint fitting are those compiled by [131]. These include observations from: [132, 133, 134, 135, 136, 137, 138, 139, 140, 141, 142, 143, 144, 145, 146, 147, 148, 149, 150, 151, 152, 153]. The binned combined star-formation rate density measurements from these works are plotted in black points with error bars in Figure 3.7.

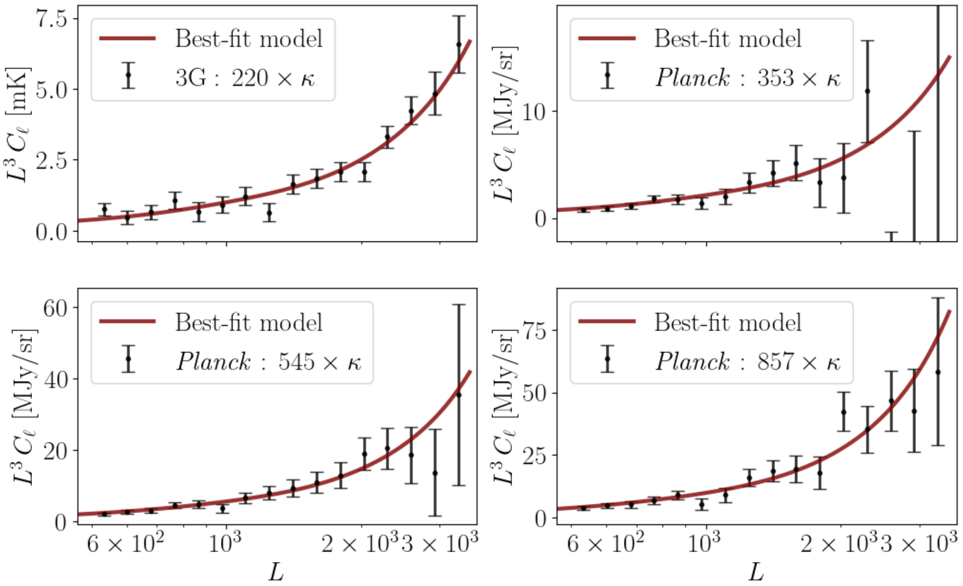

Figure 3.4: Binned bandpowers for SPT-3G and *Planck* CIB × κ spectra with the best-fit model overplotted in maroon. The χ^2 for the best-fit model is $\chi^2 = 57.5$ for 80 total bins (the four spectra shown here plus the $\rho_{\rm SFR}$ data), equating to a reduced $\chi^2/\text{bin} = 0.81$. Spectra are computed and fit in units of mK for SPT-3G data and in MJy/sr for *Planck* data.

3.4 Measurements and Analysis

3.4.1 Spectra and binning

Figure 3.4 shows the measured cross-correlation between CIB and CMB-lensing spectra for SPT-3G and the *Planck* Lenz maps. The black points on each panel represent the binned spectra used as the data vector in this analysis. Each spectrum was binned into sixteen bins spaced logarithmically from $\ell = 500 - 3500$. The error bars on these points are the square-root of the diagonal of the covariance matrix, which is assembled as described below. The observed cosmic star-formation rate density data is binned into sixteen logarithmically-spaced bins from redshift $z = 0.25 - 8$. These bins and their uncertainties are shown in black points in Figure 3.7.

3.4.2 Covariance

Excluding independent star-formation rate observations, the covariance matrices $\mathbf{\Sigma}$ in this analysis are built using the Gaussian approximation:

$$\Sigma^{ab,cd}_{\ell,\ell'} = \frac{\delta_{\ell,\ell'}}{(2\ell+1)\Delta\ell f_{\rm sky}} \left[C^{ac}_{\ell} C^{bd}_{\ell} + C^{ad}_{\ell} C^{bc}_{\ell}\right], \tag{3.20}$$

where the letters a, b, c, and d are the spectrum labels, $\Delta\ell$ denotes the bin width, $f_{\rm sky}$ is the effective fractional sky area of the combined spectra. This approximation produces a block-diagonal $\mathbf{\Sigma}$. When combining the SPT-3G and *Planck* datasets, Equation 3.20 is used to populate the off-diagonal SPT-3G × *Planck* blocks. Note that this requires computing the cross-correlations between all SPT-3G and *Planck* maps, and in this case $f_{\rm sky}$ becomes:

$$f^{\rm eff}_{\rm sky} = \frac{\min\left(\mathrm{f}^{\rm ab}_{\rm sky}\,,\, \mathrm{f}^{\rm cd}_{\rm sky}\right)}{\max\left(\mathrm{f}^{\rm ab}_{\rm sky}\,,\, \mathrm{f}^{\rm cd}_{\rm sky}\right)}. \tag{3.21}$$

When combining SPT-3G or *Planck* data with $\rho_{\rm SFR}$ data described in Section 3.3.4, the $\rho_{\rm SFR}$ dataset is treated as completely independent from both SPT-3G and *Planck*. We recognize that this is not strictly true, as the CIB is sourced by emission from star-forming regions, so there should be some correlation between the $\rho_{\rm SFR}$ measurements and the CIB power spectrum. However, we do not expect any correlation between the noise on the CIB × κ and $\rho_{\rm SFR}$ measurements. For this reason, we chose to set the $\rho_{\rm SFR}$ ×(CIB × κ) blocks of the joint covariance matrix to zero, and to acknowledge that the results of these joint fits are a best-case scenario for the constraints achievable from combining this datasets. For the SPT-3G 220 GHz × κ spectrum, Equation (3.20) requires the 220 GHz CIB auto-spectrum. Following [25], we compute this auto-spectrum by subtracting a simulated CMB power spectrum from the 220 GHz temperature auto-spectrum as described in Section 3.3.1.

3.4.3 Implementation

We used the `pyCCL` [154] software to compute model CIB × κ cross-spectra, in which both the lensing model and the [22] CIB model described above was implemented in the `pyCCL` framework, following the similar implementation of the [123] CIB model. We further modified this code to allow for our alternate expression for $\sigma_{M_\mathrm{h}}(z)$ (Equation 3.3) and our variable SED model (Equation 3.13). The raw SEDs given by $S_\nu(z)$ in Equation (3.13) were convolved with the SPT-3G 220 GHz bandpass transmission function, shown in solid green in Figure 3.3, to produce the filtered SEDs at each redshift that were fed into the `pyCCL` framework. An example of a simulated 220 GHz CIB spectrum is shown in blue in Figure 3.4. To compare the `pyCCL` CIB × κ spectrum to the measured spectrum, it is necessary to apply a color correction C and unit conversion U, which we compute following [155]:

$$U(K_\mathrm{CMB}\text{ to MJy/sr}) = \frac{\int d\nu\,\tau(\nu) b'_\nu}{\int d\nu\,\tau(\nu)(\nu_\mathrm{c}/\nu)} \times 10^{20} \left[\frac{\mathrm{MJy/sr}}{K_\mathrm{CMB}}\right] \tag{3.22}$$

$$C = \frac{\int (I_\nu/I_{\nu_\mathrm{c}})\tau(\nu) d\nu}{(\nu_\mathrm{c}/\nu)\tau(\nu) d\nu} \tag{3.23}$$

These quantities are instrument-specific since they require the knowledge of the band passes $\tau(\nu)$, and are therefore computed for SPT-3G and SPT-3G+ separately. For *Planck* frequencies, these values are taken from Appendix A of [156]. Table 3.2 gives all color corrections to unit conversion ratios used in this analysis.

The model was fit to the data through the Markov-Chain Monte Carlo (MCMC) process, for which we used the `Cobaya` [157, 158] software. This process samples a parameter space over a given set of priors to locate the regions of parameter space that minimize a predefined likelihood function $\mathcal{L}$. The likelihood function for a given point p in parameter space is:

$$\mathcal{L}(p) = (\mathbf{d} - \mathbf{m}(p))^\top \mathbf{\Sigma}^{-1} (\mathbf{d} - \mathbf{m}(p)), \tag{3.24}$$

where $\mathbf{\Sigma}$ is the covariance matrix computed using Equation (3.20), $\mathbf{d}$ is the data

Instrument	**ν (GHz)**	**Color correction/Unit conversion (μK/Jy)**
SPT-3G	220	2.045×10^{-3}
SPT-3G+	220	2.146×10^{-3}
	285	2.410×10^{-3}
	345	3.191×10^{-3}
Planck	353	3.820×10^{-3}
	545	1.841×10^{-2}
	857	4.348×10^{-1}

Table 3.2: Color correction and unit-conversion values used in this analysis. SPT values were computed from Equation 3.22 and *Planck* values were taken from [156].

vector constructed by binning the CIB × κ spectra as described in Section 3.4.1 and $\mathbf{m}(p)$ is the equivalent model vector computed by binning the simulated CIB × κ spectra generated by the `pyCCL` for the set of parameters corresponding to p.

For the ρ_{SFR} fits, the likelihood model is the same as Equation (3.20), except that $\mathbf{d}$ is the ρ_{SFR} measurements described in Section 3.3.4, shown in gray in Figure 3.7, and binned as described in Section 3.4.1. Similarly $\mathbf{m}(p)$ for the ρ_{SFR} case is the binned model star-formation rate density curve computed using Equation (3.11) at the parameter space point p. Note that Equation (3.11) does not depend on the SED of the CIB, meaning that a fit to only ρ_{SFR} measurements does not constrain the parameters T_0, α, or β. The covariance matrix $\mathbf{\Sigma}$ for the ρ_{SFR} case is simply a diagonal matrix whose values are the squared binned error bars shown in Figure 3.7.

We used uniform initial priors for all parameters in this analysis. The extents of these priors are given in Table 3.3 and can also be seen in Figures 3.5, 3.6, and 3.9. In the initial stages of this work, we used the COSMOPOWER package to construct emulators for $\mathbf{m}$ due to the long computation time of $\mathbf{m}$ and the correspondingly long timescale to run the MCMC chains to convergence. However, the error of these emulators was higher than desired, so the final chains shown here were run without emulation. In the future, it may become necessary to either improve emulator

Parameter	Fiducial	Range	Description
$\log_{10}(M_{\rm eff})$	12.6	(11.0, 14.0)	Halo mass with the most efficient star formation.
$\eta_{\rm max}$	0.37	(0.05, 1.0)	Maximum star formation efficiency
$\sigma_{\rm M}$	2.21	(0.05, 3.0)	Width of halo mass distribution at redshift 0
λ	3.98	(0.05, 5.0)	Slope variation in redshift of star-formation cutoff
$z_{\rm p}$	0.84	(0.05, 2.50)	Pivot redshift of star-formation cutoff
T_0	26.3	(18.0, 36.0)	Baseline dust temperature assumed in the modified blackbody SED
α	0.23	(0.05, 1.0)	Spectral index of dust temperature evolution with redshift
β	1.62	(1.0, 2.5)	Spectral index of dust SED modified blackbody

Table 3.3: Model parameters used in this analysis and their descriptions. Fiducial values are the best-fit points of the fits to the combined SPT-3G, Planck, and $\rho_{\rm SFR}$ datasets. Ranges are the uniform priors placed on these values.

accuracy or to explore alternative samplers to decrease the convergence times of these chains.

3.5 Results

3.5.1 Model parameter likelihoods

Figure 3.5 shows the posteriors resulting from the fits to SPT-3G 220 GHz × κ spectrum (blue), the combination of all three *Planck* $353, 545, 857$ GHz × κ spectra (orange), and the combined fit to both of these datasets (red). The SPT-3G and *Planck* datasets agree well for $\log_{10}(M_{\rm eff})$, though the other parameters are very loosely constrained or unconstrained by SPT-3G alone. The cross-correlation between *Planck* CIB and lensing has greater constraining power, though it fails to constrain the λ and $z_{\rm p}$ parameters. This discrepancy in constraining power implies that the model lacks sensitivity to small angular scales. However, when combined with the *Planck* dataset, the SPT-3G 220 GHz measurement marginally improves

Data	χ^2	χ^2/bin
SPT-3G	11.0	0.69
Planck	34.7	0.72
SPT-3G + *Planck*	51.9	0.81
$\rho_{\rm SFR}$-only	3.52	0.22
SPT-3G + *Planck* + $\rho_{\rm SFR}$	57.5	0.72

Table 3.4: Values of χ^2 and reduced χ^2/bin for the best-fit points for each chain run in this analysis.

constraints on $\log_{10}(M_{\rm eff})$, $\sigma_{\rm M}$ and β, as seen in the one-dimensional plots.

In our model, the least constrained parameters are λ and $z_{\rm p}$ as shown in Figure 3.5. As shown in Equation 3.3, these parameterize the redshift evolution of the width of the mass distribution of star-forming halos. To improve the constraints on these parameters, we combine the SPT-3G and *Planck* datasets with the independent star-formation rate density measurements described in Section 3.3.4. Figure 3.6 shows the results of the joint fits with the $\rho_{\rm SFR}$ data for SPT-3G, *Planck*, and their combination. The yellow contours in Figure 3.6 are from the $\rho_{\rm SFR}$ data alone. Note again that, since Equation 3.11 does not consider the SED of the CIB, the SED parameters T_0, α, and β are unconstrained by the $\rho_{\rm SFR}$ data. It is immediately apparent that the $\rho_{\rm SFR}$ data improves our constraints on λ and $z_{\rm p}$ relative to SPT-3G or *Planck* alone. The purple contours in Figure 3.6 are identical to the purple contours for the SPT-3G + *Planck* fit in Figure 3.5, and are shown here for comparison. The red contours show the results of the combined fit to all three of the SPT-3G, *Planck* and $\rho_{\rm SFR}$ datasets. The markers on Figure 3.5 represent the best-fit points for the combined fit. The values of these markers are summarized in Table 3.3, and are taken to be our fiducial parameter values for the SPT-3G+ forecasts below.

3.5.2 Cosmic star formation rate density evolution

The cosmic star-formation rate density can be reconstructed from the model parameters following Equation 3.11. Figure 3.7 shows the reconstructed star-formation

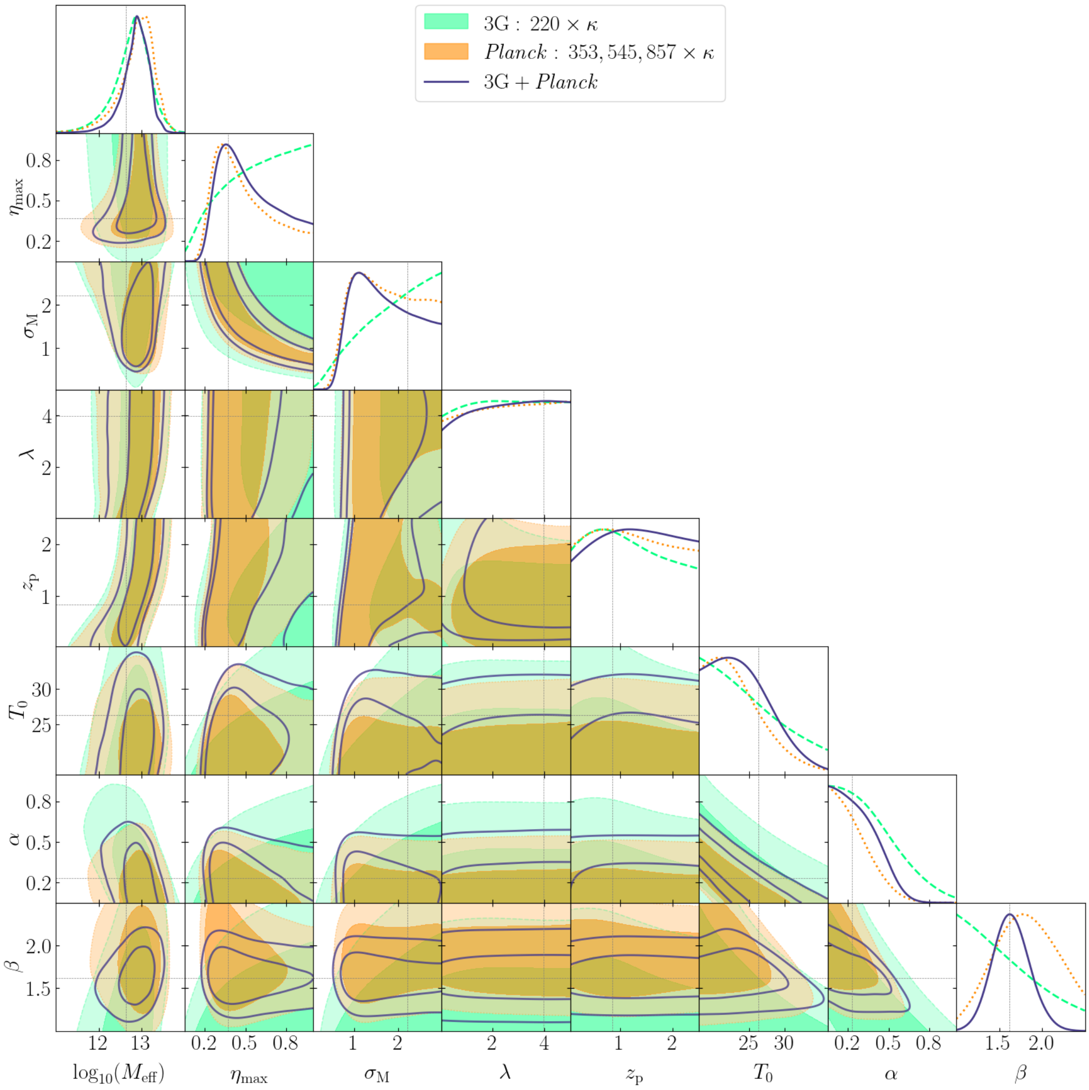

Figure 3.5: Posterior distributions for CIB model parameters using the SPT-3G 220 GHz × κ data are shown in filled green, and in dashed lines on the one-dimensional plots. Aside from $\log_{10}(M_{\rm eff})$, the SPT-3G 220 GHz data is unable to tightly constrain any model parameter. The *Planck* [25] 353, 545, and 857 GHz $\times\kappa$ posteriors are shown in filled orange, and in dotted lines on the one-dimensional plots. This combination has higher constraining power, as is expected due to its multiple frequency bands.The posteriors resulting from combining the two experiments are plotted in open purple contours.Though the SPT-3G data improves upon the *Planck* constraints for $\sigma_{\rm M}$ and β, neither dataset nor their combination fully constrains the model.

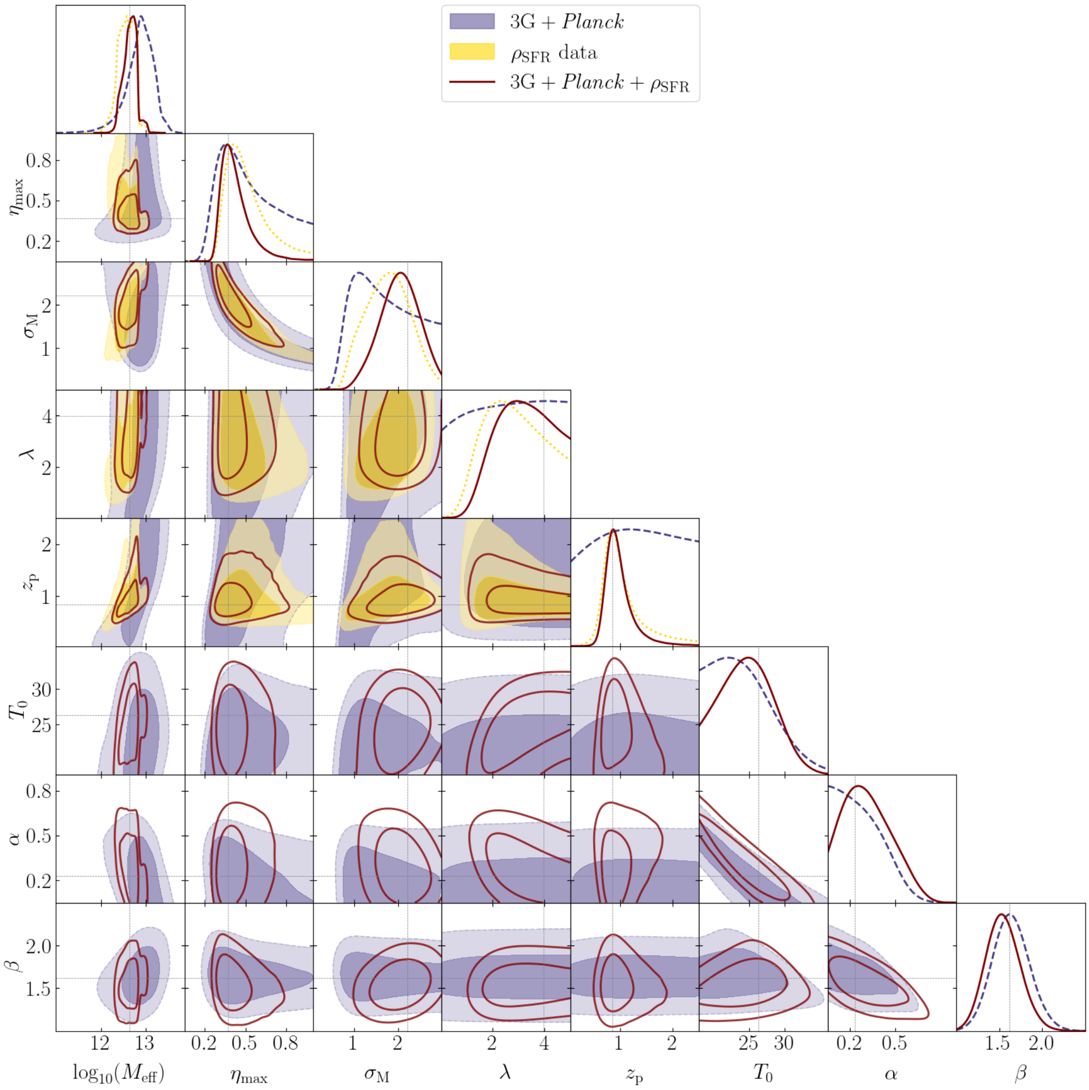

Figure 3.6: Posterior distributions for CIB model parameters incorporating independent $\rho_{\rm SFR}$ observations.The posteriors from the combined SPT-3G and *Planck* data, identical to those in Figure 3.5, are shown here in filled purple, and in dashed lines on the one-dimensional plots.The posteriors resulting from the $\rho_{\rm SFR}$ data alone are shown in solid yellow, and in dotted lines on the one-dimensional plots. The $\rho_{\rm SFR}$-only constraints are significantly tighter than those from the SPT-3G and *Planck* datasets, though the $\rho_{\rm SFR}$ data cannot place constraints on the CIB SED model parameters T_0, α, and β. The posteriors resulting from combining the SPT-3G, *Planck*, and $\rho_{\rm SFR}$ datasets are plotted in open maroon contours. The combined datasets improve constraints on the CIB SED model parameters.

rate density as a function of redshift for the best-fit model parameter values for each dataset and for their combination. The black points with error bars are the binned independent $\rho_{\rm SFR}$ measurements described in Section 3.3.4 and used to produce the yellow $\rho_{\rm SFR}$-only posteriors shown in Figure 3.6. The gray shaded region in Figure 3.7 is the star-formation rate density as a function of redshift reconstructed by sampling the posteriors of the $\rho_{\rm SFR}$-only chain using Equation 3.11. The sampling was done by choosing 1000 random points from the posterior for which $\chi^2/\nu < 1$.[3] The green SPT-3G region and the orange *Planck* region represent independent measurements of the cosmic star-formation rate density over time taken at slightly different redshifts, as indicated in Figure 3.1. These were similarly generated by sampling from the green SPT-3G+ and orange *Planck* posteriors shown in Figure 3.5. Finally, the maroon shaded region corresponds to the combined SPT-3G, *Planck*, and $\rho_{\rm SFR}$ constraint on cosmic star-formation rate density, and the solid maroon line represents the best-fit model to the combined data.

Though both the SPT-3G and *Planck* curves approximately follow the black $\rho_{\rm SFR}$ data points, these experiments separately have very little constraining power compared to the $\rho_{\rm SFR}$ observational data. The combination of these three measurements at different redshifts results in the maroon curve in Figure 3.7. The best-fit parameters used to generate the maroon line were obtained by minimizing the likelihood given in Equation 3.24 over the maroon combined posteriors in Figure 3.6. It is evident that the combined constraints offer very little improvement upon the gray $\rho_{\rm SFR}$-only result.

Figure 3.8 shows histograms of the reconstructed $\rho_{\rm SFR}$ values at four different redshifts computed at a thousand independent points in parameter space sampled from within the gray and maroon shaded regions in Figure 3.7. At each of the sampled points, Equation 3.11 was evaluated to produce an $\rho_{\rm SFR}$ versus redshift curve. Each $\rho_{\rm SFR}$ curve was then binned into linearly spaced bins from $z = 0.25$ to $z = 8$, each spanning $\Delta z = 0.25$ in redshift. The averages of these bins were then

---

[3] This criterion was chosen since selecting parameter values that lie within 1-σ is ill-defined when the parameters are highly degenerate.

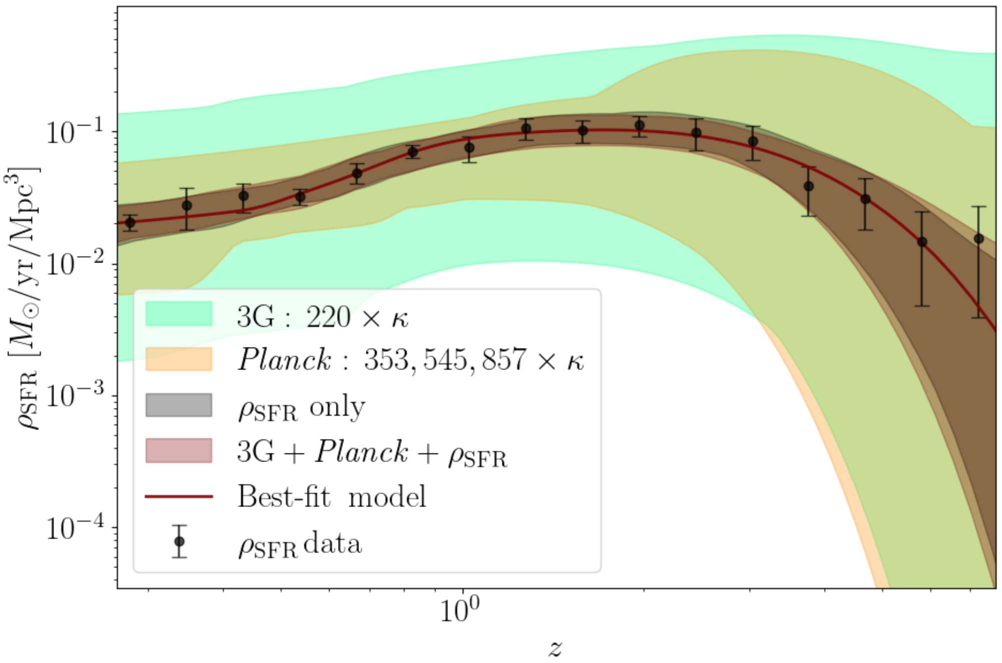

Figure 3.7: Constraints on cosmic star-formation rate density as a function of redshift for each dataset and their combination. For each dataset, 1000 random points were sampled from its posterior, and Equation 3.11 was used to compute $\rho_{\mathrm{SFR}}(z)$. The green SPT-3G and orange *Planck* regions correspond to the green and orange posteriors in Figure 3.5, while the grey and maroon regions correspond to the yellow ρ_{SFR} and maroon posteriors in Figure 3.6. The SPT-3G and Planck measurements offer little to no improvement upon the ρ_{SFR}-only measurement of cosmic star-formation rate density over time.

binned into the histograms shown in Figure 3.8 and fit with Gaussian probability density functions shown as dashed lines. The combination of SPT-3G, *Planck*, and the ρ_{SFR} measurements (maroon) produces a slightly different distribution at each redshift than is produced by the ρ_{SFR} measurements (gray) alone. The means of the maroon distributions are shifted up by 1% at redshift $z = 1$, and down at redshifts $z = 2, 3, 4$ by 6% , 5%, and 0.3% respectively from the ρ_{SFR}-only means. The maroon distributions are narrower by 7%, 6%, and 2% at redshifts $z = 1, 3, 4$ respectively and are wider by 1% at redshift $z = 2$ than the gray distributions. The overall takeaway is that while the addition of SPT-3G and *Planck* data does improve upon CIB model constraints, it does not improve upon ρ_{SFR} constraints when compared to the ρ_{SFR}-only measurements.

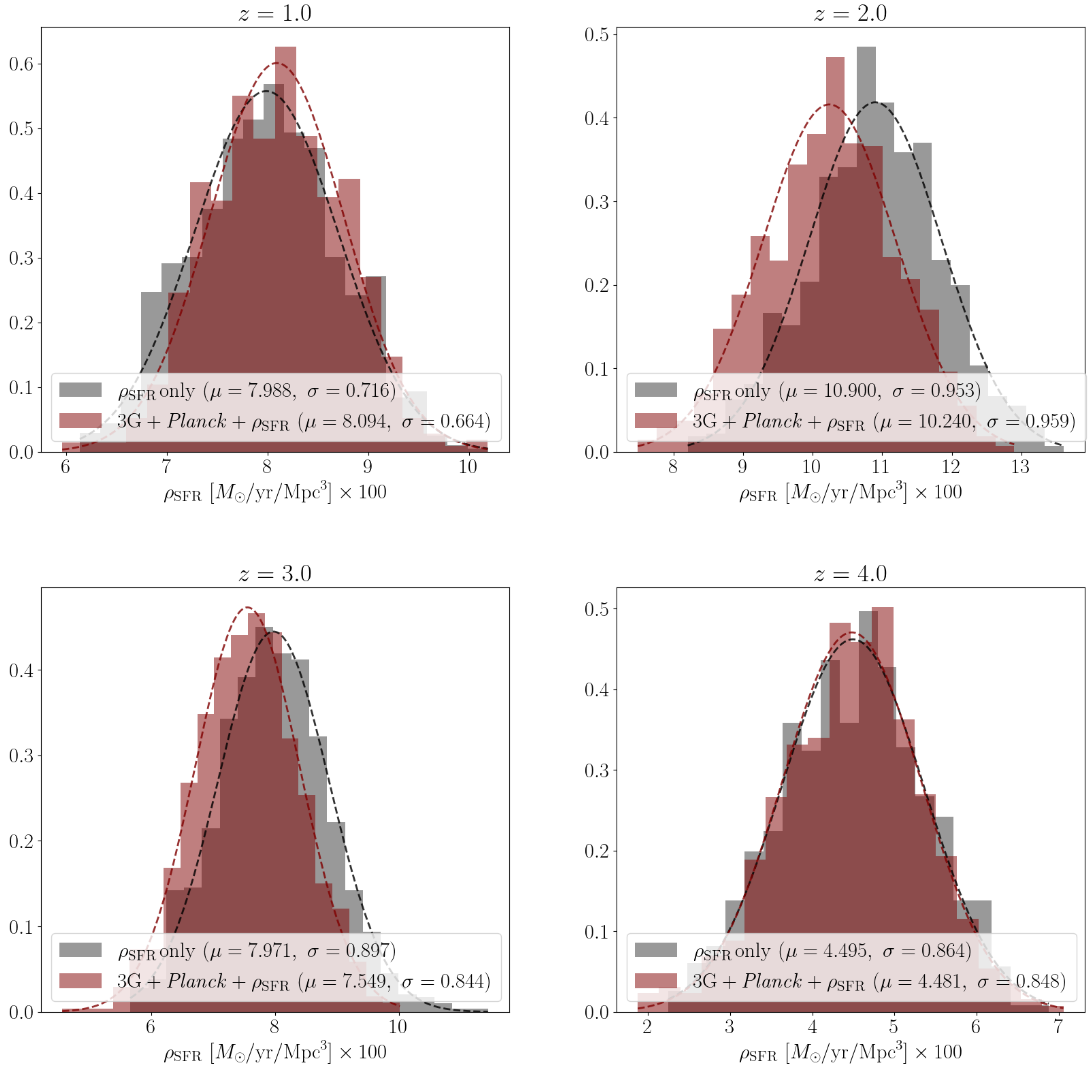

Figure 3.8: Histograms of $\rho_{\rm SFR}$ values at redshifts $z = 1 - 4$. These histograms were produced by sampling the posteriors in Figure 3.6 and selecting for points at which the reduced $\chi 2 < 1$, then using Equation 3.11 to compute the $\rho_{\rm SFR}$ as a function of redshift curve for each sampled point. The curves were binned into redshift bins of width $\Delta z = 0.25$, and the bin values were histogramed at each of the redshifts shown above. Grey histograms correspond to the $\rho_{\rm SFR}$ data alone, while red histograms correspond to the combination of SPT-3G, Planck, and $\rho_{\rm SFR}$ data. Each histogram is normalized so that it integrates to 1, and is fit with a Gaussian probability density function with mean μ and standard deviation σ. There is negligible difference in the widths of the distributions at each redshift.

3.6 Forecasts for SPT-3G+

As the SPT-3G survey nears completion, an upgrade to the SPT receiver is in the works: the next-generation camera, called SPT-3G+, will observe at 220, 285, and 345 GHz. The SPT-3G+ dataset will serve as a high-frequency, high-sensitivity complement to the SPT-3G dataset. As this analysis would be enhanced by the SPT-3G+ data, we forecast the expected CIB model constrains achievable from the SPT-3G+ survey. In this forecast, we take the best-fit values of the joint SPT-3G, *Planck*, and SFRD posteriors from Table 3.3 as the fiducial CIB model parameters. We use the model described above to generate simulated CIB × CMB lensing spectra at 220, 285, and 345 GHz. These spectra are binned using the binning scheme described in Section 3.4.1 to produce a simulated data vector.

3.6.1 SPT-3G+ covariance

The covariance for our SPT-3G+ forecasts also uses the Gaussian approximation given in Equation 3.20. To utilize Equation 3.20 it is necessary to model the cross-spectra between SPT-3G+ frequency bands $C_\ell^{\text{3G+}}(\nu_i, \nu_j)$. Our model for this includes for each frequency band the expected instrumental noise as well as the predicted atmospheric noise and the CMB itself. Instrumental and atmospheric noise are assumed to be uncorrelated between frequency bands. Our model for the SPT-3G+ spectra is:

$$C_\ell^{\text{3G+}}(\nu_i, \nu_j) = C_\ell^{\text{CIB}}(\nu_i, \nu_j) + C_\ell^{\text{CMB}} + N_\ell(\nu_i)\delta_{ij}, \tag{3.25}$$

where $C_\ell^{\text{CIB}}(\nu_i, \nu_j)$ is the sum of the one-and-two-halo CIB models and the CIB shot noise C_ℓ^{shot}. The shot noise values used for this forecast are included in Table 3.5. Here $N_\ell(\nu)$ is the combination of the instrumental detector and atmospheric noise, modeled as in [67], using the values from Table 3.5 for detector and atmospheric noise parameters:

ν (GHz)	220	285	345
$C_\ell^{\rm shot}$ (mK)^2	6.0×10^{-5}	1.0×10^{-3}	1.7×10^{-2}
$\ell_{\rm knee}$	2100	2100	2600
α	3.9	3.9	3.9

Table 3.5: Table of values used in the SPT-3G+ noise model to produce the simulated SPT-3G+ covariance matrix. Shot-noise values were estimated for 220 and 345 GHz by averaging the high-ℓ regions of the SPT-3G 220 GHz TT spectrum and *Planck* 353 GHz CIB spectrum [25] respectively. The 285 GHz value is the geometric mean of the 220 and 345 GHz estimates.

$$N_\ell(\nu) = N_{\rm white}(\nu)\left(1 + \left(\frac{\ell_{\rm knee}(\nu)}{\ell}\right)^{\alpha(\nu)}\right). \tag{3.26}$$

Equation 3.20 also requires a predicted lensing autospectrum. We used the SPT-3G lensing autospectrum here as a conservative estimate.

3.6.2 SPT-3G+ Results

Figure 3.9 shows the results of the SPT-3G+ forecasts described above. The magenta contours show the expected posteriors from the combination of all three SPT-3G+ observation frequencies, and are overplotted with the SPT-3G 220 GHz contours from Figure 3.5 above. As expected, the SPT-3G+ forecasts show a definite improvement upon the constraints, or lack thereof, from SPT-3G. However, as is consistent with the findings for the SPT-3G and Planck data, SPT-3G+ is unlikely to constrain most of the parameters in this model.

3.7 Conclusions

We have computed the cross-spectra between the SPT-3G 2019-2020 220 GHz temperature map and the SPT-3G 2019-2020 CMB lensing map, and we have fit this cross-spectrum with a modified version of the CIB model from [22]. We find that the SPT-3G cross-spectrum alone has very little constraining power alone on this model. This is expected, as a single band is unable to constrain the SED. We performed

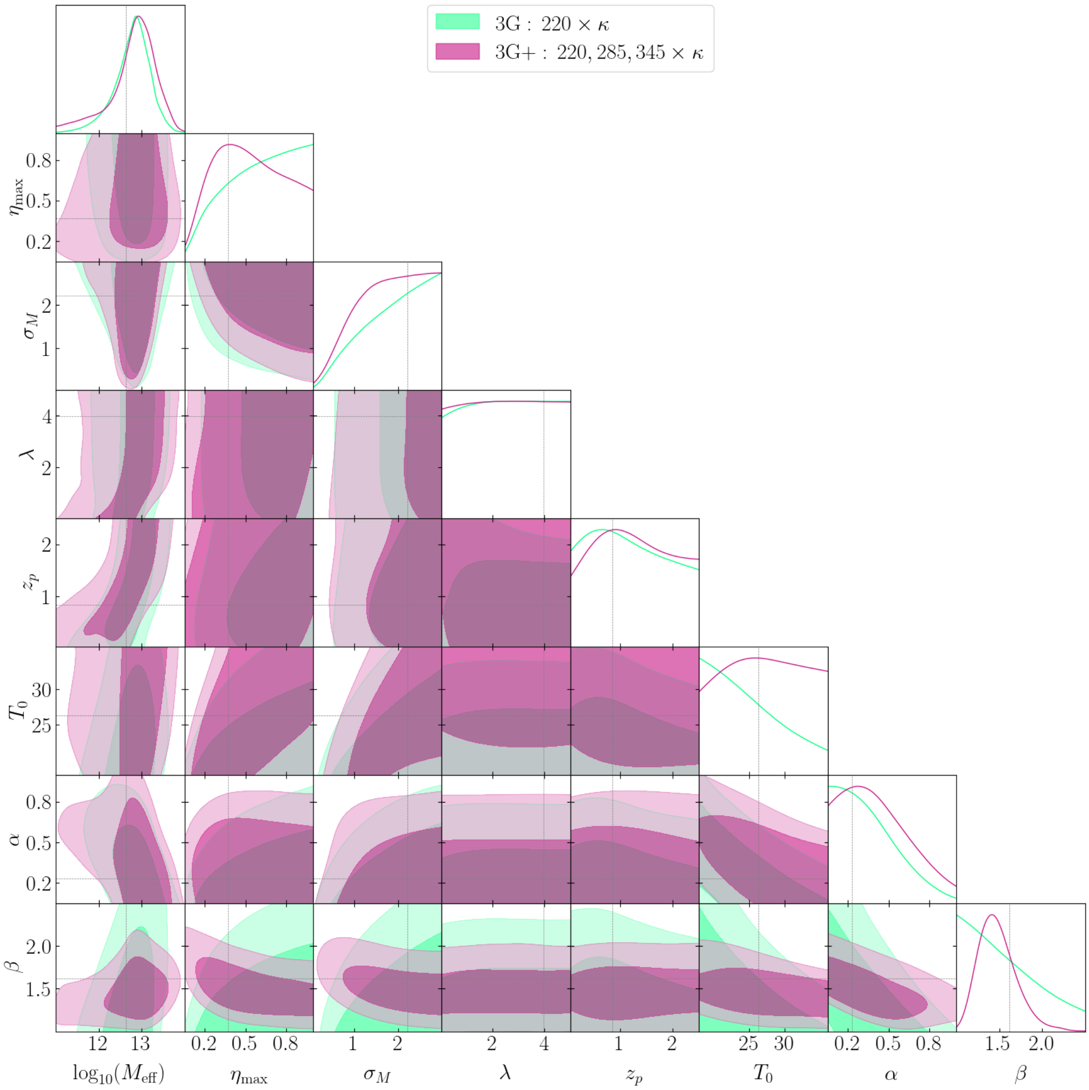

Figure 3.9: Forecasts for the constraints on this model achievable by SPT-3G+. The forecasted posteriors for SPT-3G+ are shown in magenta, atop the green SPT-3G posteriors from Figure 3.5. Like SPT-3G and *Planck*, SPT-3G+ fails to constrain most of the parameters in this model.

the same fits for the combination of all three Planck high-frequency (353, 545, and 857 GHz) bands and found that they had more constraining power. The Planck constraints were improved when fit jointly with the SPT-3G 220 GHz data. However, even when combined, the Planck and SPT-3G datasets did not constrain the full model. We then added independent observations of the cosmic star-formation rate density at various redshifts to our dataset. The combination of SPT-3G 220 GHz data, Planck high-frequency data, and the ρ_{SFR} observations was able to constrain the model, though, with the exception of $\log_{10}(M_{\mathrm{eff}})$, the vast majority of the constraining power came from the ρ_{SFR} data for all non-SED parameters. Using Equation 3.11, we reconstructed the cosmic star-formation rate density as a function of redshift for the best-fit model parameters for the combined data. The resulting curve deviated slightly from that obtained by fitting only the ρ_{SFR} observational data. The final portion of this work forecasted the constraints on this model expected from the upcoming SPT-3G+ experiment. Using the best-fit parameters to the combined SPT-3G, Planck, and ρ_{SFR} dataset as fiducial parameters, we simulated the SPT-3G+ covariance matrix using the expected instrumental and atmospheric noise. We found that SPT-3G+ was unlikely to constrain this model in any meaningful way, which is consistent with the lack of constraining power present for this model in either the SPT-3G or Planck datasets.

One conclusion to draw from this analysis is that this model contains too many degeneracies to be constrained by CIB power spectra alone. Indeed, in [22], the parameters λ, z_p, T_0, α, and β were all effectively fixed. The addition of the ρ_{SFR} data in this work served the same purpose of essentially providing all of the constraining power for the first five parameters in the model, allowing the SPT-3G and Planck data to constrain the remaining three. Further analysis is underway to determine reasonable, physically motivated ways to constrain some of the parameters in this model in order to extract some value from the SPT-3G and Planck data.

Early in this project, we also attempted fits to the CIB autospectra, but found that this model was not a good fit to the CIB autospectrum. We were unable to locate a point in parameter space which fit the data with reduced $\chi^2 < 1$. It is unclear whether the CIB autospectrum measurements were biased in some way, or whether this model simply does not fit CIB autospectra. As CMB instruments become more sensitive, it is clear that additional development is required to capture the complexity of CIB emission in a model that is constrainable by existing data. Future analyses, especially with more complex models, will require increased computation speed, increased computation resources, or more accurate emulation methods.

Chapter 4

Design & Fabrication of MKIDs for SPT-3G+

Chapters 4 and 5 concern the design, fabrication, and testing of Microwave Kinetic Inductance Detectors, or MKIDs, for SPT-3G+. As described in Chapter 1, the SPT-3G+ focal plane will contain 34,104 monochroic MKIDs, observing at 220, 285, and 345 GHz. The sensitivity requirements presented in Chapter 1 needed to achieve the science targets for SPT-3G+ impose strict requirements on the detector design. An attempt to meet these requirements is made here, but much more work remains to reliably fabricate high-quality deployment-grade arrays. At the time of this thesis, the vast majority of detector development for SPT-3G+ has been for the 220 GHz detectors, and only a few prototype devices exist for the higher frequencies.

4.1 MKID-related theory

A microwave kinetic inductance detector is a superconducting resonant circuit whose resonant frequency changes via the kinetic inductance effect depending on the amount of power absorbed by its inductive element. The following section will explain that sentence.

4.1.1 Superconductivity and kinetic inductance

Consider a piece of aluminum. At the atomic scale, the solid aluminum is made up of a lattice of atomic nuclei through whose valence electrons are shared among the entire lattice. The ability of the electrons to travel through the lattice is what makes a material electrically conductive. At all temperatures above 0°K, the nuclei in the lattice vibrate, and the amplitude of these vibrations increases with temperature. At room temperature, for all known materials, electrons collide repeatedly with the vibrating nuclei as they travel through the lattice. This "impedance" to the flow of electrons is what causes normal electrical resistance [159]. If the aluminum is cooled down, the lattice vibration amplitude decreases, allowing smaller-scale effects to become relevant. As an electron moves through the lattice, the positively charged lattice deforms slightly toward the electron, creating a positive overdensity. Elsewhere in the lattice, another electron of opposite spin becomes attracted to that positive overdensity and alters its path toward it. The movement of the second electron creates another positive overdensity, which attracts the original electron, and the movement of the two electrons becomes correlated. The phonon-mediated correlation between two electrons is known as a Cooper pair, and the temperature at which the first Cooper pair forms is called the material's transition temperature T_c [159]. For bulk aluminum, $T_c \approx 1.2$°K.

Below T_c, there exist two electron populations: the Cooper-paired electrons and the unpaired electrons, or "quasiparticles." Cooper pairs are bosons with spin zero, and as such can condense into a ground state with lower energy than their unpaired fermion counterparts. The two populations are separated by an energy band gap [159]:

$$\Delta = 1.76 k_B T_c. \tag{4.1}$$

Breaking a Cooper pair requires energy larger than 2Δ. If the material is cold enough that the lattice vibrations cannot impart this energy, then collisions are unable to scatter electrons out of their Cooper pairs, and the Cooper pair condensate moves without resistance throught the material. This is called superconductivity.

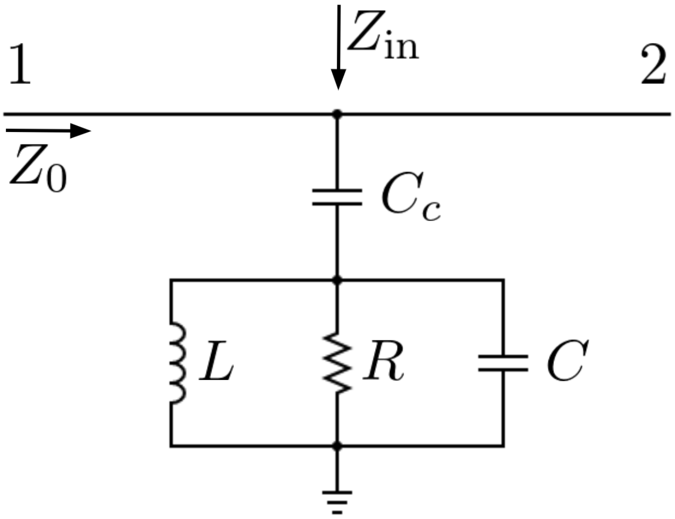

Figure 4.1: Circuit diagram of an RLC circuit coupled to a transmission line.

When a superconducting aluminum wire at a temperature $T \ll T_c$ is biased with an alternating current, its Cooper pair condensate moves back and forth through the wire. The moving Cooper pairs have mass, and hence kinetic energy. When the current alternates and the Cooper pairs turn around, the kinetic energy behaves as an inductance in the wire. This behavior is called the kinetic inductance effect. Power absorbed by the wire breaks Cooper pairs, which changes the mass of the condensate and hence the kinetic inductance of the wire. Thus the wire is essentially a variable inductor whose inductance depends on the power it absorbs. Coupling the inductor to a capacitor creates a resonator whose resonant frequency depends on the amount of power absorbed by the inductor. The resulting device is called a kinetic inductance detector, and when operated at microwave frequencies, is called a microwave kinetic inductance detector, or MKID.

4.1.2 Superconducting resonators

The MKID circuit is usually represented as the parallel combination of a resistor, inductor and capacitor, known as an RLC resonator, in series with a coupling capacitor. This circuit is shown in Figure 4.1. In this configuration, Z_0 is the characteristic impedance of the feedline, R is an equivalent resistance inversely related to the quasiparticle density, L is the resonator inductance, C is the resonator capacitance, and C_c is the coupling capacitance. The expression $\omega_0 = 1/\sqrt{LC}$ is often described as the MKID resonant frequency, but that is an idealized scenario. The true resonant frequency ω_r is the value of ω at which the input impedance Z_{in} of the series combination of the RLC resonator and the coupling capacitor is zero [160]:

$$Z_{\text{in}} = \left[\frac{1}{R} + \frac{1}{j\omega L} + j\omega C\right]^{-1} - \frac{j}{\omega C_c} \approx \frac{R}{1 + 2jQ_i x_0} - \frac{j}{\omega C_c} = 0, \tag{4.2}$$

where $x_0(\omega) = (\omega - \omega_0)/\omega$ parameterizes the fractional shift of the resonant frequency from that of the idealized LC circuit. The parameter $Q_i = \omega_0 L/R$ is called the internal quality factor, and will be discussed shortly. The equation $Z_{\text{in}} = 0$ is a quadratic in x_0:

$$\frac{4Q_i^2}{\omega_r C_c} x_0^2 + 2Q_i R x_0 + \frac{1}{\omega_r C_c} = 0. \tag{4.3}$$

In the approximation $R \gg \frac{2}{\omega_r C_c}$, which is true at low temperatures, the two solutions are:

$$x_0 = -\frac{\omega_r C_c R}{2Q_i} = -\frac{\omega_r C_c}{2\omega_0 C} \implies \omega_r = \frac{\omega_0}{1 + \frac{C_c}{2C}} \tag{4.4}$$

$$x_0 = 0 \implies \omega_r = \omega_0 \tag{4.5}$$

The first solution corresponds to most situations, and indicates that in the presence of the coupling capacitor, the expression for the fractional frequency shift from resonance changes from the idealized x_0 to the more realistic $x_r = x_0 - \frac{\omega_r C_c}{2\omega_0 C}$. The second solution corresponds to situations where the coupling capacitance is so small as to be nearly insignificant, such that to zeroth order it essentially doesn't exist.

We want to measure the power transmitted from port 1 in Figure 4.1 to port 2 as a function of frequency. The expression for this is [161]:

$$S_{21}(\omega) = \frac{2}{1+\frac{Z_0}{Z_{\text{in}}}}. \tag{4.6}$$

To put this in terms of the true resonant frequency ω_r, substitute x_r into Equation 4.2. Under the assumptions $Q_i \gg 1$, which is true for all practical purposes, and $Q_i x_r^2 \ll 1$, which is true for frequencies close to ω_r, Equation 4.2 can be approximated [160]:

$$Z_{\text{in}}(\omega) \approx \frac{2Q_i}{Q_c}\frac{1}{1+2Q_i x_r}, \tag{4.7}$$

$$Q_c = \frac{2C_r}{\omega_r Z_0 C_c}. \tag{4.8}$$

Here, Q_c is the coupling quality factor, which is derived properly in [160], and discussed further below. Combining Equations 4.6 and 4.7 produces the final expression for the power transmitted through the feedline in Figure 4.1:

$$S_{21} = \frac{Q_r/Q_i + 2Q_r x_r}{1+2Q_r x_r} = 1 - \frac{Q_r}{Q_c}\left(\frac{1}{1+2jQ_r x_r}\right), \tag{4.9}$$

where Q_r is the resonator quality factor, related to the other quality factors by $Q_r^{-1} = Q_i^{-1} + Q_c^{-1}$. For the second equality, be aware that Q_c has an imaginary component. The quality factors Q_i, Q_c, and Q_r parameterize the way that energy is dissipated in the system of the resonator and coupling capacitor. The internal quality factor Q_i is the ratio of the energy stored in the resonator to the energy dissipated by the resonator per cycle due to loss. The coupling quality factor Q_c is the ratio of the energy stored in the resonator to the energy dissipated per cycle through the coupling capacitor to the readout feedline. The resonator quality factor Q_r is the overall ratio of the energy stored in the resonator to the energy dissipated from the resonator per cycle, which is the classic definition of a quality factor, and which relates to the resonance full-width at half-maximum Δf by $Q_r = f_r/\Delta f$. How do the quality factors affect the resonance shape? When $Q_i \gg Q_c$, then $Q_r \approx Q_c$

and $|S_{21}|$ becomes a Lorentzian dip whose depth depends on Q_c. Conversely, when $Q_i \ll Q_c$, then $Q_r \approx Q_i$, and $|S_{21}| \approx 1$, so the transmission just looks flat. As discussed further in this chapter, the relationship between Q_i and Q_c can be tuned to acomplish design goals.

4.1.3 Kinetic inductance detectors

In the previous section, we determined the resonant frequency ω_r of the device consisting of the RLC circuit and coupling capacitor. We are interested in using this device to detect changes in the kinetic inductance of the inductor. Let's look at how the resonant frequency responds to a change in inductance.

$$\omega_r = \frac{\omega_0}{1 + \frac{C_c}{2C}} = (LC)^{-1/2} \left(1 + \frac{C_c}{2C}\right)^{-1} \tag{4.10}$$

The total resonator inductance L is sourced by multiple effects. We are interested in just changes in the kinetic inductance L_k, and we assume that all other sources of inductance are static, meaning $\delta L = \delta L_k$, and define the kinetic inductance fraction $\alpha_k = L_k/L$. Using this in the above equation relates the fractional frequency shift to the change in kinetic inductance:

$$x_r = \frac{\delta\omega_r}{\omega_r} = -\frac{1}{2}\frac{\delta L}{L} = -\frac{\alpha_k}{2}\frac{\delta L_k}{L_k}. \tag{4.11}$$

Relating kinetic inductance to quasiparticle density

We now want to understand how changes in L_k relate to the population of quasiparticles in a thin film. For a film whose thickness d is much smaller than the wavelength we are working at, the surface impedance is approximately [162]:

$$Z_s = \frac{1}{(\sigma_1 - j\sigma_2)d}. \tag{4.12}$$

Here σ_1 and σ_2 are the real and imaginary parts of the bulk conductivity $\sigma = \sigma_1 + j\sigma_2$. For a superconductor, $\sigma_1 \ll \sigma_2$ at temperatures far below T_c. Equating the imaginary term in the above equation to that of the surface impedance of a superconductor $Z_s = R_s + j\omega L_s$, we find that for a superconducting thin film:

$$L_s = \frac{1}{\omega \sigma_2 d} \implies \frac{\delta L_s}{L_s} = -\frac{\delta \sigma_2}{\sigma_2} = -\frac{1}{\sigma_2}\frac{d\sigma_2}{dn_{qp}}\delta n_{qp} \tag{4.13}$$

Jiansong Gao related the change in the real and imaginary parts of the conductivity to the change in quasiparticle density in his thesis [162]. Importantly, he showed that these expressions are roughly equivalent regardless of whether the quasiparticles are generated via thermal or optical means:

$$\begin{align}
\frac{\sigma_1}{\sigma_n} &= \frac{4\Delta}{\hbar\omega}\sinh(\xi)K_0(\xi) \tag{4.14}\\
\frac{\sigma_2}{\sigma_n} &= \frac{\pi\Delta}{\hbar\omega}\left(1 - 2e^{-\xi}I_0(\xi)\right) \tag{4.15}\\
\frac{d\sigma_1}{dn_{qp}} &= \frac{\sigma_n}{N_0\hbar\omega}\sqrt{\frac{2\Delta}{\pi k_B T}}\sinh(\xi)K_0(\xi) \tag{4.16}\\
\frac{d\sigma_2}{dn_{qp}} &= -\frac{\pi\sigma_n}{2N_0\hbar\omega}\left(1 + \sqrt{\frac{2\Delta}{\pi k_B T}}e^{-\xi}I_0(\xi)\right). \tag{4.17}
\end{align}$$

Here, σ_n is the material's normal conductivity I_0 and K_0 are the zeroth-order modified Bessel functions of the first and second kind, k_B is the Boltzmann constant, and $\xi = \hbar\omega/2k_BT$. N_0 is the density of superconducting states, which is $N_0 \approx 1.73 \times 10^{10}\mu\text{m}^{-3}\text{eV}^{-1}$ for aluminum. We now have the relationship between fractional frequency shift and kinetic inductance from Equation 4.11 and the relationship between a thin film surface inductance and its quasiparticle density from Equation 4.13. Putting those together and utilizing Equations 4.14-4.17 gives the response of the fractional frequency shift x_r and the internal quality factor Q_i to a change δn_{qp} in quasiparticle density:

$$x_r = -\frac{\alpha_k}{2}\frac{\delta L_k}{L_k} = \frac{\alpha_k}{2\sigma_2}\frac{d\sigma_2}{dn_{qp}}\delta n_{qp} \approx -\frac{\alpha_k}{4\Delta N_0}\left(1 + \sqrt{\frac{2\Delta}{\pi k_B T}}e^{-\xi}I_0(\xi)\right)\delta n_{qp} \tag{4.18}$$

For the final equality, recall that $T \ll T_c$ so that the coefficent of the second term in 4.17 is much greater than that of the second term in 4.15. In the dissipative direction, we can derive a similar expression for Q_i^{-1} by writing it in terms of conductivities and differentiating:

$$Q_i^{-1} = \frac{R}{\omega L} = \frac{R_s \alpha_k}{\omega L_k} \approx \frac{\alpha_k \sigma_1}{\sigma_2} \tag{4.19}$$

$$\delta Q_i^{-1} \approx \frac{\alpha_k}{\sigma_2} \frac{d\sigma_1}{dn_{qp}} \delta n_{qp} = \frac{\alpha_k}{\pi \Delta N_0} \sqrt{\frac{2\Delta}{\pi k_B T}} \sinh(\xi) K_0(\xi) \delta n_{qp} \tag{4.20}$$

4.1.4 Response to optical loading

We have now established what happens to the device's resonant frequency and quality factor as the quasiparticle population changes. To understand the resonator response to changes in thermal and optical power, we now only need to know how these changes affect the quasiparticle population. The total population is made up of quasiparticles generated both thermally and optically, and the total quasiparticle density can be expressed $n_{qp} = \sqrt{n_{\text{th}}^2 + n_{\text{opt}}^2}$. As derived in [162, 160], the thermal quasiparticle density as a function of termperature T is given by:

$$n_{th} \approx 2N_0 \sqrt{2\pi k_B T \Delta} \exp\left(-\frac{\Delta}{k_B T}\right). \tag{4.21}$$

And the optical quasiparticle density as a function of optical power P_{opt} is given by:

$$n_{\text{opt}}^2 = \frac{\tau_0 N_0 (k_B T_c)^3}{\Delta^3 V_L} \eta_e P_{\text{opt}} \implies \frac{\delta n_{\text{opt}}}{\delta P_{\text{opt}}} = \frac{\eta_e N_0 \tau_0 (k_B T_c)^3}{4\Delta^3 V_L} P_{\text{opt}}^{-1/2} \approx \frac{\eta_e \tau_{qp}}{\Delta V_L}, \tag{4.22}$$

where $\eta_e = (2\Delta/h\nu)\lfloor h\nu/2\Delta \rfloor$ is the pair-breaking efficiency of an optical photon with frequency ν, and V_L is the inductor volume. The parameter τ_{qp} is the quasiparticle lifetime, which is the characteristic time that a quasiparticle remains free before recombining into a Cooper pair [160]:

$$\tau_{qp} = \frac{\tau_0 N_0 (k_B T_c)^3}{2\Delta^2 n_{qp}} \approx \sqrt{\frac{\tau_0 N_0 (k_B T_c)^3}{4\eta_e \Delta}} \left(\frac{P_{\text{opt}}}{V_L}\right)^{-1/2}. \tag{4.23}$$

In most on-sky situations, it makes sense to assume that the quasiparticle density is dominated by optically-generated quasiparticles, or in other words to assume that $n_{\text{opt}} \gg n_{\text{th}}$. This assumption was used to approximate $n_{qp} \approx n_{\text{opt}}$ for the final step in both Equations 4.22 and 4.23. In the optically dominated case, we can multiply Equation 4.18 by the derivative in Equation 4.22 to get the resonator responsivity R_x in the frequency-shift direction:

$$\boxed{\begin{aligned} R_x &= \frac{\delta x_r}{\delta n_{qp}} \frac{\delta n_{qp}}{\delta P_{\text{opt}}} = \frac{\alpha_k \eta_e \tau_{qp}}{4 N_0 \Delta^2 V_L} \left(1 + \sqrt{\frac{2\Delta}{\pi k_B T}} e^{-\xi} I_0(\xi)\right) \\ &= \frac{\alpha_k}{4\Delta V_L} \sqrt{\frac{\eta_e \tau_0 (k_B T_c)^3}{4 N_0 \Delta^3}} \left(\frac{P_{\text{opt}}}{V_L}\right)^{-1/2} \left(1 + \sqrt{\frac{2\Delta}{\pi k_B T}} e^{-\xi} I_0(\xi)\right), \qquad (4.24) \end{aligned}}$$

where for the final step Equation 4.23 is substituted in for τ_{qp}. And similarly the responsivity in the dissipative direction is:

$$R_{Q_i^{-1}} = \frac{\delta Q_i^{-1}}{\delta n_{qp}} \frac{\delta n_{qp}}{\delta P_{\text{opt}}} = \frac{\alpha_k}{\pi \Delta V_L} \sqrt{\frac{\eta_e \tau_0 (k_B T_c)^3}{4 N_0 \Delta^3}} \left(\frac{P_{\text{opt}}}{V_L}\right)^{-1/2} \left(\sqrt{\frac{2\Delta}{\pi k_B T}} \sinh(\xi) K_0(\xi)\right), \tag{4.25}$$

whose prefactor only differs from that of R_x by a factor of $4/\pi$.

NEP

The power spectral density of quasiparticle fluctuations in the photon-dominated case can be written in terms of the quasiparticle lifetime and the power spectral density S_{ph} of the rate of absorption of incident photons per material volume. These expressions are derived by [162, 70]:

$$S_{nn} = |\delta n_{qp}|^2 = \frac{\tau_{qp}^2}{1 + (2\pi f_s \tau_{qp})^2} S_{ph} \tag{4.26}$$

$$S_{ph} = 2 \left(\frac{\eta_e}{\Delta V_L} \right)^2 \eta_{\mathrm{opt}} P_{\mathrm{opt}} h\nu (1 + \eta_{\mathrm{opt}} \bar{n}_{ph}) \tag{4.27}$$

where $\bar{n}_{ph} = [e^{h\nu/k_B T} - 1]^{-1}$ is the mean photon occupation number and η_{opt} is the detector optical efficiency. Note here that S_{nn} is the power spectral density of a number density, while S_{ph} is the power spectral density of a photon absorption rate per volume. S_{ph} is expressed as a single-sided spectrum, and therefore includes a leading factor of 2. We seek to compute the NEP in terms of fractional frequency shift, so we further convert from the power spectral density of the quasiparticle fluctuations to the power spectral density of the associated fluctuations in fractional frequency shift:

$$S_{xx} = (\frac{\delta x_r}{\delta n_{qp}})^2 S_{nn}. \tag{4.28}$$

Combining this with the responsivity from Equation 4.24, we can calculate the NEP in terms of fractional frequency shift in the photon-noise-dominated regime:

$$\boxed{\mathrm{NEP}_{xx}^2 = S_{xx} R_x^{-2} = \left(\frac{\delta x_r}{\delta n_{qp}} \right)^2 S_{nn} \left(\frac{\delta x_r}{\delta n_{qp}} \frac{\delta n_{qp}}{\delta P_{\mathrm{opt}}} \right)^{-2} = \frac{2\eta_{\mathrm{opt}} P_{\mathrm{opt}} h\nu_{\mathrm{opt}} (1 + \eta_{\mathrm{opt}} \bar{n}_{ph})}{1 + (2\pi f_s \tau_{qp})^2}, \quad (4.29)}$$

where Equation 4.22 is used for the final equality.

4.2 SPT-3G+ pixel design

This section describes the current SPT-3G+ pixel design as of the writing of this thesis. Figure 4.2, shows an image of a 220 GHz SPT-3G+ pixel, which consists of two MKIDs. The circular waveguide aperture is indicated by a yellow dashed circle. The inductor for each MKID is an aluminum meander, which is shown in

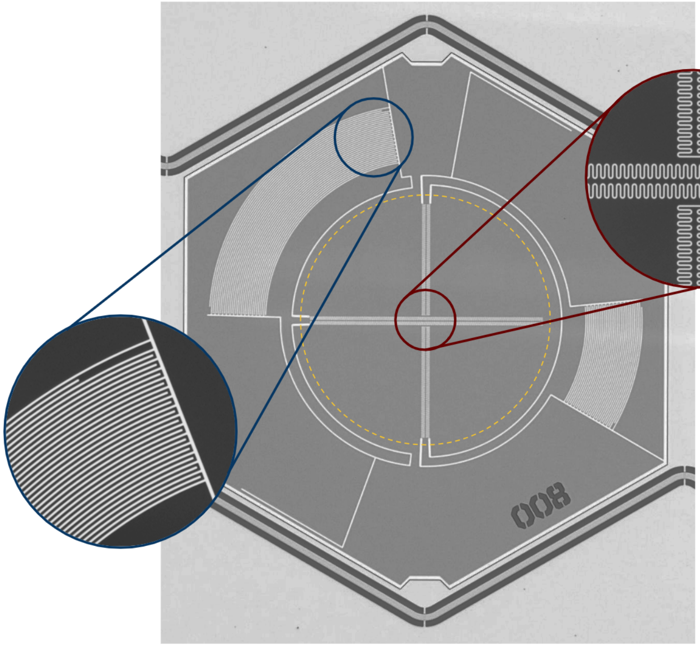

Figure 4.2: SPT-3G+ pixel design consisting of two MKIDs. The circular waveguide aperture is indicated by a yellow dashed line. The two inductor/absorbers are aligned to orthogonal polarization modes of the circular waveguide. Their meandering structure is shown in the red inset. Each inductor is coupled to an interdigitated capacitor, whose structure is shown in the blue inset. The co-planar waveguide feedline runs along the upper and lower edges of the pixel.

greater detail in the red inset to Figure 4.2. The absorbers for the two MKIDs in a pixel are aligned to orthogonal polarization modes of the circular waveguide, so that the detector is a polarimeter. To avoid crossing lines, one absorber (the vertically-aligned one in Figure 4.2), is split into two absorbers in series, connected by a wire. Each inductor/absorber is connected to an interdigitated capacitor (IDC), whose capacitance sets the resonant frequency (also called the readout frequency) of the device. The IDCs in Figure 4.2 are the arc-shaped structures located outside of the waveguide aperture,and are shown in more detail in the blue inset to Figure 4.2. Resonators are read out via a coplanar waveguide (CPW) feedline running along the edges of the pixel. The resonators are coupled to the feedline via a small coupling capacitor, which in this case is a single line that runs parallel to the CPW.

The inductor shape is largely constrained by the tradeoffs between volume, impedance, and polarization coupling efficiency described in detail below. Thus the resonant frequency of each detector is largely set by the IDC capacitance. Ap-

Figure 4.3: Image of a CPW bridge. The darker brown color is the bare silicon wafer. The cream-colored layer is the 30nm aluminum detector and ground plane layer. The blue color is the silicon dioxide layer. Note that this shows up as very pale blue when on top of aluminum and very dark blue when on top of bare silicon. This particular images is of an early device with a 120nm SiO2 layer. This thickness was later increased to 180nm, so the layer appears red in other images. Finally, the medium brown color is the 120nm niobium feedline.

proximate values for C can be selected using the equations in Section 4.1.2, but to fine-tune their placement in frequency space, it is necessary to simulate the microwave performance of the circuit. I did this using the Sonnet software, and from these simulations I set the IDC geometries. The resonant frequencies are set coarsely by the IDC arc-length, proportional to the angle subtended by the entire IDC in Figure 4.2. This is not changeable post-fabrication. However, the resonant frequency can be set more finely by the “trimming” of the outermost tines of the IDC. A trimmed tine can be seen in the blue inset to Figure 4.2. The design of these wafers also enables post-fabrication trimming of additional material off of the outermost tines to correct for scatter in resonant frequency due to fabrication non-uniformities or other inconsistencies between the simulated and fabricated detectors. This has been demonstrated for other devices [163] but post-fabrication trimming on array-scales has not yet been demonstrated for SPT-3G+.

Early detector designs used a microstrip feedline instead of a CPW. When preparing to scale from few-pixel chips to densely packed arrays, I discovered that the microstrip design allowed parasitic coupling between the IDCs and the feedline. In other words, there was a capacitance between the IDC and the feedline that dwarfed that of the coupling capacitor for any pixel diameter less that roughly 6 mm. This is equivalent to making C_c very large in Equation 4.9, resulting in wide resonances that could not be multiplexed at the intended density. The switch to a CPW feedline was motivated by the fact that the strength of the electromagnetic field surrounding the CPW centerline falls off much more rapidly with distance from the centerline than it does in the microstrip design. Indeed, as seen later, I was able to pack pixels at a center-to-center distance of 2.2 mm using a CPW feedline and retain narrow resonance profiles. Co-planar waveguides must be periodically bridged to maintain uniform ground-plane connectivity, meaning that an electrical connection must be made across the CPW that touches both sides of the ground plane without touching the feedline in the center of the CPW [162]. An image of a CPW bridge is shown in the center of Figure 4.3. The bridge is the thin vertical strip of cream-colored aluminum running beneath the brown CPW feedline. The presence of the bridge keeps the upper and lower portions of the ground plane (above and below the CPW feedline in Figure 4.3) electrically connected. Bridges are separated from the feedline by layer of silicon dioxide, which is blue in Figure 4.3. The bridge fabrication process is described later in this chapter.

4.3 Absorber optical coupling

Light that hits the illuminated portion of the SPT primary mirror passes through the telescope optics shown in Figure 1.1, the receiver optics shown in Figure 1.5, and finally arrives at the SPT-3G+ focal plane. Figure 4.4 schematically shows the final optical coupling to the detector. When light arrives at the top of the feedhorn shown in Figure 4.4, it has already passed through a low-pass metal-mesh filter located at the Lyot stop on the 4K stage (Figure 1.5). The gold-plated feedhorns couple light to a waveguide at the labeled interface in the upper panel of Figure 4.4.

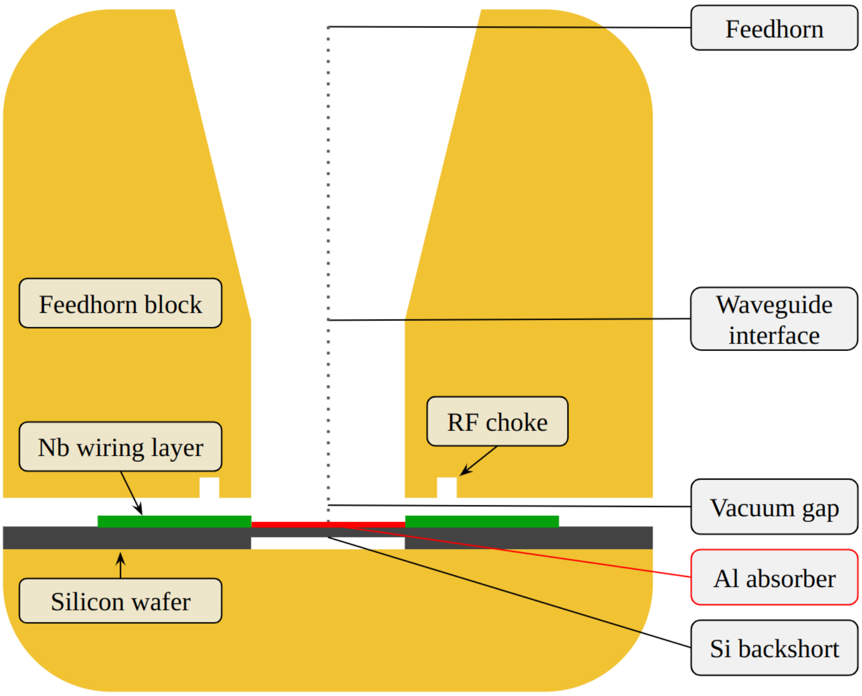

Figure 4.4: Sideview of the SPT-3G+ optical coupling scheme.

The waveguide cutoff sets the lower edge of the observation band. For a circular waveguide, this is approximately [161]:

$$\nu_{\text{cutoff}}(r) \approx \frac{1.8412c}{2\pi r}, \tag{4.30}$$

where r is the waveguide radius and c is the speed of light. The preliminary SPT-3G+ waveguide cutoffs (those producing the bands shown in Figure 4.6), are shown in Table 4.1. Light exits the waveguide and crosses a small vacuum gap before reaching the detector wafer. This gap should be as small as possible to maximize optical efficiency and minimize cross-talk. In practice, this gap is 50 μm. Light terminates on the absorptive element of the SPT-3G+ pixel, which is shown in red in the upper panel of Figure 4.4. The lower panel of Figure 4.4 shows the simulated bandpasses for all three SPT-3G+ frequencies. The waveguide is encircled by a choke, which is machined into the bottom of the feedhorn block and is designed to keep power localized to within the waveguide radius as it exits the waveguide. To increase optical efficiency, the design includes an integrated quarter-wavelength optical backshort. This is created by etching the silicon wafer so that the thickness of the region below the absorber correspondes to a quarter-wavelength in silicon [161]:

$$h_{\mathrm{wafer}} = \frac{c}{4n_{\mathrm{Si}}\nu}. \tag{4.31}$$

With the index of refraction in silicon at microwave frequencies $n_{\mathrm{Si}} = 3.4$, this comes out to just over 100 μm for the 220 GHz band. The fact that this is an existing off-the-shelf wafer thickness motivated starting SPT-3G+ detector development with the 220 GHz band.

4.3.1 Design constraints

For feedhorn-coupled direct absorbing MKIDS, the inductive element of the microwave circuit is also the absorptive element of the optical system. This structure needs to be optimized for both jobs, which results in a highly constrained design problem. The following considerations imposed constraints on the inductor design.

Fabrication: The most obvious consideration is that the device must be possible to fabricate. For the tools available to me, the minimum aluminum sheet thickness is 30 nm and the minimum linewidth (at the time) was 2 μm.

Impedance matching: For the structure to efficiently absorb the radiation coming out of the waveguide, its series impedance across the waveguide aperture must roughly match the wave impedance at the absorber plane. The quality of that impedance match sets the band-averaged optical efficiency achievable for the detector. The characteristic impedance of a vacuum-filled infinite circular waveguide is [161]:

$$Z_{wg}(\nu) = \frac{Z_{0,\ \mathrm{free}}}{\sqrt{1 - (\frac{\nu_{\mathrm{cutoff}}}{\nu})^2}}, \tag{4.32}$$

where $Z_{0,\mathrm{free}} = 377\Omega$ is the impedance of free space. However, the presence of the integrated silicon backshort makes the impedance matching much more complex. Following [164], I determined the optimal waveguide impedance range through simulation, and in rough agreement with [164], found the optimal absorber impedance

	220 x	285 x	345 x	220 y	285 y	345 y
16 μm units	125	30	18	120	30	10
24 μm units	0	30	20	0	30	20
32 μm units	0	28	40	0	22	44
Total units	125	88	78	120	82	74
Total □	4500	4544	4408	4320	4136	4392
Volume $(\mu\text{m})^3$	540	545	529	518	496	527
Z_{abs} (Ω)	2250	2272	2204	2160	2068	2196
r_{wg} (μm)	490	350	280			
ν_{cutoff} (GHz)	180	250	315			

Table 4.1: Absorber design parameters. Here "x" indicates the continuous absorber and "y" indicates the discontinuous absorber. Note that the total number of squares and total volume account for the entire absorber, which is symmetric about its long axis and thus includes all units plus their mirror images.

to be $Z_{\text{abs}} \approx 2\,\text{k}\Omega$ across the waveguide. Note that from the perspective of the waveguide, the series impedance of the absorber is calculated across the waveguide diameter, while from a microwave circuit perspective, the series impedance is calculated from one end of the aluminum meander to the other. *For these specific SPT-3G+ structures*, this means that we are trying to choose the meander length L and width w such that:

$$Z_{\text{abs}} = Z_{\square} \times \frac{L}{2w} \approx 2\text{k}\Omega. \tag{4.33}$$

For a 30 nm aluminum sheet, the sheet impedance is $Z_{\square} = 1\Omega/\square$. I chose $w = 2\mu\text{m}$ for all absorbers. Series impedances across the waveguide for each absorber are given in Table 4.1.

Responsivity: Consider Equation 4.24 for the frequency-shift responsivity of a resonator. The environmental variables are the optical power P_{opt} and the temperature T. Of the other parameters in this equation, all are material dependent except for the kinetic inductance fraction α_k and the inductor volume V_L, which are set by the design. Ignoring all other parameters, the dependence on the design variables

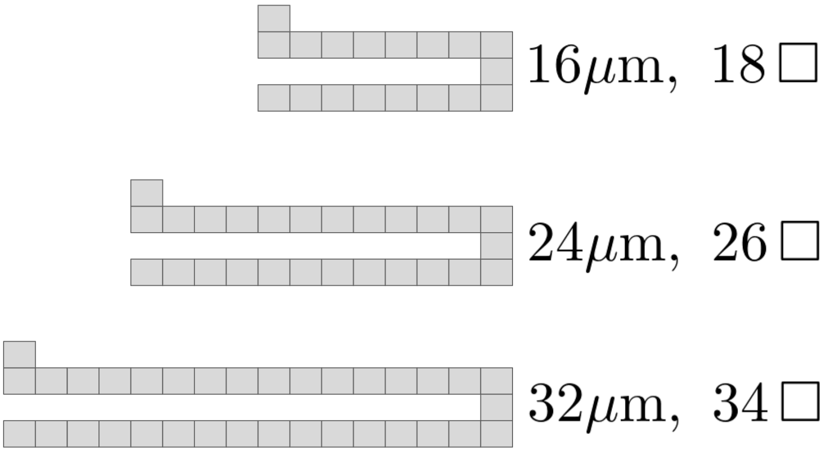

Figure 4.5: Visual explanation of what is meant by "units" in the context of SPT-3G+ absorber design. The three types of meander units are made up of 2 μm × 2 μm squares. The meander extents are of lengths 16 μm, 24 μm, and 32 μm.

is:

$$R_x \propto \alpha_k \left(P_{\mathrm{opt}} V_L\right)^{-1/2} \tag{4.34}$$

Responsivity decreases with increasing inductor volume, which makes sense in the context of Equation 4.22. Since $0 < \alpha_k < 1$, responsivity lost by increasing the inductor volume cannot really be gained back through clever geometry tricks in most cases. However, Equation 4.25 to first order has the same volume dependence. If Q_i changes too dramatically with changes in optical power, the resonance will become wide enough to overlap with its neighbors, causing cross-talk. Therefore it is also desirable that the volume be high enough to maintain a multiplexable Q_i under optical loading.

Cross-polarization pickup: The SPT-3G+ pixels are intended to be polarimeters and as such should be optimized to absorb radiation from only one polarization mode of the waveguide. Each absorber is aligned along one waveguide mode, and any large features in the orthogonal direction risk coupling to the orthogonal mode, causing cross-polarization pickup. To avoid this I attempted to keep all features orthogonal to the main alignment direction less than $\lambda/20$ in size.

Higher frequency detectors have smaller waveguide diameters. This makes it challenging to achieve the wave impedance match without creating features that lead to significant cross-polarization pickup. I addressed this by increasing the meander length towards the edges of the waveguide for the 285 and 345 GHz absorvers, where the magnitudes of the electric fields are lowest. The upper panel of Figure 4.6 shows the absorber designs for each of the three SPT-3G+ frequencies. The continuous absorber, oriented horizontally in Figure 4.6, consists of a single aluminum line that meanders across the waveguide aperture and back, while the discontinuous absorber consists of two separate meanders connected by a wire. Each absorber is made up of "units" of varying lengths of meandering aluminum line. A visual explanation of the units is given in Figure 4.5. The number of each type of unit in each type of absorber is summarized in Table 4.1.

The lower panel of Figure 4.6 shows the simulated bandpasses for each absorber design. Simulations were done using the HFSS software, and include the absorber, wafer, and waveguide. Dark solid lines indicate the expected absorption percentage of the continuous absorber when aligned to the polarization of incident light. Lighter solid lines indicate the analogous absorption percentage for the discontinuous absorber. Dark and light dashed lines indicate the percentage of cross-polarization pickup of the continuous and discontinuous absorbers respectively. Shaded regions indicate the current nominal SPT-3G+ bands. The upper band edges will be defined with a metal-mesh filter that is not included in these simulations, but the lower band edges are defined by the waveguide cutoff. As SPT-3G+ final bandpasses had not been decided at the time of the absorber design, I did not alter the waveguide cutoffs to match the shaded regions. However, when the bandpasses are fully decided, the designs will need to be altered to place the lower band edge at the appropriate frequency.

4.4 Array layouts and multiplexing

To achieve the target SPT-3G+ detector counts, pixels must be densely packed onto the SPT-3G+ focal plane. The 220 GHz pixel diameter d_{pix} was determined using the following relationships between an angular separation on the sky θ_{sky}, the

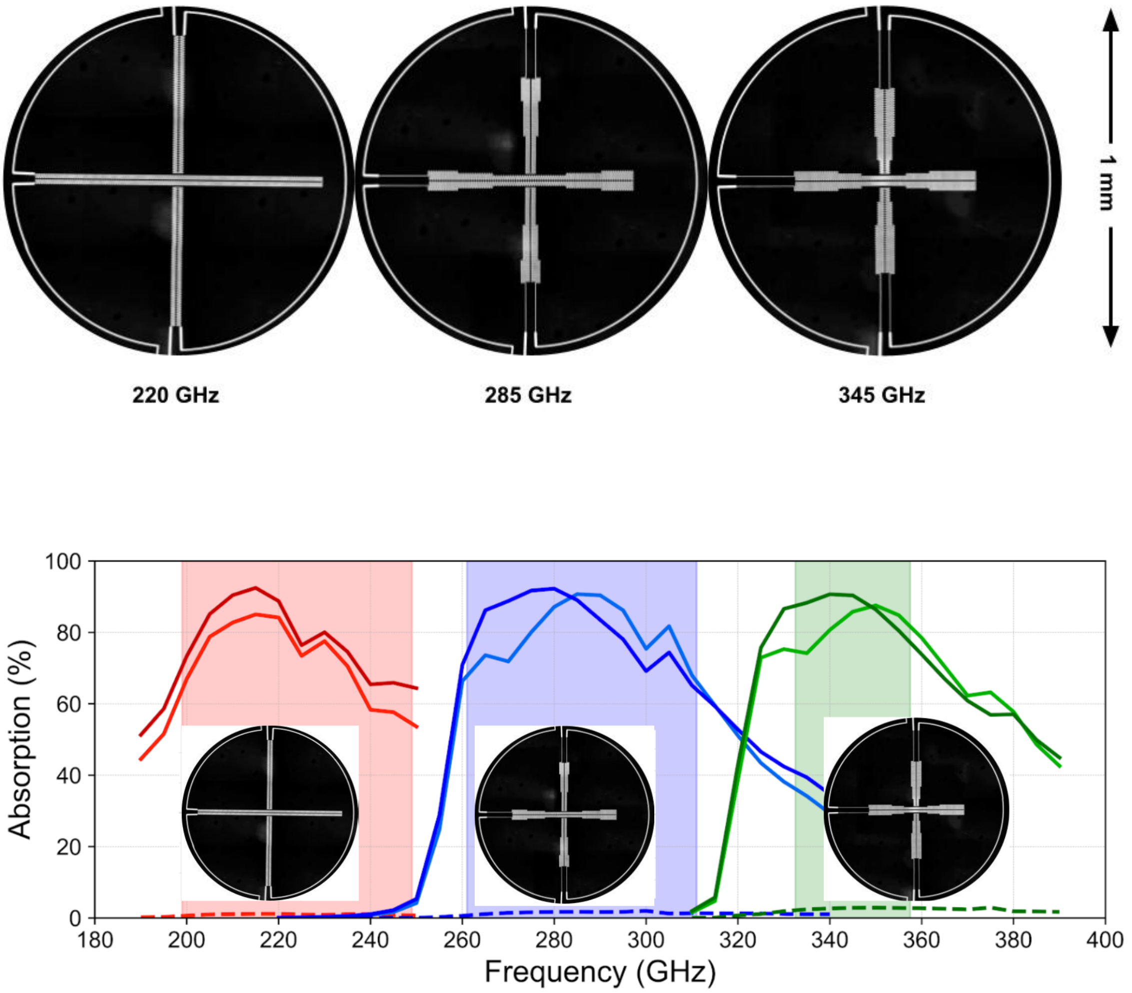

Figure 4.6: Absorber designs and simulated spectra for the SPT-3G+ detectors. *Upper*: Microscope composite images of fabricated absorbers for each frequency band, showing the changes in absorber structure with increased frequency. *Lower:* Simulated spectral response of each absorber design. Shaded regions represent the nominal SPT-3G+ bands. Dark colored lines correspond to the continuous absorber and lighter colored lines correspond to the discontinuous absorber. Dashed lines represent simulated cross-polarization pickup.

telescope focal length F, the telescope aperture diameter D, and the observation wavelength λ in the diffraction limited case:

$$\begin{aligned} d_{\text{pix}} &= \theta_{\text{sky}} F, && (4.35) \\ \theta_{\text{sky,diff}} &\approx 1.2\lambda/D, && (4.36) \\ \implies d_{\text{pix,diff}} &\approx 1.2\lambda F/D. && (4.37) \end{aligned}$$

If the pixel diameter is any larger than this, the beams of neighboring pixels will overlap on the sky, leading to correlated photon noise between detectors. The ideal pixel spacing that maximizes instrument mapping speed approaches the diffraction limit without surpassing it, so that pixel beams fill the sky without overlapping. The preliminary design for SPT-3G+ assumes an $F/D = 1.3$, meaning that for 220 GHz pixels, the pixel diameter at the diffraction limit is just under 2.2 mm. For this reason, I designed the 220 GHz SPT-3G+ pixels to have a 2.2 mm diameter. This optimizes the achievable mapping speed for the 220 GHz band. For higher frequency bands, I kept the 2.2 mm pixel spacing, despite this being slightly suboptimal (slightly larger than the spacing at the diffraction limit). This was done firstly for uniformity across wafers, which simplifies optical modelling, and secondly because the 2 GHz upper limit on the intended readout band sets a lower limit on the size of the interdigitated capacitors in the pixel. These are already curved in the 220 GHz pixels design to minimize pixel size, and I decided that keeping the IDC radii uniform across all wafers was more worthwhile than trying to push the higher frequency pixels closer together.

With a 2.2 mm pixel spacing, there is room for 2436 pixels on a hexagon inscribed in a 130 mm circle. Note that this equates to $2436 \times 2 = 4872$ detectors per wafer. Since the SPT-3G+ multiplexing goal is about 1k/GHz, it seemed natural to divide each wafer into six triangular submodules, each containing 406 pixels, or 812 detectors. This way each triangular submodule can couple to one coaxial readout line. For the seven total planned wafers, this results in a total of 42 readout lines for the

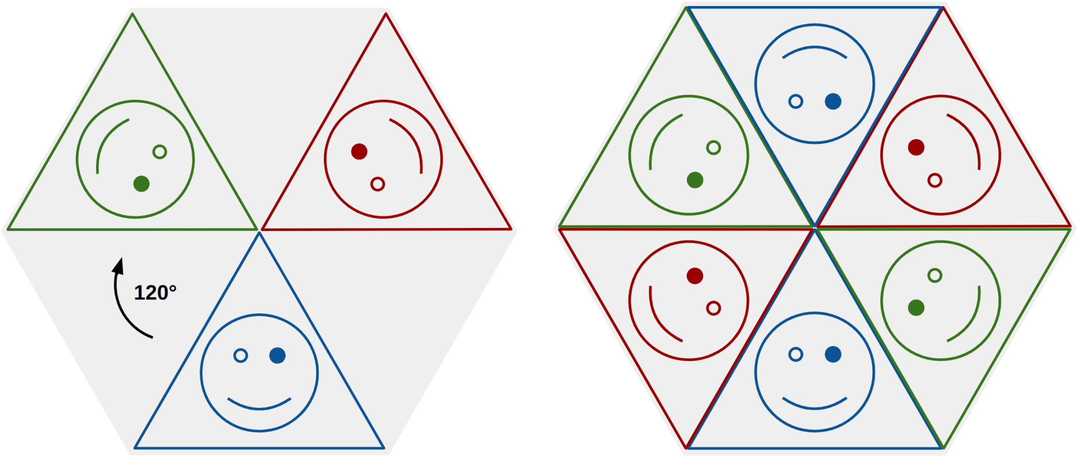

Figure 4.7: Schematic depiction of the intended orientations of triangular submodules on a wafer. The left panel shows the baseline triangle rotated in increments of 120°. Each triangle is then flipped over the center of the wafer, resulting in the configuration on the right.

full SPT-3G+ focal plane. Two pixel orientations exist in the triangular submodule design. The two orientations are offset from each other by a 45° rotation to enable better sampling of the Stokes parameters. Pixel orientations alternate across each row in the triangular array. In a full wafer of six triangles, the entire submodule pattern will be rotated into 3 orientations offset by 120° that compose half of the wafer, and then mirrored to create the remaining half of the wafer. Figure 4.7 is a visual depiction of this scheme. Under this scheme, half of the detectors on each submodule have a counterpart of identical footprint on a neighboring submodule that is aligned to the same set of polarization angles, but with the broken and unbroken absorbers swapped. This is intended to mitigate potential systematics by allowing differences between the broken and unbroken absorber designs to be calibrated out.

4.5 Fabrication

Important distinction: The fabrication section of this thesis describes the fabrication work that I did at the Pritzker Nanofabrication Facility (PNF) at the University of Chicago. These are all prototype devices fabricated on four-inch wafers. The final SPT-3G+ deployment arrays are intended to be fabricated on six-inch wafers

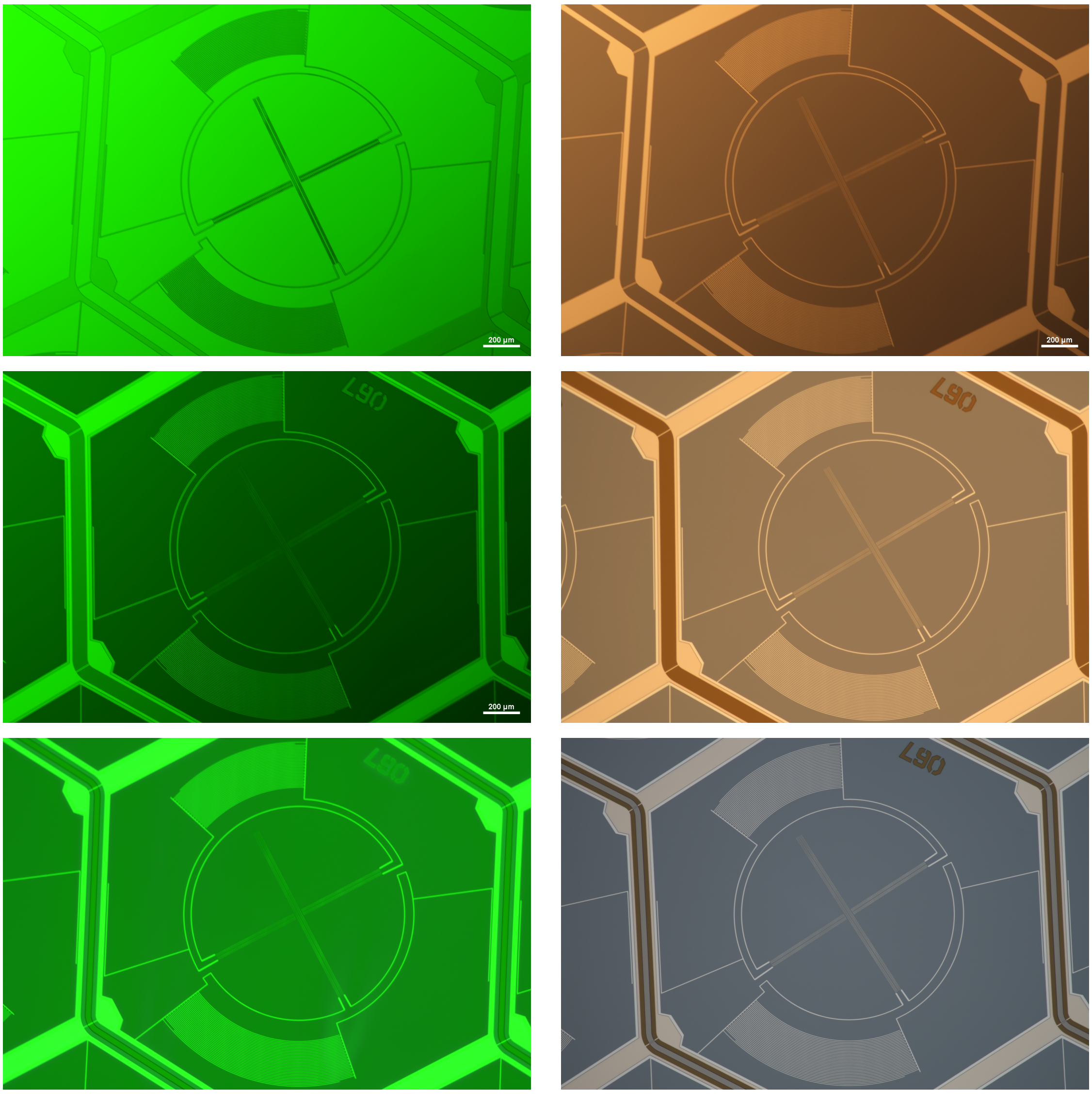

Figure 4.8: The SPT-3G+ fabrication process. *Upper left:* 30nm aluminum is deposited onto the wafer, and the first layer, consisting of the detectors, ground plane, and CPW bridges, is patterned. *Upper right:* The unwanted aluminum is dry-etched away. *Center left:* The pixel label and CPW region are patterned. *Center right:* 180nm silicon dioxide is deposited and lifted off. *Lower left:* The CPW centerline is patterned. *Lower right:* 120nm niobium is deposited and lifted off, and the device is complete.

at Argonne National Laboratory (ANL). All processes described here are specific to my PNF-based fabrication and are different from the processes used at ANL. The majority of devices that I fabricated at the PNF (and all of those characterized in the following sections) are aluminum-only; this means that the inductors, IDCs, and ground plane are all made from the same aluminum layer. This is not the intended final SPT-3G+ design, in which, as mentioned above, only the inductors will be made of aluminum, while the IDCs and ground plane will be made of niobium. However, in the PNF, I experienced significant difficulty achieving the necessary galvanic connection between aluminum and niobium. I made a few bilayer devices in which the niobium layer was deposited directly on top of the aluminum, but became concerned that the CHF_3CF_4 dry etch used to remove the niobium, which stopped on the aluminum inductor layer, was mechanically sputtering the aluminum and causing surface roughness. Since my collaborators at ANL were able to achieve the Al-Nb galvanic connection using a niobium nitride cap process, which is not an option in the PNF, I decided to just create aluminum-only device prototypes at the PNF, with the thought being that the final deployment devices will be made at ANL. The fact that my devices are aluminum-only should not affect their spectral response, but it may affect their responsivity to both thermal and optical power because the pair-breaking energy for aluminum is much lower than that of niobium, which means that the IDCs could contribute additional kinetic inductance to the resonator.

4.5.1 SPT-3G+ fabrication process

Figure 4.8 illustrates the SPT-3G+ fabrication process in the PNF for my aluminum-only devices at the time of this publication. Each photo is of the same pixel at a different stage of fabrication. The aluminum-only process consists of three layers. A new wafer is surface-prepped via ion-milling to destroy the native silicon dioxide layer, which is thought to decrease the amplitude of two-level system noise. The bare silicon wafer is the darker brown color in Figure 4.3. Immediately after this, the first 30nm aluminum layer is sputtered onto the wafer. This is the light cream-colored layer in Figure 4.3. The detectors and ground plane are then patterned in photoresist. The upper left panel of Figure 4.8 shows the photoresist for the first layer patterned atop the 30nm aluminum film. Next, the exposed aluminum is etched using a Cl_2 dry etch. The result of this process is shown in the upper right panel of Figure 4.8. This completes the first layer.

The second layer is the silicon dioxide layer separating the CPW bridges from the center feedline. This layer is blue in Figure 4.3 and is patterned via liftoff. Figure 4.3 depicts an older device, whose silicon dioxide layer was 120nm instead of the current 180nm layer. Hence this layer shows up as blue instead of red in Figure 4.3. The center left panel of Figure 4.8 shows the photoresist patterned for this layer, with resist covering everything except the CPW area and the pixel's numerical label. The 180nm silicon dioxide layer is deposited onto the wafer via thermal evaporation, with the wafer stationary to avoid sidewall deposition which could impede liftoff. (The wafer is angled to compensate for the position of the source so that the layer thickness is uniform.) After this deposition, the wafer is suspended upside-down in N-Methyl-2-pyrrolidone (NMP), at 80C, which dissolves the photoresist overnight. The center right panel of Figure 4.8 shows the result of this process. The orange-red areas are the 180nm silicon dioxide layer. As mentioned above, other photos throughout this document may have different colored silicon dioxide layers. This is because I experimented with different layer thicknesses from 100-180nm. The silicon dioxide acts as a thin film on top of the reflective silicon wafer, so this range of layer thicknesses actually spans almost the entire visible spectrum, from indigo to red. (I electrically prefer the 100nm layer for its lower Q_c and also aesthetically prefer its dark indigo color, but I found that to really consistently avoid bridge shorts, it's best to be conservative and deposit 180nm.)

The third layer is the niobium feedline at the center of the CPW. This layer is a medium brown color in Figure 4.3 and is also deposited via liftoff. The lower left panel of Figure 4.8 shows the photoresist patterned for this layer, with resist covering everything except for the center CPW feedline. The 120nm niobium layer is sputtered onto the wafer in the same chamber that is used for the inital aluminum layer. Unfortunately, there is no way to angle the wafer in this chamber, and the sources are distributed around the edge of the chamber. This means that to get a uniform layer thickness, the wafer has to be rotating, so sidewall coverage is sadly inevitable. Indeed I have found this liftoff process to be much more painful than the silicon dioxide liftoff, despite the layer being thinner. One strategy that really helped was recommended by Tom Cecil from ANL. After depositing the niobium, I suspend the wafer upside down in NMP and sonicate it for 5-10 minutes to help break up any thin niobium membranes that may coat the sidewalls. Then I transfer the wafer to a new glassware of NMP without letting it dry out, and let that lift off at 80C overnight, and finally transfer into fresh NMP in the morning for a longer sonication. I only have anecdotal evidence, but I noticed a major improvement in the speed and quality of the niobium liftoff when I implemented this suggestion. The lower right panel of Figure 4.8 shows the result after this final liftoff.

At this point, the device itself is complete, but the optical backshorts and the alignment pinholes still need to be machined. That machining is done via a CHF_3CF_4 deep silicon reactive ion etch (DRIE). The DRIE step is only done for devices that are made on SOI wafers and that are intended to be tested optically. This is either done in the PNF, ANL or at Cardiff University, depending on which institution, if any, has a functional DRIE at the time of fabrication. After the DRIE, the optical backshorts are coated with 200nm niobium, which is reflective at the SPT-3G+ frequencies. The rest of the wafer backside is coated with 100nm aluminum, which is absorptive at the SPT-3G+ frequencies, so that any stray light that makes it to the backside of the wafer will be absorbed by this layer.

4.5.2 Fabrication alternatives and challenges

This section serves to document challenges to the fabrication process and the alternatives that were trialed throughout process development.

Aluminum wet etch versus dry etch

During a period of Chlorine dry etch downtime, I attempted to wet-etch the aluminum layer. Though the etch cleared and the devices yielded, the resulting frequency scatter was severe. Microscope inspection confirmed unusually thin inductor and capacitor linewidths across the wafer. This was likely due to an overetch, and does not rule out the possibility of using the wet-etch in the future, especially if it becomes necessary to process a six-inch wafer. It is worth noting that the internal quality factors of the wet-etched devices were also low, though many dry-etched devices fabricated around the same time experienced the same low quality factors, and it was not possible to quantify the true effect of the wet etch on device quality factor.

Niobium liftoff vs CHF_3CF_4 etch

The niobium feedline, which is the top layer of the device, is currently deposited via liftoff. Throughout the fabrication process development, fully lifting this layer off has proved to be challenging. I mentioned above that this was partially solved by an aggressive sonication prior to the overnight liftoff process, but alternatives to the liftoff process were also considered. Instead of lifting off the niobium, it is possible to remove it via a dry CHF_3CF_4 reactive ion etch (RIE). This has the advantage of fully removing exactly the desired niobium, but comes with the disadvantage that CHF_3CF_4 also etches silicon dioxide. We explored this via a test wafer, in which the silicon dioxide and niobium layers are deposited back-to-back, and a CHF_3CF_4 RIE is used to etch through both layers, stopping on the aluminum ground layer. This process leaves the feedline niobium and silicon dioxide in place, with all other niobium and silicon dioxide removed. Note that this means that the coupling from the feedline to the resonator coupling capacitor is affected by this process. Both at the PNF and at Argonne, there has been some concern that stopping the etch on the aluminum detector layer affects Q_i. This is because, though CHF_3CF_4 does not chemically etch aluminum, the RIE process does mechanically sputter the stop layer to some degree. Argonne measured a factor of two increase in sheet resistance of aluminum before and after exposure to the CHF_3CF_4 RIE process. Out of fear of this effect, we attempted an additional step in which photoresist was used to cover the resonator inductors and capactitors and left in place during the RIE. The hope was that this would protect the resonators from mechanical sputtering, but results were inconclusive.

Low aluminum Q_i

Midway through year two of working in the cleanroom, I began to intermittenly make devices with low quality factors $Q_i \approx 10^5$. The source of the low quality factors was never definitively identified, but it is worth noting that this began to happen at the same time that a new high-temperature tantalum-based process was initiated in the same sputtering chamber that I use to deposit aluminum. In an effort to remove potential contamination from the surface of the aluminum source, I increased my pre-sputtering time from five to fifteen minutes. For a time, this restored the quality factors of aluminum devices (and gave creedance to the source contamination theory). However, as time progressed, quality factors began to drop again, and increased pre-sputtering time had little effect. This culminated in my final device yielding no resonators at all, despite being identical in footprint to a previous high-quality device. The working theory is that the aluminum source in the sputtering chamber has been depleted, and that particles of the crucible itself (iron) are now contaminating the aluminum. Unlike tantalum, iron is not a superconductor, and even a small amount of iron contamination in the inductive element will destroy an MKID. If this is the case, the problem is not fixable without a replacement aluminum source, which is currently unavailable in the PNF.

4.5.3 Gallery

This subsection highlights the many SPT-3G+ devices resulting from many rounds of fabrication at both the University of Chicago and Argonne. Images are spread over the following three pages. Figure 4.9 is composed of many microscope images stiched together, and shows a cluster of SPT-3G+ 220 GHz pixels fabricated in the PNF. This image provides a closer look at how pixels are packed into arrays. The central pixel in this cluster is the same pixel shown in Figure 4.8. Figure 4.10 shows the evolution of SPT-3G+ prototypes over the course of my PhD. Moving from the top left to the bottom right, the devices evolve from five-pixel microstrip-coupled chips to full triangular CPW-coupled submodules. Figure 4.11 shows two six-inch arrays fabricated at Argonne National Laboratory. The placement of triangles onto these wafers show the intended look of the full deployment-sized arrays.

Figure 4.9: Stitched image of a cluster of SPT-3G+ 220 GHz pixels fabricated by me. This layout is designed to test optical crosstalk, but provides a closer look at how pixels are packed into arrays.

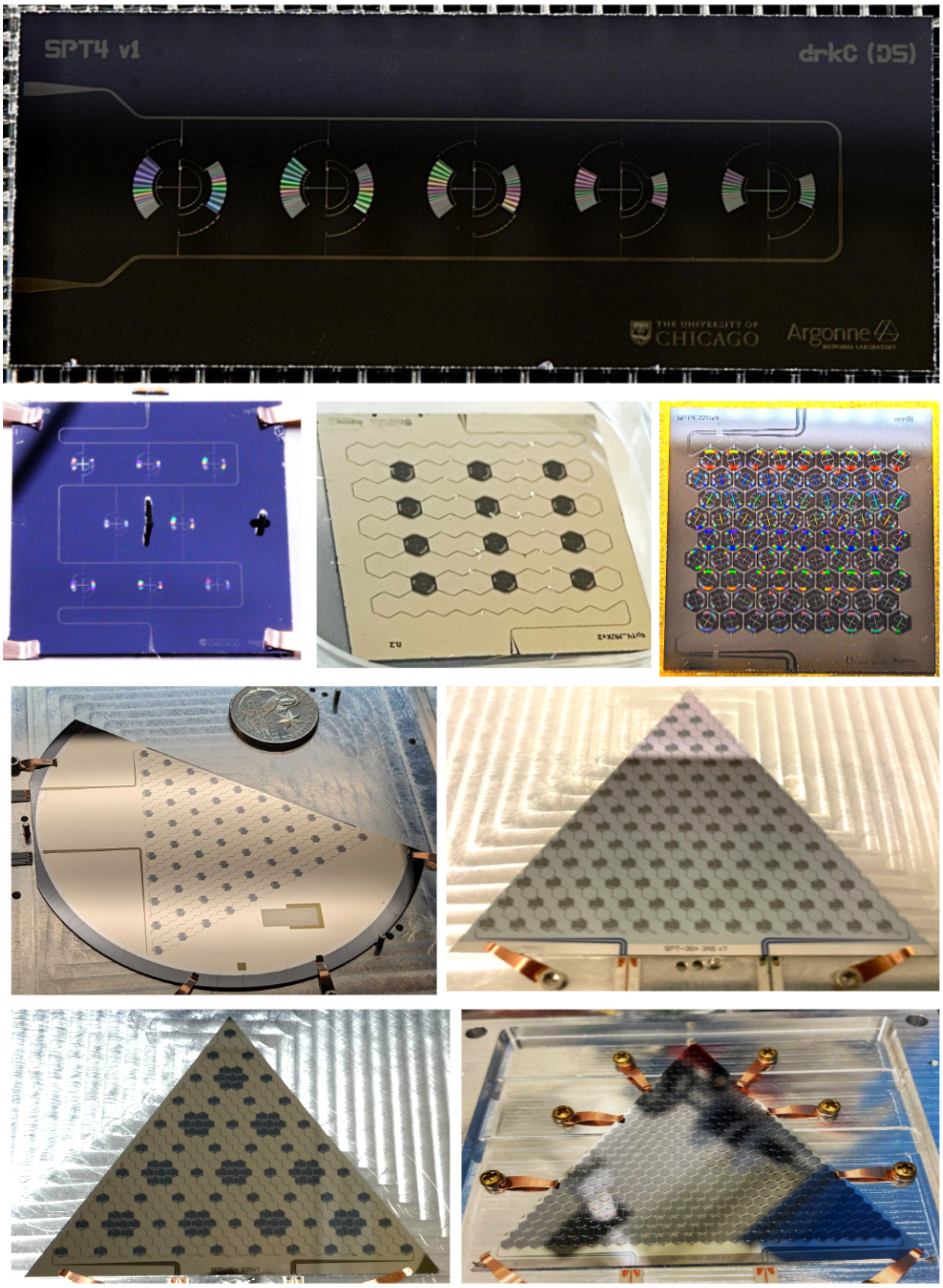

Figure 4.10: Evolution of SPT-3G+ detector prototypes. The uppermost photo was taken by Erik Shirokoff, the middle photo on the second row by Paul Chichura, and the left photo on the third row by Kyra Fichman. Other photos were taken by me.

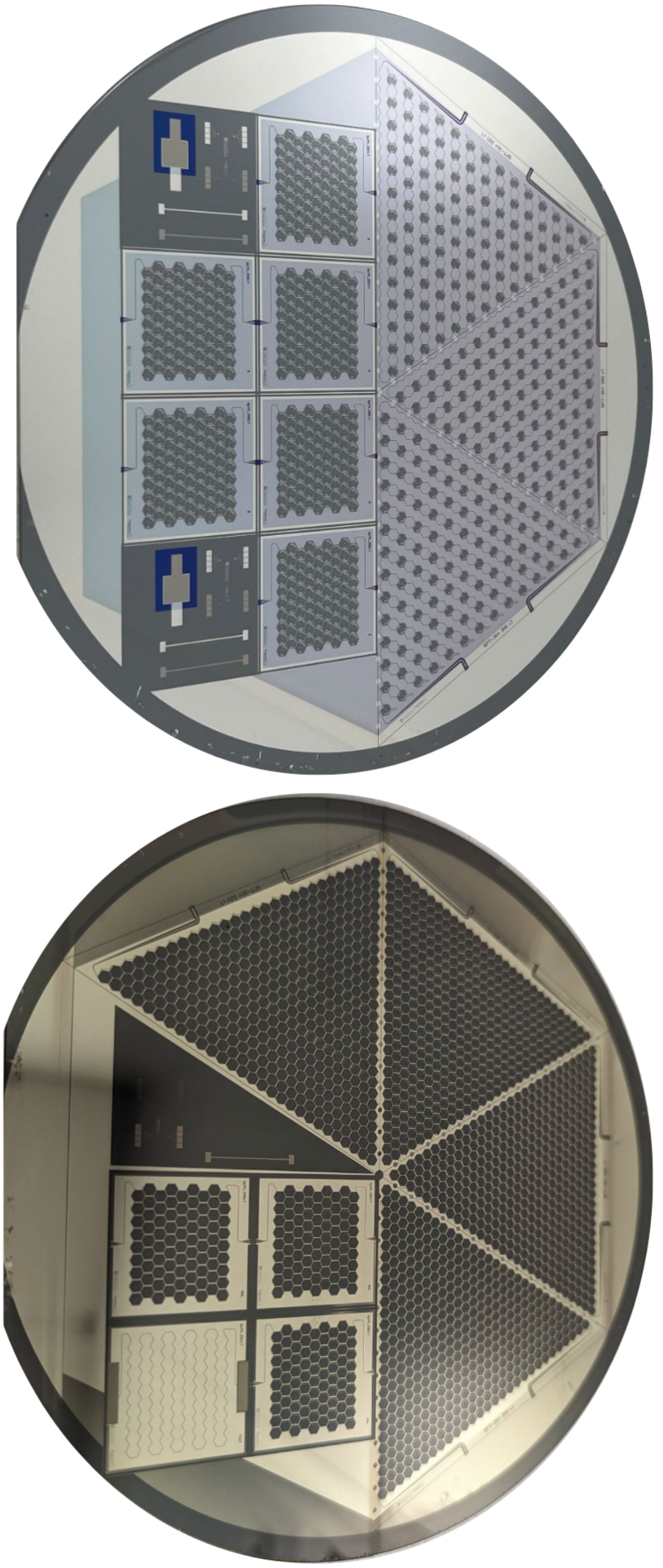

Figure 4.11: Six-inch wafer prototypes fabricated at Argonne National Laboratory. These wafers give a sense of the look of deployment-sized SPT-3G+ arrays. Fabrication and photos are by Tom Cecil and Marharyta Lisovenko.

Chapter 5

Laboratory Characterization of 220 GHz MKIDs for SPT-3G+

Laboratory characterization of MKIDs is a complex operation, in which verifying the presence of resonators is only the first step. In this chapter, I will describe the methods I used to test MKIDs throughout my PhD. I will go through the main testbed that I used, the RF chains employed, and the various configurations I used to extract dark and optical data from these detectors. I will then describe the analysis of said data, and how to extract useful information from it. My hope is that this section might be used as a reference by future users of this and similar systems.

5.1 Testbed

The majority of my testing work was done in a Bluefors LD400 Dilution Refrigerator Measurement System at the University of Chicago. This system is used to cool MKIDs to their operable temperatures so that their functionality can be tested in the lab. This system was originally set up by a combination of Erik Shirokoff, Pete Barry, Kirit Karkare, Amy Tang, and Ryan McGeehan. It is documented here for future users.

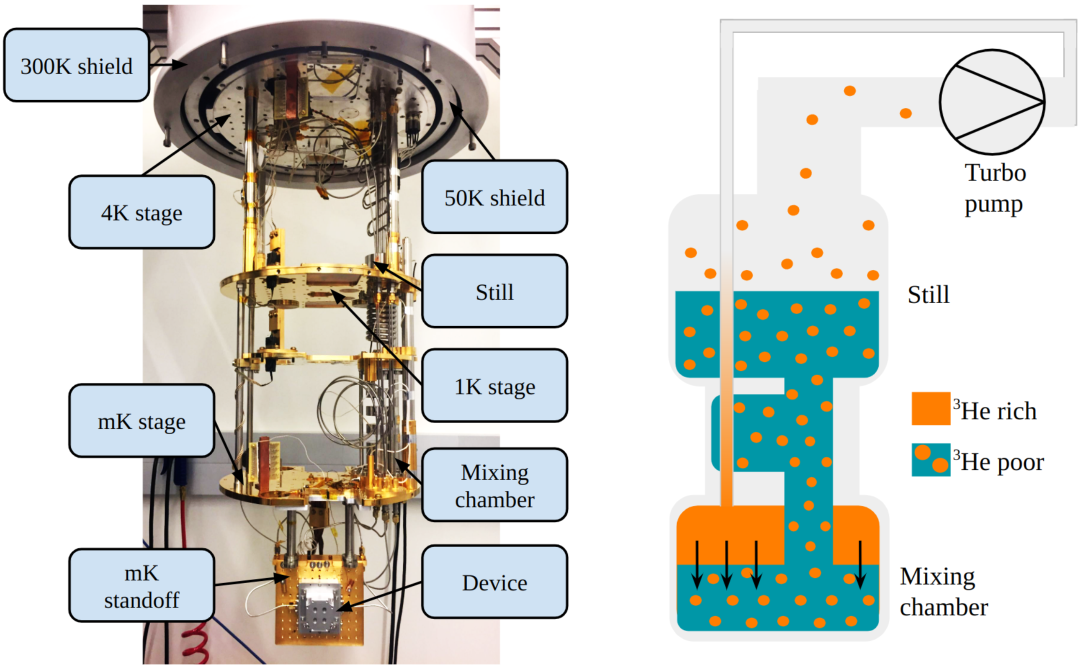

Figure 5.1: *Left:* Annotated image of the dilution refrigerator system, with an SPT-3G+ device mounted for optical testing. *Right:* Cartoon depiction of the helium dilution process by which the system is cooled to 10 mK.

5.1.1 Dilution refrigerator

The DR system consists of a series of stages cooled to progressively lower temperatures, culminating in the millikelvin (mK) stage, which reaches a base temperature of 10mK [165]. These stages are shown in Figure 5.1, and are held under vacuum to allow for thermal isolation. Each stage is surrounded by a thermal shield (not pictured) to prevent the radiative heating of colder stages by warmer ones. Detector samples are attached and thermally coupled to the mK stage, pictured at the bottom of Figure 5.1. A pulse tube cooler (PTC) cools the entire system to 4K. The PTC cold head is coupled via thick copper heat straps to the 50K and 4K stages. During PTC cooling, the 1K and mK stages are thermally linked to the 4K stage via heat switches. The heat switches are vacuum tubes containing a charcoal absorber (or "getter") which, when heated above $\sim$ 10°K, outgasses into the tubes, creating a thermal link.

The system is cooled to its 10mK base temperature by the dilution unit, pictured in Figure 5.1 When the entire system reaches 4K, the heat switches are turned off, and a gaseous mixture of ^{3}He and ^{4}He is condensed into the mixing chamber of the dilution unit. A powerful turbo pump cools this mixture evaporatively to 800mK. Because ^{3}He is a fermion and ^{4}He is a boson, the two isotopes behave very differently at low temperatures. The ^{4}He part of the mixture condenses into a superfluid state, while the ^{3}He part is prevented from doing so by the Pauli exclusion principle. Below roughly 800mK, the helium mixture separates into two phases, a ^{3}He-rich phase which is almost pure ^{3}He (orange in Figure 5.1), and a superfluid ^{3}He-poor phase which is about 93% ^{4}He (blue with orange dots in Figure 5.1). Turbo pumping on the ^{3}He-poor phase removes yet more ^{3}He vapor from it, since ^{3}He has a much lower vapor pressure than ^{4}He. The ^{3}He vapor is pumped back through the dilution unit, cooling and condensing via thermal contact with the liquid in the still, and finally added back to the top of the mixing chamber. To restore equilibrium, ^{3}He atoms from the are pulled across the phase boundary from the ^{3}He-rich phase to the ^{3}He-poor phase. Crossing the boundary increases the enthalpy of the atoms, which removes heat from the mixture. This provides the cooling power for the system, and thus the coldest point in the system is the mixing chamber. The actual temperature of the detector sample being tested depends on how well it is thermally coupled to the mixing chamber.

Once base temperature is reached, heaters on the mK stage allow the stage temperature to be adjusted. Using a software control system in conjunction with the heaters, the mK stage can be held at any constant temperature between approximately 10-350mK. There are three main testing configurations. The first is dark testing, in which no optical power reaches the detectors. Dark tests characterize the microwave performance of the detectors, including their resonance shape, quality, and response to changes in stage temperature. The second configuration, shown in the upper panel of Figure 5.2, is the vacuum-window coupled optical configuration. This setup is used when the detectors are coupled to instruments in the room. This setup was used for the spectral and polarization measurements described later in this chapter. The third configuration, shown in the lower panel of Figure 5.2, is the coldload-coupled configuration. This is when the detectors are coupled to a blackbody mounted on the 4K shell. The temperature of the blackbody can be varied to provide a controlled optical load to the detectors. Blackbody coldload measurements are also shown later in this chapter.

5.1.2 RF electronics

Figure 5.3 shows a diagram of the full RF chain used for MKID testing. At the right side of the diagram is the vacuum chamber, inside of which is drawn a schematic of the cold signal pathway. The input signal enters the vacuum chamber at 300K, then passes through cold attenuators at 4K and 10mK before reaching the device. After the device, the signal passes through the low noise amplifier (LNA) at 4K and exists the vacuum chamber at the 300K output port. There are two warm signal pathways in this diagram that share the same cold pathway. Switches control which pathway is connected to the cryostat. RF switches allow the user to choose which of the two pathways is connected to the device. The first, indicated in red is the vector network analyzer (VNA) pathway. The VNA is used to measure the power transmitted through the device as a function of frequency. On the diagram, this measurement is equal to the amount of power that exits the VNA output and makes it back into the VNA input. The signal exits the VNA and passes through a user-controlled variable attenuator, then through the cold RF chain, and finally through two warm amplifiers before arriving back at the VNA. This is a complex-valued signal, and with proper accounting for the attenuation and gain of the components between the VNA and the device, this measurement is equivalent to measuring $S_{21} = I + jQ$ of the device (recall Equation 4.6). Its amplitude in dB is reported as $|S_{21}|$ throughout this work.

The second warm signal pathway, indicated in blue, is the homodyne pathway. The homodyne system is used to measure detector noise timestreams. More precisely, the homodyne system sends a single-frequency signal, or tone, into the device and samples the device response over a given period of time. This is accomplished as

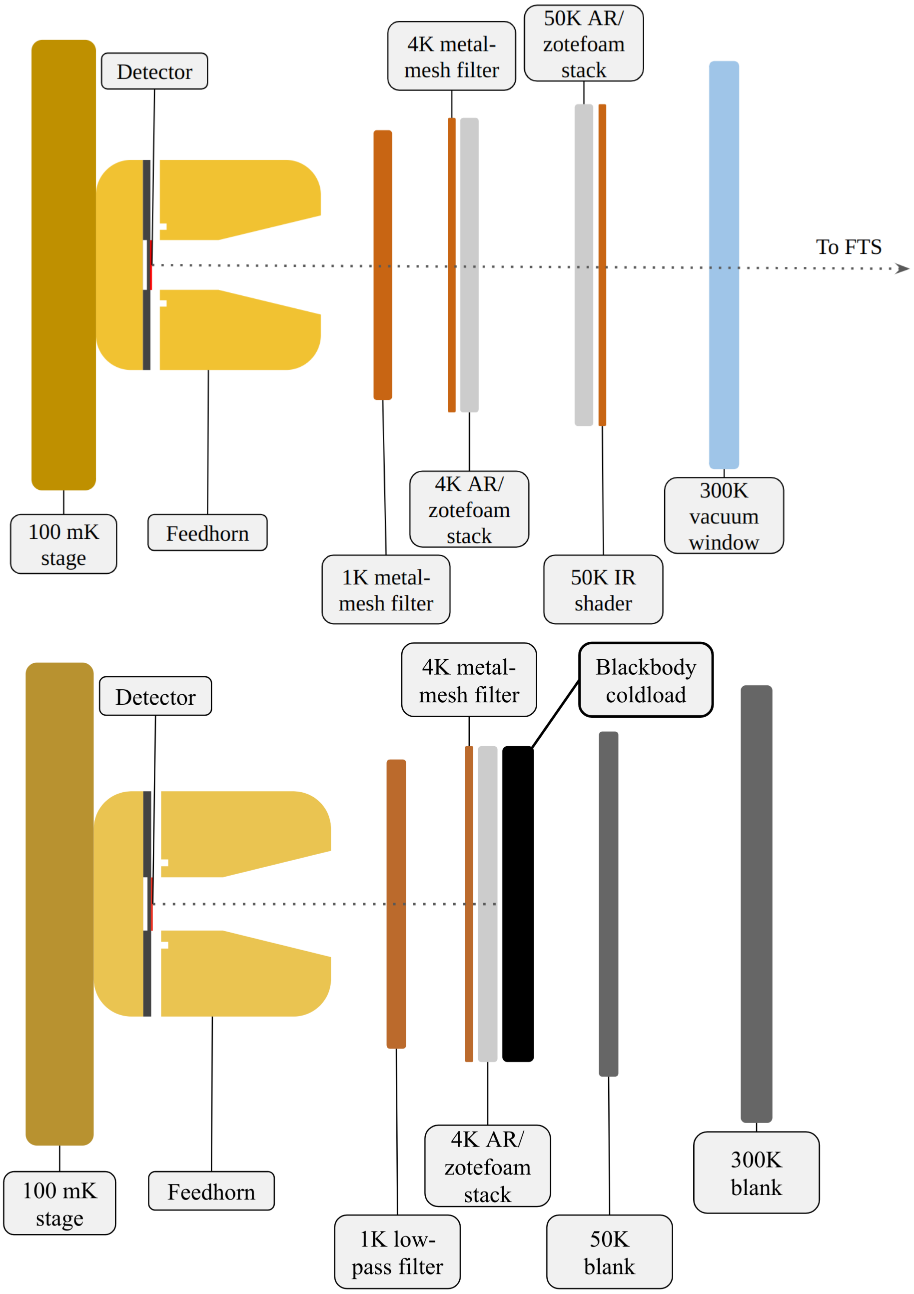

Figure 5.2: Schematics of the filter stacks used to test detectors optically. The top panel shows the configuration in which the detectors are coupled into the room. This configuration is used for Fourier transform spectrometer (FTS) and polarization angle testing. The lower panel shows the coldload blackbody configuration, which is used to test detector optical responsivity at a range of representative optical loading.

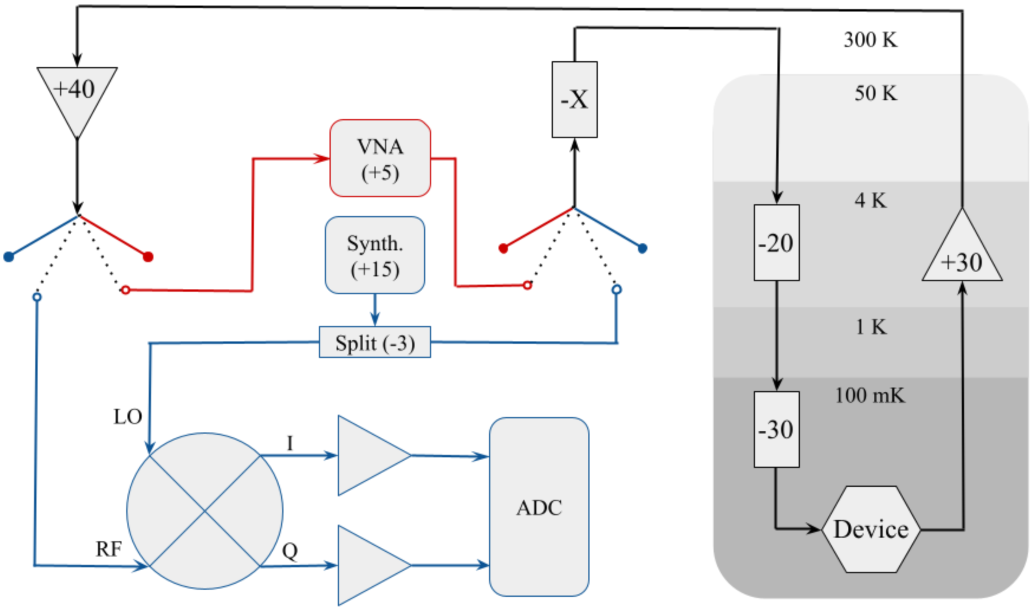

Figure 5.3: Block diagram of the RF test setup, showing the VNA signal pathway in red and the homodyne signal pathway in blue. The cryostat stages are shown in a gray gradient on the right side of this diagram, and the rest of the diagram is warm. The VNA and synthesizer outputs are in dBm, while amplifier gains and attenuations are in dB. Cable loss is not included. The X on this diagram represents a digitally-controlled variable attenuator. The blank pre-amplifiers for I and Q have variable gain set by the user. Both the VNA and ADC output digitally to the system control computer. The synthesizer is synchronized to a Rb clock that is not shown in this diagram.

follows. A signal synthesizer, synchronized to an external clock, produces a signal at the desired bias tone. The signal is then split. One half (-3dB) of the signal is sent straight into the quadrature demodulator to serve as its reference. This connection is indicated by the LO, or local oscillator, port on the demodulator in Figure 5.3. The second half of the synthesizer signal is sent through the variable attenuator and into the device. After exiting the device, this second half of the signal is amplified and returns to the demodulator via the RF port. The returning signal has acquired some phase and amplitude shift from its interaction with the device. The quadrature demodulator extracts this information by comparing the return signal (RF) with the original synthesized signal (LO). Within the demodulator, the original LO signal is multiplied by the RF input, and the result is low-pass filtered and output as I. In parallel, the same orignal LO signal is also phase shifted by 90 degrees ($\pi/2$), and multiplied by the RF input, and the result is low-pass filtered and output as Q. Thus what comes out of the I port is the component of the returning RF signal that is (I)n phase with the original LO signal, and what comes out of the Q port is the component of the RF signal that is in (Q)uadtrature phase (offset in phase by 90 degrees, or $\pi/2$, or one-quarter cycle) with the original LO signal. The I and Q waveforms output by the demodulator are amplified and then digitized by the Analog-to-Digital converter (ADC).

5.2 Resonator tuning

MKIDs are read out by probing the resonance with a bias tone, which is in essence a cosine with a frequency $\omega_0 = 2\pi f_0$ and amplitude A. Do not mistake this ω_0 for the idealized LC resonator frequency in Section 4.1.2; from now on it means the bias frequency. The bias tone is sent through the readout line and the changes in power transmitted ($S_{21} = I + jQ$) at the bias tone as the resonance moves around are what is recorded as the resonator timestream. Tuning a resonator is the process of selecting the bias power A^2 and frequency ω_0 to maximize the response of the resonator to changes in loading. It is vitally important to tune resonators

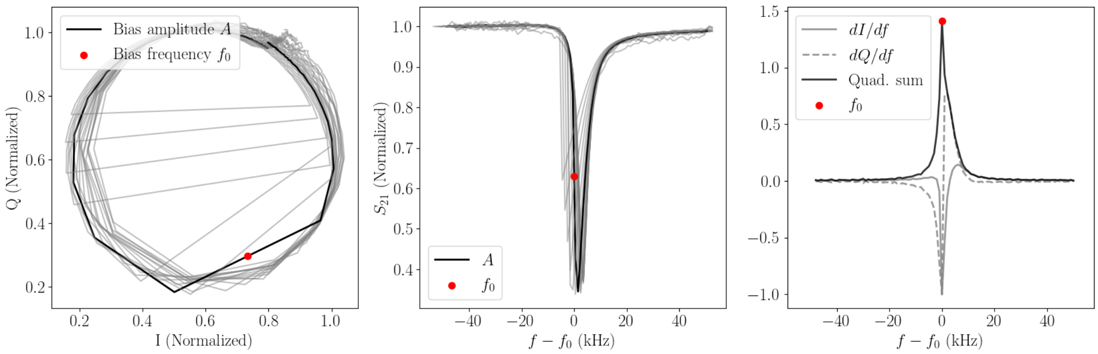

Figure 5.4: An example of resonator tuning for an SPT-3G+ detector. The left panel shows the IQ plane with normalized sweeps at multiple bias powers overplotted. As the bias power increases, the resonator bifurcates, and large portions of the IQ circle are cut off. The black line shows the bias power selected for this resonator. The center panel shows S_{21} versus frequency for the same sweeps. Bifurcation manifests here as a vertical jump in S_{21}. The right panel shows the selection of the bias frequency by maximizing the quadrature sum metric from Equation 5.3. The chosen frequency is shown in red on all three panels.

properly prior to any attempt at characterization. If a resonator is over or under-biased or is tuned to a sub-optimal frequency, its resonsivity and noise behavior will be severely degraded, and the resulting data will be difficult to interpret. During MKID operation, every time a change is made to the system that affects the baseline resonator loading, be it stage temperature, blackbody temperature, FTS mirror position, or on-sky telescope elevation angle, the resonators must be retuned.

5.2.1 Choosing the bias power

The first step in tuning is to select the correct bias power, which is the same as selecting the tone amplitude A. Naively one would set the tone amplitude to be as large as possible, so that the transmitted tone can be measured with high signal-to-noise [166]. Even better, the amplitude of the so called two-level-system (TLS) noise component that plagues MKIDs decreases with the bias power with an inverse square-root (or $1/A$) dependence [167, 168]. Sadly a phenomenon called bifurcation imposes an upper limit on the bias power with which an MKID can be operated as designed. This phenomenon is explained in detail in [166], and is based on the idea that the resonator absorbs power from the readout tone, which excites the quasiparticle population to a certain energy level, or “quasiparticle temperature”. The quasiparticles cool by dissipating energy via phonons through the resonator and into the substrate. In a normal low-bias-power scenario, these processes eventually reach equilibrium and the quasiparticle system remains at a defined steady-state temperature. For higher bias powers, there can be two stable quasiparticle temperatures at which the heating and cooling processes balance, and the system switches suddenly between these states during a frequency sweep. This results in the asymmetric resonance shape that can be seen for high bias powers in the center panel of Figure 5.4. The theoretical bifurcation power of a resonator is [169]:

$$P_{\mathrm{bif}}(\omega) = \frac{a_c \omega N_0 \Delta^2 V_L Q_c}{4Q_r^3}, \tag{5.1}$$

where $a_c = 0.77$ is the asymmetry parameter, and all the other parameters are defined in Section 4.1 [160]. In practice, the bifurcation power for a resonance is obtained for each resonator by sweeping the resonance with a series of increasing bias powers until the resonance bifurcates. Figure 5.4 shows the response of an SPT-3G+ resonator to varying bias power. In the left and center panels, the light grey lines correspond to various bias powers. As bias power increases, a discontinuity in the IQ sweep, corresponding to a vertical jump in the frequency sweep, begins to appear. The point is that the ideal resonator bias power is the highest possible power before the resonance bifurcates. The sweep corresponding to the chosen bias power for the resonator pictured in Figure 5.4 is shown in black on the left and center panels. The criterion for observing bifurcation for me is seeing a discontinuity in the IQ circle, as seen in Figure 5.4. Obviously the power at which this is observable also depends on the sweep resolution, and for large arrays a robust bifurcation threshold must be established to enable consistent tuning [76].

5.2.2 Choosing the bias tone

For maximum signal, is desirable to set the bias tone f_0 to the frequency at which the phase changes most dramatically in response to a change in frequency, or in other words where $d\phi/df$ is maximized [160]. Note that for constant A:

$$\frac{dI}{df} = -A\frac{d\phi}{df}\sin(\phi(f)), \quad \frac{dQ}{df} = A\frac{d\phi}{df}\cos(\phi(f)) \quad \Longrightarrow \quad \frac{dI}{df}^2 + \frac{dQ}{df}^2 = A^2\frac{d\phi}{df}^2, \tag{5.2}$$

so this is equivalent to choosing f_0 such that the quadrature sum

$$g(f) = \sqrt{(dI/df)^2 + (dQ/df)^2} \tag{5.3}$$

is maximized. To locate f_0 for a resonance, the synthesizer is swept through a set of frequencies centered around the resonance location. Since, in general, $d\phi/df \gg d\phi/dt$, the frequency sweep forms a circle in the I/Q plane, an example of which is shown in black in the left panel of Figure 5.4. The same sweep is plotted as S_{21} versus frequency in the center panel. The right panel of Figure 5.4 shows the derivatives of I and Q as a function of frequency along with their quadrature sum $g(f)$ from Equation 5.3 above. The bias tone f_0 corresponding to the maximum value of $g(f)$ is indicated in red on all three panels of Figure 5.4.

5.3 Measuring noise

Now that the resonators are tuned, it is time to measure noise timestreams. Noise timstreams are taken using the homodyne system described qualitatively in Section 5.1.2 above. This will be a more quantitative treatment of noise measurement and analysis. The synthesizer generates the bias tone at the bias frequency ω_0. This is split into the local oscillator (LO) signal $s_{\mathrm{LO}}(t) = \cos(\omega_0 t)$ and the identical RF signal, which is passed through the device. After passing through the device, the returning RF signal $s_{\mathrm{RF}}(t)$ has aquired a new amplitude $A(t)$ and phase shift $\phi(t)$:

$$s_{\mathrm{RF}}(t) = A(t)\cos(\omega_0 t + \phi(t)) \tag{5.4}$$

The quadrature demodulator multiplies the LO by the RF signal and applies a low-pass filter $\mathcal{F}$ to get $I(t)$. It multiplies the quarter-phase-shifted LO by the RF signal and applies the same low-pass filter to get $Q(t)$:

$$\begin{aligned} I(t) &= \mathcal{F}\left(s_{\mathrm{LO}}(t)s_{\mathrm{RF}}(t)\right) = \mathcal{F}\left(A(t)\left[\cos(\omega_0 t)\cos(\omega_0 t + \phi(t))\right]\right) \\ &= \mathcal{F}\left(\frac{A(t)}{2}\left[\cos(2\omega_0 t + \phi(t)) + \cos(\phi(t))\right]\right) = \frac{A(t)}{2}\cos(\phi(t)) \qquad (5.5) \\ Q(t) &= \mathcal{F}\left(s_{\mathrm{LO}}(t + \frac{\pi}{2\omega_0}\right) s_{\mathrm{RF}}(t)) = \mathcal{F}\left(A(t)\left[-\sin(\omega_0 t)\cos(\omega_0 t + \phi(t))\right]\right) \\ &= \mathcal{F}\left(-\frac{A(t)}{2}\left[\sin(2\omega_0 t + \phi(t)) - \sin(\phi(t))\right]\right) = \frac{A(t)}{2}\sin(\phi(t)) \qquad (5.6) \end{aligned}$$

The amplitudes of $I(t)$ and $Q(t)$ are sampled by the ADC at some rate over some period of time, and this set of samples is what is meant by the phrase “I and Q timestreams” throughout the rest of this work.

5.3.1 Converting timestreams to resonant frequency shift

To measure the frequency response of the resonator, the I and Q timestreams must be converted into a change in resonant frequency, δf. The simplest way to do this is to employ the linear approximation method described in [160] and [170]:

$$\begin{aligned} \delta f(t) &= \frac{df}{dI + j dQ}\left(\delta I(t) + j\delta Q(t)\right) = \frac{\left[\frac{dI}{df} - j\frac{dQ}{df}\right]}{\frac{dI}{df}^2 + \frac{dQ}{df}^2}\left(\delta I(t) + j\delta Q(t)\right) \\ &= \frac{\delta I(t)\frac{dI}{df} + \delta Q(t)\frac{dQ}{df}}{\frac{dI}{df}^2 + \frac{dQ}{df}^2} - j\frac{\delta I(t)\frac{dQ}{df} - \delta Q(t)\frac{dI}{df}}{\frac{dI}{df}^2 + \frac{dQ}{df}^2}. \qquad (5.7) \end{aligned}$$

This expression is evaluated at the bias tone f_0 chosen in Section 5.2.2, so that $\delta I(t) = I(f_0, t) - I_0$ and $\delta Q(t) = Q(f_0, t) - Q_0$, where I_0 and Q_0 are the values of I and Q at the bias tone f_0, which can be obtained from the frequency sweep used to select f_0. The derivatives $dI/df|_{f_0}$ and $dQ/df|_{f_0}$ can also be obtained from that frequency sweep. Calculating “δf” generally refers to taking the real part of Equation 5.7, which represents fluctuations in the resonant frequency [160, 170]. The imaginary part of Equation 5.7 is the orthogonal combination of the data, and

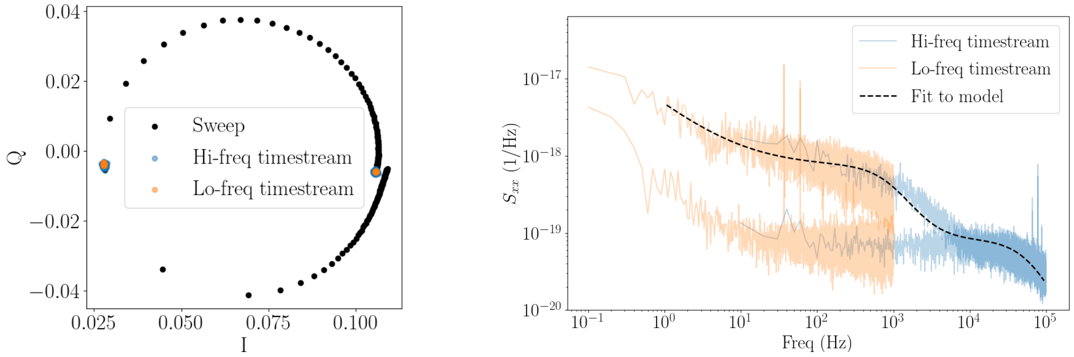

Figure 5.5: *Left:* Sweep of a resonance in the IQ plane, with on and off-resonance noise timestreams overplotted. *Right:* On and off-resonance power spectral densities for the same resonator. The on-resonance PSD is fit with Equation 5.9.

corresponds to fluctuations in the energy dissipated by the resonator per cycle, i.e. the resonator quality factor.

5.3.2 Noise power spectral density

The usual way to notate the PSD is S_{xx}, where $x = \delta f(t)/f_0$ is the fractional frequency shift of the resonator. This is the same S_{xx} as the one given in Equation 4.28. The expression is:

$$S_{xx} = \frac{2\,|\mathscr{F}(x)|^2}{f_s n_s} = \frac{2\,|\mathscr{F}(\delta f(t)/f_0)|^2}{f_s n_s}, \tag{5.8}$$

where $\mathscr{F}$ denotes a Fourier transform, f_s is the ADC sample frequency and n_s is the number of samples in the timestream. The factor of 2 is present because the frequency domain of $\mathscr{F}(x)$ is restricted to positive frequencies. By using the fractional frequency shift x, the units of the PSD become inverse Hz. Figure 5.5 shows an example of a noise measurement from an SPT-3G+ detector. The left panel shows the IQ sweep at the chosen bias power with the on-resonance timestreams $I(f_0, t)$ and $Q(f_0, t)$ overplotted. Note that timestreams are also taken off-resonance, and are processed into PSDs in the same manner as the timestreams taken at the tone f_0. Even for the off-resonance timestreams, Equation 5.7 is still evaluated at the bias tone f_0. This forces the on and off-resonance PSDs to match at high frequency and allows the off-resonance PSD to serve as a measure of the system noise, i.e. the noise that would be expected at f_0 if no resonance were present there. On and off-resonance noise PSDs are shown in the right panel of Figure 5.5. The noise PSD has a distinct shape, which is fit with the following model:

$$S_{xx}(f) = \left(\frac{A + Bf^{-n}}{1 + (2\pi f \tau_{qp})^2} + 1\right)\left(\frac{W}{1 + (2\pi f \tau_{\text{filt}})^2}\right) \tag{5.9}$$

There are seven parameters in this model. A is the generation-recombination (GR) noise amplitude above the white noise level. B is the amplitude of a generic power-law $1/f$ noise component which has spectral index n. τ_{qp} is the quasiparticle lifetime in the inductor, W is the system white noise level, and τ_{filt} is the system high-frequency filter rolloff time constant [171, 163]. The on-resonance PSD in the right panel of Figure 5.5 is fit with Equation 5.9. The resulting GR-noise level value is $AW = 6.6 \times 10^{-19}$ Hz^{-1}, and the quasiparticle lifetime is $\tau_{qp} = 170$ μs.

5.4 Dark MKID characterization

A detailed characterization of individual dark 220 GHz detectors was presented in [75]. The findings of that characterization have been consistent across larger dark arrays. Figure 5.6 shows a VNA sweep of such an array, and the temperature response of a resonator is shown in the inset. Figure 5.7 shows histograms of the inductor quality factor Q_i (minimum target value: 10^5), critical temperature T_c, and kinetic inductance fraction α_k (simulated value: 0.34) for a dark chip containing 124 functional dark detectors (97% yield). T_c and α_k were extracted from fits to the resonant frequency versus temperature curves of the resonators, and Q_i was extracted from fits to the resonance shapes at an operating temperature of 100 mK. The mean Q_i was $\bar{Q}_i = 5 \times 10^5$, with $\sigma(Q_i) = 3 \times 10^5$, with the entire Q_i distribution greater than twice our minimum target value. Assuming a $\Delta = 1.76 k_B T_c$ relationship between the energy gap and critical temperature of the Al film, we found $\bar{T}_c = 1.19$K, $\sigma(T_c) = 0.02$K. The distribution of α was consistent with the simulated expectation,

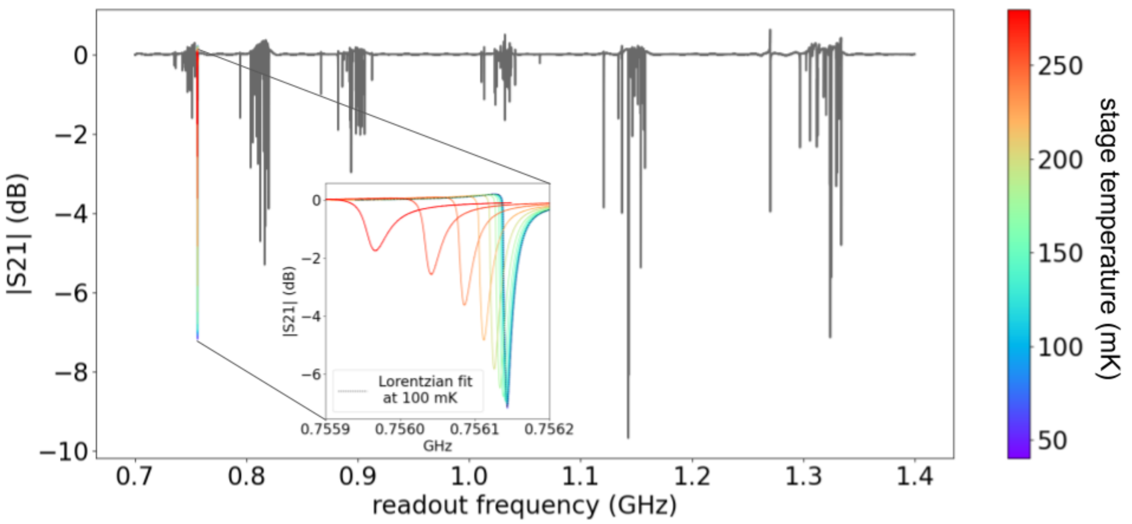

Figure 5.6: Example sweep from a prototype SPT-3G+ chip. The gray line shows the transmission at the operating temperature of 100 mK. Resonators on this device have been intentionally placed into six banks. The inset plot shows the expected change in resonance shape and frequency as the stage temperature is increased. A high-pass filter has been applied to this sweep for aesthetic purposes.

with $\bar{\alpha}_k = 0.32$, $\sigma(\alpha_k) = 0.03$.

5.4.1 Dark NEP

Much of this section is reproduced from [77]

The frequency vs temperature data can be combined with noise power spectral densities to produce an estimate of the dark noise-equivalent-power (NEP) of the detector (recall Equation 4.29). The right axis Figure 5.8 shows the PSD of an SPT-3G+ MKID measured at an operating temperature of 110 mK. The left axis shows the conversion of this power spectral density to a dark NEP. The dark NEP is estimated using Equation 4.29 as

$$\mathrm{NEP} = \sqrt{S_{xx}}\Big[(\frac{1}{f_0}\frac{\delta f_0}{\delta n_{qp}})\frac{\delta n_{qp}}{\delta P_{opt}}\Big]^{-1}, \tag{5.10}$$

where the product in the brackets represents dark responsivity. The term in parentheses is obtained by performing dark frequency sweeps of the resonance at multiple

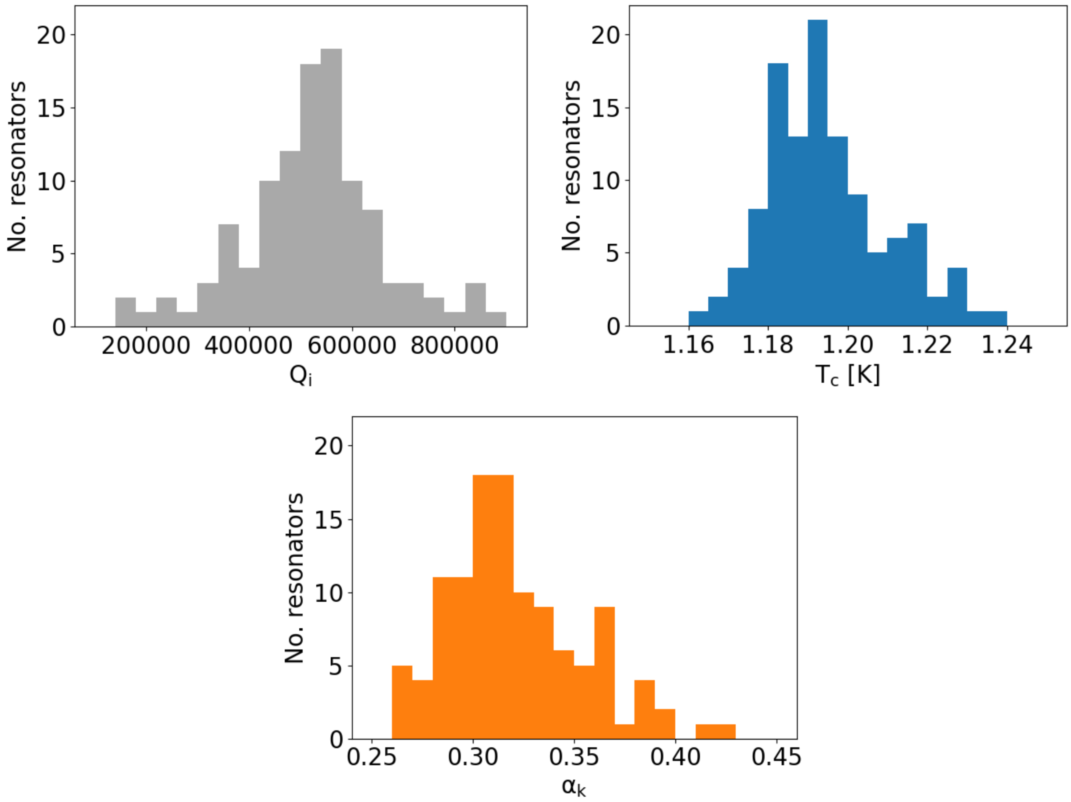

Figure 5.7: Distributions of inductor quality factor Q_i *(Upper left)*, Aluminum critical temperature T_c *(Upper right)*, and kinetic inductance fraction α_k *(Lower center)* for a 63-pixel (126 resonator) dark 220 GHz array, of which 124 resonators yielded. The Q_i distribution lies above our target multiplexing value of 10^5. The T_c for the Al film was found to be $\sim$1.19K, and the α_k distribution is consistent with our simulated expectation of 0.34.

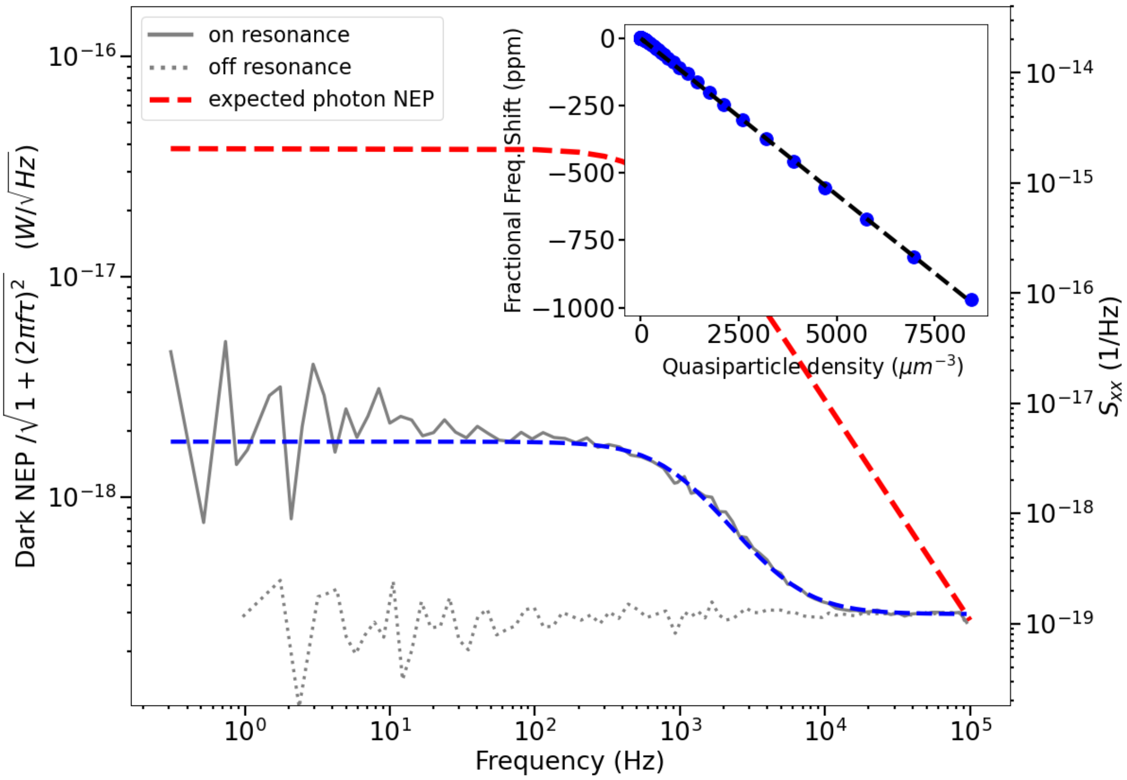

Figure 5.8: The left axis shows the dark NEP corrected for the responsivity roll off (gray) for an aluminum-only device as compared to the expected photon NEP (red dashed) with 5 pW optical loading, indicating background domination in this optimized ($\eta_{\text{opt}} = 1$) scenario. The dark NEP was calculated from the dark responsivity (see inset) and the detector noise. On the right axis, the grey lines are power spectral densities of on and off-resonance noise timestreams measured at 110mK. The blue dashed line is a fit to the on-resonance dark detector noise, which is dominated by the generation-recombination noise of the device. Inset: Linear fit to fractional frequency shift vs quasiparticle number density. The slope of this fit was used to calculate the dark responsivity of the resonator.

temperatures. The expected quasiparticle density is calculated for each temperature using Equation 4.21:

$$n_{qp} = 2N_0\sqrt{2\pi k_B T\Delta}e^{-\frac{\Delta}{k_B T}}, \tag{5.11}$$

where, as in Equation 4.21, $N_0 = 1.73 \times 10^{10}\,\mu\text{m}^{-3}\text{eV}^{-1}$ is the single-spin density of states for aluminum, k_B is the Boltzmann constant, T is the temperature of the resonator, and $\Delta = 1.76k_BT_c$, with $T_c = 1.2$ K for the aluminum inductor. The critical temperature T_c was extracted from a fit to the resonant frequency shift versus device temperature. Each blue point on the inset to Figure 5.8 represents the fractional frequency shift of the device in the presence of a given quasiparticle density. The value of $\frac{1}{f_0}\frac{\delta f_0}{\delta n_{qp}}$ is then the magnitude of the slope of the fit to $\frac{\delta f_0}{f_0}$ vs n_{qp}. This fit is shown in the inset to Figure 5.8, and was performed at high temperatures where the quasiparticle response is dominant. The remaining term in the brackets, from Equation 4.22, is

$$\frac{\delta n_{qp}}{\delta P_{opt}} = \frac{\eta_e \tau_{qp}}{\Delta V_L}, \tag{5.12}$$

where $\eta_e \sim 0.8$ is the theoretical pair breaking efficiency for 220 GHz photons in superconducting aluminum, V_L is the inductor volume, and $\tau_{qp} = 220\ \mu$s is the quasiparticle lifetime, which is derived from the fit to the dark noise power spectral density rolloff (blue dashed line in Figure 5.8) at 110 mK. The fit to the noise rolloff here is well represented by a single-pole Lorentzian with time constant τ_{qp}, as expected since the the measured quasiparticle lifetime is significantly longer than the resonator ringdown time $\tau_{res} = 2Q_r/\omega_0 \approx 20\ \mu$s. The red dashed line in Figure 5.8 represents the expected NEP due to photon noise with 5 pW optical loading, which is the estimated loading at 220 GHz due to atmospheric and instrument emissivity. Within the resonator bandwidth, this photon noise limited NEP is given by

$$\text{NEP}^2_{\text{photon}} = 2\eta_{opt}P_{opt}h\nu(1 + \eta_{opt}\bar{n}_{ph}). \tag{5.13}$$

As in Equation 4.27, $\bar{n}_{ph} = [e^{h\nu/k_BT} - 1]^{-1}$ is the mean photon occupation number and $\eta_{opt} = 1$ is the best-case detector optical efficiency. Note that this expression is just the numerator of Equation 4.29, and that the axis on the left side of Figure 5.8 is formatted in the same way. This estimate suggests that the intrinsic device noise is well below the expected photon NEP at 220 GHz, and provides strong evidence that this detector design is well suited to achieve the sensitivity requirements of SPT-3G+.

5.5 Optical efficiency

Much of this text is reproduced from [78].

With dark microwave properties relatively well-understood, the next step on the development timeline is to test the detectors under an optical load. The detectors' response to a controlled optical load was measured in a closed cryostat with the feedhorn-coupled detectors facing a blackbody coldload of variable temperature. Assuming a single-polarization, beam-filling single-moded system, such that the etendue of the system is approximated $A\Omega = \lambda^2 = (c/\nu)^2$, the optical power reaching the detector at a given blackbody temperature T_{bb} can be expressed as the product of the total filter stack transmission Γ_{filt} and the integral of the blackbody flux:

$$P_{\text{opt}}(T_{bb}) = \Gamma_{\text{filt}} \int_{\nu_{\text{wg}}}^{\nu_{\text{filt}}} \frac{h\nu}{\exp(\frac{h\nu}{k_B T_{bb}}) - 1} d\nu. \tag{5.14}$$

The bounds of the integral, $\nu_{\text{wg}} = 176$ GHz and $\nu_{\text{filt}} = 240$ GHz, are the lower and upper band edges which in this case are defined by the waveguide cutoff frequency and metal-mesh low-pass filter frequency respectively. Γ_{filt} characterizes the band-averaged efficiency of the metal-mesh filters in the cryostat, which is of order 0.70-0.90, depending on the exact optical configuration used. Frequency sweeps and timestream data for optically coupled resonators were collected at each blackbody temperature, with the device kept at the intended operating temperature of 140 mK. The frequency vs blackbody temperature curve obtained from the sweeps are converted to detector responsivity R_x via:

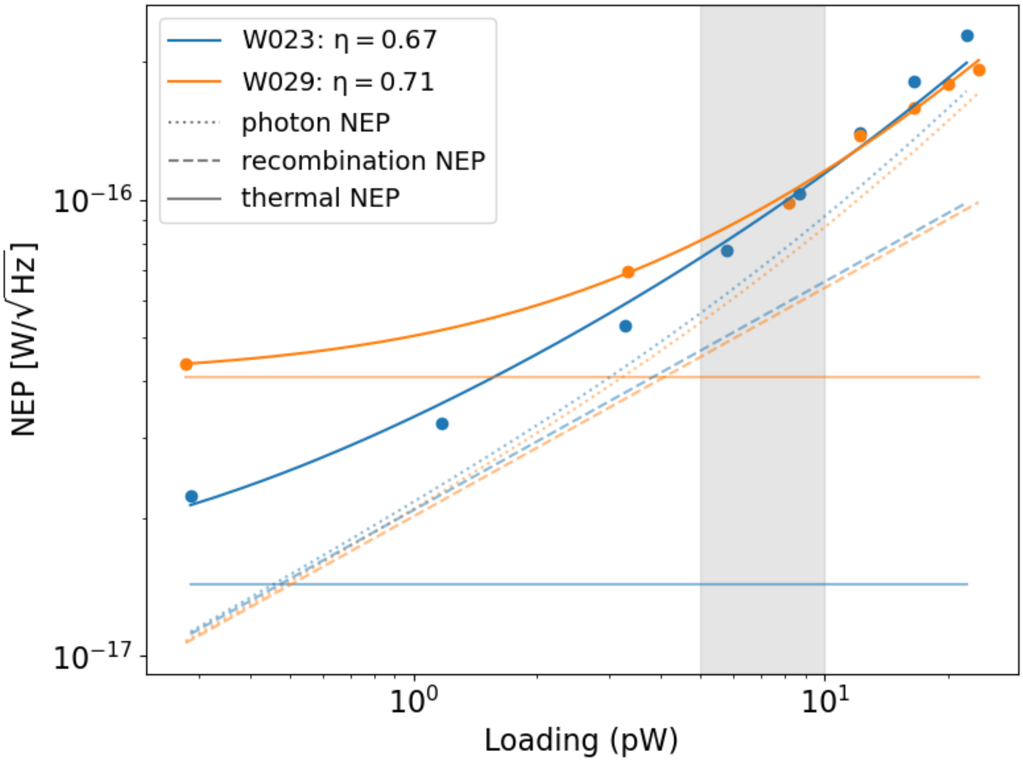

Figure 5.9: The measured NEP at several different optical loads for both the microstrip (W023, blue) and CPW (W029, orange) chips. These points are fit with a theoretical model (Equation 5.19) to extract an optical efficiency, η, reported in the legend. Fits to the data are represented by solid lines, while other line styles represent the photon, recombination, and thermal components in Equation 5.19 that make up the total NEP. The gray vertical band is the expected range of optical loading for SPT-3G+.

$$R_x(P_{\text{opt}}) = \frac{d}{dP_{\text{opt}}}\left(\frac{\Delta f_0(P_{\text{opt}}(T_{bb}))}{f_0}\right). \tag{5.15}$$

The power spectral densities of the timestream data are fit with a model to extract the detector white noise level S_{xx} at each optical power. Combining the white noise with the responsivity produces an NEP at each optical loading:

$$\text{NEP}(P_{\text{opt}}) = \frac{\sqrt{S_{xx}(P_{\text{opt}})}}{R_x(P_{\text{opt}})}. \tag{5.16}$$

Two chips were tested with this setup: W023 has the old microstrip feedline, and W029 has the new CPW feedline. Both chips are single-layer aluminum test devices, as opposed to the fiducial design with aluminum inductors and niobium IDCs, feedline and ground plane. (We have not observed a difference in dark responsivity, noise, or resonator quality, between the all-aluminum test devices and the fiducal aluminum and niobium design.) The blue and orange points in Figure 5.9 show the calculated NEP as a function of optical power for both a microstrip (blue) and a CPW (orange) feedline. Within the expected SPT-3G+ optical loading range (gray vertical bar), both resonators have an NEP of roughly 10^{-16} W/$\sqrt{\text{Hz}}$. The loaded NEP as a function of optical power is then fit with a theoretical model [172]:

$$\text{NEP}^2 = \frac{\text{NEP}^2_{\text{photon}} + \text{NEP}^2_{\text{R}}}{\eta_{\text{opt}}} + \text{NEP}^2_{\text{therm}}, \tag{5.17}$$

where NEP_R is the optical recombination noise, and NEP_therm is a catch-all for any thermal-like contributions that remain constant with optical power. The photon and optical recombination contributions to the overall NEP are given by:

$$\text{NEP}^2_{\text{photon}} = 2P_{\text{opt}}h\nu\big(1 + \eta_{\text{opt}}\bar{n}_{\text{ph}}(\nu, T_{\text{bb}})\big), \tag{5.18}$$

$$\text{NEP}^2_{\text{R}} = 2P_{\text{opt}}h\nu, \tag{5.19}$$

where ν is the observation frequency, set to 220 GHz, and $\bar{n}_{\text{ph}}(\nu, T_{\text{bb}})$ is the mean photon occupation number per mode at the observation frequency for a given blackbody temperature. The optical efficiency η_{opt} and the thermal term NEP_therm are the fit parameters. The fit to this model is shown in Figure 5.9 for two resonators, a breakdown into the photon, recombination, and thermal NEP is overplotted in dotted, dashed, and solid lines, respectively. Both fits indicate an optical efficiency of $\sim 70\%$. Though this is approximately 15% lower than the simulated expectation, the simulation does not account for feedhorn loss or other sources of optical power loss.

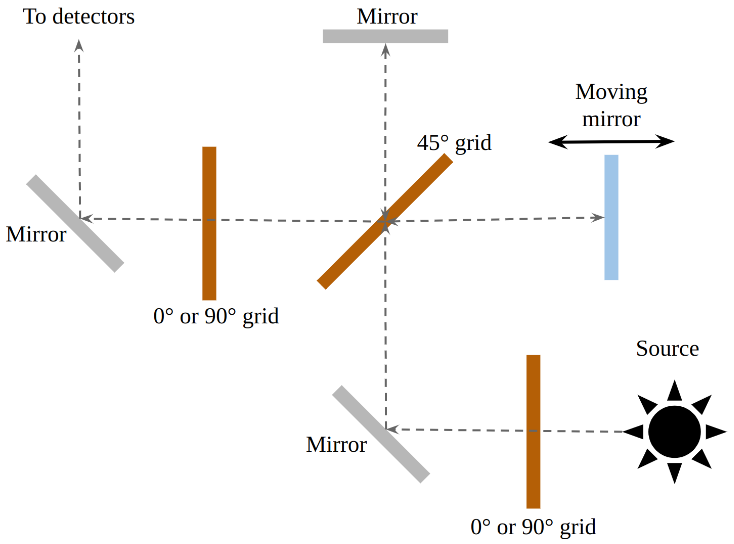

Figure 5.10: Cartoon diagram of the Fourier transform spectrometer (FTS) used for spectral response measurements. The intensity of light incident on the detectors is set by the position of a moving mirror. The mirror is swept through a range of positions over the course of an FTS scan, creating an interference pattern whose shape depends on the detectors' spectral response.

5.6 Spectral response

It is important to understand the spectral response of an instrument, and this starts with laboratory measurements of detector spectral response. In addition to making this measurement for SPT-3G+ prototypes, I developed the pipeline for measuring detector spectra using the RF-ICE system for the SPT-SLIM project [173]. Spectral measurements are taken by coupling a Fourier Transform Spectrometer (FTS) to the detectors through a vacuum window into the cryostat. The FTS works in a similar manner to a Michelson interferometer, creating an interference pattern as the moveable mirror is swept through a range of positions. A cartoon diagram of the FTS configuration used for this work is shown in Figure 5.10. The detectors are mounted within the cryostat on a stage facing the vacuum window. Between the cryostat vacuum window and the detectors are three layers of filtering, shown in the upper panel of Figure 5.2. For SPT-3G+ 220 GHz detectors, the final low-pass filter is an 8.5 cm^{-1} filter with a cutoff frequency around 250 GHz. Resonators must first be biased and tuned following Section 5.3 with the source on, and with the FTS mirror located at its white-light fringe position. Detectors should be retuned after every change to the setup.

5.6.1 Taking and processing FTS scans

The mirror is swept at some velocity v, and the ADC is sampling at some sample rate f_s. Then the path length difference between consecutive samples is $\delta = 2v/f_s$. The following equation is derived in [174], and this derivation is reproduced in Appendix B:

$$\mathscr{P}(k) = \int_{-\infty}^{\infty} [I(\delta) - \frac{1}{2}I(0)] \cos(2\pi k\delta) d\delta \tag{5.20}$$

This equation states that power spectrum of the light incident on detector is the Fourier transform of the intensity of light hitting the detector as a function of path length. Here $k = 2\pi/\lambda$ is the wave number of incident light and I is the intensity of light incident on the detector. After the FTS scan, the existing data products are a known tone frequency f_0 and bias power A, a reference sweep, and the timestreams $I(t)$ and $Q(t)$. The first step is to convert the timestreams to fractional frequency shift timestreams $x(t) = \delta f(t)/f_0$, using the method described by Equation 5.7. The reference sweep and known tone are used to calculate the linear coefficients in Equation 5.7. The resulting timestream $x(t)$ is the interferogram term in Equation 5.20. The x-axis of the interferogram can be put into units of path length difference using the FTS mirror velocity: $\delta = 2vt$. Then the power spectrum $\mathscr{P}(k)$ can be computed by taking the Fourier transform of $x(t)$. It may also be useful to apply a Hanning window to the interferogram prior to the Fourier transform to avoid artifacts caused by non-smooth behavior of the interferogram at the beginning and end of the FTS scan.

5.6.2 SPT-3G+ 220 GHz spectral response

The devices from Section 5.5 were tested in a second configuration, this time with the detectors facing an open cryostat vacuum window, as in the lower panel of Figure 5.2. An FTS was coupled through the vacuum window to the detectors

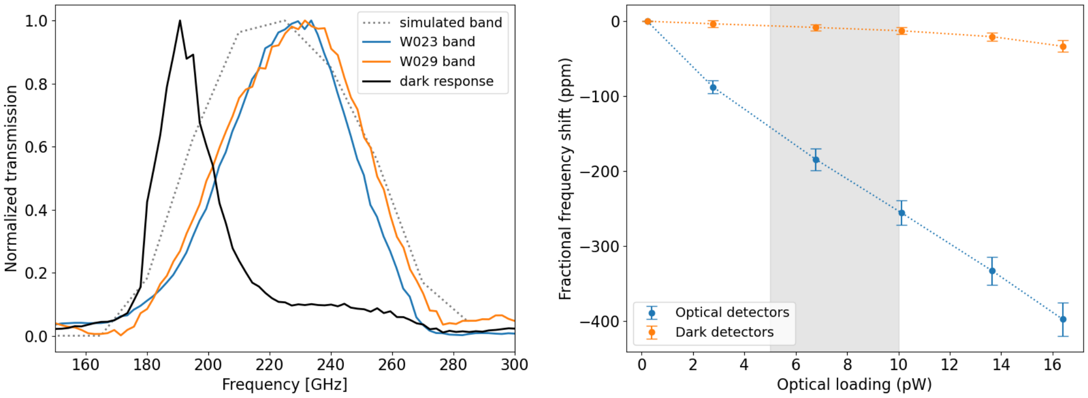

Figure 5.11: *Left:* The simulated (grey dotted) optical band overplotted with the measured optical band for a resonator from each of the microstrip (W023, blue) and CPW (W029, orange) chips. The black line is the measured spectrum from the dark detectors on W029. All bands here are normalized to have a maximum transmission of 1. *Right:* Comparison of the averaged fractional frequency shift of dark detectors on W029 to that of optically loaded detectors as a function of incident optical power. This ratio of dark to optically loaded frequency shift is less than 5% within the expected SPT-3G+ optical loading range (gray vertical band).

as shown schematically in Figure 5.10. The left panel of Figure 5.11 shows the spectral response of optical pixels on both the microstrip (W023, blue) and CPW (W029, orange) chips. All spectra on this plot are normalized to have unit maximum transmission. These are overplotted with the simulated optical band, indicated by the gray dotted line. Test results mostly agree with the simulation, except for a discrepancy in the lower part of the band. This could potentially be explained by a slight deviation from simulation in the machined RF choke, or unexpected coupling to the RF choke by nearby structures.

The W029 chip contains several structures in which a feedhorn-coupled central pixel is surrounded by six "dark" pixels that are not coupled to a feedhorn. This enables measurements of a dark pixel's response to a change in the power incident on its optically coupled neighbor. The black solid line in the left panel of Figure 5.11 shows the measured spectrum of the dark resonators on W029. The dark spectral response peaks at the lower edge of the simulated band, indicating that some of the in-band photons that were not absorbed by the optical detector were scattered and eventually absorbed by neighboring dark detectors. The right panel of Figure 5.11 shows the averaged fractional frequency shift of dark detectors on

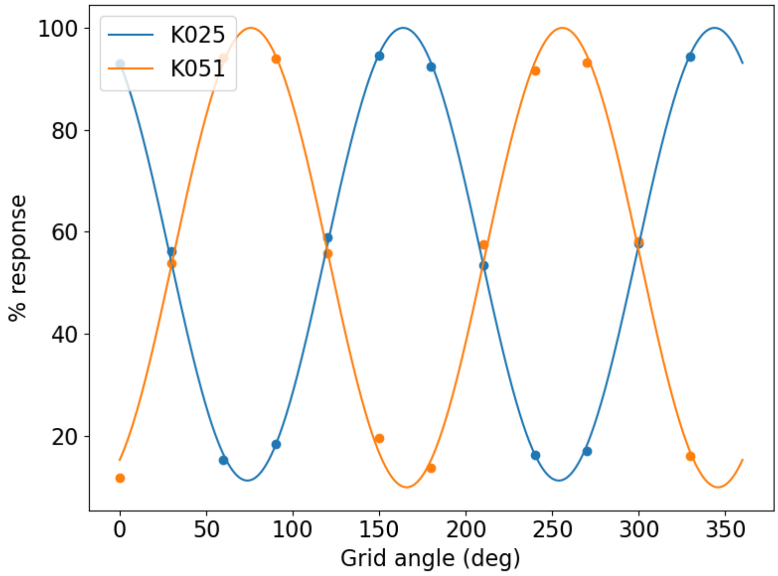

Figure 5.12: Polarization response of an x-aligned (blue) and y-aligned (orange) SPT-3G+ detector. The detectors show the expected behavior. The minima of these curves indicate cross-polarization leakage of about 10%.

W029 as compared to that of optically loaded detectors as a function of incident optical power. Within the expected range of optical loading for SPT-3G+, the ratio of dark to optically loaded frequency shift is less than 5%. Note that since optical load decreases detector responsivity, this ratio is an overestimate of the expected cross-coupling between two adjacent optically loaded detectors.

5.6.3 Polarization response

The polarization response of two resonators with orthogonally aligned optically coupled absorbers is shown in Figure 5.12. These measurements were obtained by directing a hot blackbody source onto the detectors through the cryostat vacuum window, with a rotating polarizing grid between the source and detectors. For each polarization angle, the detectors' resonant frequencies were measured with and without the source. The fractional shift in resonant frequency as a function of source polarization angle is fit with the model [175]:

$$\frac{\Delta f_0}{f_0}(\theta) = A\Big[\cos(2(\theta - \phi)) + \frac{1+\epsilon}{1-\epsilon}\Big]. \tag{5.21}$$

These fits are represented by the solid lines in Figure 5.12, and are rescaled to show frequency shift as a percentage of the maximum response. Here ϵ is the 'cross-polarization parameter,' which corresponds to the minimum of each curve in Figure 5.12. The other fit parameters, A and ϕ are an amplitude and phase shift respectively. For both detectors, the cross-polarization was found to be about 10%. This is higher than the simulated value of 3%, however, the simulation includes only the waveguide, RF choke, and detectors. The simple conical feedhorn used in this setup is expected to contribute about 4% to the cross-polarization [176]. Further contributions may come from errors in manually-adjusted polarization grid angle, or from stray reflections in the fully on-axis measurement setup.

5.7 Conclusions and Additional Work

Dark testing of a 63-pixel array of these CPW-coupled resonators produces results consistent with the science requirements for SPT-3G+. Inductor quality factors are well above our $Q_i = 10^5$ multiplexing target, and the transition temperature T_c and kinetic inductance fraction α_k are tightly distributed around expected values that meet our requirements. Testing of optically coupled pixels from both the microstrip and CPW feedline devices show good agreement in both the measured optical band and optical efficiency, with both detectors having effectively identical bands and an optical efficiency of $\sim 70\%$. The measured bands agree with predictions from simulations, except at the lower band edge, where the detector response is less than expected. The polarization of the CPW-coupled optical pixels was also measured, with cross-polarization response of $\sim 10\%$ for both polarities. Dark detectors on the CPW chip were found to have less than 5% of the frequency shift of their optically loaded neighbors within the 5-10 pW range of optical loading. The majority of the dark spectral response was seen to come from the lower edge of the band, just past the waveguide cutoff. Further simulations are underway to understand and mitigate this effect, potentially by making slight adjustments to the integrating cavity design or by adding dedicated structures to the pixel to absorb stray photons.

Scaling up to triangular submodules

My goal for this project was to repeat the optical testing described in this chapter on a full-scale triangular submodule. This would demonstrate that the 220 GHz detector arrays are suitable for eventual deployment. I first designed and fabricated a sparsely-populated triangle as a test of the feedline design. The feedline of this device functioned as intended, and did not possess any unintentional resonant features in the intended readout band. I then designed a second triangle wafer whose pixels were spaced in clusters, with the intention of having the central pixel of each cluster coupled to a feedhorn. The feedhorn-coupled pixels could be used to repeat the optical tests, and the neighboring dark pixels could be monitored to measure optical crosstalk. I fabricated a dark version of this sparse triangle, shown in the upper left panel of Figure 5.13. The majority of resonators on this wafer were of high internal quality, as seen in the upper right panel of Figure 5.13, and the resonators were distributed as designed into six banks depending on the polarization and position of each resonator, as seen in the lower panel of Figure 5.13. Dark noise performance was also reasonable; in fact the plots in Figure 5.5 are created from a detector on this wafer.

Having verified this design, I fabricated a second copy of the mask on a silicon-on-insulator (SOI) wafer with a 100 μm device layer. The DRIE process to machine the silicon backshort proved to be challenging, and the wafer was sent to Argonne and then to Cardiff over the course of several months. At the same time, the specialized sample box required for the optical tests was designed and fabricated. When both the box and the wafer arrived, there was only time for a single cooldown. Tragically, I discovered upon cooling down that while feedline transmission was excellent, not a single resonance had yielded. After ruling out concerns related to the sample mounting and box temperature, I was forced to conclude that the issue was within the inductor material. Consultation with Argonne has led me to the conclusion that the long pre-sputtering times I have been using to avoid tantalum contamination of the aluminum source have over time depleted the aluminum source such that

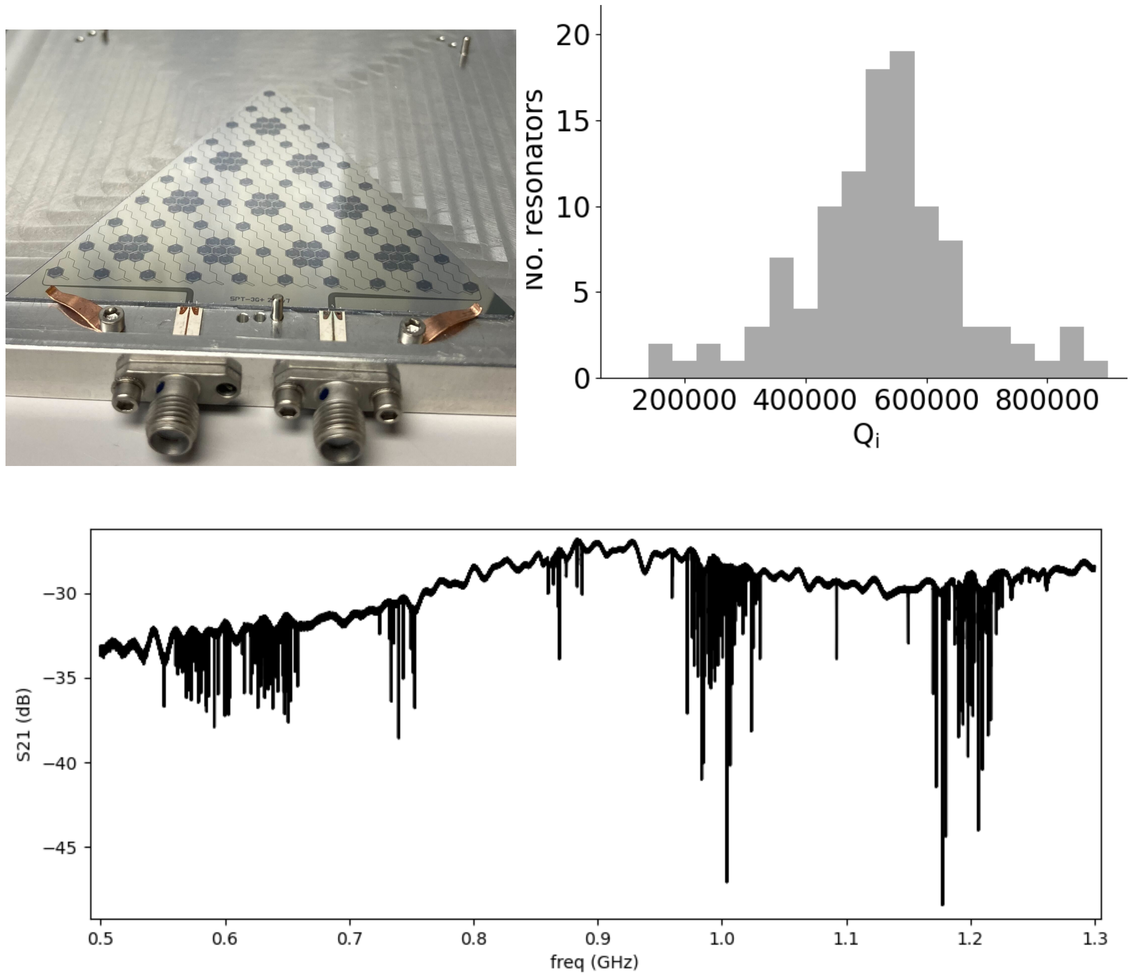

Figure 5.13: Dark performance of a 220 GHz triangle designed to serve as a prototype for an eventual array-scale optical test. For the most part, quality factors and resonant frequency scheduling matched the design. This mask was re-fabricated on a SOI wafer, but that device did not yield resonators due to likely material contamination.

sputtered material now contains particles of the iron crucible in which the source is held. As time did not permit fabrication and testing of a second optical wafer, the full submodule optical data is not included in this thesis.

However, all is not lost. Due to the promising dark performance of my initial triangular submodule, it seems likely that good array-scale optical data could be measured were this mask to be fabricated on a SOI wafer using high-quality aluminum. Plans are already underway to do this fabrication at Cardiff, and to test the resulting wafer optically either at Cardiff or in Chicago. I plan to combine the data from these optical tests with the dark data from my original wafer to produce a publication that describes the array-scale performance of the 220 GHz detectors.

Chapter 6

Conclusions

In this thesis, I have presented a collection of forecasting, analysis, and instrumentation work related to the science case and hardware development of the SPT-3G+ camera. In Chapter 2, I forecasted the expected sensitivity of SPT-3G+ to the Rayleigh scattering signal, and found that, in combination with SPT-3G and Planck data, the expected detection significance is $\sim 1.6\,\sigma$. An important conclusion of that work was that for SPT, the CIB is the major foreground inhibiting higher detection significance of the Rayleigh Scattering signal. This motivated me to look more closely at the CIB as both a foreground and an astrophysical signal. In Chapter 3 I attempted to characterize the CIB using SPT-3G data. I used an existing physically motivated model that relates CIB emission to an underlying star-formation rate. Instead of fitting the CIB autospectrum, I fit the CIB x CMB lensing spectrum, which is less susceptible to systematic bias from contaminants such as galactic dust. The 220 GHz CMB temperature and lensing maps used for this project came from the 2019-2020 SPT-3G observation seasons. Unfortuately, the model was unconstrained by SPT-3G, and even the addition of Planck data did not constrain the model. Forecasts for SPT-3G+ showed the same lack of contstraining ability, despite the high-sensitivity of SPT-3G+ high-frequency bands. Constraining the model required adding in independent cosmic star-formation rate density observations. Because many parameters in this model are co-degenerate, future work entails fixing some of the parameters to physically and literature-motivated values and repeating this analysis. Regardless, this analysis will need to be repeated on finalized versions of the 2019-2020 220 GHz and lensing maps. This analysis also highlights the need for improved CIB models as experiments seek detections of small-amplitude secondary anisotropies for which the CIB is a significant foreground.

The instrumentation component of my PhD concerned the development of microwave kinetic inductance detectors (MKIDs) for SPT-3G+. In Chapter 4 I describe my work designing and fabricating feedhorn-coupled direct absorbing MKIDs for the 220, 285, and 345 GHz bands of SPT-3G+. The design evolved from small chips with a few microstrip-coupled pixels to deployment-scale triangular submodules with pixels packed 2.2 mm apart. In Chapter 5 I describe the laboratory testing of the 220 GHz SPT-3G+ detectors. The detectors performed well from both a microwave and an optical perspective. Resonances were of the intended width and quality, and were located within the intended microwave readout bandwidth. They showed photon-dominated performance under a representative optical load, indicating that they possess the required sensitivity for use on the SPT-3G+ focal plane. They also showed roughly the expected spectral response and response to the polarization angle of incident light, with some small deviations that still need to be addressed. I began scaling up to triangular submodule fabrication, and fabricated submodules with various fill factors that I tested dark. One of my goals had been to repeat the optical testing on a full triangular submodule. Due to a combination of timing constraints and a failed fabrication run, this final optical test did not take place, and because I am immenintly deploying to the South Pole for a year, I will not be able to repeat the fabrication. However, efforts are underway to repeat the optical fabrication at Cardiff University, and collaborators at the University of Chicago have agreed to perform the optical tests. I plan to remotely analyze the data from this testing and to combine it with existing dark triangular submodule data to thoroughly characterize the microwave and optical properties of the submodule design.

This concludes my PhD thesis. My projects, though not particularly cohesive, exposed me to many different aspects of the early stages of SPT-3G+ develpment. The combination of forecasting, analysis and instrumentation work along with observing the proposal writing process has helped me understand what is needed to create a scientific instrument and to process its data into scientific results. I have also gained practical skills in computing, nanofabrication, vacuum systems, cryogenics, and RF electronics, and have particularly enjoyed the operation and maintenence of the dilution refrigerator at the University of Chicago. These skills will benefit me in my immediate future at the South Pole, and will remain valuable over the course of my scientific career. I am grateful to have done work in which I find meaning, and to the many people who have enabled me to do so.

Appendix A

Model details for the Rayleigh scattering project

A.1 Noise model parameters

A.1.1 Instrument and atmospheric parameters

Table A1 lists the values of beam size (FWHM), map depth, and atmospheric model parameters (ℓ_{knee} and α) for each band of each ground-based instrument considered in this analysis. Assumed full-survey map depths for SPT-3G are taken from [?]; map depths for SPT-3G+ are calculated from design detector noise values and assuming four years of observation with efficiency similar to SPT-3G. Atmospheric parameter values for SPT-3G are estimated from on-sky data; values for SPT-3G+ at 220 GHz are assumed to be identical to SPT-3G, while numbers for higher-frequency bands are scaled using the measured levels of precipitable water vapor (PWV) at the South Pole integrated over the design SPT-3G+ bands.

Sources for other experiments' values are given in the caption to Table A1. Map depth values for Planck, though not included in Table A1, are taken from Table 4 of [96]. Some experiments use a different atmospheric model in which ℓ_{knee} is fixed and $N_{\mathrm{atmos}} = N_{\mathrm{red}}(\frac{\ell_{\mathrm{knee}}}{\ell})^{\alpha} + N_{\mathrm{white}}$, where N_{white} is the detector noise. For these experiments, we convert their parameters to the equivalent ones in our model,

Instrument	Band (GHz)	Beam (arcmin)	T Map Depth (μK-arcmin)	E Map Depth (μK-arcmin)	$\ell_{\mathrm{knee},T}$	α_T	$\ell_{\mathrm{knee},E}$	α_E
SPT-3G	95	1.7	2.7	3.8	1200	-4.2	200	-2.6
($f_{\mathrm{sky}} = 0.03$)	150	1.2	2.2	3.1	1900	-4.1		-2.2
	220	1.1	8.8	12.4	2100	-3.9		-2.2
SPT-3G+	225	0.8	2.9	4.1	2100	-3.9	200	-2.2
($f_{\mathrm{sky}} = 0.03$)	285	0.6	5.6	7.9				
	345	0.5	28	39.6	2600			
Simons Obs.	27	7.4	52	74	400	-3.5	700	-1.4
($f_{\mathrm{sky}} = 0.40$)	39	5.1	27	38				
	93	2.2	5.8	8.2	1900			
	145	1.4	6.5	9.2	3900			
	225	1.0	15	21.2	6700			
	280	0.9	37	52.3	6800			
CCAT-p	220	1.0	15	21.2	7300	-3.5	700	-1.4
($f_{\mathrm{sky}} = 0.50$)	280	0.8	28	39.6	8800			
	350	0.6	107	151	10600			
	410	0.5	407	576	8200			
	850	0.3	6.8×10^5	9.6×10^5	4600			
CMB-S4-Wide	27	7.4	21.5	30.4	400	-3.5	700	-1.4
(Chilean LAT)	39	5.1	11.9	16.8				
	93	2.2	1.9	2.7	1900			
	145	1.2	2.1	2.9	3900			
($f_{\mathrm{sky}} = 0.65$)	225	0.9	6.9	9.7	6700			
	278	0.7	17	23.8	6800			
CMB-S4-Deep	20	11.4	8.7	12.3	400	-4.2	150	-2.7
(S. Pole TMA)	27	8.4	5.1	7.1				
($f_{\mathrm{sky}} = 0.03$)	39	5.8	3.3	4.6				
	95	2.5	0.5	0.71	1200			-2.6
	150	1.6	0.5	0.66	1900	-4.1	200	-2.2
	220	1.1	1.5	2.05	2100	-3.9		
	285	1.0	3.4	4.85		-3.9		

Table A1: Instrument and atmospheric parameters for all ground-based experiments considered in this analysis. N_{det} in Section 2.4 is defined as the square of the map depth. SPT-3G map depth values come from [?], while SPT-3G+ values are calculated using design detector noise and assuming four years of observation with similar efficiency to SPT-3G. SPT-3G atmospheric noise parameters come from on-sky measurements, and SPT-3G+ values are scaled from these using PWV values in each band. CCAT-prime values come from [74]. CMB-S4 Deep map depths, bands, and beams are taken from the CMB-S4 wiki.[1] Since atmospheric parameters on that wiki were not updated at the time of writing, CMB-S4 Deep atmospheric parameters were assumed to be identical to those of the corresponding SPT bands. Official CMB-S4 Wide values were also not publicly available at the time of writing, so values were taken from Table VIII of [84]. Simons Observatory map depths, bands, and beams come from [79], and atmospheric parameters were assumed to be identical to those of the corresponding CMB-S4 Wide bands. Since CMB-S4 Wide and CCAT-prime use a different atmospheric model to the one described in Section 2.4, parameters have been converted to ones that produce equivalent atmospheric noise in our model. Planck values for map depth, though not included in Table A1, are taken from Table 4 of [96].

Foreground	Parameter	Deep TT	Wide TT	Deep EE	Wide EE
Galactic	$A_{\text{dust},145}$ [μK^2]	3.253	1168	0.048	1.161
	$\alpha_{\text{dust},145}$	-0.400	-0.246	-0.400	-0.371
	$A_{\text{synch},93}$ [μK^2]	0.005	0.055	0.001	0.010
	$\alpha_{\text{synch},93}$	-0.4			
Extragalactic	$A_{\text{tSZ},150}$ [μK^2]	4		N/A	
	$\alpha_{\text{tSZ},150}$	0			
	$A_{\text{Cl-lo}z\text{,220}}$ [μK^2]	40			
	$\alpha_{\text{Cl-lo}z\text{,220}}$	0.8			
	$A_{\text{Cl-hi}z\text{,220}}$ [μK^2]	20			
	$\alpha_{\text{Cl-hi}z\text{,220}}$	0.8			
	$A_{\text{Po-lo}z\text{,220}}$ [μK^2]	20			
	$\alpha_{\text{Po-lo}z\text{,220}}$	2			
	$A_{\text{Po-hi}z\text{,220}}$ [μK^2]	50			
	$\alpha_{\text{Po-hi}z\text{,220}}$	2			
	$A_{\text{Radio},150}$ [μK^2]	0.17		8×10^{-5}	
	$\alpha_{\text{Radio},150}$	2			

Table A2: Anchor values for galactic and extragalactic foreground amplitudes and power law slopes. Galactic foregrounds include galactic dust and galactic synchrotron radiation, while extragalactic foregrounds include the thermal Sunyaev Zel'dovich effect, the four-component CIB model presented in Section IV.D, and extragalactic radio sources. The models for each of these components are detailed in § 2.4.3 and § 2.4.4. These values are scaled to other frequency bands as described in Appendix A.1.2 and A.1.3.

using:

$$\ell_{\text{knee}} = \ell_{\text{fixed}} \left(\frac{N_{\text{red}}}{N_{\text{white}}} \right)^{\frac{1}{\alpha}}, \tag{A.1}$$

where ℓ_{fixed} is the fixed value of ℓ_{knee} used in their atmospheric model.

A.1.2 Galactic dust and synchrotron amplitudes

We rely on the publicly available Python Sky Model (pySM) simulations [88, 89] developed based on the *Planck* Sky Model code [177] for galactic foregrounds. The approach is similar to the one followed in [87]. For both the Deep and Wide surveys, we estimate the power spectrum of the galactic dust and synchrotron signals in pySM, both in temperature C_ℓ^{TT} and polarization C_ℓ^{EE}. Since $C_\ell^{TE} = 0$ in pySM, we set the TE correlation using the geometric mean of the two signals as $C_\ell^{TE} = \rho_{TE}^{\text{gal}} \sqrt{C_\ell^{TT} C_\ell^{EE}}$ with $\rho_{TE}^{\text{gal}} = 0.35$ for all galactic foregrounds [178]. We use the pySM `SO_d0` dust and `SO_s0` synchrotron models in this work.

We fit a power law of the form $D_\ell = A \left(\frac{\ell}{80} \right)^\alpha$ to determine the dust and synchrotron amplitudes at our reference frequencies of 145 and 93 GHz, respectively, and we scale those amplitudes to other bands as:

$$C_{\ell,\nu_1\nu_2} = C_{\ell,\nu_0\nu_0}\ \epsilon_{\nu_1,\nu_2}\ \frac{\eta_{\nu_1}\eta_{\nu_2}}{\eta_{\nu_0}\eta_{\nu_0}}, \tag{A.2}$$

where $\nu_0 = 145$ or 93 GHz, and ν_1, ν_2 correspond to frequency bands listed in Table A1. The terms ϵ_{ν_1} and ϵ_{ν_2} in Eq.(A.2) encode the conversion of radiance to equivalent fluctuation temperature of a 2.7K blackbody:

$$\epsilon_{\nu_1,\nu_2} = \left. \frac{\frac{dB_{\nu_0}}{dT}\frac{dB_{\nu_0}}{dT}}{\frac{dB_{\nu_1}}{dT}\frac{dB_{\nu_2}}{dT}} \right|_{T=T_{\text{CMB}}}, \tag{A.3}$$

while η_ν represents the spectral energy distribution of either dust or synchrotron.

For dust we use a modified blackbody of the form

$$\eta_\nu = \nu^{\beta_d}\ B_\nu(T_d), \tag{A.4}$$

with $\beta_d = 1.6$, and $T_d = 19.6$ K, while for synchrotron we assume a power law in frequency

$$\eta_\nu = \nu^{2+\beta_s} \tag{A.5}$$

with $\beta_s = -3.10$.

For simplicity, we assume in the estimation of dust and synchrotron amplitudes that the observing regions for the three "wide" experiments (SO, CCAT-prime, and CMB-S4 Wide) are identical and equal to the 57% of sky available between decl. 68° and 25° and with galactic latitude $b > 10°$. This means that the assumed galactic foreground amplitudes will be slightly pessimistic for SO and CCAT-prime and slightly optimistic for CMB-S4 Wide. Similarly, we assume the observing regions for the two "deep" experiments (SPT-3G/3G+ and CMB-S4 Deep) are identical and equal to the SPT-3G region defined by $-50° <$ R.A. $< 50°$ and $-70° <$ decl. $< -42°$. The galactic foreground parameters derived from this procedure are given in Table A2.

A.1.3 Extragalactic foreground amplitudes

Like the galactic dust model, both the tSZ and CIB models are defined at fiducial frequencies, and the amplitudes are scaled to other frequency bands. The CIB clustered and Poisson amplitudes are defined in Section III.D at 220 GHz and are scaled in exactly the same way as the galactic dust amplitudes above, but with

$$\eta_\nu = B\left(\nu, \frac{T_{\mathrm{CIB}}}{1+z}\right)\nu^2, \tag{A.6}$$

where $T_{\mathrm{CIB}} = 30$K, and z is one of $z_{\mathrm{low}} = 0.5$ or $z_{\mathrm{hi}} = 3.5$ corresponding to the low and high redshift CIB components respectively. The clustered and Poisson CIB components are considered unpolarized.

The tSZ amplitude is defined in Section III.D at 150 GHz and is scaled to other bands using the tSZ spectral shape relative to $dB(\nu)/dT_{\mathrm{CMB}}$:

$$f(\nu)_{\mathrm{tSZ}} = x\frac{e^x+1}{e^x-1} - 4, \tag{A.7}$$

where $x = \nu/56.8$ GHz. The tSZ amplitude at frequency ν is:

$$A(\nu)_{\mathrm{tSZ}} = \frac{A_{0,\mathrm{tSZ}}}{f(\nu)^2_{SZ}}. \tag{A.8}$$

We assume the tSZ is unpolarized, and thus all tSZ amplitudes for polarization are zero. Finally, the extragalactic radio source amplitude, also defined in Section III.D scales to other frequency bands in a similar way to Equation A.5, but with the $2+\beta_s$ exponent replaced by -0.7 (e.g., [179]). Extragalactic radio sources are considered 3% polarized following [95], [93], so that extragalactic radio amplitudes for E polarization are 4.5×10^{-4} times the extragalactic radio amplitudes for temperature.

Appendix B

FTS derivation

The following derivation follows [174], but I modified the wording and variable names to make it flow with this thesis. The mirror is swept at some velocity v, and the ADC is sampling at some sample rate f_s. Then the path length difference between consecutive samples is $\delta = 2v/f_s$. The factor of 2 is due to the fact that light has to travel twice the physical distance traveled by the mirror. For a monochromatic source with wavelength λ, the recombined wavefunction is the sum of the original and phase-shifted waves:

$$w(x, k) = E(k)e^{2\pi jkx} + E(k)e^{2\pi jk(x-\delta)} = E(k)\left(1 + e^{-jk\delta}\right)e^{jkx} \tag{B.1}$$

where $k = 2\pi/\lambda$ is the wavenumber. For a polychromatic source, the wavefunction is an integrated over all wavenumbers:

$$w(x) = \int_{-\infty}^{\infty} w(x, k)dk = \int_{-\infty}^{\infty} E(k, \delta)e^{jkx}dk, \tag{B.2}$$

where $E(k, \delta) = E(k)e^{-2\pi jk\delta}$ is the complex amplitude of the recombined wave. The local intensity of the polychromatic wave (assuming electrical permittivity, refractive index, and speed of light are all 1 for simplicity) is the integral of the square norm of the amplitude of the wave:

$$I(\delta) = \frac{1}{\bar{k}} \int_{-\infty}^{\infty} E(k,\delta) E^*(k,\delta) dk = \frac{1}{\bar{k}} \int_{-\infty}^{\infty} 2E(k)^2 [1 + \cos(k\delta)] dk \tag{B.3}$$

Use the definition of cosine to get the last step. Notice that for $\delta = 0$:

$$\frac{1}{2} I(0) = \frac{1}{2\bar{k}} \int_{-\infty}^{\infty} 4E(k)^2 dk = \frac{1}{\bar{k}} \int_{-\infty}^{\infty} 2E(k)^2 dk. \tag{B.4}$$

So Equation B.3 can be rewritten by substituting for the first term:

$$I(\delta) = \frac{1}{2} I(0) + \frac{1}{\bar{k}} \int_{-\infty}^{\infty} 2E(k)^2 \cos(k\delta) dk \tag{B.5}$$

At this point, it is useful to note a few things. First, the expression $[I(\delta) - \frac{1}{2}I(0)]$ is the intensity as a function of path length difference compared to the mean intensity when the path length difference is zero. This is the interferogram if the detector is tuned at the white-light fringe. Second, the Fourier transform $\mathscr{F}(k)$ of an even function $f(x) = f(-x)$ looks exactly like that final term:

$$\mathscr{F}(k) = \int_{-\infty}^{\infty} f(x) e^{-2\pi jkx} dx = \int_{0}^{\infty} f(x) \left[e^{2\pi jkx} + e^{-2\pi jkx} \right] dx = 2 \int_{0}^{\infty} f(x) \cos(2\pi kx) dx \tag{B.6}$$

The same is true for the inverse Fourier transform. Putting these two pieces of information together, Equation $B.5$ is the statement that the interferogram is the inverse Fourier transform of the square-amplitude as a function of frequency, (the power spectrum). Applying the Fourier transform gives:

$$\mathscr{P}(k) = \frac{1}{\bar{k}} E(k)^2 = 2 \int_{0}^{\infty} [I(\delta) - \frac{1}{2} I(0)] \cos(2\pi k\delta) d\delta = \int_{-\infty}^{\infty} [I(\delta) - \frac{1}{2} I(0)] \cos(2\pi k\delta) d\delta, \tag{B.7}$$

which is Equation 5.20.

Bibliography

[1] R. H. Dicke, P. J. E. Peebles, P. G. Roll, and D. T. Wilkinson. Cosmic Black-Body Radiation. , 142:414–419, July 1965. doi: 10.1086/148306.

[2] Wayne Hu and Scott Dodelson. Cosmic microwave background anisotropies. *Annual Review of Astronomy and Astrophysics*, 40(1):171–216, September 2002. ISSN 1545-4282. doi: 10.1146/annurev.astro.40.060401.093926. URL `http://dx.doi.org/10.1146/annurev.astro.40.060401.093926`.

[3] Wayne Hu and Martin White. A cmb polarization primer. *New Astronomy*, 2(4):323–344, October 1997. ISSN 1384-1076. doi: 10.1016/s1384-1076(97) 00022-5. URL `http://dx.doi.org/10.1016/S1384-1076(97)00022-5`.

[4] A. A. Penzias and R. W. Wilson. A Measurement of Excess Antenna Temperature at 4080 Mc/s. , 142:419–421, July 1965. doi: 10.1086/148307.

[5] G. F. Smoot, C. L. Bennett, A. Kogut, E. L. Wright, J. Aymon, N. W. Boggess, E. S. Cheng, G. de Amici, S. Gulkis, M. G. Hauser, G. Hinshaw, P. D. Jackson, M. Janssen, E. Kaita, T. Kelsall, P. Keegstra, C. Lineweaver, K. Loewenstein, P. Lubin, J. Mather, S. S. Meyer, S. H. Moseley, T. Murdock, L. Rokke, R. F. Silverberg, L. Tenorio, R. Weiss, and D. T. Wilkinson. Structure in the COBE Differential Microwave Radiometer First-Year Maps. , 396:L1, September 1992. doi: 10.1086/186504.

[6] J. C. Mather, E. S. Cheng, D. A. Cottingham, Jr. Eplee, R. E., D. J. Fixsen, T. Hewagama, R. B. Isaacman, K. A. Jensen, S. S. Meyer, P. D. Noerdlinger, S. M. Read, L. P. Rosen, R. A. Shafer, E. L. Wright, C. L. Bennett, N. W. Boggess, M. G. Hauser, T. Kelsall, Jr. Moseley, S. H., R. F. Silverberg, G. F. Smoot, R. Weiss, and D. T. Wilkinson. Measurement of the Cosmic Microwave Background Spectrum by the COBE FIRAS Instrument. , 420:439, January 1994. doi: 10.1086/173574.

[7] J. M. Kovac, E. M. Leitch, C. Pryke, J. E. Carlstrom, N. W. Halverson, and W. L. Holzapfel. Detection of polarization in the cosmic microwave background using dasi. *Nature*, 420(6917):772–787, December 2002. ISSN 1476-4687. doi: 10.1038/nature01269. URL `http://dx.doi.org/10.1038/nature01269`.

[8] D. Hanson, S. Hoover, A. Crites, P. A. R. Ade, K. A. Aird, J. E. Austermann, J. A. Beall, A. N. Bender, B. A. Benson, L. E. Bleem, J. J. Bock, J. E. Carlstrom, C. L. Chang, H. C. Chiang, H-M. Cho, A. Conley, T. M. Crawford, T. de Haan, M. A. Dobbs, W. Everett, J. Gallicchio, J. Gao, E. M. George, N. W. Halverson, N. Harrington, J. W. Henning, G. C. Hilton, G. P.

Holder, W. L. Holzapfel, J. D. Hrubes, N. Huang, J. Hubmayr, K. D. Irwin, R. Keisler, L. Knox, A. T. Lee, E. Leitch, D. Li, C. Liang, D. Luong-Van, G. Marsden, J. J. McMahon, J. Mehl, S. S. Meyer, L. Mocanu, T. E. Montroy, T. Natoli, J. P. Nibarger, V. Novosad, S. Padin, C. Pryke, C. L. Reichardt, J. E. Ruhl, B. R. Saliwanchik, J. T. Sayre, K. K. Schaffer, B. Schulz, G. Smecher, A. A. Stark, K. T. Story, C. Tucker, K. Vanderlinde, J. D. Vieira, M. P. Viero, G. Wang, V. Yefremenko, O. Zahn, and M. Zemcov. Detection of¡mml:math xmlns:mml="http://www.w3.org/1998/math/mathml" display="inline"¿¡mml:mi¿b¡/mml:mi¿¡/mml:math¿-mode polarization in the cosmic microwave background with data from the south pole telescope. *Physical Review Letters*, 111(14), September 2013. ISSN 1079-7114. doi: 10.1103/physrevlett.111.141301. URL `http://dx.doi.org/10.1103/PhysRevLett.111.141301`.

[9] et.al. Bennett, C. L. Nine-year Wilkinson Microwave Anisotropy Probe (WMAP) Observations: Final Maps and Results. , 2012.

[10] Y. Akrami, M. Ashdown, J. Aumont, C. Baccigalupi, M. Ballardini, A. J. Banday, R. B. Barreiro, N. Bartolo, S. Basak, K. Benabed, J.-P. Bernard, M. Bersanelli, P. Bielewicz, J. R. Bond, J. Borrill, F. R. Bouchet, F. Boulanger, A. Bracco, M. Bucher, C. Burigana, E. Calabrese, J.-F. Cardoso, J. Carron, H. C. Chiang, C. Combet, B. P. Crill, P. de Bernardis, G. de Zotti, J. Delabrouille, J.-M. Delouis, E. Di Valentino, C. Dickinson, J. M. Diego, A. Ducout, X. Dupac, G. Efstathiou, F. Elsner, T. A. Enßlin, E. Falgarone, Y. Fantaye, K. Ferrière, F. Finelli, F. Forastieri, M. Frailis, A. A. Fraisse, E. Franceschi, A. Frolov, S. Galeotta, S. Galli, K. Ganga, R. T. Génova-Santos, T. Ghosh, J. González-Nuevo, K. M. Górski, A. Gruppuso, J. E. Gudmundsson, V. Guillet, W. Handley, F. K. Hansen, D. Herranz, Z. Huang, A. H. Jaffe, W. C. Jones, E. Keihänen, R. Keskitalo, K. Kiiveri, J. Kim, N. Krachmalnicoff, M. Kunz, H. Kurki-Suonio, J.-M. Lamarre, A. Lasenby, M. Le Jeune, F. Levrier, M. Liguori, P. B. Lilje, V. Lindholm, M. López-Caniego, P. M. Lubin, Y.-Z. Ma, J. F. Macías-Pérez, G. Maggio, D. Maino, N. Mandolesi, A. Mangilli, P. G. Martin, E. Martínez-González, S. Matarrese, J. D. McEwen, P. R. Meinhold, A. Melchiorri, M. Migliaccio, M.-A. Miville-Deschênes, D. Molinari, A. Moneti, L. Montier, G. Morgante, P. Natoli, L. Pagano, D. Paoletti, V. Pettorino, F. Piacentini, G. Polenta, J.-L. Puget, J. P. Rachen, M. Reinecke, M. Remazeilles, A. Renzi, G. Rocha, C. Rosset, G. Roudier, J. A. Rubiño-Martín, B. Ruiz-Granados, L. Salvati, M. Sandri, M. Savelainen, D. Scott, J. D. Soler, L. D. Spencer, J. A. Tauber, D. Tavagnacco, L. Toffolatti, M. Tomasi, T. Trombetti, J. Valiviita, F. Vansyngel, B. Van Tent, P. Vielva, F. Villa, N. Vittorio, I. K. Wehus, A. Zacchei, and A. Zonca. Planck 2018 results. *Astronomy Astrophysics*, 641: A11, Sep 2020. ISSN 1432-0746. doi: 10.1051/0004-6361/201832618. URL `http://dx.doi.org/10.1051/0004-6361/201832618`.

[11] A. H. Guth and S. Y. Pi. Fluctuations in the New Inflationary Universe. , 49 (15):1110–1113, October 1982. doi: 10.1103/PhysRevLett.49.1110.

[12] Blake Crouch, Megan McDonnell, Jacquelyn Ben-Zekry, and Ihuoma Ofordire. Dark Matter. *Apple television*, 2024.

[13] Takemi Okamoto and Wayne Hu. Cosmic microwave background lensing reconstruction on the full sky. *Physical Review D*, 67(8), April 2003. ISSN 1089-4918. doi: 10.1103/physrevd.67.083002. URL `http://dx.doi.org/10.1103/PhysRevD.67.083002`.

[14] S. Raghunathan, P. A. R. Ade, A. J. Anderson, B. Ansarinejad, M. Archipley, J. E. Austermann, L. Balkenhol, J. A. Beall, K. Benabed, A. N. Bender, B. A. Benson, F. Bianchini, L. E. Bleem, J. Bock, F. R. Bouchet, L. Bryant, E. Camphuis, J. E. Carlstrom, T. W. Cecil, C. L. Chang, P. Chaubal, H. C. Chiang, P. M. Chichura, T. L. Chou, R. Citron, A. Coerver, T. M. Crawford, A. T. Crites, A. Cukierman, C. Daley, K. R. Dibert, M. A. Dobbs, A. Doussot, D. Dutcher, W. Everett, C. Feng, K. R. Ferguson, K. Fichman, A. Foster, S. Galli, J. Gallicchio, A. E. Gambrel, R. W. Gardner, F. Ge, E. M. George, N. Goeckner-Wald, R. Gualtieri, F. Guidi, S. Guns, N. Gupta, T. de Haan, N. W. Halverson, E. Hivon, G. P. Holder, W. L. Holzapfel, J. C. Hood, J. D. Hrubes, A. Hryciuk, N. Huang, J. Hubmayr, K. D. Irwin, F. Kéruzoré, A. R. Khalife, L. Knox, M. Korman, K. Kornoelje, C. L. Kuo, A. T. Lee, K. Levy, D. Li, A. E. Lowitz, C. Lu, A. Maniyar, E. S. Martsen, J. J. McMahon, F. Menanteau, M. Millea, J. Montgomery, C. Corbett Moran, Y. Nakato, T. Natoli, J. P. Nibarger, G. I. Noble, V. Novosad, Y. Omori, S. Padin, Z. Pan, P. Paschos, S. Patil, K. A. Phadke, K. Prabhu, C. Pryke, W. Quan, M. Rahimi, A. Rahlin, C. L. Reichardt, M. Rouble, J. E. Ruhl, B. R. Saliwanchik, K. K. Schaffer, E. Schiappucci, C. Sievers, G. Smecher, J. A. Sobrin, A. A. Stark, J. Stephen, A. Suzuki, C. Tandoi, K. L. Thompson, B. Thorne, C. Trendafilova, C. Tucker, C. Umilta, T. Veach, J. D. Vieira, M. P. Viero, Y. Wan, G. Wang, N. Whitehorn, W. L. K. Wu, V. Yefremenko, M. R. Young, J. A. Zebrowski, and M. Zemcov. First constraints on the epoch of reionization using the non-gaussianity of the kinematic sunyaev-zel'dovich effect from the south pole telescope and *herschel*-spire observations, 2024. URL `https://arxiv.org/abs/2403.02337`.

[15] Marcelo A. Alvarez, Simone Ferraro, J. Colin Hill, Renée Hložek, and Margaret Ikape. Mitigating the optical depth degeneracy using the kinematic sunyaev-zel'dovich effect with cmb-s4 data. *Physical Review D*, 103(6), Mar 2021. ISSN 2470-0029. doi: 10.1103/physrevd.103.063518. URL `http://dx.doi.org/10.1103/PhysRevD.103.063518`.

[16] Kendrick M. Smith and Simone Ferraro. Detecting patchy reionization in the cosmic microwave background. *Phys. Rev. Lett.*, 119:021301, Jul 2017. doi: 10.1103/PhysRevLett.119.021301. URL `https://link.aps.org/doi/10.1103/PhysRevLett.119.021301`.

[17] M Birkinshaw. The sunyaev–zel'dovich effect. *Physics Reports*, 310(2–3): 97–195, March 1999. ISSN 0370-1573. doi: 10.1016/s0370-1573(98)00080-5. URL `http://dx.doi.org/10.1016/S0370-1573(98)00080-5`.

[18] L. E. Bleem, B. Stalder, T. de Haan, K. A. Aird, S. W. Allen, D. E. Applegate, M. L. N. Ashby, M. Bautz, M. Bayliss, B. A. Benson, S. Bocquet, M. Brodwin, J. E. Carlstrom, C. L. Chang, I. Chiu, H. M. Cho, A. Clocchiatti, T. M. Crawford, A. T. Crites, S. Desai, J. P. Dietrich, M. A. Dobbs, R. J. Foley,

W. R. Forman, E. M. George, M. D. Gladders, A. H. Gonzalez, N. W. Halverson, C. Hennig, H. Hoekstra, G. P. Holder, W. L. Holzapfel, J. D. Hrubes, C. Jones, R. Keisler, L. Knox, A. T. Lee, E. M. Leitch, J. Liu, M. Lueker, D. Luong-Van, A. Mantz, D. P. Marrone, M. McDonald, J. J. McMahon, S. S. Meyer, L. Mocanu, J. J. Mohr, S. S. Murray, S. Padin, C. Pryke, C. L. Reichardt, A. Rest, J. Ruel, J. E. Ruhl, B. R. Saliwanchik, A. Saro, J. T. Sayre, K. K. Schaffer, T. Schrabback, E. Shirokoff, J. Song, H. G. Spieler, S. A. Stanford, Z. Staniszewski, A. A. Stark, K. T. Story, C. W. Stubbs, K. Vanderlinde, J. D. Vieira, A. Vikhlinin, R. Williamson, O. Zahn, and A. Zenteno. Galaxy clusters discovered via the sunyaev-zel'dovich effect in the 2500-square-degree spt-sz survey. *The Astrophysical Journal Supplement Series*, 216(2):27, January 2015. ISSN 1538-4365. doi: 10.1088/0067-0049/216/2/27. URL `http://dx.doi.org/10.1088/0067-0049/216/2/27`.

[19] Antony Lewis. Rayleigh scattering: blue sky thinking for future cmb observations. *Journal of Cosmology and Astroparticle Physics*, 2013(08):053–053, Aug 2013. ISSN 1475-7516. doi: 10.1088/1475-7516/2013/08/053. URL `http://dx.doi.org/10.1088/1475-7516/2013/08/053`.

[20] Elham Alipour, Kris Sigurdson, and Christopher M. Hirata. Effects of rayleigh scattering on the cmb and cosmic structure. *Physical Review D*, 91(8), Apr 2015. ISSN 1550-2368. doi: 10.1103/physrevd.91.083520. URL `http://dx.doi.org/10.1103/PhysRevD.91.083520`.

[21] H. Dole, G. Lagache, J. L. Puget, K. I. Caputi, N. Fernández-Conde, E. Le Floc'h, C. Papovich, P. G. Pérez-González, G. H. Rieke, and M. Blaylock. The cosmic infrared background resolved by Spitzer. Contributions of mid-infrared galaxies to the far-infrared background. , 451(2):417–429, May 2006. doi: 10.1051/0004-6361:20054446.

[22] A. Maniyar, M. Béthermin, and G. Lagache. Simple halo model formalism for the cosmic infrared background and its correlation with the thermal Sunyaev-Zel'dovich effect. , 645:A40, January 2021. doi: 10.1051/0004-6361/202038790.

[23] E. M. George, C. L. Reichardt, K. A. Aird, B. A. Benson, L. E. Bleem, J. E. Carlstrom, C. L. Chang, H-M. Cho, T. M. Crawford, A. T. Crites, T. de Haan, M. A. Dobbs, J. Dudley, N. W. Halverson, N. L. Harrington, G. P. Holder, W. L. Holzapfel, Z. Hou, J. D. Hrubes, R. Keisler, L. Knox, A. T. Lee, E. M. Leitch, M. Lueker, D. Luong-Van, J. J. McMahon, J. Mehl, S. S. Meyer, M. Millea, L. M. Mocanu, J. J. Mohr, T. E. Montroy, S. Padin, T. Plagge, C. Pryke, J. E. Ruhl, K. K. Schaffer, L. Shaw, E. Shirokoff, H. G. Spieler, Z. Staniszewski, A. A. Stark, K. T. Story, A. van Engelen, K. Vanderlinde, J. D. Vieira, R. Williamson, and O. Zahn. A measurement of secondary cosmic microwave background anisotropies from the 2500 square-degree spt-sz survey. *The Astrophysical Journal*, 799(2):177, Jan 2015. ISSN 1538-4357. doi: 10.1088/0004-637x/799/2/177. URL `http://dx.doi.org/10.1088/0004-637X/799/2/177`.

[24] C. L. Reichardt, S. Patil, P. A. R. Ade, A. J. Anderson, J. E. Austermann, J. S. Avva, E. Baxter, J. A. Beall, A. N. Bender, B. A. Benson, F. Bianchini,

L. E. Bleem, J. E. Carlstrom, C. L. Chang, P. Chaubal, H. C. Chiang, T. L. Chou, R. Citron, C. Corbett Moran, T. M. Crawford, A. T. Crites, T. de Haan, M. A. Dobbs, W. Everett, J. Gallicchio, E. M. George, A. Gilbert, N. Gupta, N. W. Halverson, N. Harrington, J. W. Henning, G. C. Hilton, G. P. Holder, W. L. Holzapfel, J. D. Hrubes, N. Huang, J. Hubmayr, K. D. Irwin, L. Knox, A. T. Lee, D. Li, A. Lowitz, D. Luong-Van, J. J. McMahon, J. Mehl, S. S. Meyer, M. Millea, L. M. Mocanu, J. J. Mohr, J. Montgomery, A. Nadolski, T. Natoli, J. P. Nibarger, G. Noble, V. Novosad, Y. Omori, S. Padin, C. Pryke, J. E. Ruhl, B. R. Saliwanchik, J. T. Sayre, K. K. Schaffer, E. Shirokoff, C. Sievers, G. Smecher, H. G. Spieler, Z. Staniszewski, A. A. Stark, C. Tucker, K. Vanderlinde, T. Veach, J. D. Vieira, G. Wang, N. Whitehorn, R. Williamson, W. L. K. Wu, and V. Yefremenko. An improved measurement of the secondary cosmic microwave background anisotropies from the spt-sz + sptpol surveys. *The Astrophysical Journal*, 908(2):199, February 2021. ISSN 1538-4357. doi: 10.3847/1538-4357/abd407. URL `http://dx.doi.org/10.3847/1538-4357/abd407`.

[25] Daniel Lenz, Olivier Doré, and Guilaine Lagache. Large-scale maps of the cosmic infrared background from planck. *The Astrophysical Journal*, 883(1): 75, September 2019. ISSN 1538-4357. doi: 10.3847/1538-4357/ab3c2b. URL `http://dx.doi.org/10.3847/1538-4357/ab3c2b`.

[26] R. D. Davies and A. Wilkinson. Synchrotron Emission from the Galaxy. *arXiv e-prints*, art. astro-ph/9804208, April 1998. doi: 10.48550/arXiv.astro-ph/9804208.

[27] A. Coerver, J. A. Zebrowski, S. Takakura, W. L. Holzapfel, P. A. R. Ade, A. J. Anderson, Z. Ahmed, B. Ansarinejad, M. Archipley, L. Balkenhol, D. Barron, K. Benabed, A. N. Bender, B. A. Benson, F. Bianchini, L. E. Bleem, F. R. Bouchet, L. Bryant, E. Camphuis, J. E. Carlstrom, T. W. Cecil, C. L. Chang, P. Chaubal, P. M. Chichura, A. Chokshi, T. L. Chou, T. M. Crawford, A. Cukierman, C. Daley, T. de Haan, K. R. Dibert, M. A. Dobbs, A. Doussot, D. Dutcher, W. Everett, C. Feng, K. R. Ferguson, K. Fichman, A. Foster, S. Galli, A. E. Gambrel, R. W. Gardner, F. Ge, N. Goeckner-Wald, R. Gualtieri, F. Guidi, S. Guns, N. W. Halverson, E. Hivon, G. P. Holder, J. C. Hood, A. Hryciuk, N. Huang, F. Keruzore, A. R. Khalife, L. Knox, M. Korman, K. Kornoelje, C. L. Kuo, A. T. Lee, K. Levy, A. E. Lowitz, C. Lu, A. Maniyar, E. S. Martsen, F. Menanteau, M. Millea, J. Montgomery, Y. Nakato, T. Natoli, G. I. Noble, V. Novosad, Y. Omori, S. Padin, Z. Pan, P. Paschos, K. A. Phadke, A. W. Pollak, K. Prabhu, W. Quan, M. Rahimi, A. Rahlin, C. L. Reichardt, M. Rouble, J. E. Ruhl, E. Schiappucci, G. Smecher, J. A. Sobrin, A. A. Stark, J. Stephen, A. Suzuki, C. Tandoi, K. L. Thompson, B. Thorne, C. Trendafilova, C. Tucker, C. Umilta, J. D. Vieira, A. Vitrier, Y. Wan, G. Wang, N. Whitehorn, W. L. K. Wu, V. Yefremenko, and M. R. Young. Measurement and modeling of polarized atmosphere at the south pole with spt-3g, 2024. URL `https://arxiv.org/abs/2407.20579`.

[28] J. A. Sobrin, A. J. Anderson, A. N. Bender, B. A. Benson, D. Dutcher, A. Foster, N. Goeckner-Wald, J. Montgomery, A. Nadolski, A. Rahlin, P. A. R. Ade, Z. Ahmed, E. Anderes, M. Archipley, J. E. Austermann, J. S. Avva, K. Aylor,

L. Balkenhol, P. S. Barry, R. Basu Thakur, K. Benabed, F. Bianchini, L. E. Bleem, F. R. Bouchet, L. Bryant, K. Byrum, J. E. Carlstrom, F. W. Carter, T. W. Cecil, C. L. Chang, P. Chaubal, G. Chen, H.-M. Cho, T.-L. Chou, J.-F. Cliche, T. M. Crawford, A. Cukierman, C. Daley, T. de Haan, E. V. Denison, K. Dibert, J. Ding, M. A. Dobbs, W. Everett, C. Feng, K. R. Ferguson, J. Fu, S. Galli, A. E. Gambrel, R. W. Gardner, R. Gualtieri, S. Guns, N. Gupta, R. Guyser, N. W. Halverson, A. H. Harke-Hosemann, N. L. Harrington, J. W. Henning, G. C. Hilton, E. Hivon, G. P. Holder, W. L. Holzapfel, J. C. Hood, D. Howe, N. Huang, K. D. Irwin, O. B. Jeong, M. Jonas, A. Jones, T. S. Khaire, L. Knox, A. M. Kofman, M. Korman, D. L. Kubik, S. Kuhlmann, C.-L. Kuo, A. T. Lee, E. M. Leitch, A. E. Lowitz, C. Lu, S. S. Meyer, D. Michalik, M. Millea, T. Natoli, H. Nguyen, G. I. Noble, V. Novosad, Y. Omori, S. Padin, Z. Pan, P. Paschos, J. Pearson, C. M. Posada, K. Prabhu, W. Quan, C. L. Reichardt, D. Riebel, B. Riedel, M. Rouble, J. E. Ruhl, B. Saliwanchik, J. T. Sayre, E. Schiappucci, E. Shirokoff, G. Smecher, A. A. Stark, J. Stephen, K. T. Story, A. Suzuki, C. Tandoi, K. L. Thompson, B. Thorne, C. Tucker, C. Umilta, L. R. Vale, K. Vanderlinde, J. D. Vieira, G. Wang, N. Whitehorn, W. L. K. Wu, V. Yefremenko, K. W. Yoon, and M. R. Young. The design and integrated performance of SPT-3g. *The Astrophysical Journal Supplement Series*, 258(2):42, feb 2022. doi: 10.3847/1538-4365/ac374f. URL `https://doi.org/10.3847%2F1538-4365%2Fac374f`.

[29] John Ruhl, Peter A. R. Ade, John E. Carlstrom, Hsiao-Mei Cho, Thomas Crawford, Matt Dobbs, Chris H. Greer, Nils w. Halverson, William L. Holzapfel, Trevor M. Lanting, Adrian T. Lee, Erik M. Leitch, Jon Leong, Wenyang Lu, Martin Lueker, Jared Mehl, Stephan S. Meyer, Joe J. Mohr, Steve Padin, T. Plagge, Clem Pryke, Marcus C. Runyan, Dan Schwan, M. K. Sharp, Helmuth Spieler, Zak Staniszewski, and Antony A. Stark. The south pole telescope. In Jonas Zmuidzinas, Wayne S. Holland, and Stafford Withington, editors, *Millimeter and Submillimeter Detectors for Astronomy II*. SPIE, October 2004. doi: 10.1117/12.552473. URL `http://dx.doi.org/10.1117/12.552473`.

[30] J. E. Carlstrom, P. A. R. Ade, K. A. Aird, B. A. Benson, L. E. Bleem, S. Busetti, C. L. Chang, E. Chauvin, H.-M. Cho, T. M. Crawford, A. T. Crites, M. A. Dobbs, N. W. Halverson, S. Heimsath, W. L. Holzapfel, J. D. Hrubes, M. Joy, R. Keisler, T. M. Lanting, A. T. Lee, E. M. Leitch, J. Leong, W. Lu, M. Lueker, D. Luong-Van, J. J. McMahon, J. Mehl, S. S. Meyer, J. J. Mohr, T. E. Montroy, S. Padin, T. Plagge, C. Pryke, J. E. Ruhl, K. K. Schaffer, D. Schwan, E. Shirokoff, H. G. Spieler, Z. Staniszewski, A. A. Stark, C. Tucker, K. Vanderlinde, J. D. Vieira, and R. Williamson. The 10 meter south pole telescope. *Publications of the Astronomical Society of the Pacific*, 123(903):568–581, May 2011. ISSN 1538-3873. doi: 10.1086/659879. URL `http://dx.doi.org/10.1086/659879`.

[31] R. S. Bussmann, W. L. Holzapfel, and C. L. Kuo. Millimeter wavelength brightness fluctuations of the atmosphere above the south pole. *The Astrophysical Journal*, 622(2):1343, apr 2005. doi: 10.1086/427935. URL `https://dx.doi.org/10.1086/427935`.

[32] S. Padin, Z. Staniszewski, R. Keisler, M. Joy, A. A. Stark, P. A. R. Ade, K. A. Aird, B. A. Benson, L. E. Bleem, J. E. Carlstrom, C. L. Chang, T. M. Crawford, A. T. Crites, M. A. Dobbs, N. W. Halverson, S. Heimsath, R. E. Hills, W. L. Holzapfel, C. Lawrie, A. T. Lee, E. M. Leitch, J. Leong, W. Lu, M. Lueker, J. J. McMahon, S. S. Meyer, J. J. Mohr, T. E. Montroy, T. Plagge, C. Pryke, J. E. Ruhl, K. K. Schaffer, E. Shirokoff, H. G. Spieler, and J. D. Vieira. South pole telescope optics. *Appl. Opt.*, 47(24):4418–4428, Aug 2008. doi: 10.1364/AO.47.004418. URL `https://opg.optica.org/ao/abstract.cfm?URI=ao-47-24-4418`.

[33] J. E. Austermann, K. A. Aird, J. A. Beall, D. Becker, A. Bender, B. A. Benson, L. E. Bleem, J. Britton, J. E. Carlstrom, C. L. Chang, H. C. Chiang, H.-M. Cho, T. M. Crawford, A. T. Crites, A. Datesman, T. de Haan, M. A. Dobbs, E. M. George, N. W. Halverson, N. Harrington, J. W. Henning, G. C. Hilton, G. P. Holder, W. L. Holzapfel, S. Hoover, N. Huang, J. Hubmayr, K. D. Irwin, R. Keisler, J. Kennedy, L. Knox, A. T. Lee, E. Leitch, D. Li, M. Lueker, D. P. Marrone, J. J. McMahon, J. Mehl, S. S. Meyer, T. E. Montroy, T. Natoli, J. P. Nibarger, M. D. Niemack, V. Novosad, S. Padin, C. Pryke, C. L. Reichardt, J. E. Ruhl, B. R. Saliwanchik, J. T. Sayre, K. K. Schaffer, E. Shirokoff, A. A. Stark, K. Story, K. Vanderlinde, J. D. Vieira, G. Wang, R. Williamson, V. Yefremenko, K. W. Yoon, and O. Zahn. Sptpol: an instrument for cmb polarization measurements with the south pole telescope. In Wayne S. Holland, editor, *Millimeter, Submillimeter, and Far-Infrared Detectors and Instrumentation for Astronomy VI*. SPIE, September 2012. doi: 10.1117/12.927286. URL `http://dx.doi.org/10.1117/12.927286`.

[34] E. Shirokoff, C. L. Reichardt, L. Shaw, M. Millea, P. A. R. Ade, K. A. Aird, B. A. Benson, L. E. Bleem, J. E. Carlstrom, C. L. Chang, H. M. Cho, T. M. Crawford, A. T. Crites, T. de Haan, M. A. Dobbs, J. Dudley, E. M. George, N. W. Halverson, G. P. Holder, W. L. Holzapfel, J. D. Hrubes, M. Joy, R. Keisler, L. Knox, A. T. Lee, E. M. Leitch, M. Lueker, D. Luong-Van, J. J. McMahon, J. Mehl, S. S. Meyer, J. J. Mohr, T. E. Montroy, S. Padin, T. Plagge, C. Pryke, J. E. Ruhl, K. K. Schaffer, H. G. Spieler, Z. Staniszewski, A. A. Stark, K. Story, K. Vanderlinde, J. D. Vieira, R. Williamson, and O. Zahn. Improved constraints on cosmic microwave background secondary anisotropies from the complete 2008 south pole telescope data. *The Astrophysical Journal*, 736(1):61, July 2011. ISSN 1538-4357. doi: 10.1088/0004-637x/736/1/61. URL `http://dx.doi.org/10.1088/0004-637X/736/1/61`.

[35] R. Keisler, C. L. Reichardt, K. A. Aird, B. A. Benson, L. E. Bleem, J. E. Carlstrom, C. L. Chang, H. M. Cho, T. M. Crawford, A. T. Crites, T. de Haan, M. A. Dobbs, J. Dudley, E. M. George, N. W. Halverson, G. P. Holder, W. L. Holzapfel, S. Hoover, Z. Hou, J. D. Hrubes, M. Joy, L. Knox, A. T. Lee, E. M. Leitch, M. Lueker, D. Luong-Van, J. J. McMahon, J. Mehl, S. S. Meyer, M. Millea, J. J. Mohr, T. E. Montroy, T. Natoli, S. Padin, T. Plagge, C. Pryke, J. E. Ruhl, K. K. Schaffer, L. Shaw, E. Shirokoff, H. G. Spieler, Z. Staniszewski, A. A. Stark, K. Story, A. van Engelen, K. Vanderlinde, J. D. Vieira, R. Williamson, and O. Zahn. A measurement of the damping tail of the cosmic microwave background power spec-

trum with the south pole telescope. *The Astrophysical Journal*, 743(1):28, November 2011. ISSN 1538-4357. doi: 10.1088/0004-637x/743/1/28. URL `http://dx.doi.org/10.1088/0004-637X/743/1/28`.

[36] C. L. Reichardt, L. Shaw, O. Zahn, K. A. Aird, B. A. Benson, L. E. Bleem, J. E. Carlstrom, C. L. Chang, H. M. Cho, T. M. Crawford, A. T. Crites, T. de Haan, M. A. Dobbs, J. Dudley, E. M. George, N. W. Halverson, G. P. Holder, W. L. Holzapfel, S. Hoover, Z. Hou, J. D. Hrubes, M. Joy, R. Keisler, L. Knox, A. T. Lee, E. M. Leitch, M. Lueker, D. Luong-Van, J. J. McMahon, J. Mehl, S. S. Meyer, M. Millea, J. J. Mohr, T. E. Montroy, T. Natoli, S. Padin, T. Plagge, C. Pryke, J. E. Ruhl, K. K. Schaffer, E. Shirokoff, H. G. Spieler, Z. Staniszewski, A. A. Stark, K. Story, A. van Engelen, K. Vanderlinde, J. D. Vieira, and R. Williamson. A measurement of secondary cosmic microwave background anisotropies with two years of south pole telescope observations. *The Astrophysical Journal*, 755(1):70, July 2012. ISSN 1538-4357. doi: 10.1088/0004-637x/755/1/70. URL `http://dx.doi.org/10.1088/0004-637X/755/1/70`.

[37] K. T. Story, C. L. Reichardt, Z. Hou, R. Keisler, K. A. Aird, B. A. Benson, L. E. Bleem, J. E. Carlstrom, C. L. Chang, H.-M. Cho, T. M. Crawford, A. T. Crites, T. de Haan, M. A. Dobbs, J. Dudley, B. Follin, E. M. George, N. W. Halverson, G. P. Holder, W. L. Holzapfel, S. Hoover, J. D. Hrubes, M. Joy, L. Knox, A. T. Lee, E. M. Leitch, M. Lueker, D. Luong-Van, J. J. McMahon, J. Mehl, S. S. Meyer, M. Millea, J. J. Mohr, T. E. Montroy, S. Padin, T. Plagge, C. Pryke, J. E. Ruhl, J. T. Sayre, K. K. Schaffer, L. Shaw, E. Shirokoff, H. G. Spieler, Z. Staniszewski, A. A. Stark, A. van Engelen, K. Vanderlinde, J. D. Vieira, R. Williamson, and O. Zahn. A measurement of the cosmic microwave background damping tail from the 2500-square-degree spt-sz survey. *The Astrophysical Journal*, 779(1):86, November 2013. ISSN 1538-4357. doi: 10.1088/0004-637x/779/1/86. URL `http://dx.doi.org/10.1088/0004-637X/779/1/86`.

[38] C. L. Reichardt, B. Stalder, L. E. Bleem, T. E. Montroy, K. A. Aird, K. Andersson, R. Armstrong, M. L. N. Ashby, M. Bautz, M. Bayliss, G. Bazin, B. A. Benson, M. Brodwin, J. E. Carlstrom, C. L. Chang, H. M. Cho, A. Clocchiatti, T. M. Crawford, A. T. Crites, T. de Haan, S. Desai, M. A. Dobbs, J. P. Dudley, R. J. Foley, W. R. Forman, E. M. George, M. D. Gladders, A. H. Gonzalez, N. W. Halverson, N. L. Harrington, F. W. High, G. P. Holder, W. L. Holzapfel, S. Hoover, J. D. Hrubes, C. Jones, M. Joy, R. Keisler, L. Knox, A. T. Lee, E. M. Leitch, J. Liu, M. Lueker, D. Luong-Van, A. Mantz, D. P. Marrone, M. McDonald, J. J. McMahon, J. Mehl, S. S. Meyer, L. Mocanu, J. J. Mohr, S. S. Murray, T. Natoli, S. Padin, T. Plagge, C. Pryke, A. Rest, J. Ruel, J. E. Ruhl, B. R. Saliwanchik, A. Saro, J. T. Sayre, K. K. Schaffer, L. Shaw, E. Shirokoff, J. Song, H. G. Spieler, Z. Staniszewski, A. A. Stark, K. Story, C. W. Stubbs, R. Šuhada, A. van Engelen, K. Vanderlinde, J. D. Vieira, A. Vikhlinin, R. Williamson, O. Zahn, and A. Zenteno. Galaxy clusters discovered via the sunyaev-zel'dovich effect in the first 720 square degrees of the south pole telescope survey. *The Astrophysical Journal*, 763(2):127,

January 2013. ISSN 1538-4357. doi: 10.1088/0004-637x/763/2/127. URL `http://dx.doi.org/10.1088/0004-637X/763/2/127`.

[39] B. A. Benson, T. de Haan, J. P. Dudley, C. L. Reichardt, K. A. Aird, K. Andersson, R. Armstrong, M. L. N. Ashby, M. Bautz, M. Bayliss, G. Bazin, L. E. Bleem, M. Brodwin, J. E. Carlstrom, C. L. Chang, H. M. Cho, A. Clocchiatti, T. M. Crawford, A. T. Crites, S. Desai, M. A. Dobbs, R. J. Foley, W. R. Forman, E. M. George, M. D. Gladders, A. H. Gonzalez, N. W. Halverson, N. Harrington, F. W. High, G. P. Holder, W. L. Holzapfel, S. Hoover, J. D. Hrubes, C. Jones, M. Joy, R. Keisler, L. Knox, A. T. Lee, E. M. Leitch, J. Liu, M. Lueker, D. Luong-Van, A. Mantz, D. P. Marrone, M. McDonald, J. J. McMahon, J. Mehl, S. S. Meyer, L. Mocanu, J. J. Mohr, T. E. Montroy, S. S. Murray, T. Natoli, S. Padin, T. Plagge, C. Pryke, A. Rest, J. Ruel, J. E. Ruhl, B. R. Saliwanchik, A. Saro, J. T. Sayre, K. K. Schaffer, L. Shaw, E. Shirokoff, J. Song, H. G. Spieler, B. Stalder, Z. Staniszewski, A. A. Stark, K. Story, C. W. Stubbs, R. Suhada, A. van Engelen, K. Vanderlinde, J. D. Vieira, A. Vikhlinin, R. Williamson, O. Zahn, and A. Zenteno. Cosmological constraints from sunyaev–zel'dovich-selected clusters with x-ray observations in the first 178 deg2 of the south pole telescope survey. *The Astrophysical Journal*, 763(2):147, January 2013. ISSN 1538-4357. doi: 10.1088/0004-637x/763/2/147. URL `http://dx.doi.org/10.1088/0004-637X/763/2/147`.

[40] J. D. Vieira, T. M. Crawford, E. R. Switzer, P. A. R. Ade, K. A. Aird, M. L. N. Ashby, B. A. Benson, L. E. Bleem, M. Brodwin, J. E. Carlstrom, C. L. Chang, H.-M. Cho, A. T. Crites, T. de Haan, M. A. Dobbs, W. Everett, E. M. George, M. Gladders, N. R. Hall, N. W. Halverson, F. W. High, G. P. Holder, W. L. Holzapfel, J. D. Hrubes, M. Joy, R. Keisler, L. Knox, A. T. Lee, E. M. Leitch, M. Lueker, D. P. Marrone, V. McIntyre, J. J. McMahon, J. Mehl, S. S. Meyer, J. J. Mohr, T. E. Montroy, S. Padin, T. Plagge, C. Pryke, C. L. Reichardt, J. E. Ruhl, K. K. Schaffer, L. Shaw, E. Shirokoff, H. G. Spieler, B. Stalder, Z. Staniszewski, A. A. Stark, K. Vanderlinde, W. Walsh, R. Williamson, Y. Yang, O. Zahn, and A. Zenteno. Extragalactic millimeter-wave sources in south pole telescope survey data: Source counts, catalog, and statistics for an 87 square-degree field. *The Astrophysical Journal*, 719(1): 763–783, July 2010. ISSN 1538-4357. doi: 10.1088/0004-637x/719/1/763. URL `http://dx.doi.org/10.1088/0004-637X/719/1/763`.

[41] J. D. Vieira, D. P. Marrone, S. C. Chapman, C. De Breuck, Y. D. Hezaveh, A. Weiβ, J. E. Aguirre, K. A. Aird, M. Aravena, M. L. N. Ashby, M. Bayliss, B. A. Benson, A. D. Biggs, L. E. Bleem, J. J. Bock, M. Bothwell, C. M. Bradford, M. Brodwin, J. E. Carlstrom, C. L. Chang, T. M. Crawford, A. T. Crites, T. de Haan, M. A. Dobbs, E. B. Fomalont, C. D. Fassnacht, E. M. George, M. D. Gladders, A. H. Gonzalez, T. R. Greve, B. Gullberg, N. W. Halverson, F. W. High, G. P. Holder, W. L. Holzapfel, S. Hoover, J. D. Hrubes, T. R. Hunter, R. Keisler, A. T. Lee, E. M. Leitch, M. Lueker, D. Luong-van, M. Malkan, V. McIntyre, J. J. McMahon, J. Mehl, K. M. Menten, S. S. Meyer, L. M. Mocanu, E. J. Murphy, T. Natoli, S. Padin, T. Plagge, C. L. Reichardt, A. Rest, J. Ruel, J. E. Ruhl, K. Sharon, K. K. Schaffer, L. Shaw, E. Shirokoff, J. S. Spilker, B. Stalder, Z. Staniszewski, A. A. Stark, K. Story,

K. Vanderlinde, N. Welikala, and R. Williamson. Dusty starburst galaxies in the early Universe as revealed by gravitational lensing. , 495:344–347, March 2013. doi: 10.1038/nature12001.

[42] Erik Shirokoff, Bradford A. Benson, Lindsey E. Bleem, Clarence L. Chang, Hsiao-Mei Cho, Abigail T. Crites, Matt A. Dobbs, William L. Holzapfel, Trevor Lanting, Adrian T. Lee, Martin Lueker, Jared Mehl, Thomas Plagge, Helmuth G. Spieler, and Joaquin D. Vieira. The south pole telescope sz-receiver detectors. *IEEE Transactions on Applied Superconductivity*, 19(3): 517–519, 2009. doi: 10.1109/TASC.2009.2018229.

[43] R. Keisler, S. Hoover, N. Harrington, J. W. Henning, P. A. R. Ade, K. A. Aird, J. E. Austermann, J. A. Beall, A. N. Bender, B. A. Benson, L. E. Bleem, J. E. Carlstrom, C. L. Chang, H. C. Chiang, H-M. Cho, R. Citron, T. M. Crawford, A. T. Crites, T. de Haan, M. A. Dobbs, W. Everett, J. Gallicchio, J. Gao, E. M. George, A. Gilbert, N. W. Halverson, D. Hanson, G. C. Hilton, G. P. Holder, W. L. Holzapfel, Z. Hou, J. D. Hrubes, N. Huang, J. Hubmayr, K. D. Irwin, L. Knox, A. T. Lee, E. M. Leitch, D. Li, D. Luong-Van, D. P. Marrone, J. J. McMahon, J. Mehl, S. S. Meyer, L. Mocanu, T. Natoli, J. P. Nibarger, V. Novosad, S. Padin, C. Pryke, C. L. Reichardt, J. E. Ruhl, B. R. Saliwanchik, J. T. Sayre, K. K. Schaffer, E. Shirokoff, G. Smecher, A. A. Stark, K. T. Story, C. Tucker, K. Vanderlinde, J. D. Vieira, G. Wang, N. Whitehorn, V. Yefremenko, and O. Zahn. Measurements of sub-degreeb-mode polarization in the cosmic microwave background from 100 square degrees of sptpol data. *The Astrophysical Journal*, 807(2):151, July 2015. ISSN 1538-4357. doi: 10.1088/0004-637x/807/2/151. URL `http://dx.doi.org/10.1088/0004-637X/807/2/151`.

[44] A. Manzotti, K. T. Story, W. L. K. Wu, J. E. Austermann, J. A. Beall, A. N. Bender, B. A. Benson, L. E. Bleem, J. J. Bock, J. E. Carlstrom, C. L. Chang, H. C. Chiang, H-M. Cho, R. Citron, A. Conley, T. M. Crawford, A. T. Crites, T. de Haan, M. A. Dobbs, S. Dodelson, W. Everett, J. Gallicchio, E. M. George, A. Gilbert, N. W. Halverson, N. Harrington, J. W. Henning, G. C. Hilton, G. P. Holder, W. L. Holzapfel, S. Hoover, Z. Hou, J. D. Hrubes, N. Huang, J. Hubmayr, K. D. Irwin, R. Keisler, L. Knox, A. T. Lee, E. M. Leitch, D. Li, J. J. McMahon, S. S. Meyer, L. M. Mocanu, T. Natoli, J. P. Nibarger, V. Novosad, S. Padin, C. Pryke, C. L. Reichardt, J. E. Ruhl, B. R. Saliwanchik, J. T. Sayre, K. K. Schaffer, G. Smecher, A. A. Stark, K. Vanderlinde, J. D. Vieira, M. P. Viero, G. Wang, N. Whitehorn, V. Yefremenko, and M. Zemcov. Cmb polarization b-mode delensing with sptpol and herschel. *The Astrophysical Journal*, 846 (1):45, August 2017. ISSN 1538-4357. doi: 10.3847/1538-4357/aa82bb. URL `http://dx.doi.org/10.3847/1538-4357/aa82bb`.

[45] J.T. Sayre, C.L. Reichardt, J.W. Henning, P.A.R. Ade, A.J. Anderson, J.E. Austermann, J.S. Avva, J.A. Beall, A.N. Bender, B.A. Benson, F. Bianchini, L.E. Bleem, J.E. Carlstrom, C.L. Chang, P. Chaubal, H.C. Chiang, R. Citron, C. Corbett Moran, T.M. Crawford, A.T. Crites, T. de Haan, M.A. Dobbs, W. Everett, J. Gallicchio, E.M. George, A. Gilbert, N. Gupta, N.W. Halverson, N. Harrington, G.C. Hilton, G.P. Holder, W.L. Holzapfel,

J.D. Hrubes, N. Huang, J. Hubmayr, K.D. Irwin, L. Knox, A.T. Lee, D. Li, A. Lowitz, J.J. McMahon, S.S. Meyer, L.M. Mocanu, J. Montgomery, A. Nadolski, T. Natoli, J.P. Nibarger, G. Noble, V. Novosad, S. Padin, S. Patil, C. Pryke, J.E. Ruhl, B.R. Saliwanchik, K.K. Schaffer, C. Sievers, G. Smecher, A.A. Stark, C. Tucker, K. Vanderlinde, T. Veach, J.D. Vieira, G. Wang, N. Whitehorn, W.L.K. Wu, and V. Yefremenko. Measurements of ¡mml:math xmlns:mml=”http://www.w3.org/1998/math/mathml” display=”inline”¿¡mml:mi¿b¡/mml:mi¿¡/mml:math¿ -mode polarization of the cosmic microwave background from 500 square degrees of sptpol data. *Physical Review D*, 101(12), June 2020. ISSN 2470-0029. doi: 10.1103/physrevd.101.122003. URL `http://dx.doi.org/10.1103/PhysRevD.101.122003`.

[46] A. T. Crites, J. W. Henning, P. A. R. Ade, K. A. Aird, J. E. Austermann, J. A. Beall, A. N. Bender, B. A. Benson, L. E. Bleem, J. E. Carlstrom, C. L. Chang, H. C. Chiang, H-M. Cho, R. Citron, T. M. Crawford, T. de Haan, M. A. Dobbs, W. Everett, J. Gallicchio, J. Gao, E. M. George, A. Gilbert, N. W. Halverson, D. Hanson, N. Harrington, G. C. Hilton, G. P. Holder, W. L. Holzapfel, S. Hoover, Z. Hou, J. D. Hrubes, N. Huang, J. Hubmayr, K. D. Irwin, R. Keisler, L. Knox, A. T. Lee, E. M. Leitch, D. Li, C. Liang, D. Luong-Van, J. J. McMahon, J. Mehl, S. S. Meyer, L. Mocanu, T. E. Montroy, T. Natoli, J. P. Nibarger, V. Novosad, S. Padin, C. Pryke, C. L. Reichardt, J. E. Ruhl, B. R. Saliwanchik, J. T. Sayre, K. K. Schaffer, G. Smecher, A. A. Stark, K. T. Story, C. Tucker, K. Vanderlinde, J. D. Vieira, G. Wang, N. Whitehorn, V. Yefremenko, and O. Zahn. Measurements of e-mode polarization and temperature-e-mode correlation in the cosmic microwave background from 100 square degrees of sptpol data. *The Astrophysical Journal*, 805 (1):36, May 2015. ISSN 1538-4357. doi: 10.1088/0004-637x/805/1/36. URL `http://dx.doi.org/10.1088/0004-637X/805/1/36`.

[47] J. W. Henning, J. T. Sayre, C. L. Reichardt, P. A. R. Ade, A. J. Anderson, J. E. Austermann, J. A. Beall, A. N. Bender, B. A. Benson, L. E. Bleem, J. E. Carlstrom, C. L. Chang, H. C. Chiang, H-M. Cho, R. Citron, C. Corbett Moran, T. M. Crawford, A. T. Crites, T. de Haan, M. A. Dobbs, W. Everett, J. Gallicchio, E. M. George, A. Gilbert, N. W. Halverson, N. Harrington, G. C. Hilton, G. P. Holder, W. L. Holzapfel, S. Hoover, Z. Hou, J. D. Hrubes, N. Huang, J. Hubmayr, K. D. Irwin, R. Keisler, L. Knox, A. T. Lee, E. M. Leitch, D. Li, A. Lowitz, A. Manzotti, J. J. McMahon, S. S. Meyer, L. Mocanu, J. Montgomery, A. Nadolski, T. Natoli, J. P. Nibarger, V. Novosad, S. Padin, C. Pryke, J. E. Ruhl, B. R. Saliwanchik, K. K. Schaffer, C. Sievers, G. Smecher, A. A. Stark, K. T. Story, C. Tucker, K. Vanderlinde, T. Veach, J. D. Vieira, G. Wang, N. Whitehorn, W. L. K. Wu, and V. Yefremenko. Measurements of the temperature and e-mode polarization of the cmb from 500 square degrees of sptpol data. *The Astrophysical Journal*, 852(2):97, January 2018. ISSN 1538-4357. doi: 10.3847/1538-4357/aa9ff4. URL `http://dx.doi.org/10.3847/1538-4357/aa9ff4`.

[48] K. T. Story, D. Hanson, P. A. R. Ade, K. A. Aird, J. E. Austermann, J. A. Beall, A. N. Bender, B. A. Benson, L. E. Bleem, J. E. Carlstrom, C. L. Chang, H. C. Chiang, H-M. Cho, R. Citron, T. M. Crawford, A. T.

Crites, T. de Haan, M. A. Dobbs, W. Everett, J. Gallicchio, J. Gao, E. M. George, A. Gilbert, N. W. Halverson, N. Harrington, J. W. Henning, G. C. Hilton, G. P. Holder, W. L. Holzapfel, S. Hoover, Z. Hou, J. D. Hrubes, N. Huang, J. Hubmayr, K. D. Irwin, R. Keisler, L. Knox, A. T. Lee, E. M. Leitch, D. Li, C. Liang, D. Luong-Van, J. J. McMahon, J. Mehl, S. S. Meyer, L. Mocanu, T. E. Montroy, T. Natoli, J. P. Nibarger, V. Novosad, S. Padin, C. Pryke, C. L. Reichardt, J. E. Ruhl, B. R. Saliwanchik, J. T. Sayre, K. K. Schaffer, G. Smecher, A. A. Stark, C. Tucker, K. Vanderlinde, J. D. Vieira, G. Wang, N. Whitehorn, V. Yefremenko, and O. Zahn. A measurement of the cosmic microwave background gravitational lensing potential from 100 square degrees of sptpol data. *The Astrophysical Journal*, 810(1): 50, August 2015. ISSN 1538-4357. doi: 10.1088/0004-637x/810/1/50. URL `http://dx.doi.org/10.1088/0004-637X/810/1/50`.

[49] W. L. K. Wu, L. M. Mocanu, P. A. R. Ade, A. J. Anderson, J. E. Austermann, J. S. Avva, J. A. Beall, A. N. Bender, B. A. Benson, F. Bianchini, L. E. Bleem, J. E. Carlstrom, C. L. Chang, H. C. Chiang, R. Citron, C. Corbett Moran, T. M. Crawford, A. T. Crites, T. de Haan, M. A. Dobbs, W. Everett, J. Gallicchio, E. M. George, A. Gilbert, N. Gupta, N. W. Halverson, N. Harrington, J. W. Henning, G. C. Hilton, G. P. Holder, W. L. Holzapfel, Z. Hou, J. D. Hrubes, N. Huang, J. Hubmayr, K. D. Irwin, L. Knox, A. T. Lee, D. Li, A. Lowitz, A. Manzotti, J. J. McMahon, S. S. Meyer, M. Millea, J. Montgomery, A. Nadolski, T. Natoli, J. P. Nibarger, G. I. Noble, V. Novosad, Y. Omori, S. Padin, S. Patil, C. Pryke, C. L. Reichardt, J. E. Ruhl, B. R. Saliwanchik, J. T. Sayre, K. K. Schaffer, C. Sievers, G. Simard, G. Smecher, A. A. Stark, K. T. Story, C. Tucker, K. Vanderlinde, T. Veach, J. D. Vieira, G. Wang, N. Whitehorn, and V. Yefremenko. A measurement of the cosmic microwave background lensing potential and power spectrum from 500 deg2 of sptpol temperature and polarization data. *The Astrophysical Journal*, 884 (1):70, October 2019. ISSN 1538-4357. doi: 10.3847/1538-4357/ab4186. URL `http://dx.doi.org/10.3847/1538-4357/ab4186`.

[50] M. Millea, C. M. Daley, T-L. Chou, E. Anderes, P. A. R. Ade, A. J. Anderson, J. E. Austermann, J. S. Avva, J. A. Beall, A. N. Bender, B. A. Benson, F. Bianchini, L. E. Bleem, J. E. Carlstrom, C. L. Chang, P. Chaubal, H. C. Chiang, R. Citron, C. Corbett Moran, T. M. Crawford, A. T. Crites, T. de Haan, M. A. Dobbs, W. Everett, J. Gallicchio, E. M. George, N. Goeckner-Wald, S. Guns, N. Gupta, N. W. Halverson, J. W. Henning, G. C. Hilton, G. P. Holder, W. L. Holzapfel, J. D. Hrubes, N. Huang, J. Hubmayr, K. D. Irwin, L. Knox, A. T. Lee, D. Li, A. Lowitz, J. J. McMahon, S. S. Meyer, L. M. Mocanu, J. Montgomery, T. Natoli, J. P. Nibarger, G. Noble, V. Novosad, Y. Omori, S. Padin, S. Patil, C. Pryke, C. L. Reichardt, J. E. Ruhl, B. R. Saliwanchik, K. K. Schaffer, C. Sievers, G. Smecher, A. A. Stark, B. Thorne, C. Tucker, T. Veach, J. D. Vieira, G. Wang, N. Whitehorn, W. L. K. Wu, and V. Yefremenko. Optimal cosmic microwave background lensing reconstruction and parameter estimation with sptpol data. *The Astrophysical Journal*, 922 (2):259, December 2021. ISSN 1538-4357. doi: 10.3847/1538-4357/ac02bb. URL `http://dx.doi.org/10.3847/1538-4357/ac02bb`.

[51] N. Huang, L. E. Bleem, B. Stalder, P. A. R. Ade, S. W. Allen, A. J. Anderson, J. E. Austermann, J. S. Avva, J. A. Beall, A. N. Bender, B. A. Benson, F. Bianchini, S. Bocquet, M. Brodwin, J. E. Carlstrom, C. L. Chang, H. C. Chiang, R. Citron, C. Corbett Moran, T. M. Crawford, A. T. Crites, T. de Haan, M. A. Dobbs, W. Everett, B. Floyd, J. Gallicchio, E. M. George, A. Gilbert, M. D. Gladders, S. Guns, N. Gupta, N. W. Halverson, N. Harrington, J. W. Henning, G. C. Hilton, G. P. Holder, W. L. Holzapfel, J. D. Hrubes, J. Hubmayr, K. D. Irwin, G. Khullar, L. Knox, A. T. Lee, D. Li, A. Lowitz, M. McDonald, J. J. McMahon, S. S. Meyer, L. M. Mocanu, J. Montgomery, A. Nadolski, T. Natoli, J. P. Nibarger, G. Noble, V. Novosad, S. Padin, S. Patil, C. Pryke, C. L. Reichardt, J. E. Ruhl, B. R. Saliwanchik, A. Saro, J. T. Sayre, K. K. Schaffer, K. Sharon, C. Sievers, G. Smecher, A. A. Stark, K. T. Story, C. Tucker, K. Vanderlinde, T. Veach, J. D. Vieira, G. Wang, N. Whitehorn, W. L. K. Wu, and V. Yefremenko. Galaxy clusters selected via the sunyaev–zel'dovich effect in the sptpol 100-square-degree survey. *The Astronomical Journal*, 159(3): 110, February 2020. ISSN 1538-3881. doi: 10.3847/1538-3881/ab6a96. URL `http://dx.doi.org/10.3847/1538-3881/ab6a96`.

[52] L. E. Bleem, S. Bocquet, B. Stalder, M. D. Gladders, P. A. R. Ade, S. W. Allen, A. J. Anderson, J. Annis, M. L. N. Ashby, J. E. Austermann, S. Avila, J. S. Avva, M. Bayliss, J. A. Beall, K. Bechtol, A. N. Bender, B. A. Benson, E. Bertin, F. Bianchini, C. Blake, M. Brodwin, D. Brooks, E. Buckley-Geer, D. L. Burke, J. E. Carlstrom, A. Carnero Rosell, M. Carrasco Kind, J. Carretero, C. L. Chang, H. C. Chiang, R. Citron, C. Corbett Moran, M. Costanzi, T. M. Crawford, A. T. Crites, L. N. da Costa, T. de Haan, J. De Vicente, S. Desai, H. T. Diehl, J. P. Dietrich, M. A. Dobbs, T. F. Eifler, W. Everett, B. Flaugher, B. Floyd, J. Frieman, J. Gallicchio, J. García-Bellido, E. M. George, D. W. Gerdes, A. Gilbert, D. Gruen, R. A. Gruendl, J. Gschwend, N. Gupta, G. Gutierrez, N. W. Halverson, N. Harrington, J. W. Henning, C. Heymans, G. P. Holder, D. L. Hollowood, W. L. Holzapfel, K. Honscheid, J. D. Hrubes, N. Huang, J. Hubmayr, K. D. Irwin, D. J. James, T. Jeltema, S. Joudaki, G. Khullar, M. Klein, L. Knox, N. Kuropatkin, A. T. Lee, D. Li, C. Lidman, A. Lowitz, N. MacCrann, G. Mahler, M. A. G. Maia, J. L. Marshall, M. McDonald, J. J. McMahon, P. Melchior, F. Menanteau, S. S. Meyer, R. Miquel, L. M. Mocanu, J. J. Mohr, J. Montgomery, A. Nadolski, T. Natoli, J. P. Nibarger, G. Noble, V. Novosad, S. Padin, A. Palmese, D. Parkinson, S. Patil, F. Paz-Chinchón, A. A. Plazas, C. Pryke, N. S. Ramachandra, C. L. Reichardt, J. D. Remolina González, A. K. Romer, A. Roodman, J. E. Ruhl, E. S. Rykoff, B. R. Saliwanchik, E. Sanchez, A. Saro, J. T. Sayre, K. K. Schaffer, T. Schrabback, S. Serrano, K. Sharon, C. Sievers, G. Smecher, M. Smith, M. Soares-Santos, A. A. Stark, K. T. Story, E. Suchyta, G. Tarle, C. Tucker, K. Vanderlinde, T. Veach, J. D. Vieira, G. Wang, J. Weller, N. Whitehorn, W. L. K. Wu, V. Yefremenko, and Y. Zhang. The sptpol extended cluster survey. *The Astrophysical Journal Supplement Series*, 247 (1):25, March 2020. ISSN 1538-4365. doi: 10.3847/1538-4365/ab6993. URL `http://dx.doi.org/10.3847/1538-4365/ab6993`.

[53] L. E. Bleem, M. Klein, T. M. C. Abbot, P. A. R. Ade, M. Aguena, O. Alves, A.J. Anderson, F. Andrade-Oliveira, B. Ansarinejad, M. Archipley, M. L. N.

Ashby, J. E. Austermann, D. Bacon, J. A. Beall, A. N. Bender, B. A. Benson, F. Bianchini, S. Bocquet, D. Brooks, D. L. Burke, M. Calzadilla, J. E. Carlstrom, A. Carnero Rosell, J. Carretero, C. L. Chang, P. Chaubal, H. C. Chiang, T-L. Chou, R. Citron, C. Corbett Moran, M. Costanzi, M. Constanzi, T. M. Crawford, A. T. Crites, L. N. da Costa, T. de Haan, J. De Vicente, S. Desai, M. A. Dobbs, P. Doel, W. Everett, I. Ferrero, B. Flaugher, B. Floyd, D. Friedel, J. Frieman, J. Gallicchio, J. Garc'ia-Bellido, M. Gatti, E. M. George, G. Giannini, S. Grandis, D. Gruen, R. A. Gruendl, N. Gupta, G. Gutierrez, N. W. Halverson, S. R. Hinton, S. R. Hinton, G. P. Holder, D. L. Hollowood, W. L. Holzapfel, K. Honscheid, J. D. Hrubes, N. Huang, J. Hubmayr, K. D. Irwin, J. Mena-Fernández, D. J. James, F. Kéruzoré, L. Knox, K. Kuehn, O. Lahav, A. T. Lee, S. Lee, D. Li, A. Lowitz, J. L. Marshal, M. McDonald, J. J. McMahon, F. Menanteau, S. S. Meyer, R. Miquel, J. J. Mohr, J. Montgomery, J. Myles, T. Natoli, J. P. Nibarger, G. I. Noble, V. Novosad, R. L. C. Ogando, S. Padin, S. Patil, M. E. S. Pereira, A. Pieres, A. A. Plazas Malag'on, C. Pryke, C. L. Reichardt, M. Rodr'iguez-Monroy, A. K. Romer, J. E. Ruhl, B. R. Saliwanchik, L. Salvati, E. Sanchez, A. Saro, K. K. Schaffer, T. Schrabback, I. Sevilla-Noarbe, C. Sievers, G. Smecher, M. Smith, T. Somboonpanyakul, B. Stalder, A. A. Stark, E. Suchyta, M. E. C. Swanson, G. Tarle, C. To, C. Tucker, T. Veach, J. D. Vieira, M. Vincenzi, G. Wang, J. Weller, N. Whitehorn, P. Wiseman, W. L. K. Wu, V. Yefremenko, J. A. Zebrowski, and Y. Zhang. Galaxy clusters discovered via the thermal sunyaev-zel'dovich effect in the 500-square-degree sptpol survey. *The Open Journal of Astrophysics*, 7, February 2024. ISSN 2565-6120. doi: 10.21105/astro.2311.07512. URL `http://dx.doi.org/10.21105/astro.2311.07512`.

[54] A. N. Bender, P. A. R. Ade, Z. Ahmed, A. J. Anderson, J. S. Avva, K. Aylor, P. S. Barry, R. Basu Thakur, B. A. Benson, L. S. Bleem, S. Bocquet, K. Byrum, J. E. Carlstrom, F. W. Carter, T. W. Cecil, C. L. Chang, H. M. Cho, J. F. Cliche, T. M. Crawford, A. Cukierman, T. de Haan, E. V. Denison, J. Ding, M. A. Dobbs, S. Dodelson, D. Dutcher, W. Everett, A. Foster, J. Gallicchio, A. Gilbert, J. C. Groh, S. T. Guns, N. W. Halverson, A. H. Harke-Hosemann, N. L. Harrington, J. W. Henning, G. C. Hilton, G. P. Holder, W. L. Holzapfel, N. Huang, K. D. Irwin, O. B. Jeong, M. Jonas, A. Jones, T. S. Khaire, L. Knox, A. M. Kofman, M. Korman, D. L. Kubik, S. Kuhlmann, C. L. Kuo, A. T. Lee, E. M. Leitch, A. E. Lowitz, S. S. Meyer, D. Michalik, J. Montgomery, A. Nadolski, T. Natoli, H. Ngyuen, G. I. Noble, V. Novosad, S. Padin, Z. Pan, J. Pearson, C. M. Posada, W. Quan, S. Raghunathan, A. Rahlin, C. L. Reichardt, J. E. Ruhl, J. T. Sayre, E. Shirokoff, G. Smecher, J. A. Sobrin, A. A. Stark, K. T. Story, A. Suzuki, K. L. Thompson, C. Tucker, L. R. Vale, K. Vanderlinde, J. D. Vieira, G. Wang, N. Whitehorn, W. L. K. Wu, V. Yefremenko, K. W. Yoon, and M. R. Young. Year two instrument status of the spt-3g cosmic microwave background receiver. In Jonas Zmuidzinas and Jian-Rong Gao, editors, *Millimeter, Submillimeter, and Far-Infrared Detectors and Instrumentation for Astronomy IX*, volume 10708 of *Society of Photo-Optical Instrumentation Engineers (SPIE) Conference Series*, page 1070803, July 2018. doi: 10.1117/12.2312426.

[55] B. A. Benson, P. A. R. Ade, Z. Ahmed, S. W. Allen, K. Arnold, J. E. Auster-

mann, A. N. Bender, L. E. Bleem, J. E. Carlstrom, C. L. Chang, H. M. Cho, J. F. Cliche, T. M. Crawford, A. Cukierman, T. de Haan, M. A. Dobbs, D. Dutcher, W. Everett, A. Gilbert, N. W. Halverson, D. Hanson, N. L. Harrington, K. Hattori, J. W. Henning, G. C. Hilton, G. P. Holder, W. L. Holzapfel, K. D. Irwin, R. Keisler, L. Knox, D. Kubik, C. L. Kuo, A. T. Lee, E. M. Leitch, D. Li, M. McDonald, S. S. Meyer, J. Montgomery, M. Myers, T. Natoli, H. Nguyen, V. Novosad, S. Padin, Z. Pan, J. Pearson, C. Reichardt, J. E. Ruhl, B. R. Saliwanchik, G. Simard, G. Smecher, J. T. Sayre, E. Shirokoff, A. A. Stark, K. Story, A. Suzuki, K. L. Thompson, C. Tucker, K. Vanderlinde, J. D. Vieira, A. Vikhlinin, G. Wang, V. Yefremenko, and K. W. Yoon. Spt-3g: a next-generation cosmic microwave background polarization experiment on the south pole telescope. *Millimeter, Submillimeter, and Far-Infrared Detectors and Instrumentation for Astronomy VII*, Jul 2014. ISSN 0277-786X. doi: 10.1117/12.2057305. URL `http://dx.doi.org/10.1117/12.2057305`.

[56] K. Prabhu, S. Raghunathan, M. Millea, G. Lynch, P. A. R. Ade, E. Anderes, A. J. Anderson, B. Ansarinejad, M. Archipley, L. Balkenhol, K. Benabed, A. N. Bender, B. A. Benson, F. Bianchini, L. E. Bleem, F. R. Bouchet, L. Bryant, E. Camphuis, J. E. Carlstrom, T. W. Cecil, C. L. Chang, P. Chaubal, P. M. Chichura, T. L. Chou, A. Coerver, T. M. Crawford, A. Cukierman, C. Daley, T. de Haan, K. R. Dibert, M. A. Dobbs, A. Doussot, D. Dutcher, W. Everett, C. Feng, K. R. Ferguson, K. Fichman, A. Foster, S. Galli, A. E. Gambrel, R. W. Gardner, F. Ge, N. Goeckner-Wald, R. Gualtieri, F. Guidi, S. Guns, N. W. Halverson, E. Hivon, G. P. Holder, W. L. Holzapfel, J. C. Hood, A. Hryciuk, N. Huang, F. Kéruzoré, L. Knox, M. Korman, K. Kornoelje, C. L. Kuo, A. T. Lee, K. Levy, A. E. Lowitz, C. Lu, A. Maniyar, F. Menanteau, J. Montgomery, Y. Nakato, T. Natoli, G. I. Noble, V. Novosad, Y. Omori, S. Padin, Z. Pan, P. Paschos, K. A. Phadke, W. Quan, M. Rahimi, A. Rahlin, C. L. Reichardt, M. Rouble, J. E. Ruhl, E. Schiappucci, G. Smecher, J. A. Sobrin, A. A. Stark, J. Stephen, A. Suzuki, C. Tandoi, K. L. Thompson, B. Thorne, C. Trendafilova, C. Tucker, C. Umilta, A. Vitrier, J. D. Vieira, Y. Wan, G. Wang, N. Whitehorn, W. L. K. Wu, V. Yefremenko, M. R. Young, and J. A. Zebrowski. Testing the $\mathbf{\Lambda}$cdm cosmological model with forthcoming measurements of the cosmic microwave background with spt-3g, 2024. URL `https://arxiv.org/abs/2403.17925`.

[57] D. Dutcher and L. Balkenhol et al. Measurements of the E-Mode Polarization and Temperature-E-Mode Correlation of the CMB from SPT-3G 2018 Data. *arXiv e-prints*, art. arXiv:2101.01684, January 2021.

[58] L. Balkenhol and D. Dutcher, et al. Constraints on ΛCDM Extensions from the SPT-3G 2018 EE and TE Power Spectra. *arXiv e-prints*, art. arXiv:2103.13618, March 2021.

[59] L. Balkenhol, D. Dutcher, A. Spurio Mancini, A. Doussot, K. Benabed, S. Galli, P.A.R. Ade, A.J. Anderson, B. Ansarinejad, M. Archipley, A.N. Bender, B.A. Benson, F. Bianchini, L.E. Bleem, F.R. Bouchet, L. Bryant, E. Camphuis, J.E. Carlstrom, T.W. Cecil, C.L. Chang, P. Chaubal, P.M. Chichura, T.-L. Chou, A. Coerver, T.M. Crawford, A. Cukierman, C. Daley, T. de Haan, K.R. Dibert, M.A. Dobbs, W. Everett, C. Feng, K.R. Ferguson,

A. Foster, A.E. Gambrel, R.W. Gardner, N. Goeckner-Wald, R. Gualtieri, F. Guidi, S. Guns, N.W. Halverson, E. Hivon, G.P. Holder, W.L. Holzapfel, J.C. Hood, N. Huang, L. Knox, M. Korman, C.-L. Kuo, A.T. Lee, A.E. Lowitz, C. Lu, M. Millea, J. Montgomery, Y. Nakato, T. Natoli, G.I. Noble, V. Novosad, Y. Omori, S. Padin, Z. Pan, P. Paschos, K. Prabhu, W. Quan, M. Rahimi, A. Rahlin, C.L. Reichardt, M. Rouble, J.E. Ruhl, E. Schiappucci, G. Smecher, J.A. Sobrin, A.A. Stark, J. Stephen, A. Suzuki, C. Tandoi, K.L. Thompson, B. Thorne, C. Tucker, C. Umilta, J.D. Vieira, G. Wang, N. Whitehorn, W.L.K. Wu, V. Yefremenko, M.R. Young, and J.A. Zebrowski. Measurement of the cmb temperature power spectrum and constraints on cosmology from the spt-3g 2018 ¡tt¿ and ¡ee¿ dataset. *Physical Review D*, 108 (2), July 2023. ISSN 2470-0029. doi: 10.1103/physrevd.108.023510. URL `http://dx.doi.org/10.1103/PhysRevD.108.023510`.

[60] Z. Pan, F. Bianchini, W.L.K. Wu, P.A.R. Ade, Z. Ahmed, E. Anderes, A.J. Anderson, B. Ansarinejad, M. Archipley, K. Aylor, L. Balkenhol, P.S. Barry, R. Basu Thakur, K. Benabed, A.N. Bender, B.A. Benson, L.E. Bleem, F.R. Bouchet, L. Bryant, K. Byrum, E. Camphuis, J.E. Carlstrom, F.W. Carter, T.W. Cecil, C.L. Chang, P. Chaubal, G. Chen, P.M. Chichura, H.-M. Cho, T.-L. Chou, J.-F. Cliche, A. Coerver, T.M. Crawford, A. Cukierman, C. Daley, T. de Haan, E.V. Denison, K.R. Dibert, J. Ding, M.A. Dobbs, A. Doussot, D. Dutcher, W. Everett, C. Feng, K.R. Ferguson, K. Fichman, A. Foster, J. Fu, S. Galli, A.E. Gambrel, R.W. Gardner, F. Ge, N. Goeckner-Wald, R. Gualtieri, F. Guidi, S. Guns, N. Gupta, N.W. Halverson, A.H. Harke-Hosemann, N.L. Harrington, J.W. Henning, G.C. Hilton, E. Hivon, G.P. Holder, W.L. Holzapfel, J.C. Hood, D. Howe, N. Huang, K.D. Irwin, O. Jeong, M. Jonas, A. Jones, F. Kéruzoré, T.S. Khaire, L. Knox, A.M. Kofman, M. Korman, D.L. Kubik, S. Kuhlmann, C.-L. Kuo, A.T. Lee, E.M. Leitch, K. Levy, A.E. Lowitz, C. Lu, A. Maniyar, F. Menanteau, S.S. Meyer, D. Michalik, M. Millea, J. Montgomery, A. Nadolski, Y. Nakato, T. Natoli, H. Nguyen, G.I. Noble, V. Novosad, Y. Omori, S. Padin, P. Paschos, J. Pearson, C.M. Posada, K. Prabhu, W. Quan, S. Raghunathan, M. Rahimi, A. Rahlin, C.L. Reichardt, D. Riebel, B. Riedel, J.E. Ruhl, J.T. Sayre, E. Schiappucci, E. Shirokoff, G. Smecher, J.A. Sobrin, A.A. Stark, J. Stephen, K.T. Story, A. Suzuki, S. Takakura, C. Tandoi, K.L. Thompson, B. Thorne, C. Trendafilova, C. Tucker, C. Umilta, L.R. Vale, K. Vanderlinde, J.D. Vieira, G. Wang, N. Whitehorn, V. Yefremenko, K.W. Yoon, M.R. Young, and J.A. Zebrowski. Measurement of gravitational lensing of the cosmic microwave background using spt-3g 2018 data. *Physical Review D*, 108(12), December 2023. ISSN 2470-0029. doi: 10.1103/physrevd.108.122005. URL `http://dx.doi.org/10.1103/PhysRevD.108.122005`.

[61] S. Guns, et al. Detection of Galactic and Extragalactic Millimeter-Wavelength Transient Sources with SPT-3G. *arXiv e-prints*, art. arXiv:2103.06166, March 2021.

[62] P. M. Chichura, A. Foster, C. Patel, N. Ossa-Jaen, P. A. R. Ade, Z. Ahmed, A. J. Anderson, M. Archipley, J. E. Austermann, J. S. Avva, L. Balkenhol, P. S. Barry, R. Basu Thakur, J. A. Beall, K. Benabed, A. N. Bender, B. A.

Benson, F. Bianchini, L. E. Bleem, F. R. Bouchet, L. Bryant, K. Byrum, J. E. Carlstrom, F. W. Carter, T. W. Cecil, C. L. Chang, P. Chaubal, G. Chen, H. C. Chiang, H.-M. Cho, T-L. Chou, R. Citron, J.-F. Cliche, T. M. Crawford, A. T. Crites, A. Cukierman, C. M. Daley, E. V. Denison, K. Dibert, J. Ding, M. A. Dobbs, D. Dutcher, W. Everett, C. Feng, K. R. Ferguson, J. Fu, S. Galli, J. Gallicchio, A. E. Gambrel, R. W. Gardner, E. M. George, N. Goeckner-Wald, R. Gualtieri, S. Guns, N. Gupta, R. Guyser, T. de Haan, N. W. Halverson, A. H. Harke-Hosemann, N. L. Harrington, J. W. Henning, G. C. Hilton, E. Hivon, G. P. Holder, W. L. Holzapfel, J. C. Hood, D. Howe, J. D. Hrubes, N. Huang, J. Hubmayr, K. D. Irwin, O. B. Jeong, M. Jonas, A. Jones, T. S. Khaire, L. Knox, A. M. Kofman, M. Korman, D. L. Kubik, S. Kuhlmann, C.-L. Kuo, A. T. Lee, E. M. Leitch, D. Li, A. Lowitz, C. Lu, D. P. Marrone, J. J. McMahon, S. S. Meyer, D. Michalik, M. Millea, L. M. Mocanu, J. Montgomery, C. Corbett Moran, A. Nadolski, T. Natoli, H. Nguyen, J. P. Nibarger, G. Noble, V. Novosad, Y. Omori, S. Padin, Z. Pan, P. Paschos, S. Patil, J. Pearson, K. A. Phadke, C. M. Posada, K. Prabhu, C. Pryke, W. Quan, A. Rahlin, C. L. Reichardt, D. Riebel, B. Riedel, M. Rouble, J. E. Ruhl, B. R. Saliwanchik, J. T. Sayre, K. K. Schaffer, E. Schiappucci, E. Shirokoff, C. Sievers, G. Smecher, J. A. Sobrin, A. Springmann, A. A. Stark, J. Stephen, K. T. Story, A. Suzuki, C. Tandoi, K. L. Thompson, B. Thorne, C. Tucker, C. Umilta, L. R. Vale, T. Veach, J. D. Vieira, G. Wang, N. Whitehorn, W. L. K. Wu, V. Yefremenko, K. W. Yoon, and M. R. Young. Asteroid measurements at millimeter wavelengths with the south pole telescope. *The Astrophysical Journal*, 936(2): 173, September 2022. ISSN 1538-4357. doi: 10.3847/1538-4357/ac89ec. URL `http://dx.doi.org/10.3847/1538-4357/ac89ec`.

[63] C. Tandoi, S. Guns, A. Foster, P. A. R. Ade, A. J. Anderson, B. Ansarinejad, M. Archipley, L. Balkenhol, K. Benabed, A. N. Bender, B. A. Benson, F. Bianchini, L. E. Bleem, F. R. Bouchet, L. Bryant, E. Camphuis, J. E. Carlstrom, T. W. Cecil, C. L. Chang, P. Chaubal, P. M. Chichura, T. L. Chou, A. Coerver, T. M. Crawford, A. Cukierman, C. Daley, T. de Haan, K. R. Dibert, M. A. Dobbs, A. Doussot, D. Dutcher, W. Everett, C. Feng, K. R. Ferguson, K. Fichman, S. Galli, A. E. Gambrel, R. W. Gardner, F. Ge, N. Goeckner-Wald, R. Gualtieri, F. Guidi, N. W. Halverson, E. Hivon, G. P. Holder, W. L. Holzapfel, J. C. Hood, N. Huang, F. Kéruzoré, L. Knox, M. Korman, K. Kornoelje, C. L. Kuo, A. T. Lee, K. Levy, A. E. Lowitz, C. Lu, A. Maniyar, F. Menanteau, M. Millea, J. Montgomery, Y. Moon, Y. Nakato, T. Natoli, G. I. Noble, V. Novosad, Y. Omori, S. Padin, Z. Pan, P. Paschos, K. A. Phadke, K. Prabhu, Z. Qu, W. Quan, M. Rahimi, A. Rahlin, C. L. Reichardt, C. Reuter, M. Rouble, J. E. Ruhl, E. Schiappucci, G. Smecher, J. A. Sobrin, A. A. Stark, J. Stephen, A. Suzuki, K. L. Thompson, B. Thorne, C. Trendafilova, C. Tucker, C. Umilta, J. D. Vieira, Y. Wan, G. Wang, N. Whitehorn, W. L. K. Wu, V. Yefremenko, M. R. Young, and J. A. Zebrowski. Flaring stars in a non-targeted mm-wave survey with spt-3g, 2024. URL `https://arxiv.org/abs/2401.13525`.

[64] A. N. Bender, P. A. R. Ade, A. J. Anderson, J. Avva, Z. Ahmed, K. Arnold, J. E. Austermann, R. Basu Thakur, B. A. Benson, L. E. Bleem, K. Byrum, J. E. Carlstrom, F. W. Carter, C. L. Chang, H. M. Cho, J. F. Cliche, T. M.

Crawford, A. Cukierman, D. A. Czaplewski, J. Ding, R. Divan, T. de Haan, M. A. Dobbs, D. Dutcher, W. Everett, A. Gilbert, J. C. Groh, R. Guyser, N. W. Halverson, A. Harke-Hosemann, N. L. Harrington, K. Hattori, J. W. Henning, G. C. Hilton, W. L. Holzapfel, N. Huang, K. D. Irwin, O. Jeong, T. Khaire, M. Korman, D. Kubik, C. L. Kuo, A. T. Lee, E. M. Leitch, S. Lendinez, S. S. Meyer, C. S. Miller, J. Montgomery, A. Nadolski, T. Natoli, H. Nguyen, V. Novosad, S. Padin, Z. Pan, J. Pearson, C. M. Posada, A. Rahlin, C. L. Reichardt, J. E. Ruhl, B. R. Saliwanchik, J. T. Sayre, J. A. Shariff, Ian Shirley, E. Shirokoff, G. Smecher, J. Sobrin, L. Stan, A. A. Stark, K. Story, A. Suzuki, Q. Y. Tang, K. L. Thompson, C. Tucker, K. Vanderlinde, J. D. Vieira, G. Wang, N. Whitehorn, V. Yefremenko, and K. W. Yoon. Integrated performance of a frequency domain multiplexing readout in the SPT-3G receiver. In Wayne S. Holland and Jonas Zmuidzinas, editors, *Millimeter, Submillimeter, and Far-Infrared Detectors and Instrumentation for Astronomy VIII*, volume 9914, page 99141D. International Society for Optics and Photonics, SPIE, 2016. doi: 10.1117/12.2232146. URL `https://doi.org/10.1117/12.2232146`.

[65] Avi Loeb. The dark ages of the universe. In *Scientific American*, volume 295, November 2006. doi: 10.1038/scientificamerican112006-2jrkRVe32VGFRMBCEkBWCB.

[66] A. J. Anderson, P. Barry, A. N. Bender, B. A. Benson, L. E. Bleem, J. E. Carlstrom, T. W. Cecil, C. L. Chang, T. M. Crawford, K. R. Dibert, M. A. Dobbs, K. Fichman, N. W. Halverson, W. L. Holzapfel, A. Hryciuk, K. S. Karkare, J. Li, M. Lisovenko, D. Marrone, J. McMahon, J. Montgomery, T. Natoli, Z. Pan, S. Raghunathan, C. L. Reichardt, M. Rouble, E. Shirokoff, G. Smecher, A. A. Stark, J. D. Vieira, and M. R. Young. Spt-3g+: Mapping the high-frequency cosmic microwave background using kinetic inductance detectors, 2022. URL `https://arxiv.org/abs/2208.08559`.

[67] Karia R. Dibert, Adam J. Anderson, Amy N. Bender, Bradford A. Benson, Federico Bianchini, John E. Carlstrom, Thomas M. Crawford, Riccardo Gualtieri, Yuuki Omori, Zhaodi Pan, Srinivasan Raghunathan, Christian L. Reichardt, and W.L. Kimmy Wu. Forecasting ground-based sensitivity to the rayleigh scattering of the cmb in the presence of astrophysical foregrounds. *Physical Review D*, 106(6), September 2022. ISSN 2470-0029. doi: 10.1103/physrevd.106.063502. URL `http://dx.doi.org/10.1103/PhysRevD.106.063502`.

[68] J. C. Hood II, A. Simpson, A. McDaniel, A. Foster, P. A. R. Ade, M. Ajello, A. J. Anderson, J. E. Austermann, J. A. Beall, A. N. Bender, B. A. Benson, F. Bianchini, L. E. Bleem, J. E. Carlstrom, C. L. Chang, P. Chaubal, H. C. Chiang, T-L. Chou, R. Citron, C. Corbett Moran, T. M. Crawford, A. T. Crites, T. de Haan, M. A. Dobbs, W. Everett, J. Gallicchio, E. M. George, N. Gupta, N. W. Halverson, G. C. Hilton, G. P. Holder, W. L. Holzapfel, J. D. Hrubes, N. Huang, J. Hubmayr, K. D. Irwin, L. Knox, A. T. Lee, D. Li, A. Lowitz, G. Madejski, M. Malkan, J. J. McMahon, S. S. Meyer, J. Montgomery, T. Natoli, J. P. Nibarger, G. Noble, V. Novosad, Y. Omori, S. Padin, S. Patil, C. Pryke, C. L. Reichardt, J. E. Ruhl, B. R. Saliwanchik,

K. K. Schaffer, C. Sievers, G. Smecher, A. A. Stark, C. Tucker, T. Veach, J. D. Vieira, G. Wang, N. Whitehorn, W. L. K. Wu, V. Yefremenko, J. A. Zebrowski, and L. Zhang. Simultaneous millimeter-wave, gamma-ray, and optical monitoring of the blazar pks 2326-502 during a flaring state. *The Astrophysical Journal Letters*, 945(2):L23, March 2023. ISSN 2041-8213. doi: 10.3847/2041-8213/acbf45. URL `http://dx.doi.org/10.3847/2041-8213/acbf45`.

[69] B. A. Benson, P. A. R. Ade, Z. Ahmed, S. W. Allen, K. Arnold, J. E. Austermann, A. N. Bender, L. E. Bleem, J. E. Carlstrom, C. L. Chang, H. M. Cho, J. F. Cliche, T. M. Crawford, A. Cukierman, T. de Haan, M. A. Dobbs, D. Dutcher, W. Everett, A. Gilbert, N. W. Halverson, D. Hanson, N. L. Harrington, K. Hattori, J. W. Henning, G. C. Hilton, G. P. Holder, W. L. Holzapfel, K. D. Irwin, R. Keisler, L. Knox, D. Kubik, C. L. Kuo, A. T. Lee, E. M. Leitch, D. Li, M. McDonald, S. S. Meyer, J. Montgomery, M. Myers, T. Natoli, H. Nguyen, V. Novosad, S. Padin, Z. Pan, J. Pearson, C. Reichardt, J. E. Ruhl, B. R. Saliwanchik, G. Simard, G. Smecher, J. T. Sayre, E. Shirokoff, A. A. Stark, K. Story, A. Suzuki, K. L. Thompson, C. Tucker, K. Vanderlinde, J. D. Vieira, A. Vikhlinin, G. Wang, V. Yefremenko, and K. W. Yoon. SPT-3G: a next-generation cosmic microwave background polarization experiment on the South Pole telescope. In Wayne S. Holland and Jonas Zmuidzinas, editors, *Millimeter, Submillimeter, and Far-Infrared Detectors and Instrumentation for Astronomy VII*, volume 9153 of *Society of Photo-Optical Instrumentation Engineers (SPIE) Conference Series*, page 91531P, July 2014. doi: 10.1117/12.2057305.

[70] Jonas Zmuidzinas. Superconducting microresonators: Physics and applications. *Annual Review of Condensed Matter Physics*, 3(1):169–214, 2012. doi: 10.1146/annurev-conmatphys-020911-125022. URL `https://doi.org/10.1146/annurev-conmatphys-020911-125022`.

[71] R. Adam, A. Adane, P. A. R. Ade, P. André, A. Andrianasolo, H. Aussel, A. Beelen, A. Benoît, A. Bideaud, N. Billot, and et al. The nika2 large-field-of-view millimetre continuum camera for the 30 m iram telescope. *Astronomy & Astrophysics*, 609:A115, Jan 2018. ISSN 1432-0746. doi: 10.1051/0004-6361/201731503. URL `http://dx.doi.org/10.1051/0004-6361/201731503`.

[72] J. J. A. Baselmans, J. Bueno, S. J. C. Yates, O. Yurduseven, N. Llombart, K. Karatsu, A. M. Baryshev, L. Ferrari, A. Endo, D. J. Thoen, P. J. de Visser, R. M. J. Janssen, V. Murugesan, E. F. C. Driessen, G. Coiffard, J. Martin-Pintado, P. Hargrave, and M. Griffin. A kilo-pixel imaging system for future space based far-infrared observatories using microwave kinetic inductance detectors. *Astronomy and Astrophysics*, 601:A89, May 2017. ISSN 0004-6361. doi: 10.1051/0004-6361/201629653. URL `http://adsabs.harvard.edu/abs/2017A%26A...601A..89B`.

[73] J. E. Austermann, et al. Millimeter-Wave Polarimeters Using Kinetic Inductance Detectors for TolTEC and Beyond. *Journal of Low Temperature Physics*, 193(3-4):120–127, November 2018. doi: 10.1007/s10909-018-1949-5.

[74] CCAT-Prime collaboration, M. Aravena, J. E. Austermann, K. Basu, N. Battaglia, B. Beringue, F. Bertoldi, F. Bigiel, J. R. Bond, P. C. Breysse, C. Broughton, R. Bustos, S. C. Chapman, M. Charmetant, S. K. Choi, D. T. Chung, S. E. Clark, N. F. Cothard, A. T. Crites, A. Dev, K. Douglas, C. J. Duell, H. Ebina, J. Erler, M. Fich, L. M. Fissel, S. Foreman, J. Gao, Pablo García, R. Giovanelli, M. P. Haynes, B. Hensley, T. Herter, R. Higgins, Z. Huber, J. Hubmayr, D. Johnstone, C. Karoumpis, Laura C. Keating, E. Komatsu, Y. Li, Benjamin Magnelli, B. C. Matthews, P. D. Meerburg, J. Meyers, V. Muralidhara, N. W. Murray, M. D. Niemack, T. Nikola, Y. Okada, D. A. Riechers, E. Rosolowsky, A. Roy, S. I. Sadavoy, R. Schaaf, P. Schilke, D. Scott, R. Simon, Adrian K. Sinclair, G. R. Sivakoff, G. J. Stacey, Amelia M. Stutz, J. Stutzki, M. Tahani, K. Thanjavur, R. A. Timmermann, J. N. Ullom, A. van Engelen, E. M. Vavagiakis, M. R. Vissers, J. D. Wheeler, S. D. M. White, Y. Zhu, and B. Zou. CCAT-prime Collaboration: Science Goals and Forecasts with Prime-Cam on the Fred Young Submillimeter Telescope. *arXiv e-prints*, art. arXiv:2107.10364, July 2021.

[75] Karia R. Dibert, Adam J. Anderson, Amy N. Bender, Bradford A. Benson, Federico Bianchini, John E. Carlstrom, Thomas M. Crawford, Riccardo Gualtieri, Yuuki Omori, Zhaodi Pan, Srinivasan Raghunathan, Christian L. Reichardt, and W. L. Kimmy Wu. Forecasting ground-based sensitivity to the Rayleigh scattering of the CMB in the presence of astrophysical foregrounds. *Physics Rev. D*, 106(6):063502, September 2022. doi: 10.1103/PhysRevD.106.063502.

[76] Maclean Rouble, Graeme M. Smecher, Adam J. Anderson, Peter S. Barry, Karia Dibert, Matt Dobbs, Kirit S. Karkare, and Joshua Montgomery. Rfice: large-scale gigahertz readout of frequency-multiplexed microwave kinetic inductance detectors. In Jonas Zmuidzinas and Jian-Rong Gao, editors, *Millimeter, Submillimeter, and Far-Infrared Detectors and Instrumentation for Astronomy XI*, page 139. SPIE, August 2022. doi: 10.1117/12.2630286. URL `http://dx.doi.org/10.1117/12.2630286`.

[77] Karia Dibert, Pete Barry, Zhaodi Pan, Adam Anderson, Bradford Benson, Clarence Chang, Kirit Karkare, Juliang Li, Tyler Natoli, Maclean Rouble, Erik Shirokoff, and Antony Stark. Development of mkids for measurement of the cosmic microwave background with the south pole telescope, 2021. URL `https://arxiv.org/abs/2111.04816`.

[78] K. R. Dibert, P. S. Barry, A. J. Anderson, B. A. Benson, T. Cecil, C. L. Chang, K. N. Fichman, K. Karkare, J. Li, T. Natoli, Z. Pan, M. Rouble, E. Shirokoff, and M. Young. Characterization of mkids for cmb observation at 220 ghz with the south pole telescope. *IEEE Transactions on Applied Superconductivity*, 33 (5):1–5, August 2023. ISSN 2378-7074. doi: 10.1109/tasc.2023.3250386. URL `http://dx.doi.org/10.1109/TASC.2023.3250386`.

[79] Peter Ade, James Aguirre, Zeeshan Ahmed, Simone Aiola, Aamir Ali, David Alonso, Marcelo A. Alvarez, Kam Arnold, Peter Ashton, Jason Austermann, Humna Awan, Carlo Baccigalupi, Taylor Baildon, Darcy Barron, Nick Battaglia, Richard Battye, Eric Baxter, Andrew Bazarko, James A. Beall,

Rachel Bean, Dominic Beck, Shawn Beckman, Benjamin Beringue, Federico Bianchini, Steven Boada, David Boettger, J. Richard Bond, Julian Borrill, Michael L. Brown, Sarah Marie Bruno, Sean Bryan, Erminia Calabrese, Victoria Calafut, Paolo Calisse, Julien Carron, Anthony Challinor, Grace Chesmore, Yuji Chinone, Jens Chluba, Hsiao-Mei Sherry Cho, Steve Choi, Gabriele Coppi, Nicholas F. Cothard, Kevin Coughlin, Devin Crichton, Kevin D. Crowley, Kevin T. Crowley, Ari Cukierman, John M. D'Ewart, Rolando Dünner, Tijmen de Haan, Mark Devlin, Simon Dicker, Joy Didier, Matt Dobbs, Bradley Dober, Cody J. Duell, Shannon Duff, Adri Duivenvoorden, Jo Dunkley, John Dusatko, Josquin Errard, Giulio Fabbian, Stephen Feeney, Simone Ferraro, Pedro Fluxà, Katherine Freese, Josef C. Frisch, Andrei Frolov, George Fuller, Brittany Fuzia, Nicholas Galitzki, Patricio A. Gallardo, Jose Tomas Galvez Ghersi, Jiansong Gao, Eric Gawiser, Martina Gerbino, Vera Gluscevic, Neil Goeckner-Wald, Joseph Golec, Sam Gordon, Megan Gralla, Daniel Green, Arpi Grigorian, John Groh, Chris Groppi, Yilun Guan, Jon E. Gudmundsson, Dongwon Han, Peter Hargrave, Masaya Hasegawa, Matthew Hasselfield, Makoto Hattori, Victor Haynes, Masashi Hazumi, Yizhou He, Erin Healy, Shawn W. Henderson, Carlos Hervias-Caimapo, Charles A. Hill, J. Colin Hill, Gene Hilton, Matt Hilton, Adam D. Hincks, Gary Hinshaw, Renée Hložek, Shirley Ho, Shuay-Pwu Patty Ho, Logan Howe, Zhiqi Huang, Johannes Hubmayr, Kevin Huffenberger, John P. Hughes, Anna Ijjas, Margaret Ikape, Kent Irwin, Andrew H. Jaffe, Bhuvnesh Jain, Oliver Jeong, Daisuke Kaneko, Ethan D. Karpel, Nobuhiko Katayama, Brian Keating, Sarah S. Kernasovskiy, Reijo Keskitalo, Theodore Kisner, Kenji Kiuchi, Jeff Klein, Kenda Knowles, Brian Koopman, Arthur Kosowsky, Nicoletta Krachmalnicoff, Stephen E. Kuenstner, Chao-Lin Kuo, Akito Kusaka, Jacob Lashner, Adrian Lee, Eunseong Lee, David Leon, Jason S.-Y. Leung, Antony Lewis, Yaqiong Li, Zack Li, Michele Limon, Eric Linder, Carlos Lopez-Caraballo, Thibaut Louis, Lindsay Lowry, Marius Lungu, Mathew Madhavacheril, Daisy Mak, Felipe Maldonado, Hamdi Mani, Ben Mates, Frederick Matsuda, Loïc Maurin, Phil Mauskopf, Andrew May, Nialh McCallum, Chris McKenney, Jeff McMahon, P. Daniel Meerburg, Joel Meyers, Amber Miller, Mark Mirmelstein, Kavilan Moodley, Moritz Munchmeyer, Charles Munson, Sigurd Naess, Federico Nati, Martin Navaroli, Laura Newburgh, Ho Nam Nguyen, Michael Niemack, Haruki Nishino, John Orlowski-Scherer, Lyman Page, Bruce Partridge, Julien Peloton, Francesca Perrotta, Lucio Piccirillo, Giampaolo Pisano, Davide Poletti, Roberto Puddu, Giuseppe Puglisi, Chris Raum, Christian L. Reichardt, Mathieu Remazeilles, Yoel Rephaeli, Dominik Riechers, Felipe Rojas, Anirban Roy, Sharon Sadeh, Yuki Sakurai, Maria Salatino, Mayuri Sathyanarayana Rao, Emmanuel Schaan, Marcel Schmittfull, Neelima Sehgal, Joseph Seibert, Uros Seljak, Blake Sherwin, Meir Shimon, Carlos Sierra, Jonathan Sievers, Precious Sikhosana, Maximiliano Silva-Feaver, Sara M. Simon, Adrian Sinclair, Praween Siritanasak, Kendrick Smith, Stephen R. Smith, David Spergel, Suzanne T. Staggs, George Stein, Jason R. Stevens, Radek Stompor, Aritoki Suzuki, Osamu Tajima, Satoru Takakura, Grant Teply, Daniel B. Thomas, Ben Thorne, Robert Thornton, Hy Trac, Calvin Tsai, Carole Tucker, Joel Ullom, Sunny Vagnozzi, Alexander van Engelen, Jeff Van Lanen, Daniel D. Van Winkle, Eve M. Vava-

giakis, Clara Vergès, Michael Vissers, Kasey Wagoner, Samantha Walker, Jon Ward, Ben Westbrook, Nathan Whitehorn, Jason Williams, Joel Williams, Edward J. Wollack, Zhilei Xu, Byeonghee Yu, Cyndia Yu, Fernando Zago, Hezi Zhang, and Ningfeng Zhu. The simons observatory: science goals and forecasts. *Journal of Cosmology and Astroparticle Physics*, 2019(02):056–056, Feb 2019. ISSN 1475-7516. doi: 10.1088/1475-7516/2019/02/056. URL `http://dx.doi.org/10.1088/1475-7516/2019/02/056`.

[80] S. K. Choi, J. Austermann, K. Basu, N. Battaglia, F. Bertoldi, D. T. Chung, N. F. Cothard, S. Duff, C. J. Duell, P. A. Gallardo, J. Gao, T. Herter, J. Hubmayr, M. D. Niemack, T. Nikola, D. Riechers, K. Rossi, G. J. Stacey, J. R. Stevens, E. M. Vavagiakis, M. Vissers, and S. Walker. Sensitivity of the prime-cam instrument on the ccat-prime telescope. *Journal of Low Temperature Physics*, 199(3–4):1089–1097, Mar 2020. ISSN 1573-7357. doi: 10.1007/s10909-020-02428-z. URL `http://dx.doi.org/10.1007/s10909-020-02428-z`.

[81] Kevork Abazajian, Graeme E. Addison, Peter Adshead, Zeeshan Ahmed, Daniel Akerib, Aamir Ali, Steven W. Allen, David Alonso, Marcelo Alvarez, Mustafa A. Amin, Adam Anderson, Kam S. Arnold, Peter Ashton, Carlo Baccigalupi, Debbie Bard, Denis Barkats, Darcy Barron, Peter S. Barry, James G. Bartlett, Ritoban Basu Thakur, Nicholas Battaglia, Rachel Bean, Chris Bebek, Amy N. Bender, Bradford A. Benson, Federico Bianchini, Colin A. Bischoff, Lindsey Bleem, James J. Bock, Sebastian Bocquet, Kimberly K. Boddy, J. Richard Bond, Julian Borrill, François R. Bouchet, Thejs Brinckmann, Michael L. Brown, Sean Bryan, Victor Buza, Karen Byrum, Carlos Hervias Caimapo, Erminia Calabrese, Victoria Calafut, Robert Caldwell, John E. Carlstrom, Julien Carron, Thomas Cecil, Anthony Challinor, Clarence L. Chang, Yuji Chinone, Hsiao-Mei Sherry Cho, Asantha Cooray, Will Coulton, Thomas M. Crawford, Abigail Crites, Ari Cukierman, Francis-Yan Cyr-Racine, Tijmen de Haan, Jacques Delabrouille, Mark Devlin, Eleonora Di Valentino, Marion Dierickx, Matt Dobbs, Shannon Duff, Cora Dvorkin, Joseph Eimer, Tucker Elleflot, Josquin Errard, Thomas Essinger-Hileman, Giulio Fabbian, Chang Feng, Simone Ferraro, Jeffrey P. Filippini, Raphael Flauger, Brenna Flaugher, Aurelien A. Fraisse, Andrei Frolov, Nicholas Galitzki, Patricio A. Gallardo, Silvia Galli, Ken Ganga, Martina Gerbino, Vera Gluscevic, Neil Goeckner-Wald, Daniel Green, Daniel Grin, Evan Grohs, Riccardo Gualtieri, Jon E. Gudmundsson, Ian Gullett, Nikhel Gupta, Salman Habib, Mark Halpern, Nils W. Halverson, Shaul Hanany, Kathleen Harrington, Masaya Hasegawa, Matthew Hasselfield, Masashi Hazumi, Katrin Heitmann, Shawn Henderson, Brandon Hensley, Charles Hill, J. Colin Hill, Renée Hložek, Shuay-Pwu Patty Ho, Thuong Hoang, Gil Holder, William Holzapfel, John Hood, Johannes Hubmayr, Kevin M. Huffenberger, Howard Hui, Kent Irwin, Oliver Jeong, Bradley R. Johnson, William C. Jones, Jae Hwan Kang, Kirit S. Karkare, Nobuhiko Katayama, Reijo Keskitalo, Theodore Kisner, Lloyd Knox, Brian J. Koopman, Arthur Kosowsky, John Kovac, Ely D. Kovetz, Steve Kuhlmann, Chaolin Kuo, Akito Kusaka, Anne Lähteenmäki, Charles R. Lawrence, Adrian T. Lee, Antony Lewis, Dale Li, Eric Linder, Marilena Loverde, Amy Lowitz,

Phil Lubin, Mathew S. Madhavacheril, Adam Mantz, Gabriela Marques, Frederick Matsuda, Philip Mauskopf, Heather McCarrick, Jeffrey McMahon, P. Daniel Meerburg, Jean-Baptiste Melin, Felipe Menanteau, Joel Meyers, Marius Millea, Joseph Mohr, Lorenzo Moncelsi, Maria Monzani, Tony Mroczkowski, Suvodip Mukherjee, Johanna Nagy, Toshiya Namikawa, Federico Nati, Tyler Natoli, Laura Newburgh, Michael D. Niemack, Haruki Nishino, Brian Nord, Valentine Novosad, Roger O'Brient, Stephen Padin, Steven Palladino, Bruce Partridge, Don Petravick, Elena Pierpaoli, Levon Pogosian, Karthik Prabhu, Clement Pryke, Giuseppe Puglisi, Benjamin Racine, Alexandra Rahlin, Mayuri Sathyanarayana Rao, Marco Raveri, Christian L. Reichardt, Mathieu Remazeilles, Graca Rocha, Natalie A. Roe, Anirban Roy, John E. Ruhl, Maria Salatino, Benjamin Saliwanchik, Emmanuel Schaan, Alessandro Schillaci, Benjamin Schmitt, Marcel M. Schmittfull, Douglas Scott, Neelima Sehgal, Sarah Shandera, Blake D. Sherwin, Erik Shirokoff, Sara M. Simon, Anže Slosar, David Spergel, Tyler St. Germaine, Suzanne T. Staggs, Antony Stark, Glenn D. Starkman, Radek Stompor, Chris Stoughton, Aritoki Suzuki, Osamu Tajima, Grant P. Teply, Keith Thompson, Ben Thorne, Peter Timbie, Maurizio Tomasi, Matthieu Tristram, Gregory Tucker, Caterina Umiltà, Alexander van Engelen, Eve M. Vavagiakis, Joaquin D. Vieira, Abigail G. Vieregg, Kasey Wagoner, Benjamin Wallisch, Gensheng Wang, Scott Watson, Ben Westbrook, Nathan Whitehorn, Edward J. Wollack, W. L. Kimmy Wu, Zhilei Xu, H. Y. Eric Yang, Siavash Yasini, Volodymyr G. Yefremenko, Ki Won Yoon, Edward Young, Cyndia Yu, and Andrea Zonca. Cmb-s4: Forecasting constraints on primordial gravitational waves. *The Astrophysical Journal*, 926(1):54, Feb 2022. ISSN 1538-4357. doi: 10.3847/1538-4357/ac1596. URL `http://dx.doi.org/10.3847/1538-4357/ac1596`.

[82] Qingjuan Yu, David N. Spergel, and Jeremiah P. Ostriker. Rayleigh Scattering and Microwave Background Fluctuations. , 558(1):23–28, September 2001. doi: 10.1086/322482.

[83] William R. Coulton, Benjamin Beringue, and P. Daniel Meerburg. Primordial information content of rayleigh anisotropies. *Physical Review D*, 103(4), feb 2021. doi: 10.1103/physrevd.103.043501. URL `https://doi.org/10.1103%2Fphysrevd.103.043501`.

[84] Benjamin Beringue, P. Daniel Meerburg, Joel Meyers, and Nicholas Battaglia. Cosmology with Rayleigh scattering of the cosmic microwave background. , 2021(1):060, January 2021. doi: 10.1088/1475-7516/2021/01/060.

[85] Hee-Won Lee and Hee Il Kim. Rayleigh scattering cross-section redward of Lyα by atomic hydrogen. *Monthly Notices of the Royal Astronomical Society*, 347 (3):802–806, 01 2004. ISSN 0035-8711. doi: 10.1111/j.1365-2966.2004.07255.x. URL `https://doi.org/10.1111/j.1365-2966.2004.07255.x`.

[86] M Remazeilles and J Chluba. Extracting foreground-obscured mu-distortion anisotropies to constrain primordial non-gaussianity. *Monthly Notices of the Royal Astronomical Society*, 478(1):807–824, Apr 2018. ISSN 1365-2966. doi: 10.1093/mnras/sty1034. URL `http://dx.doi.org/10.1093/mnras/sty1034`.

[87] Srinivasan Raghunathan, Nathan Whitehorn, Marcelo A. Alvarez, Han Aung, Nicholas Battaglia, Gilbert P. Holder, Daisuke Nagai, Elena Pierpaoli, Christian L. Reichardt, and Joaquin D. Vieira. Constraining Cluster Virialization Mechanism and Cosmology Using Thermal-SZ-selected Clusters from Future CMB Surveys. , 926(2):172, February 2022. doi: 10.3847/1538-4357/ac4712.

[88] B. Thorne, J. Dunkley, D. Alonso, and S. Næss. The Python Sky Model: software for simulating the Galactic microwave sky. *Monthly Notices of the Royal Astronomical Society*, 469(3):2821–2833, 05 2017. ISSN 0035-8711. doi: 10.1093/mnras/stx949. URL `https://doi.org/10.1093/mnras/stx949`.

[89] Andrea Zonca, Ben Thorne, Nicoletta Krachmalnicoff, and Julian Borrill. The python sky model 3 software. *Journal of Open Source Software*, 6(67):3783, Nov 2021. ISSN 2475-9066. doi: 10.21105/joss.03783. URL `http://dx.doi.org/10.21105/joss.03783`.

[90] G. Lagache, H. Dole, and J.-L. Puget. Modelling infrared galaxy evolution using a phenomenological approach. , 338:555–571, January 2003. doi: 10.1046/j.1365-8711.2003.05971.x.

[91] Cien Shang, Zoltán. Haiman, Lloyd Knox, and S. Peng Oh. Improved models for cosmic infrared background anisotropies: new constraints on the infrared galaxy population. , 421(4):2832–2845, April 2012. doi: 10.1111/j.1365-2966.2012.20510.x.

[92] M. P. Viero, C. L. Reichardt, B. A. Benson, L. E. Bleem, J. Bock, J. E. Carlstrom, C. L. Chang, H. M. Cho, T. M. Crawford, A. T. Crites, T. de Haan, M. A. Dobbs, W. B. Everett, E. M. George, N. W. Halverson, N. L. Harrington, G. Holder, W. L. Holzapfel, Z. Hou, J. D. Hrubes, L. Knox, A. T. Lee, D. Luong-Van, D. P. Marrone, J. J. McMahon, S. S. Meyer, M. Millea, L. M. Mocanu, J. J. Mohr, L. Moncelsi, S. Padin, C. Pryke, J. E. Ruhl, K. K. Schaffer, P. Serra, E. Shirokoff, Z. Staniszewski, A. A. Stark, K. T. Story, K. Vand erlinde, J. D. Vieira, R. Williamson, and M. Zemcov. Measurements of the Cross-spectra of the Cosmic Infrared and Microwave Backgrounds from 95 to 1200 GHz. , 881(2):96, Aug 2019. doi: 10.3847/1538-4357/ab2da0.

[93] N Gupta, C L Reichardt, P A R Ade, A J Anderson, M Archipley, J E Austermann, J S Avva, J A Beall, A N Bender, B A Benson, F Bianchini, L E Bleem, J E Carlstrom, C L Chang, H C Chiang, R Citron, C Corbett Moran, T M Crawford, A T Crites, T de Haan, M A Dobbs, W Everett, C Feng, J Gallicchio, E M George, A Gilbert, N W Halverson, N Harrington, J W Henning, G C Hilton, G P Holder, W L Holzapfel, Z Hou, J D Hrubes, N Huang, J Hubmayr, K D Irwin, L Knox, A T Lee, D Li, A Lowitz, D Luong-Van, D P Marrone, J J McMahon, S S Meyer, L M Mocanu, J J Mohr, J Montgomery, A Nadolski, T Natoli, J P Nibarger, G I Noble, V Novosad, S Padin, S Patil, C Pryke, J E Ruhl, B R Saliwanchik, J T Sayre, K K Schaffer, E Shirokoff, C Sievers, G Smecher, Z Staniszewski, A A Stark, K T Story, E R Switzer, C Tucker, K Vanderlinde, T Veach, J D Vieira, G Wang, N Whitehorn, R Williamson, W L K Wu, V Yefremenko, and L Zhang. Fractional polarization of extragalactic sources in the 500 deg2 SPTpol survey. *Monthly Notices of the Royal As-*

tronomical Society, 490(4):5712–5721, oct 2019. doi: 10.1093/mnras/stz2905. URL `https://doi.org/10.1093%2Fmnras%2Fstz2905`.

[94] Z.-Y. Cai, A. Lapi, J.-Q. Xia, G. De Zotti, M. Negrello, C. Gruppioni, E. Rigby, G. Castex, J. Delabrouille, and L. Danese. A Hybrid Model for the Evolution of Galaxies and Active Galactic Nuclei in the Infrared. , 768: 21, May 2013. doi: 10.1088/0004-637X/768/1/21.

[95] Rahul Datta, Simone Aiola, Steve K Choi, Mark Devlin, Joanna Dunkley, Rolando Dünner, Patricio A Gallardo, Megan Gralla, Mark Halpern, Matthew Hasselfield, Matt Hilton, Adam D Hincks, Shuay-Pwu P Ho, Johannes Hubmayr, Kevin M Huffenberger, John P Hughes, Arthur Kosowsky, Carlos H Ló pez-Caraballo, Thibaut Louis, Marius Lungu, Tobias Marriage, Loïc Maurin, Jeff McMahon, Kavilan Moodley, Sigurd K Naess, Federico Nati, Michael D Niemack, Lyman A Page, Bruce Partridge, Heather Prince, Suzanne T Staggs, Eric R Switzer, Edward J Wollack, and Gerrit Farren. The atacama cosmology telescope: two-season ACTPol extragalactic point sources and their polarization properties. *Monthly Notices of the Royal Astronomical Society*, 486(4):5239–5262, nov 2018. doi: 10.1093/mnras/sty2934. URL `https://doi.org/10.1093%2Fmnras%2Fsty2934`.

[96] Planck Collaboration, Aghanim, N., Akrami, Y., Arroja, F., Ashdown, M., Aumont, J., Baccigalupi, C., Ballardini, M., Banday, A. J., Barreiro, R. B., Bartolo, N., Basak, S., Battye, R., Benabed, K., Bernard, J.-P., Bersanelli, M., Bielewicz, P., Bock, J. J., Bond, J. R., Borrill, J., Bouchet, F. R., Boulanger, F., Bucher, M., Burigana, C., Butler, R. C., Calabrese, E., Cardoso, J.-F., Carron, J., Casaponsa, B., Challinor, A., Chiang, H. C., Colombo, L. P. L., Combet, C., Contreras, D., Crill, B. P., Cuttaia, F., de Bernardis, P., de Zotti, G., Delabrouille, J., Delouis, J.-M., Désert, F.-X., Di Valentino, E., Dickinson, C., Diego, J. M., Donzelli, S., Doré, O., Douspis, M., Ducout, A., Dupac, X., Efstathiou, G., Elsner, F., Enßlin, T. A., Eriksen, H. K., Falgarone, E., Fantaye, Y., Fergusson, J., Fernandez-Cobos, R., Finelli, F., Forastieri, F., Frailis, M., Franceschi, E., Frolov, A., Galeotta, S., Galli, S., Ganga, K., Génova-Santos, R. T., Gerbino, M., Ghosh, T., González-Nuevo, J., Górski, K. M., Gratton, S., Gruppuso, A., Gudmundsson, J. E., Hamann, J., Handley, W., Hansen, F. K., Helou, G., Herranz, D., Hildebrandt, S. R., Hivon, E., Huang, Z., Jaffe, A. H., Jones, W. C., Karakci, A., Keihänen, E., Keskitalo, R., Kiiveri, K., Kim, J., Kisner, T. S., Knox, L., Krachmalnicoff, N., Kunz, M., Kurki-Suonio, H., Lagache, G., Lamarre, J.-M., Langer, M., Lasenby, A., Lattanzi, M., Lawrence, C. R., Le Jeune, M., Leahy, J. P., Lesgourgues, J., Levrier, F., Lewis, A., Liguori, M., Lilje, P. B., Lilley, M., Lindholm, V., López-Caniego, M., Lubin, P. M., Ma, Y.-Z., Macías-Pérez, J. F., Maggio, G., Maino, D., Mandolesi, N., Mangilli, A., Marcos-Caballero, A., Maris, M., Martin, P. G., Martinelli, M., Martínez-González, E., Matarrese, S., Mauri, N., McEwen, J. D., Meerburg, P. D., Meinhold, P. R., Melchiorri, A., Mennella, A., Migliaccio, M., Millea, M., Mitra, S., Miville-Deschênes, M.-A., Molinari, D., Moneti, A., Montier, L., Morgante, G., Moss, A., Mottet, S., Münchmeyer, M., Natoli, P., Nørgaard-Nielsen, H. U., Oxborrow, C. A., Pagano, L., Paoletti, D., Partridge, B., Patanchon, G., Pearson, T. J., Peel, M., Peiris, H. V.,

Perrotta, F., Pettorino, V., Piacentini, F., Polastri, L., Polenta, G., Puget, J.-L., Rachen, J. P., Reinecke, M., Remazeilles, M., Renault, C., Renzi, A., Rocha, G., Rosset, C., Roudier, G., Rubiño-Martín, J. A., Ruiz-Granados, B., Salvati, L., Sandri, M., Savelainen, M., Scott, D., Shellard, E. P. S., Shiraishi, M., Sirignano, C., Sirri, G., Spencer, L. D., Sunyaev, R., Suur-Uski, A.-S., Tauber, J. A., Tavagnacco, D., Tenti, M., Terenzi, L., Toffolatti, L., Tomasi, M., Trombetti, T., Valiviita, J., Van Tent, B., Vibert, L., Vielva, P., Villa, F., Vittorio, N., Wandelt, B. D., Wehus, I. K., White, M., White, S. D. M., Zacchei, A., and Zonca, A. Planck 2018 results - i. overview and the cosmological legacy of planck. *A&A*, 641:A1, 2020. doi: 10.1051/0004-6361/201833880. URL `https://doi.org/10.1051/0004-6361/201833880`.

[97] W. L. Holzapfel, T. M. Wilbanks, P. A. R. Ade, S. E. Church, M. L. Fischer, P. D. Mauskopf, D. E. Osgood, and A. E. Lange. The sunyaev-zeldovich infrared experiment: A millimeter-wave receiver for cluster cosmology. *The Astrophysical Journal*, 479(1):17–30, Apr 1997. ISSN 1538-4357. doi: 10.1086/303840. URL `http://dx.doi.org/10.1086/303840`.

[98] P. D. Mauskopf, P. A. R. Ade, S. W. Allen, S. E. Church, A. C. Edge, K. M. Ganga, W. L. Holzapfel, A. E. Lange, B. K. Rownd, B. J. Philhour, and M. C. Runyan. A Determination of the Hubble Constant Using Measurements of X-Ray Emission and the Sunyaev-Zeldovich Effect at Millimeter Wavelengths in the Cluster Abell 1835. , 538(2):505–516, August 2000. doi: 10.1086/309137.

[99] J. A. Tauber, N. Mandolesi, J. L. Puget, T. Banos, M. Bersanelli, F. R. Bouchet, R. C. Butler, J. Charra, G. Crone, J. Dodsworth, G. Efstathiou, R. Gispert, G. Guyot, A. Gregorio, J. J. Juillet, J. M. Lamarre, R. J. Laureijs, C. R. Lawrence, H. U. Nørgaard-Nielsen, T. Passvogel, J. M. Reix, D. Texier, L. Vibert, A. Zacchei, P. A. R. Ade, N. Aghanim, B. Aja, E. Alippi, L. Aloy, P. Armand, M. Arnaud, A. Arondel, A. Arreola-Villanueva, E. Artal, E. Artina, A. Arts, M. Ashdown, J. Aumont, M. Azzaro, A. Bacchetta, C. Baccigalupi, M. Baker, M. Balasini, A. Balbi, A. J. Banday, G. Barbier, R. B. Barreiro, M. Bartelmann, P. Battaglia, E. Battaner, K. Benabed, J. L. Beney, R. Beneyton, K. Bennett, A. Benoit, J. P. Bernard, P. Bhandari, R. Bhatia, M. Biggi, R. Biggins, G. Billig, Y. Blanc, H. Blavot, J. J. Bock, A. Bonaldi, R. Bond, J. Bonis, J. Borders, J. Borrill, L. Boschini, F. Boulanger, J. Bouvier, M. Bouzit, R. Bowman, E. Bréelle, T. Bradshaw, M. Braghin, M. Bremer, D. Brienza, D. Broszkiewicz, C. Burigana, M. Burkhalter, P. Cabella, T. Cafferty, M. Cairola, S. Caminade, P. Camus, C. M. Cantalupo, B. Cappellini, J. F. Cardoso, R. Carr, A. Catalano, L. Cayón, M. Cesa, M. Chaigneau, A. Challinor, A. Chamballu, J. P. Chambelland, M. Charra, L. Y. Chiang, G. Chlewicki, P. R. Christensen, S. Church, E. Ciancietta, M. Cibrario, R. Cizeron, D. Clements, B. Collaudin, J. M. Colley, S. Colombi, A. Colombo, F. Colombo, O. Corre, F. Couchot, B. Cougrand, A. Coulais, P. Couzin, B. Crane, B. Crill, M. Crook, D. Crumb, F. Cuttaia, U. Dörl, P. da Silva, R. Daddato, C. Damasio, L. Danese, G. D'Aquino, O. D'Arcangelo, K. Dassas, R. D. Davies, W. Davies, R. J. Davis, P. de Bernardis, D. de Chambure, G. de Gasperis, M. L. de La Fuente, P. de Paco, A. de Rosa, G. de Troia, G. de Zotti, M. Dehamme, J. Delabrouille, J. M. Delouis, F. X. Désert,

G. di Girolamo, C. Dickinson, E. Doelling, K. Dolag, I. Domken, M. Douspis, D. Doyle, S. Du, D. Dubruel, C. Dufour, C. Dumesnil, X. Dupac, P. Duret, C. Eder, A. Elfving, T. A. Enßlin, P. Eng, K. English, H. K. Eriksen, P. Estaria, M. C. Falvella, F. Ferrari, F. Finelli, A. Fishman, S. Fogliani, S. Foley, A. Fonseca, G. Forma, O. Forni, P. Fosalba, J. J. Fourmond, M. Frailis, C. Franceschet, E. Franceschi, S. François, M. Frerking, M. F. Gómez-Reñasco, K. M. Górski, T. C. Gaier, S. Galeotta, K. Ganga, J. García Lázaro, A. Garnica, M. Gaspard, E. Gavila, M. Giard, G. Giardino, G. Gienger, Y. Giraud-Heraud, J. M. Glorian, M. Griffin, A. Gruppuso, L. Guglielmi, D. Guichon, B. Guillaume, P. Guillouet, J. Haissinski, F. K. Hansen, J. Hardy, D. Harrison, A. Hazell, M. Hechler, V. Heckenauer, D. Heinzer, R. Hell, S. Henrot-Versillé, C. Hernández-Monteagudo, D. Herranz, J. M. Herreros, V. Hervier, A. Heske, A. Heurtel, S. R. Hildebrandt, R. Hills, E. Hivon, M. Hobson, D. Hollert, W. Holmes, A. Hornstrup, W. Hovest, R. J. Hoyland, G. Huey, K. M. Huffenberger, N. Hughes, U. Israelsson, B. Jackson, A. Jaffe, T. R. Jaffe, T. Jagemann, N. C. Jessen, J. Jewell, W. Jones, M. Juvela, J. Kaplan, P. Karlman, F. Keck, E. Keihänen, M. King, T. S. Kisner, P. Kletzkine, R. Kneissl, J. Knoche, L. Knox, T. Koch, M. Krassenburg, H. Kurki-Suonio, A. Lähteenmäki, G. Lagache, E. Lagorio, P. Lami, J. Lande, A. Lange, F. Langlet, R. Lapini, M. Lapolla, A. Lasenby, M. Le Jeune, J. P. Leahy, M. Lefebvre, F. Legrand, G. Le Meur, R. Leonardi, B. Leriche, C. Leroy, P. Leutenegger, S. M. Levin, P. B. Lilje, C. Lindensmith, M. Linden-Vørnle, A. Loc, Y. Longval, P. M. Lubin, T. Luchik, I. Luthold, J. F. Macias-Perez, T. Maciaszek, C. MacTavish, S. Madden, B. Maffei, C. Magneville, D. Maino, A. Mambretti, B. Mansoux, D. Marchioro, M. Maris, F. Marliani, J. C. Marrucho, J. Martí-Canales, E. Martínez-González, A. Martín-Polegre, P. Martin, C. Marty, W. Marty, S. Masi, M. Massardi, S. Matarrese, F. Matthai, P. Mazzotta, A. McDonald, P. McGrath, A. Mediavilla, P. R. Meinhold, J. B. Mélin, F. Melot, L. Mendes, A. Mennella, C. Mervier, L. Meslier, M. Miccolis, M. A. Miville-Deschenes, A. Moneti, D. Montet, L. Montier, J. Mora, G. Morgante, G. Morigi, G. Morinaud, N. Morisset, D. Mortlock, S. Mottet, J. Mulder, D. Munshi, A. Murphy, P. Murphy, P. Musi, J. Narbonne, P. Naselsky, A. Nash, F. Nati, P. Natoli, B. Netterfield, J. Newell, M. Nexon, C. Nicolas, P. H. Nielsen, N. Ninane, F. Noviello, D. Novikov, I. Novikov, I. J. O'Dwyer, P. Oldeman, P. Olivier, L. Ouchet, C. A. Oxborrow, L. Pérez-Cuevas, L. Pagan, C. Paine, F. Pajot, R. Paladini, F. Pancher, J. Panh, G. Parks, P. Parnaudeau, B. Partridge, B. Parvin, J. P. Pascual, F. Pasian, D. P. Pearson, T. Pearson, M. Pecora, O. Perdereau, L. Perotto, F. Perrotta, F. Piacentini, M. Piat, E. Pierpaoli, O. Piersanti, E. Plaige, S. Plaszczynski, P. Platania, E. Pointecouteau, G. Polenta, N. Ponthieu, L. Popa, G. Poulleau, T. Poutanen, G. Prézeau, L. Pradell, M. Prina, S. Prunet, J. P. Rachen, D. Rambaud, F. Rame, I. Rasmussen, J. Rautakoski, W. T. Reach, R. Rebolo, M. Reinecke, J. Reiter, C. Renault, S. Ricciardi, P. Rideau, T. Riller, I. Ristorcelli, J. B. Riti, G. Rocha, Y. Roche, R. Pons, R. Rohlfs, D. Romero, S. Roose, C. Rosset, S. Rouberol, M. Rowan-Robinson, J. A. Rubiño-Martín, P. Rusconi, B. Rusholme, M. Salama, E. Salerno, M. Sandri, D. Santos, J. L. Sanz, L. Sauter, F. Sauvage, G. Savini, M. Schmelzel, A. Schnorhk, W. Schwarz, D. Scott, M. D. Seiffert, P. Shellard, C. Shih, M. Sias, J. I. Silk, R. Sil-

vestri, R. Sippel, G. F. Smoot, J. L. Starck, P. Stassi, J. Sternberg, F. Stivoli, V. Stolyarov, R. Stompor, L. Stringhetti, D. Strommen, T. Stute, R. Sudiwala, R. Sugimura, R. Sunyaev, J. F. Sygnet, M. Türler, E. Taddei, J. Tallon, C. Tamiatto, M. Taurigna, D. Taylor, L. Terenzi, S. Thuerey, J. Tillis, G. Tofani, L. Toffolatti, E. Tommasi, M. Tomasi, E. Tonazzini, J. P. Torre, S. Tosti, F. Touze, M. Tristram, J. Tuovinen, M. Tuttlebee, G. Umana, L. Valenziano, D. Vallée, M. van der Vlis, F. van Leeuwen, J. C. Vanel, B. van-Tent, J. Varis, E. Vassallo, C. Vescovi, F. Vezzu, D. Vibert, P. Vielva, J. Vierra, F. Villa, N. Vittorio, C. Vuerli, L. A. Wade, A. R. Walker, B. D. Wandelt, C. Watson, D. Werner, M. White, S. D. M. White, A. Wilkinson, P. Wilson, A. Woodcraft, B. Yoffo, M. Yun, V. Yurchenko, D. Yvon, B. Zhang, O. Zimmermann, A. Zonca, and D. Zorita. Planck pre-launch status: The Planck mission. , 520:A1, September 2010. doi: 10.1051/0004-6361/200912983.

[100] R. J. Thornton, P. A. R. Ade, S. Aiola, F. E. Angilè, M. Amiri, J. A. Beall, D. T. Becker, H. M. Cho, S. K. Choi, P. Corlies, K. P. Coughlin, R. Datta, M. J. Devlin, S. R. Dicker, R. Dünner, J. W. Fowler, A. E. Fox, P. A. Gallardo, J. Gao, E. Grace, M. Halpern, M. Hasselfield, S. W. Henderson, G. C. Hilton, A. D. Hincks, S. P. Ho, J. Hubmayr, K. D. Irwin, J. Klein, B. Koopman, Dale Li, T. Louis, M. Lungu, L. Maurin, J. McMahon, C. D. Munson, S. Naess, F. Nati, L. Newburgh, J. Nibarger, M. D. Niemack, P. Niraula, M. R. Nolta, L. A. Page, C. G. Pappas, A. Schillaci, B. L. Schmitt, N. Sehgal, J. L. Sievers, S. M. Simon, S. T. Staggs, C. Tucker, M. Uehara, J. van Lanen, J. T. Ward, and E. J. Wollack. The Atacama Cosmology Telescope: The Polarization-sensitive ACTPol Instrument. , 227(2):21, December 2016. doi: 10.3847/1538-4365/227/2/21.

[101] J. E. Geach, J. S. Dunlop, M. Halpern, Ian Smail, P. van der Werf, D. M. Alexander, O. Almaini, I. Aretxaga, V. Arumugam, V. Asboth, M. Banerji, J. Beanlands, P. N. Best, A. W. Blain, M. Birkinshaw, E. L. Chapin, S. C. Chapman, C-C. Chen, A. Chrysostomou, C. Clarke, D. L. Clements, C. Conselice, K. E. K. Coppin, W. I. Cowley, A. L. R. Danielson, S. Eales, A. C. Edge, D. Farrah, A. Gibb, C. M. Harrison, N. K. Hine, D. Hughes, R. J. Ivison, M. Jarvis, T. Jenness, S. F. Jones, A. Karim, M. Koprowski, K. K. Knudsen, C. G. Lacey, T. Mackenzie, G. Marsden, K. McAlpine, R. McMahon, R. Meijerink, M. J. Michałowski, S. J. Oliver, M. J. Page, J. A. Peacock, D. Rigopoulou, E. I. Robson, I. Roseboom, K. Rotermund, Douglas Scott, S. Serjeant, C. Simpson, J. M. Simpson, D. J. B. Smith, M. Spaans, F. Stanley, J. A. Stevens, A. M. Swinbank, T. Targett, A. P. Thomson, E. Valiante, D. A. Wake, T. M. A. Webb, C. Willott, J. A. Zavala, and M. Zemcov. The scuba-2 cosmology legacy survey: 850 m maps, catalogues and number counts. *Monthly Notices of the Royal Astronomical Society*, 465 (2):1789–1806, November 2016. ISSN 1365-2966. doi: 10.1093/mnras/stw2721. URL `http://dx.doi.org/10.1093/mnras/stw2721`.

[102] Chian-Chou Chen, Cheng-Lin Liao, Ian Smail, A. M. Swinbank, Y. Ao, A. J. Bunker, S. C. Chapman, B. Hatsukade, R. J. Ivison, Minju M. Lee, Stephen Serjeant, Hideki Umehata, Wei-Hao Wang, and Y. Zhao. An alma spectroscopic survey of the brightest submillimeter galaxies in the scuba-2-cosmos

field (as2cospec): Survey description and first results. *The Astrophysical Journal*, 929(2):159, April 2022. ISSN 1538-4357. doi: 10.3847/1538-4357/ac61df. URL `http://dx.doi.org/10.3847/1538-4357/ac61df`.

[103] Samuel J. Schmidt, Brice Ménard, Ryan Scranton, Christopher B. Morrison, Mubdi Rahman, and Andrew M. Hopkins. Inferring the redshift distribution of the cosmic infrared background. , 446(3):2696–2708, January 2015. doi: 10.1093/mnras/stu2275.

[104] Masato Shirasaki. Impact of radio sources and cosmic infrared background on thermal Sunyaev-Zel'dovich - gravitational lensing cross-correlation. , 483(1): 342–351, February 2019. doi: 10.1093/mnras/sty3162.

[105] Mathew S. Madhavacheril, J. Colin Hill, Sigurd Næss, Graeme E. Addison, Simone Aiola, Taylor Baildon, Nicholas Battaglia, Rachel Bean, J. Richard Bond, Erminia Calabrese, Victoria Calafut, Steve K. Choi, Omar Darwish, Rahul Datta, Mark J. Devlin, Joanna Dunkley, Rolando Dünner, Simone Ferraro, Patricio A. Gallardo, Vera Gluscevic, Mark Halpern, Dongwon Han, Matthew Hasselfield, Matt Hilton, Adam D. Hincks, Renée Hložek, Shuay-Pwu Patty Ho, Kevin M. Huffenberger, John P. Hughes, Brian J. Koopman, Arthur Kosowsky, Martine Lokken, Thibaut Louis, Marius Lungu, Amanda MacInnis, Loïc Maurin, Jeffrey J. McMahon, Kavilan Moodley, Federico Nati, Michael D. Niemack, Lyman A. Page, Bruce Partridge, Naomi Robertson, Neelima Sehgal, Emmanuel Schaan, Alessandro Schillaci, Blake D. Sherwin, Cristóbal Sifón, Sara M. Simon, David N. Spergel, Suzanne T. Staggs, Emilie R. Storer, Alexander van Engelen, Eve M. Vavagiakis, Edward J. Wollack, and Zhilei Xu. Atacama Cosmology Telescope: Component-separated maps of CMB temperature and the thermal Sunyaev-Zel'dovich effect. , 102(2):023534, July 2020. doi: 10.1103/PhysRevD.102.023534.

[106] L. E. Bleem, T. M. Crawford, B. Ansarinejad, B. A. Benson, S. Bocquet, J. E. Carlstrom, C. L. Chang, R. Chown, A. T. Crites, T. de Haan, M. A. Dobbs, W. B. Everett, E. M. George, R. Gualtieri, N. W. Halverson, G. P. Holder, W. L. Holzapfel, J. D. Hrubes, L. Knox, A. T. Lee, D. Luong-Van, D. P. Marrone, J. J. McMahon, S. S. Meyer, M. Millea, L. M. Mocanu, J. J. Mohr, T. Natoli, Y. Omori, S. Padin, C. Pryke, S. Raghunathan, C. L. Reichardt, J. E. Ruhl, K. K. Schaffer, E. Shirokoff, Z. Staniszewski, A. A. Stark, J. D. Vieira, and R. Williamson. CMB/kSZ and Compton-y Maps from 2500 deg^2 of SPT-SZ and Planck Survey Data. , 258(2):36, February 2022. doi: 10.3847/1538-4365/ac35e9.

[107] Tilman Tröster, Alexander J. Mead, Catherine Heymans, Ziang Yan, David Alonso, Marika Asgari, Maciej Bilicki, Andrej Dvornik, Hendrik Hildebrandt, Benjamin Joachimi, Arun Kannawadi, Konrad Kuijken, Peter Schneider, Huan Yuan Shan, Ludovic van Waerbeke, and Angus H. Wright. Joint constraints on cosmology and the impact of baryon feedback: Combining KiDS-1000 lensing with the thermal Sunyaev-Zeldovich effect from Planck and ACT. , 660:A27, April 2022. doi: 10.1051/0004-6361/202142197.

[108] J. Sánchez, Y. Omori, C. Chang, L. E. Bleem, T. Crawford, A. Drlica-Wagner, S. Raghunathan, G. Zacharegkas, T. M. C. Abbott, M. Aguena,

A. Alarcon, S. Allam, O. Alves, A. Amon, S. Avila, E. Baxter, K. Bechtol, B. A. Benson, G. M. Bernstein, E. Bertin, S. Bocquet, D. Brooks, D. L. Burke, A. Campos, J. E. Carlstrom, A. Carnero Rosell, M. Carrasco Kind, J. Carretero, F. J. Castander, R. Cawthon, C. L. Chang, A. Chen, A. Choi, R. Chown, M. Costanzi, A. T. Crites, M. Crocce, L. N. da Costa, M. E. S. Pereira, T. de Haan, J. De Vicente, J. DeRose, S. Desai, H. T. Diehl, M. A. Dobbs, S. Dodelson, P. Doel, J. Elvin-Poole, W. Everett, S. Everett, I. Ferrero, B. Flaugher, P. Fosalba, J. Frieman, J. García-Bellido, M. Gatti, E. M. George, D. W. Gerdes, G. Giannini, D. Gruen, R. A. Gruendl, J. Gschwend, G. Gutierrez, N. W. Halverson, S. R. Hinton, G. P. Holder, D. L. Hollowood, W. L. Holzapfel, K. Honscheid, J. D. Hrubes, D. J. James, L. Knox, K. Kuehn, N. Kuropatkin, O. Lahav, A. T. Lee, D. Luong-Van, N. MacCrann, J. L. Marshall, J. McCullough, J. J. McMahon, P. Melchior, J. Mena-Fernández, F. Menanteau, R. Miquel, L. Mocanu, J. J. Mohr, J. Muir, J. Myles, T. Natoli, S. Padin, A. Palmese, S. Pandey, F. Paz-Chinchón, A. Pieres, A. A. Plazas Malagón, A. Porredon, C. Pryke, M. Raveri, C. L. Reichardt, M. Rodriguez-Monroy, A. J. Ross, J. E. Ruhl, E. Rykoff, C. Sánchez, E. Sanchez, V. Scarpine, K. K. Schaffer, I. Sevilla-Noarbe, E. Sheldon, E. Shirokoff, M. Smith, M. Soares-Santos, Z. Staniszewski, A. A. Stark, E. Suchyta, M. E. C. Swanson, G. Tarle, D. Thomas, M. A. Troxel, D. L. Tucker, J. D. Vieira, M. Vincenzi, N. Weaverdyck, R. Williamson, B. Yanny, B. Yin, DES Collaboration, and SPT Collaboration. Mapping gas around massive galaxies: cross-correlation of DES Y3 galaxies and Compton-y maps from SPT and Planck. , 522(2):3163–3182, June 2023. doi: 10.1093/mnras/stad1167.

[109] Stephen J. Osborne, Duncan Hanson, and Olivier Doré. Extragalactic foreground contamination in temperature-based CMB lens reconstruction. , 2014 (3):024, March 2014. doi: 10.1088/1475-7516/2014/03/024.

[110] A. van Engelen, S. Bhattacharya, N. Sehgal, G. P. Holder, O. Zahn, and D. Nagai. CMB Lensing Power Spectrum Biases from Galaxies and Clusters Using High-angular Resolution Temperature Maps. , 786(1):13, May 2014. doi: 10.1088/0004-637X/786/1/13.

[111] Yuuki Omori. Agora: Multi-Component Simulation for Cross-Survey Science. *arXiv e-prints*, art. arXiv:2212.07420, December 2022. doi: 10.48550/arXiv.2212.07420.

[112] Planck Collaboration, P. A. R. Ade, N. Aghanim, C. Armitage-Caplan, M. Arnaud, M. Ashdown, F. Atrio-Barandela, J. Aumont, C. Baccigalupi, A. J. Banday, R. B. Barreiro, J. G. Bartlett, S. Basak, E. Battaner, K. Benabed, A. Benoît, A. Benoit-Lévy, J. P. Bernard, M. Bersanelli, M. Bethermin, P. Bielewicz, J. Bobin, J. J. Bock, A. Bonaldi, J. R. Bond, J. Borrill, F. R. Bouchet, F. Boulanger, M. Bridges, M. Bucher, C. Burigana, R. C. Butler, J. F. Cardoso, A. Catalano, A. Challinor, A. Chamballu, H. C. Chiang, L. Y. Chiang, P. R. Christensen, S. Church, D. L. Clements, S. Colombi, L. P. L. Colombo, F. Couchot, A. Coulais, B. P. Crill, A. Curto, F. Cuttaia, L. Danese, R. D. Davies, P. de Bernardis, A. de Rosa, G. de Zotti, J. Delabrouille, J. M. Delouis, F. X. Désert, J. M. Diego, H. Dole, S. Donzelli, O. Doré, M. Douspis, X. Dupac, G. Efstathiou, T. A. Enßlin, H. K. Eriksen, F. Finelli, O. Forni,

M. Frailis, E. Franceschi, S. Galeotta, K. Ganga, M. Giard, G. Giardino, Y. Giraud-Héraud, J. González-Nuevo, K. M. Górski, S. Gratton, A. Gregorio, A. Gruppuso, J. E. Gudmundsson, F. K. Hansen, D. Hanson, D. Harrison, S. Henrot-Versillé, C. Hernández-Monteagudo, D. Herranz, S. R. Hildebrandt, E. Hivon, M. Hobson, W. A. Holmes, A. Hornstrup, W. Hovest, K. M. Huffenberger, A. H. Jaffe, T. R. Jaffe, W. C. Jones, M. Juvela, E. Keihänen, R. Keskitalo, T. S. Kisner, R. Kneissl, J. Knoche, L. Knox, M. Kunz, H. Kurki-Suonio, F. Lacasa, G. Lagache, A. Lähteenmäki, J. M. Lamarre, A. Lasenby, R. J. Laureijs, C. R. Lawrence, R. Leonardi, J. León-Tavares, J. Lesgourgues, M. Liguori, P. B. Lilje, M. Linden-Vørnle, M. López-Caniego, P. M. Lubin, J. F. Macías-Pérez, B. Maffei, D. Maino, N. Mandolesi, M. Maris, D. J. Marshall, P. G. Martin, E. Martínez-González, S. Masi, M. Massardi, S. Matarrese, F. Matthai, P. Mazzotta, A. Melchiorri, L. Mendes, A. Mennella, M. Migliaccio, S. Mitra, M. A. Miville-Deschênes, A. Moneti, L. Montier, G. Morgante, D. Mortlock, D. Munshi, P. Naselsky, F. Nati, P. Natoli, C. B. Netterfield, H. U. Nørgaard-Nielsen, F. Noviello, D. Novikov, I. Novikov, S. Osborne, C. A. Oxborrow, F. Paci, L. Pagano, F. Pajot, D. Paoletti, F. Pasian, G. Patanchon, O. Perdereau, L. Perotto, F. Perrotta, F. Piacentini, M. Piat, E. Pierpaoli, D. Pietrobon, S. Plaszczynski, E. Pointecouteau, G. Polenta, N. Ponthieu, L. Popa, T. Poutanen, G. W. Pratt, G. Prézeau, S. Prunet, J. L. Puget, J. P. Rachen, R. Rebolo, M. Reinecke, M. Remazeilles, C. Renault, S. Ricciardi, T. Riller, I. Ristorcelli, G. Rocha, C. Rosset, G. Roudier, M. Rowan-Robinson, B. Rusholme, M. Sandri, D. Santos, G. Savini, D. Scott, M. D. Seiffert, P. Serra, E. P. S. Shellard, L. D. Spencer, J. L. Starck, V. Stolyarov, R. Stompor, R. Sudiwala, R. Sunyaev, F. Sureau, D. Sutton, A. S. Suur-Uski, J. F. Sygnet, J. A. Tauber, D. Tavagnacco, L. Terenzi, L. Toffolatti, M. Tomasi, M. Tristram, M. Tucci, J. Tuovinen, L. Valenziano, J. Valiviita, B. Van Tent, P. Vielva, F. Villa, N. Vittorio, L. A. Wade, B. D. Wandelt, S. D. M. White, D. Yvon, A. Zacchei, and A. Zonca. Planck 2013 results. XVIII. The gravitational lensing-infrared background correlation. , 571:A18, November 2014. doi: 10.1051/0004-6361/201321540.

[113] Planck Collaboration, P. A. R. Ade, N. Aghanim, C. Armitage-Caplan, M. Arnaud, M. Ashdown, F. Atrio-Barandela, J. Aumont, C. Baccigalupi, A. J. Banday, R. B. Barreiro, J. G. Bartlett, E. Battaner, K. Benabed, A. Benoît, A. Benoit-Lévy, J. P. Bernard, M. Bersanelli, M. Bethermin, P. Bielewicz, K. Blagrave, J. Bobin, J. J. Bock, A. Bonaldi, J. R. Bond, J. Borrill, F. R. Bouchet, F. Boulanger, M. Bridges, M. Bucher, C. Burigana, R. C. Butler, J. F. Cardoso, A. Catalano, A. Challinor, A. Chamballu, X. Chen, H. C. Chiang, L. Y. Chiang, P. R. Christensen, S. Church, D. L. Clements, S. Colombi, L. P. L. Colombo, F. Couchot, A. Coulais, B. P. Crill, A. Curto, F. Cuttaia, L. Danese, R. D. Davies, R. J. Davis, P. de Bernardis, A. de Rosa, G. de Zotti, J. Delabrouille, J. M. Delouis, F. X. Désert, C. Dickinson, J. M. Diego, H. Dole, S. Donzelli, O. Doré, M. Douspis, X. Dupac, G. Efstathiou, T. A. Enßlin, H. K. Eriksen, F. Finelli, O. Forni, M. Frailis, E. Franceschi, S. Galeotta, K. Ganga, T. Ghosh, M. Giard, Y. Giraud-Héraud, J. González-Nuevo, K. M. Górski, S. Gratton, A. Gregorio, A. Gruppuso, F. K. Hansen, D. Hanson, D. Harrison, G. Helou, S. Henrot-Versillé, C. Hernández-Monteagudo, D. Herranz, S. R. Hildebrandt, E. Hivon, M. Hobson, W. A. Holmes, A. Horn-

strup, W. Hovest, K. M. Huffenberger, A. H. Jaffe, T. R. Jaffe, W. C. Jones, M. Juvela, P. Kalberla, E. Keihänen, J. Kerp, R. Keskitalo, T. S. Kisner, R. Kneissl, J. Knoche, L. Knox, M. Kunz, H. Kurki-Suonio, F. Lacasa, G. Lagache, A. Lähteenmäki, J. M. Lamarre, M. Langer, A. Lasenby, R. J. Laureijs, C. R. Lawrence, R. Leonardi, J. León-Tavares, J. Lesgourgues, M. Liguori, P. B. Lilje, M. Linden-Vørnle, M. López-Caniego, P. M. Lubin, J. F. Macías-Pérez, B. Maffei, D. Maino, N. Mandolesi, M. Maris, D. J. Marshall, P. G. Martin, E. Martínez-González, S. Masi, M. Massardi, S. Matarrese, F. Matthai, P. Mazzotta, A. Melchiorri, L. Mendes, A. Mennella, M. Migliaccio, S. Mitra, M. A. Miville-Deschênes, A. Moneti, L. Montier, G. Morgante, D. Mortlock, D. Munshi, J. A. Murphy, P. Naselsky, F. Nati, P. Natoli, C. B. Netterfield, H. U. Nørgaard-Nielsen, F. Noviello, D. Novikov, I. Novikov, S. Osborne, C. A. Oxborrow, F. Paci, L. Pagano, F. Pajot, R. Paladini, D. Paoletti, B. Partridge, F. Pasian, G. Patanchon, O. Perdereau, L. Perotto, F. Perrotta, F. Piacentini, M. Piat, E. Pierpaoli, D. Pietrobon, S. Plaszczynski, E. Pointecouteau, G. Polenta, N. Ponthieu, L. Popa, T. Poutanen, G. W. Pratt, G. Prézeau, S. Prunet, J. L. Puget, J. P. Rachen, W. T. Reach, R. Rebolo, M. Reinecke, M. Remazeilles, C. Renault, S. Ricciardi, T. Riller, I. Ristorcelli, G. Rocha, C. Rosset, G. Roudier, M. Rowan-Robinson, J. A. Rubiño-Martín, B. Rusholme, M. Sandri, D. Santos, G. Savini, D. Scott, M. D. Seiffert, P. Serra, E. P. S. Shellard, L. D. Spencer, J. L. Starck, V. Stolyarov, R. Stompor, R. Sudiwala, R. Sunyaev, F. Sureau, D. Sutton, A. S. Suur-Uski, J. F. Sygnet, J. A. Tauber, D. Tavagnacco, L. Terenzi, L. Toffolatti, M. Tomasi, M. Tristram, M. Tucci, J. Tuovinen, M. Türler, L. Valenziano, J. Valiviita, B. Van Tent, P. Vielva, F. Villa, N. Vittorio, L. A. Wade, B. D. Wandelt, N. Welikala, M. White, S. D. M. White, B. Winkel, D. Yvon, A. Zacchei, and A. Zonca. Planck 2013 results. XXX. Cosmic infrared background measurements and implications for star formation. , 571:A30, November 2014. doi: 10.1051/0004-6361/201322093.

[114] A. Curto, M. Tucci, M. Kunz, and E. Martínez-González. The CIB-lensing bispectrum: impact on primordial non-Gaussianity and detectability for the Planck mission. , 450(4):3778–3801, July 2015. doi: 10.1093/mnras/stv849.

[115] Daisy Suet Ying Mak, Anthony Challinor, George Efstathiou, and Guilaine Lagache. Measurement of CIB power spectra over large sky areas from Planck HFI maps. , 466(1):286–319, April 2017. doi: 10.1093/mnras/stw3112.

[116] Fiona McCarthy and Mathew S. Madhavacheril. Improving models of the cosmic infrared background using cmb lensing mass maps. *Physical Review D*, 103(10), May 2021. ISSN 2470-0029. doi: 10.1103/physrevd.103.103515. URL `http://dx.doi.org/10.1103/PhysRevD.103.103515`.

[117] Fiona McCarthy, Mathew S. Madhavacheril, and Abhishek S. Maniyar. Constraints on primordial non-gaussianity from halo bias measured through cmb lensing cross-correlations, 2022. URL `https://arxiv.org/abs/2210.01049`.

[118] M. P. Viero, L. Wang, M. Zemcov, G. Addison, A. Amblard, V. Arumugam, H. Aussel, M. Béthermin, J. Bock, A. Boselli, V. Buat, D. Burgarella, C. M. Casey, D. L. Clements, A. Conley, L. Conversi, A. Cooray, G. De Zotti, C. D.

Dowell, D. Farrah, A. Franceschini, J. Glenn, M. Griffin, E. Hatziminaoglou, S. Heinis, E. Ibar, R. J. Ivison, G. Lagache, L. Levenson, L. Marchetti, G. Marsden, H. T. Nguyen, B. O'Halloran, S. J. Oliver, A. Omont, M. J. Page, A. Papageorgiou, C. P. Pearson, I. Pérez-Fournon, M. Pohlen, D. Rigopoulou, I. G. Roseboom, M. Rowan-Robinson, B. Schulz, D. Scott, N. Seymour, D. L. Shupe, A. J. Smith, M. Symeonidis, M. Vaccari, I. Valtchanov, J. D. Vieira, J. Wardlow, and C. K. Xu. HerMES: Cosmic Infrared Background Anisotropies and the Clustering of Dusty Star-forming Galaxies. , 772(1):77, July 2013. doi: 10.1088/0004-637X/772/1/77.

[119] Omar Darwish, Mathew S Madhavacheril, Blake D Sherwin, Simone Aiola, Nicholas Battaglia, James A Beall, Daniel T Becker, J Richard Bond, Erminia Calabrese, Steve K Choi, Mark J Devlin, Jo Dunkley, Rolando Dünner, Simone Ferraro, Anna E Fox, Patricio A Gallardo, Yilun Guan, Mark Halpern, Dongwon Han, Matthew Hasselfield, J Colin Hill, Gene C Hilton, Matt Hilton, Adam D Hincks, Shuay-Pwu Patty Ho, J Hubmayr, John P Hughes, Brian J Koopman, Arthur Kosowsky, J Van Lanen, Thibaut Louis, Marius Lungu, Amanda MacInnis, Loïc Maurin, Jeffrey McMahon, Kavilan Moodley, Sigurd Naess, Toshiya Namikawa, Federico Nati, Laura Newburgh, John P Nibarger, Michael D Niemack, Lyman A Page, Bruce Partridge, Frank J Qu, Naomi Robertson, Alessandro Schillaci, Benjamin Schmitt, Neelima Sehgal, Cristóbal Sifón, David N Spergel, Suzanne Staggs, Emilie Storer, Alexander van Engelen, and Edward J Wollack. The atacama cosmology telescope: a cmb lensing mass map over 2100 square degrees of sky and its cross-correlation with boss-cmass galaxies. *Monthly Notices of the Royal Astronomical Society*, 500(2): 2250–2263, November 2020. ISSN 1365-2966. doi: 10.1093/mnras/staa3438. URL `http://dx.doi.org/10.1093/mnras/staa3438`.

[120] Alexander van Engelen, Blake D. Sherwin, Neelima Sehgal, Graeme E. Addison, Rupert Allison, Nick Battaglia, Francesco de Bernardis, J. Richard Bond, Erminia Calabrese, Kevin Coughlin, Devin Crichton, Rahul Datta, Mark J. Devlin, Joanna Dunkley, Rolando Dünner, Patricio Gallardo, Emily Grace, Megan Gralla, Amir Hajian, Matthew Hasselfield, Shawn Henderson, J. Colin Hill, Matt Hilton, Adam D. Hincks, Renée Hlozek, Kevin M. Huffenberger, John P. Hughes, Brian Koopman, Arthur Kosowsky, Thibaut Louis, Marius Lungu, Mathew Madhavacheril, Loïc Maurin, Jeff McMahon, Kavilan Moodley, Charles Munson, Sigurd Naess, Federico Nati, Laura Newburgh, Michael D. Niemack, Michael R. Nolta, Lyman A. Page, Christine Pappas, Bruce Partridge, Benjamin L. Schmitt, Jonathan L. Sievers, Sara Simon, David N. Spergel, Suzanne T. Staggs, Eric R. Switzer, Jonathan T. Ward, and Edward J. Wollack. The atacama cosmology telescope: Lensing of cmb temperature and polarization derived from cosmic infrared background cross-correlation. *The Astrophysical Journal*, 808(1):7, July 2015. ISSN 1538-4357. doi: 10.1088/0004-637x/808/1/7. URL `http://dx.doi.org/10.1088/0004-637X/808/1/7`.

[121] G. P. Holder, M. P. Viero, O. Zahn, K. A. Aird, B. A. Benson, S. Bhattacharya, L. E. Bleem, J. Bock, M. Brodwin, J. E. Carlstrom, C. L. Chang, H-M. Cho, A. Conley, T. M. Crawford, A. T. Crites, T. de Haan, M. A.

Dobbs, J. Dudley, E. M. George, N. W. Halverson, W. L. Holzapfel, S. Hoover, Z. Hou, J. D. Hrubes, R. Keisler, L. Knox, A. T. Lee, E. M. Leitch, M. Lueker, D. Luong-Van, G. Marsden, D. P. Marrone, J. J. McMahon, J. Mehl, S. S. Meyer, M. Millea, J. J. Mohr, T. E. Montroy, S. Padin, T. Plagge, C. Pryke, C. L. Reichardt, J. E. Ruhl, J. T. Sayre, K. K. Schaffer, B. Schulz, L. Shaw, E. Shirokoff, H. G. Spieler, Z. Staniszewski, A. A. Stark, K. T. Story, A. van Engelen, K. Vanderlinde, J. D. Vieira, R. Williamson, and M. Zemcov. A cosmic microwave background lensing mass map and its correlation with the cosmic infrared background. *The Astrophysical Journal*, 771(1): L16, June 2013. ISSN 2041-8213. doi: 10.1088/2041-8205/771/1/l16. URL `http://dx.doi.org/10.1088/2041-8205/771/1/L16`.

[122] F. Lacasa, A. Pénin, and N. Aghanim. Non-Gaussianity of the cosmic infrared background anisotropies - I. Diagrammatic formalism and application to the angular bispectrum. , 439(1):123–142, March 2014. doi: 10.1093/mnras/stt2373.

[123] Cien Shang, Zoltán. Haiman, Lloyd Knox, and S. Peng Oh. Improved models for cosmic infrared background anisotropies: new constraints on the infrared galaxy population. , 421(4):2832–2845, April 2012. doi: 10.1111/j.1365-2966.2012.20510.x.

[124] Jeremy Tinker, Andrey V. Kravtsov, Anatoly Klypin, Kevork Abazajian, Michael Warren, Gustavo Yepes, Stefan Gottlöber, and Daniel E. Holz. Toward a halo mass function for precision cosmology: The limits of universality. *The Astrophysical Journal*, 688(2):709–728, dec 2008. doi: 10.1086/591439. URL `https://doi.org/10.1086%2F591439`.

[125] Jeremy L. Tinker and Andrew R. Wetzel. WHAT DOES CLUSTERING TELL US ABOUT THE BUILDUP OF THE RED SEQUENCE? *The Astrophysical Journal*, 719(1):88–103, jul 2010. doi: 10.1088/0004-637x/719/1/88. URL `https://doi.org/10.1088%2F0004-637x%2F719%2F1%2F88`.

[126] Matthieu Béthermin, Lingyu Wang, Olivier Doré, Guilaine Lagache, Mark Sargent, Emanuele Daddi, Morgane Cousin, and Hervé Aussel. The redshift evolution of the distribution of star formation among dark matter halos as seen in the infrared. *Astronomy amp; Astrophysics*, 557:A66, September 2013. ISSN 1432-0746. doi: 10.1051/0004-6361/201321688. URL `http://dx.doi.org/10.1051/0004-6361/201321688`.

[127] N. R. Hall, R. Keisler, L. Knox, C. L. Reichardt, P. A. R. Ade, K. A. Aird, B. A. Benson, L. E. Bleem, J. E. Carlstrom, C. L. Chang, H. M. Cho, T. M. Crawford, A. T. Crites, T. de Haan, M. A. Dobbs, E. M. George, N. W. Halverson, G. P. Holder, W. L. Holzapfel, J. D. Hrubes, M. Joy, A. T. Lee, E. M. Leitch, M. Lueker, J. J. McMahon, J. Mehl, S. S. Meyer, J. J. Mohr, T. E. Montroy, S. Padin, T. Plagge, C. Pryke, J. E. Ruhl, K. K. Schaffer, L. Shaw, E. Shirokoff, H. G. Spieler, B. Stalder, Z. Staniszewski, A. A. Stark, E. R. Switzer, K. Vanderlinde, J. D. Vieira, R. Williamson, and O. Zahn. Angular Power Spectra of the Millimeter-wavelength Background Light from Dusty Star-forming Galaxies with the South Pole Telescope. , 718(2):632–646, August 2010. doi: 10.1088/0004-637X/718/2/632.

[128] Wei Quan. *Analysis of Cosmic Microwave Background Temperature and E-Mode Polarization Anisotropies with 2019 and 2020 Data from the South Pole Telescope.* Phd thesis, University of Chicago, Chicago, IL, 2024. `http://proxy.uchicago.edu/login?url=https://www.proquest.com/dissertations-theses/analysis-cosmic-microwave-background-temperature/docview/3063316723/se-2`.

[129] N. Aghanim, Y. Akrami, M. Ashdown, J. Aumont, C. Baccigalupi, M. Ballardini, A. J. Banday, R. B. Barreiro, N. Bartolo, S. Basak, R. Battye, K. Benabed, J.-P. Bernard, M. Bersanelli, P. Bielewicz, J. J. Bock, J. R. Bond, J. Borrill, F. R. Bouchet, F. Boulanger, M. Bucher, C. Burigana, R. C. Butler, E. Calabrese, J.-F. Cardoso, J. Carron, A. Challinor, H. C. Chiang, J. Chluba, L. P. L. Colombo, C. Combet, D. Contreras, B. P. Crill, F. Cuttaia, P. de Bernardis, G. de Zotti, J. Delabrouille, J.-M. Delouis, E. Di Valentino, J. M. Diego, O. Doré, M. Douspis, A. Ducout, X. Dupac, S. Dusini, G. Efstathiou, F. Elsner, T. A. Enßlin, H. K. Eriksen, Y. Fantaye, M. Farhang, J. Fergusson, R. Fernandez-Cobos, F. Finelli, F. Forastieri, M. Frailis, A. A. Fraisse, E. Franceschi, A. Frolov, S. Galeotta, S. Galli, K. Ganga, R. T. Génova-Santos, M. Gerbino, T. Ghosh, J. González-Nuevo, K. M. Górski, S. Gratton, A. Gruppuso, J. E. Gudmundsson, J. Hamann, W. Handley, F. K. Hansen, D. Herranz, S. R. Hildebrandt, E. Hivon, Z. Huang, A. H. Jaffe, W. C. Jones, A. Karakci, E. Keihänen, R. Keskitalo, K. Kiiveri, J. Kim, T. S. Kisner, L. Knox, N. Krachmalnicoff, M. Kunz, H. Kurki-Suonio, G. Lagache, J.-M. Lamarre, A. Lasenby, M. Lattanzi, C. R. Lawrence, M. Le Jeune, P. Lemos, J. Lesgourgues, F. Levrier, A. Lewis, M. Liguori, P. B. Lilje, M. Lilley, V. Lindholm, M. López-Caniego, P. M. Lubin, Y.-Z. Ma, J. F. Macías-Pérez, G. Maggio, D. Maino, N. Mandolesi, A. Mangilli, A. Marcos-Caballero, M. Maris, P. G. Martin, M. Martinelli, E. Martínez-González, S. Matarrese, N. Mauri, J. D. McEwen, P. R. Meinhold, A. Melchiorri, A. Mennella, M. Migliaccio, M. Millea, S. Mitra, M.-A. Miville-Deschênes, D. Molinari, L. Montier, G. Morgante, A. Moss, P. Natoli, H. U. Nørgaard-Nielsen, L. Pagano, D. Paoletti, B. Partridge, G. Patanchon, H. V. Peiris, F. Perrotta, V. Pettorino, F. Piacentini, L. Polastri, G. Polenta, J.-L. Puget, J. P. Rachen, M. Reinecke, M. Remazeilles, A. Renzi, G. Rocha, C. Rosset, G. Roudier, J. A. Rubiño-Martín, B. Ruiz-Granados, L. Salvati, M. Sandri, M. Savelainen, D. Scott, E. P. S. Shellard, C. Sirignano, G. Sirri, L. D. Spencer, R. Sunyaev, A.-S. Suur-Uski, J. A. Tauber, D. Tavagnacco, M. Tenti, L. Toffolatti, M. Tomasi, T. Trombetti, L. Valenziano, J. Valiviita, B. Van Tent, L. Vibert, P. Vielva, F. Villa, N. Vittorio, B. D. Wandelt, I. K. Wehus, M. White, S. D. M. White, A. Zacchei, and A. Zonca. Planck2018 results: Vi. cosmological parameters. *Astronomy amp; Astrophysics*, 641:A6, September 2020. ISSN 1432-0746. doi: 10.1051/0004-6361/201833910. URL `http://dx.doi.org/10.1051/0004-6361/201833910`.

[130] N. Aghanim, Y. Akrami, M. Ashdown, J. Aumont, C. Baccigalupi, M. Ballardini, A. J. Banday, R. B. Barreiro, N. Bartolo, S. Basak, K. Benabed, J.-P. Bernard, M. Bersanelli, P. Bielewicz, J. J. Bock, J. R. Bond, J. Borrill, F. R. Bouchet, F. Boulanger, M. Bucher, C. Burigana, E. Calabrese, J.-F. Cardoso,

J. Carron, A. Challinor, H. C. Chiang, L. P. L. Colombo, C. Combet, B. P. Crill, F. Cuttaia, P. de Bernardis, G. de Zotti, J. Delabrouille, E. Di Valentino, J. M. Diego, O. Doré, M. Douspis, A. Ducout, X. Dupac, G. Efstathiou, F. Elsner, T. A. Enßlin, H. K. Eriksen, Y. Fantaye, R. Fernandez-Cobos, F. Finelli, F. Forastieri, M. Frailis, A. A. Fraisse, E. Franceschi, A. Frolov, S. Galeotta, S. Galli, K. Ganga, R. T. Génova-Santos, M. Gerbino, T. Ghosh, J. González-Nuevo, K. M. Górski, S. Gratton, A. Gruppuso, J. E. Gudmundsson, J. Hamann, W. Handley, F. K. Hansen, D. Herranz, E. Hivon, Z. Huang, A. H. Jaffe, W. C. Jones, A. Karakci, E. Keihänen, R. Keskitalo, K. Kiiveri, J. Kim, L. Knox, N. Krachmalnicoff, M. Kunz, H. Kurki-Suonio, G. Lagache, J.-M. Lamarre, A. Lasenby, M. Lattanzi, C. R. Lawrence, M. Le Jeune, F. Levrier, A. Lewis, M. Liguori, P. B. Lilje, V. Lindholm, M. López-Caniego, P. M. Lubin, Y.-Z. Ma, J. F. Macías-Pérez, G. Maggio, D. Maino, N. Mandolesi, A. Mangilli, A. Marcos-Caballero, M. Maris, P. G. Martin, E. Martínez-González, S. Matarrese, N. Mauri, J. D. McEwen, A. Melchiorri, A. Mennella, M. Migliaccio, M.-A. Miville-Deschênes, D. Molinari, A. Moneti, L. Montier, G. Morgante, A. Moss, P. Natoli, L. Pagano, D. Paoletti, B. Partridge, G. Patanchon, F. Perrotta, V. Pettorino, F. Piacentini, L. Polastri, G. Polenta, J.-L. Puget, J. P. Rachen, M. Reinecke, M. Remazeilles, A. Renzi, G. Rocha, C. Rosset, G. Roudier, J. A. Rubiño-Martín, B. Ruiz-Granados, L. Salvati, M. Sandri, M. Savelainen, D. Scott, C. Sirignano, R. Sunyaev, A.-S. Suur-Uski, J. A. Tauber, D. Tavagnacco, M. Tenti, L. Toffolatti, M. Tomasi, T. Trombetti, J. Valiviita, B. Van Tent, P. Vielva, F. Villa, N. Vittorio, B. D. Wandelt, I. K. Wehus, M. White, S. D. M. White, A. Zacchei, and A. Zonca. Planck2018 results: Viii. gravitational lensing. *Astronomy amp; Astrophysics*, 641:A8, September 2020. ISSN 1432-0746. doi: 10.1051/0004-6361/201833886. URL `http://dx.doi.org/10.1051/0004-6361/201833886`.

[131] Peter Behroozi, Risa H Wechsler, Andrew P Hearin, and Charlie Conroy. Universemachine: The correlation between galaxy growth and dark matter halo assembly from z = 010. *Monthly Notices of the Royal Astronomical Society*, 488(3):3143–3194, May 2019. ISSN 1365-2966. doi: 10.1093/mnras/stz1182. URL `http://dx.doi.org/10.1093/mnras/stz1182`.

[132] A. S. G. Robotham and S. P. Driver. Thegalex-sdss nuv and fuv flux density and local star formation rate: Thegalex-sdss and local star formation rate. *Monthly Notices of the Royal Astronomical Society*, 413(4):2570–2582, March 2011. ISSN 0035-8711. doi: 10.1111/j.1365-2966.2011.18327.x. URL `http://dx.doi.org/10.1111/j.1365-2966.2011.18327.x`.

[133] Samir Salim, R. Michael Rich, Stephane Charlot, Jarle Brinchmann, Benjamin D. Johnson, David Schiminovich, Mark Seibert, Ryan Mallery, Timothy M. Heckman, Karl Forster, Peter G. Friedman, D. Christopher Martin, Patrick Morrissey, Susan G. Neff, Todd Small, Ted K. Wyder, Luciana Bianchi, Jose Donas, Young-Wook Lee, Barry F. Madore, Bruno Milliard, Alex S. Szalay, Barry Y. Welsh, and Sukyoung K. Yi. Uv star formation rates in the local universe. *The Astrophysical Journal Supplement Series*, 173 (2):267–292, December 2007. ISSN 1538-4365. doi: 10.1086/519218. URL `http://dx.doi.org/10.1086/519218`.

[134] M. L. P. Gunawardhana, A. M. Hopkins, J. Bland-Hawthorn, S. Brough, R. Sharp, J. Loveday, E. Taylor, D. H. Jones, M. A. Lara-López, A. E. Bauer, M. Colless, M. Owers, I. K. Baldry, A. R. López–Sánchez, C. Foster, S. Bamford, M. J. I. Brown, S. P. Driver, M. J. Drinkwater, J. Liske, M. Meyer, P. Norberg, A. S. G. Robotham, J. H. Y. Ching, M. E. Cluver, S. Croom, L. Kelvin, M. Prescott, O. Steele, D. Thomas, and L. Wang. Galaxy and mass assembly: evolution of the h luminosity function and star formation rate density up to z lt; 0.35. *Monthly Notices of the Royal Astronomical Society*, 433(4):2764–2789, June 2013. ISSN 0035-8711. doi: 10.1093/mnras/stt890. URL `http://dx.doi.org/10.1093/mnras/stt890`.

[135] Chun Ly, Janice C. Lee, Daniel A. Dale, Ivelina Momcheva, Samir Salim, Shawn Staudaher, Carolynn A. Moore, and Rose Finn. The h luminosity function and star formation rate volume density atz= 0.8 from the newfirm h survey. *The Astrophysical Journal*, 726(2):109, December 2010. ISSN 1538-4357. doi: 10.1088/0004-637x/726/2/109. URL `http://dx.doi.org/10.1088/0004-637X/726/2/109`.

[136] Chun Ly, Matthew A. Malkan, Masao Hayashi, Kentaro Motohara, Nobunari Kashikawa, Kazuhiro Shimasaku, Tohru Nagao, and Celestine Grady. A census of star-forming galaxies atz= 1-3 in the subaru deep field. *The Astrophysical Journal*, 735(2):91, June 2011. ISSN 1538-4357. doi: 10.1088/0004-637x/735/2/91. URL `http://dx.doi.org/10.1088/0004-637X/735/2/91`.

[137] Xian Zhong Zheng, Eric F. Bell, Casey Papovich, Christian Wolf, Klaus Meisenheimer, Hans-Walter Rix, George H. Rieke, and Rachel Somerville. The dependence of star formation on galaxy stellar mass. *The Astrophysical Journal*, 661(1):L41–L44, April 2007. ISSN 1538-4357. doi: 10.1086/518690. URL `http://dx.doi.org/10.1086/518690`.

[138] Wiphu Rujopakarn, Daniel J. Eisenstein, George H. Rieke, Casey Papovich, Richard J. Cool, John Moustakas, Buell T. Jannuzi, Christopher S. Kochanek, Marcia J. Rieke, Arjun Dey, Peter Eisenhardt, Steve S. Murray, Michael J. I. Brown, and Emeric Le Floc'h. The evolution of the star formation rate of galaxies at 0.0 z 1.2. *The Astrophysical Journal*, 718(2):1171–1185, July 2010. ISSN 1538-4357. doi: 10.1088/0004-637x/718/2/1171. URL `http://dx.doi.org/10.1088/0004-637X/718/2/1171`.

[139] Alyssa B. Drake, Chris Simpson, Ivan K. Baldry, Phil A. James, Chris A. Collins, Masami Ouchi, Suraphong Yuma, James S. Dunlop, and Daniel J. B. Smith. Evolution of star formation in the ukidss ultra deep survey field – ii. star formation as a function of stellar mass betweenz = 1.46 and 0.63. *Monthly Notices of the Royal Astronomical Society*, 454(2):2015–2025, October 2015. ISSN 1365-2966. doi: 10.1093/mnras/stv2027. URL `http://dx.doi.org/10.1093/mnras/stv2027`.

[140] Hyunjin Shim, James Colbert, Harry Teplitz, Alaina Henry, Mattew Malkan, Patrick McCarthy, and Lin Yan. Global star formation rate density over 0.7 lt;zlt; 1.9. *The Astrophysical Journal*, 696(1):785–796, April 2009. ISSN 1538-4357. doi: 10.1088/0004-637x/696/1/785. URL `http://dx.doi.org/10.1088/0004-637X/696/1/785`.

[141] David Sobral, Philip N. Best, Ian Smail, Bahram Mobasher, John Stott, and David Nisbet. The stellar mass function of star-forming galaxies and the mass-dependent sfr function since z = 2.23 from hizels. *Monthly Notices of the Royal Astronomical Society*, 437(4):3516–3528, December 2013. ISSN 1365-2966. doi: 10.1093/mnras/stt2159. URL `http://dx.doi.org/10.1093/mnras/stt2159`.

[142] B. Magnelli, D. Elbaz, R. R. Chary, M. Dickinson, D. Le Borgne, D. T. Frayer, and C. N. A. Willmer. Evolution of the dusty infrared luminosity function fromz = 0toz = 2.3using observations fromspitzer. *Astronomy amp; Astrophysics*, 528:A35, February 2011. ISSN 1432-0746. doi: 10.1051/0004-6361/200913941. URL `http://dx.doi.org/10.1051/0004-6361/200913941`.

[143] A. Karim, E. Schinnerer, A. Martínez-Sansigre, M. T. Sargent, A. van der Wel, H.-W. Rix, O. Ilbert, V. Smolčić, C. Carilli, M. Pannella, A. M. Koekemoer, E. F. Bell, and M. Salvato. The star formation history of mass-selected galaxies in the cosmos field. *The Astrophysical Journal*, 730(2):61, March 2011. ISSN 1538-4357. doi: 10.1088/0004-637x/730/2/61. URL `http://dx.doi.org/10.1088/0004-637X/730/2/61`.

[144] P. Santini, A. Fontana, A. Grazian, S. Salimbeni, F. Fiore, F. Fontanot, K. Boutsia, M. Castellano, S. Cristiani, C. De Santis, S. Gallozzi, E. Giallongo, N. Menci, M. Nonino, D. Paris, L. Pentericci, and E. Vanzella. Star formation and mass assembly in high redshift galaxies. *Astronomy amp; Astrophysics*, 504(3):751–767, July 2009. ISSN 1432-0746. doi: 10.1051/0004-6361/200811434. URL `http://dx.doi.org/10.1051/0004-6361/200811434`.

[145] M. Kajisawa, T. Ichikawa, T. Yamada, Y. K. Uchimoto, T. Yoshikawa, M. Akiyama, and M. Onodera. Moircs deep survey. viii. evolution of star formation activity as a function of stellar mass in galaxies sincez 3. *The Astrophysical Journal*, 723(1):129–145, October 2010. ISSN 1538-4357. doi: 10.1088/0004-637x/723/1/129. URL `http://dx.doi.org/10.1088/0004-637X/723/1/129`.

[146] C. Schreiber, M. Pannella, D. Elbaz, M. Béthermin, H. Inami, M. Dickinson, B. Magnelli, T. Wang, H. Aussel, E. Daddi, S. Juneau, X. Shu, M. T. Sargent, V. Buat, S. M. Faber, H. C. Ferguson, M. Giavalisco, A. M. Koekemoer, G. Magdis, G. E. Morrison, C. Papovich, P. Santini, and D. Scott. Theherschelview of the dominant mode of galaxy growth fromz= 4 to the present day. *Astronomy amp; Astrophysics*, 575:A74, February 2015. ISSN 1432-0746. doi: 10.1051/0004-6361/201425017. URL `http://dx.doi.org/10.1051/0004-6361/201425017`.

[147] L. Dunne, R. J. Ivison, S. Maddox, M. Cirasuolo, A. M. Mortier, S. Foucaud, E. Ibar, O. Almaini, C. Simpson, and R. McLure. The star formation history ofk-selected galaxies. *Monthly Notices of the Royal Astronomical Society*, 394(1):3–20, March 2009. ISSN 1365-2966. doi: 10.1111/j.1365-2966.2008.13900.x. URL `http://dx.doi.org/10.1111/j.1365-2966.2008.13900.x`.

[148] O. Cucciati, L. Tresse, O. Ilbert, O. Le Fèvre, B. Garilli, V. Le Brun, P. Cassata, P. Franzetti, D. Maccagni, M. Scodeggio, E. Zucca, G. Zamorani,

S. Bardelli, M. Bolzonella, R. M. Bielby, H. J. McCracken, A. Zanichelli, and D. Vergani. The star formation rate density and dust attenuation evolution over 12 gyr with the vvds surveys. *Astronomy amp; Astrophysics*, 539:A31, February 2012. ISSN 1432-0746. doi: 10.1051/0004-6361/201118010. URL `http://dx.doi.org/10.1051/0004-6361/201118010`.

[149] D. Le Borgne, D. Elbaz, P. Ocvirk, and C. Pichon. Cosmic star-formation history from a non-parametric inversion of infrared galaxy counts. *Astronomy amp; Astrophysics*, 504(3):727–740, July 2009. ISSN 1432-0746. doi: 10.1051/0004-6361/200809945. URL `http://dx.doi.org/10.1051/0004-6361/200809945`.

[150] R. F. J. van der Burg, H. Hildebrandt, and T. Erben. The uv galaxy luminosity function atz=3–5 from the cfht legacy survey deep fields. *Astronomy amp; Astrophysics*, 523:A74, November 2010. ISSN 1432-0746. doi: 10.1051/0004-6361/200913812. URL `http://dx.doi.org/10.1051/0004-6361/200913812`.

[151] Naoki Yoshida, Kazuyuki Omukai, Lars Hernquist, and Tom Abel. Formation of primordial stars in a cdm universe. *The Astrophysical Journal*, 652(1):6–25, November 2006. ISSN 1538-4357. doi: 10.1086/507978. URL `http://dx.doi.org/10.1086/507978`.

[152] Steven L. Finkelstein, Russell E. Ryan, Casey Papovich, Mark Dickinson, Mimi Song, Rachel S. Somerville, Henry C. Ferguson, Brett Salmon, Mauro Giavalisco, Anton M. Koekemoer, Matthew L. N. Ashby, Peter Behroozi, Marco Castellano, James S. Dunlop, Sandy M. Faber, Giovanni G. Fazio, Adriano Fontana, Norman A. Grogin, Nimish Hathi, Jason Jaacks, Dale D. Kocevski, Rachael Livermore, Ross J. McLure, Emiliano Merlin, Bahram Mobasher, Jeffrey A. Newman, Marc Rafelski, Vithal Tilvi, and S. P. Willner. The evolution of the galaxy rest-frame ultraviolet luminosity function over the first two billion years. *The Astrophysical Journal*, 810(1):71, September 2015. ISSN 1538-4357. doi: 10.1088/0004-637x/810/1/71. URL `http://dx.doi.org/10.1088/0004-637X/810/1/71`.

[153] Matthew D. Kistler, Hasan Yuksel, and Andrew M. Hopkins. The cosmic star formation rate from the faintest galaxies in the unobservable universe, 2013. URL `https://arxiv.org/abs/1305.1630`.

[154] Nora Elisa Chisari, David Alonso, Elisabeth Krause, C. Danielle Leonard, Philip Bull, Jérémy Neveu, Antonia Sierra Villarreal, Sukhdeep Singh, Thomas McClintock, John Ellison, Zilong Du, Joe Zuntz, Alexander Mead, Shahab Joudaki, Christiane S. Lorenz, Tilman Tröster, Javier Sanchez, Francois Lanusse, Mustapha Ishak, Renée Hlozek, Jonathan Blazek, Jean-Eric Campagne, Husni Almoubayyed, Tim Eifler, Matthew Kirby, David Kirkby, Stéphane Plaszczynski, Anže Slosar, Michal Vrastil, Erika L. Wagoner, and LSST Dark Energy Science Collaboration. Core Cosmology Library: Precision Cosmological Predictions for LSST. , 242(1):2, May 2019. doi: 10.3847/1538-4365/ab1658.

[155] Planck Collaboration, P. A. R. Ade, N. Aghanim, C. Armitage-Caplan, M. Arnaud, M. Ashdown, F. Atrio-Barandela, J. Aumont, C. Baccigalupi, A. J. Banday, R. B. Barreiro, E. Battaner, K. Benabed, A. Benoît, A. Benoit-Lévy, J. P. Bernard, M. Bersanelli, P. Bielewicz, J. Bobin, J. J. Bock, J. R. Bond, J. Borrill, F. R. Bouchet, F. Boulanger, M. Bridges, M. Bucher, C. Burigana, J. F. Cardoso, A. Catalano, A. Challinor, A. Chamballu, R. R. Chary, X. Chen, H. C. Chiang, L. Y. Chiang, P. R. Christensen, S. Church, D. L. Clements, S. Colombi, L. P. L. Colombo, C. Combet, B. Comis, F. Couchot, A. Coulais, B. P. Crill, A. Curto, F. Cuttaia, L. Danese, R. D. Davies, P. de Bernardis, A. de Rosa, G. de Zotti, J. Delabrouille, J. M. Delouis, F. X. Désert, C. Dickinson, J. M. Diego, H. Dole, S. Donzelli, O. Doré, M. Douspis, X. Dupac, G. Efstathiou, T. A. Enßlin, H. K. Eriksen, E. Falgarone, F. Finelli, O. Forni, M. Frailis, E. Franceschi, S. Galeotta, K. Ganga, M. Giard, Y. Giraud-Héraud, J. González-Nuevo, K. M. Górski, S. Gratton, A. Gregorio, A. Gruppuso, F. K. Hansen, D. Hanson, D. Harrison, S. Henrot-Versillé, C. Hernández-Monteagudo, D. Herranz, S. R. Hildebrandt, E. Hivon, M. Hobson, W. A. Holmes, A. Hornstrup, W. Hovest, K. M. Huffenberger, G. Hurier, A. H. Jaffe, T. R. Jaffe, W. C. Jones, M. Juvela, E. Keihänen, R. Keskitalo, T. S. Kisner, R. Kneissl, J. Knoche, L. Knox, M. Kunz, H. Kurki-Suonio, G. Lagache, J. M. Lamarre, A. Lasenby, R. J. Laureijs, C. R. Lawrence, J. P. Leahy, R. Leonardi, C. Leroy, J. Lesgourgues, M. Liguori, P. B. Lilje, M. Linden-Vørnle, M. López-Caniego, P. M. Lubin, J. F. Macías-Pérez, B. Maffei, N. Mandolesi, M. Maris, D. J. Marshall, P. G. Martin, E. Martínez-González, S. Masi, M. Massardi, S. Matarrese, F. Matthai, P. Mazzotta, P. McGehee, A. Melchiorri, L. Mendes, A. Mennella, M. Migliaccio, S. Mitra, M. A. Miville-Deschênes, A. Moneti, L. Montier, G. Morgante, D. Mortlock, D. Munshi, J. A. Murphy, P. Naselsky, F. Nati, P. Natoli, C. B. Netterfield, H. U. Nørgaard-Nielsen, C. North, F. Noviello, D. Novikov, I. Novikov, S. Osborne, C. A. Oxborrow, F. Paci, L. Pagano, F. Pajot, D. Paoletti, F. Pasian, G. Patanchon, O. Perdereau, L. Perotto, F. Perrotta, F. Piacentini, M. Piat, E. Pierpaoli, D. Pietrobon, S. Plaszczynski, E. Pointecouteau, G. Polenta, N. Ponthieu, L. Popa, T. Poutanen, G. W. Pratt, G. Prézeau, S. Prunet, J. L. Puget, J. P. Rachen, M. Reinecke, M. Remazeilles, C. Renault, S. Ricciardi, T. Riller, I. Ristorcelli, G. Rocha, C. Rosset, G. Roudier, B. Rusholme, D. Santos, G. Savini, D. Scott, E. P. S. Shellard, L. D. Spencer, J. L. Starck, V. Stolyarov, R. Stompor, R. Sudiwala, F. Sureau, D. Sutton, A. S. Suur-Uski, J. F. Sygnet, J. A. Tauber, D. Tavagnacco, L. Terenzi, M. Tomasi, M. Tristram, M. Tucci, G. Umana, L. Valenziano, J. Valiviita, B. Van Tent, P. Vielva, F. Villa, N. Vittorio, L. A. Wade, B. D. Wandelt, D. Yvon, A. Zacchei, and A. Zonca. Planck 2013 results. IX. HFI spectral response. , 571:A9, November 2014. doi: 10.1051/0004-6361/201321531.

[156] G. Lagache, M. Béthermin, L. Montier, P. Serra, and M. Tucci. Impact of polarised extragalactic sources on the measurement of cmbb-mode anisotropies. *Astronomy amp; Astrophysics*, 642:A232, October 2020. ISSN 1432-0746. doi: 10.1051/0004-6361/201937147. URL `http://dx.doi.org/10.1051/0004-6361/201937147`.

[157] Jesús Torrado and Antony Lewis. Cobaya: Bayesian analysis in cosmology.

Astrophysics Source Code Library, record ascl:1910.019, October 2019.

[158] Jesús Torrado and Antony Lewis. Cobaya: code for Bayesian analysis of hierarchical physical models. , 2021(5):057, May 2021. doi: 10.1088/1475-7516/2021/05/057.

[159] J. Bardeen, L. N. Cooper, and J. R. Schrieffer. Theory of superconductivity. *Phys. Rev.*, 108:1175–1204, Dec 1957. doi: 10.1103/PhysRev.108.1175. URL `https://link.aps.org/doi/10.1103/PhysRev.108.1175`.

[160] P.S. Barry. On the development of SuperSpec: a fully integrated on-chip spectrometer for far-infrared astronomy. *PhD Thesis, Cardiff University*, 2014.

[161] David M Pozar. *Microwave engineering; 3rd ed.* Wiley, Hoboken, NJ, 2005. URL `https://cds.cern.ch/record/882338`.

[162] Jiansong Gao. *The Physics of Superconducting Microwave Resonators.* Phd thesis, California Institute of Technology, Pasadena, CA, 2008. `https://resolver.caltech.edu/CaltechETD:etd-06092008-235549`.

[163] R. McGeehan, P. S. Barry, E. Shirokoff, C. M. Bradford, G. Che, J. Glenn, S. Gordon, S. Hailey-Dunsheath, M. Hollister, A. Kovács, H. G. LeDuc, P. Mauskopf, C. McKenney, T. Reck, J. Redford, C. Tucker, J. Turner, S. Walker, J. Wheeler, and J. Zmuidzinas. Low-Temperature Noise Performance of SuperSpec and Other Developments on the Path to Deployment. *Journal of Low Temperature Physics*, 193(5):1024–1032, December 2018. ISSN 1573-7357. doi: 10.1007/s10909-018-2061-6. URL `https://doi.org/10.1007/s10909-018-2061-6`.

[164] M. R. Vissers, J. E. Austermann, M. Malnou, C. M. McKenney, B. Dober, J. Hubmayr, G. C. Hilton, J. N. Ullom, and J. Gao. Ultrastable millimeter-wave kinetic inductance detectors. *Applied Physics Letters*, 116(3):032601, January 2020. doi: 10.1063/1.5138122.

[165] Bluefors Oy. Ld dilution refrigerator measurement system, 2024. URL `https://bluefors.com/products/dilution-refrigerator-measurement-systems/ld-dilution-refrigerator-measurement-system/`.

[166] P. J. de Visser, S. Withington, and D. J. Goldie. Readout-power heating and hysteretic switching between thermal quasiparticle states in kinetic inductance detectors. *Journal of Applied Physics*, 108(11):114504-114504-9, December 2010. doi: 10.1063/1.3517152.

[167] Jiansong Gao, Miguel Daal, John M. Martinis, Anastasios Vayonakis, Jonas Zmuidzinas, Bernard Sadoulet, Benjamin A. Mazin, Peter K. Day, and Henry G. Leduc. A semiempirical model for two-level system noise in superconducting microresonators. *Applied Physics Letters*, 92(21):212504, May 2008. doi: 10.1063/1.2937855.

[168] Jiansong Gao, Benjamin Mazin, Miguel Daal, Peter Day, Henry LeDuc, and Jonas Zmuidzinas. Power dependence of phase noise in microwave kinetic inductance detectors. In Jonas Zmuidzinas, Wayne S. Holland, Stafford Withington, and William D. Duncan, editors, *Millimeter and Submillimeter Detectors and Instrumentation for Astronomy III*, volume 6275, page 627509. International Society for Optics and Photonics, SPIE, 2006. doi: 10.1117/12.672590. URL `https://doi.org/10.1117/12.672590`.

[169] L. J. Swenson, P. K. Day, B. H. Eom, H. G. Leduc, N. Llombart, C. M. McKenney, O. Noroozian, and J. Zmuidzinas. Operation of a titanium nitride superconducting microresonator detector in the nonlinear regime. *Journal of Applied Physics*, 113(10), March 2013. ISSN 1089-7550. doi: 10.1063/1.4794808. URL `http://dx.doi.org/10.1063/1.4794808`.

[170] P. D. Mauskopf, S. Doyle, P. Barry, S. Rowe, A. Bidead, P. A. R. Ade, C. Tucker, E. Castillo, A. Monfardini, J. Goupy, and M. Calvo. Photon-Noise Limited Performance in Aluminum LEKIDs. *Journal of Low Temperature Physics*, 176(3-4):545–552, August 2014. doi: 10.1007/s10909-013-1069-1.

[171] P. J. de Visser, J. J. A. Baselmans, P. Diener, S. J. C. Yates, A. Endo, and T. M. Klapwijk. Generation-Recombination Noise: The Fundamental Sensitivity Limit for Kinetic Inductance Detectors. *Journal of Low Temperature Physics*, 167(3):335–340, May 2012. ISSN 1573-7357. doi: 10.1007/s10909-012-0519-5. URL `https://doi.org/10.1007/s10909-012-0519-5`.

[172] J. Hubmayr, J. Beall, D. Becker, H.-M. Cho, M. Devlin, B. Dober, C. Groppi, G. C. Hilton, K. D. Irwin, D. Li, and et al. Photon-noise limited sensitivity in titanium nitride kinetic inductance detectors. *Applied Physics Letters*, 106 (7):073505, Feb 2015. ISSN 1077-3118. doi: 10.1063/1.4913418. URL `http://dx.doi.org/10.1063/1.4913418`.

[173] K. S. Karkare, A. J. Anderson, P. S. Barry, B. A. Benson, J. E. Carlstrom, T. Cecil, C. L. Chang, M. A. Dobbs, M. Hollister, G. K. Keating, D. P. Marrone, J. McMahon, J. Montgomery, Z. Pan, G. Robson, M. Rouble, E. Shirokoff, and G. Smecher. Spt-slim: A line intensity mapping pathfinder for the south pole telescope. *Journal of Low Temperature Physics*, 209(5–6): 758–765, March 2022. ISSN 1573-7357. doi: 10.1007/s10909-022-02702-2. URL `http://dx.doi.org/10.1007/s10909-022-02702-2`.

[174] Julius Cohen. Introduction to fourier transform spectroscopy:, 1986-01-01 05:01:00 1986.

[175] P. A. R. Ade, R. W. Aikin, D. Barkats, S. J. Benton, C. A. Bischoff, J. J. Bock, K. J. Bradford, J. A. Brevik, I. Buder, E. Bullock, C. D. Dowell, L. Duband, J. P. Filippini, S. Fliescher, S. R. Golwala, M. Halpern, M. Hasselfield, S. R. Hildebrandt, G. C. Hilton, H. Hui, K. D. Irwin, J. H. Kang, K. S. Karkare, J. P. Kaufman, B. G. Keating, S. Kefeli, S. A. Kernasovskiy, J. M. Kovac, C. L. Kuo, E. M. Leitch, M. Lueker, K. G. Megerian, C. B. Netterfield, H. T. Nguyen, R. O'Brient, R. W. Ogburn IV, A. Orlando, C. Pryke, S. Richter, R. Schwarz, C. D. Sheehy, Z. K. Staniszewski, R. V. Sudiwala, G. P. Teply, K. Thompson, J. E. Tolan, A. D. Turner, A. G. Vieregg, A. C. Weber, C. L. Wong, and K. W.

Yoon. BICEP2 KECK ARRAY. IV. OPTICAL CHARACTERIZATION AND PERFORMANCE OF THE BICEP2 ANDKECK ARRAY EXPERIMENTS. *The Astrophysical Journal*, 806(2):206, jun 2015. doi: 10.1088/0004-637x/806/2/206. URL `https://doi.org/10.1088%2F0004-637x%2F806%2F2%2F206`.

[176] Paul F. Goldsmith. *Quasioptical systems: Gaussian beam quasioptical propogation and applications*. IEEE press, 1998. ISBN 0-7803-3439-6.

[177] J. Delabrouille, M. Betoule, J.-B. Melin, M.-A. Miville-Deschênes, J. Gonzalez-Nuevo, M. Le Jeune, G. Castex, G. de Zotti, S. Basak, M. Ashdown, J. Aumont, C. Baccigalupi, A. J. Banday, J.-P. Bernard, F. R. Bouchet, D. L. Clements, A. da Silva, C. Dickinson, F. Dodu, K. Dolag, F. Elsner, L. Fauvet, G. Faÿ, G. Giardino, S. Leach, J. Lesgourgues, M. Liguori, J. F. Macías-Pérez, M. Massardi, S. Matarrese, P. Mazzotta, L. Montier, S. Mottet, R. Paladini, B. Partridge, R. Piffaretti, G. Prezeau, S. Prunet, S. Ricciardi, M. Roman, B. Schaefer, and L. Toffolatti. The pre-launchplancksky model: a model of sky emission at submillimetre to centimetre wavelengths. *Astronomy & Astrophysics*, 553:A96, May 2013. ISSN 1432-0746. doi: 10.1051/0004-6361/201220019. URL `http://dx.doi.org/10.1051/0004-6361/201220019`.

[178] Planck Collaboration, Y. Akrami, M. Ashdown, J. Aumont, C. Baccigalupi, M. Ballardini, A. J. Band ay, R. B. Barreiro, N. Bartolo, S. Basak, K. Benabed, J. P. Bernard, M. Bersanelli, P. Bielewicz, J. R. Bond, J. Borrill, F. R. Bouchet, F. Boulanger, A. Bracco, M. Bucher, C. Burigana, E. Calabrese, J. F. Cardoso, J. Carron, H. C. Chiang, C. Combet, B. P. Crill, P. de Bernardis, G. de Zotti, J. Delabrouille, J. M. Delouis, E. Di Valentino, C. Dickinson, J. M. Diego, A. Ducout, X. Dupac, G. Efstathiou, F. Elsner, T. A. Enßlin, E. Falgarone, Y. Fantaye, K. Ferrière, F. Finelli, F. Forastieri, M. Frailis, A. A. Fraisse, E. Franceschi, A. Frolov, S. Galeotta, S. Galli, K. Ganga, R. T. Génova-Santos, T. Ghosh, J. González-Nuevo, K. M. Górski, A. Gruppuso, J. E. Gudmundsson, V. Guillet, W. Handley, F. K. Hansen, D. Herranz, Z. Huang, A. H. Jaffe, W. C. Jones, E. Keihänen, R. Keskitalo, K. Kiiveri, J. Kim, N. Krachmalnicoff, M. Kunz, H. Kurki-Suonio, J. M. Lamarre, A. Lasenby, M. Le Jeune, F. Levrier, M. Liguori, P. B. Lilje, V. Lindholm, M. López-Caniego, P. M. Lubin, Y. Z. Ma, J. F. Macías-Pérez, G. Maggio, D. Maino, N. Mandolesi, A. Mangilli, P. G. Martin, E. Martínez-González, S. Matarrese, J. D. McEwen, P. R. Meinhold, A. Melchiorri, M. Migliaccio, M. A. Miville-Deschênes, D. Molinari, A. Moneti, L. Montier, G. Morgante, P. Natoli, L. Pagano, D. Paoletti, V. Pettorino, F. Piacentini, G. Polenta, J. L. Puget, J. P. Rachen, M. Reinecke, M. Remazeilles, A. Renzi, G. Rocha, C. Rosset, G. Roudier, J. A. Rubiño-Martín, B. Ruiz-Granados, L. Salvati, M. Sandri, M. Savelainen, D. Scott, J. D. Soler, L. D. Spencer, J. A. Tauber, D. Tavagnacco, L. Toffolatti, M. Tomasi, T. Trombetti, J. Valiviita, F. Vansyngel, B. Van Tent, P. Vielva, F. Villa, N. Vittorio, I. K. Wehus, A. Zacchei, and A. Zonca. Planck 2018 results. XI. Polarized dust foregrounds. , 641:A11, September 2020. doi: 10.1051/0004-6361/201832618.

[179] L. M. Mocanu, T. M. Crawford, J. D. Vieira, K. A. Aird, M. Aravena, J. E. Austermann, B. A. Benson, M. Béthermin, L. E. Bleem, M. Bothwell, J. E. Carlstrom, C. L. Chang, S. Chapman, H.-M. Cho, A. T. Crites, T. de Haan,

M. A. Dobbs, W. B. Everett, E. M. George, N. W. Halverson, N. Harrington, Y. Hezaveh, G. P. Holder, W. L. Holzapfel, S. Hoover, J. D. Hrubes, R. Keisler, L. Knox, A. T. Lee, E. M. Leitch, M. Lueker, D. Luong-Van, D. P. Marrone, J. J. McMahon, J. Mehl, S. S. Meyer, J. J. Mohr, T. E. Montroy, T. Natoli, S. Padin, T. Plagge, C. Pryke, A. Rest, C. L. Reichardt, J. E. Ruhl, J. T. Sayre, K. K. Schaffer, E. Shirokoff, H. G. Spieler, J. S. Spilker, B. Stalder, Z. Staniszewski, A. A. Stark, K. T. Story, E. R. Switzer, K. Vanderlinde, and R. Williamson. Extragalactic Millimeter-wave Point-source Catalog, Number Counts and Statistics from 771 deg^2 of the SPT-SZ Survey. , 779:61, December 2013. doi: 10.1088/0004-637X/779/1/61.